

**On a Finite Element Based Approach to the Design and
Optimisation of Elastomeric Additively Manufactured
Cellular Structures for Impact Mitigation in Helmets**

A thesis presented for the degree of
Doctor of Philosophy



Rhosslyn Adams

Cardiff University
United Kingdom
August 9, 2022

Abstract

Physical activity that includes elevation or speed, such as cycling, carries the risk of head injury. The risk of injury is mitigated by wearing safety helmets. Whilst cycling is adopted as an exemplar when evaluating new helmets, garnering notable research interest in recent years, head injury remains a notable cause of mortality and morbidity in cycling accidents. Indeed, head injury still causes 69–93% of fatal bicycle accidents; hence, new helmet technologies have significant social importance.

A critical strategy in head injury mitigation in cycling accidents is the use of a protective helmet and is strongly advocated by The World Health Organisation. It has been reported that the likelihood of sustaining a traumatic brain injury (TBI) is reduced (18%) when wearing a helmet compared to non-helmet cyclists (48%). Current bicycle helmets are designed to protect the user by deforming to mitigate the impact energy and reduce the resultant acceleration. Due to the onset of permanent deformation within the helmet following an impact, its protective capacity is diminished. Consequently, they do not provide adequate performance when subject to a history of loading, such as multiple or consecutive impacts. Indeed, it is common to wear a previously damaged helmet despite contrary advice. Current multi-hit solutions are derived from elastomeric foams which have been applied in several other sporting helmets. These materials, however, suffer from a lack of development in recent years. Furthermore, they have limited geometric freedom, which precludes optimisation. This thesis describes four related investigations which present a finite-element based optimisation approach to the development of new helmet liners leveraging the mechanical benefits of cellular structures and elastomeric materials realised through additive manufacturing.

A laser sintered elastomer was characterised by performing low, intermediate and high rate uniaxial tension tests manufactured under three build orientations. Furthermore, planar, equibiaxial tension and stress relaxation tests were carried out. These data demonstrated notable anisotropy, as well as significantly different behaviour across strain rates and deformation modes, necessitating fit of an augmented hyperelastic and linear viscoelastic model. FE software was then used to calibrate material model coefficients, with their validity evaluated by comparing the simulated and experimental behaviour of the material in isolated (uniaxial tensile) and mixed modal (honeycomb compression) deformation states. Close correlation demonstrated that the material model coefficients were valid, removing a barrier to adopting exclusive finite-element based in future investigations.

Further, laser sintering was used to manufacture different structural variations of a novel pre-buckled circular honeycomb. The mechanical behaviour of these structures was examined under both quasi-static and dynamic impact loading. Pre-buckled circular honeycombs with aspect ratios, defined as the ratio of minor to major axis of the honeycomb elliptical profile, $e = 0.8$ and $e = 0.6$ were compared to a traditional, straight-walled honeycomb, $e = 1.0$. It was found that the mechanical behaviour of the honeycomb can be tailored to yield different mechanical responses. Principally, decreasing the aspect ratio reduced the stress at yield, as well as the total energy absorbed until densification, however, this alleviated the characteristic stress-softening response of traditional honeycombs under static and impact conditions. When subjected to multiple cycles of loading, a stabilised response was observed. Finite element simulation closely agreed with the experimental results. A simplified, periodic boundary condition model was also investigated, which closely represented the experimental results whilst alleviating computational run time by nominally 75%. The numerical full factorial parameter design sweep identified a broad range of mechanical behaviour, enabling identification of geometric bounds to be used in future optimisation studies.

Finite element simulation was used to analyse the response of an elastomeric pre-buckled honeycomb structure under impact loading, to establish its suitability for use in helmet liners. Finite element-based optimisation was performed using a search algorithm that uses a radial basis function. This approach identified optimal configurations of the pre-buckled honeycomb structure, based on struc-

tural bounds identified from previous investigations, subject to impact loading conditions. Furthermore, the influence of objective function, peak acceleration and head injury criterion was analysed with respect to the resultant mechanical behaviour of the structure. Numerical results demonstrate that this class of structure can exceed the performance threshold of a common helmet design standard and minimise the resultant injury index. Experimental testing, facilitated through laser sintering, validated the output of the numerical optimisation. When subject to initial impact loading, the fabricated samples satisfied their objective functions. Successive impact loading was performed to assess the performance and degradation. Samples optimised for peak acceleration demonstrated superior performance after stabilisation, relative to their initial response.

The finite-element based optimisation sequence was repeated using boundary conditions (contact area, mass and velocity) associated with the helmet design envelope and standard. Two optimal configurations, based on different objective functions, peak translational acceleration and head injury criterion, were then proliferated throughout a helmet liner before being subjected to typical frontal head impacts under direct and oblique conditions. Comparison was drawn relative to two densities of a common multi-hit material used in helmet liners, vinyl nitrile foam. Kinematic-based injury criteria were calculated, as well as tissue-based injury criteria, using a validated finite element model of the human head for each impact. Results demonstrated that the optimal pre-buckled honeycomb liners had the best performance, yielding reductions in both kinematic and tissue-based injury criteria. Under direct impacts, values for head injury criterion, maximum principal strain and cumulative strain damage measure were reduced by 34%, 8.6% and 23.7%. Under oblique impact, values for head injury criterion, rotational injury criterion, generalized model for brain injury threshold, head impact power, maximum principal strain and cumulative strain damage measure were reduced by 49.9%, 56%, 29.6%, 40.8%, 14.9% and 66.7%. Honeycombs optimised using head injury criteria as the objective function yielded a reduction in all severity metrics relative to honeycombs optimised using peak translational acceleration, though design standards mandate an acceptable threshold for peak translational acceleration yet not for other injury metrics. The work reported in this thesis identifies a successful design and optimisation strategy to aid and inform the development of next generation helmet liners.

Dedication

To my friends and family, I could not have done this without you. Thank you for all your love and support along the way.

Declaration

This work has not previously been accepted in substance for any degree and is not concurrently submitted in candidature for any degree.

Signed: *R. Adams*

Date: *August 9, 2022*

Statement 1

This thesis is being submitted in partial fulfilment of the requirements for the degree of PhD.

Signed: *R. Adams*

Date: *August 9, 2022*

Statement 2

This thesis is the result of my own independent work/investigation, except where otherwise stated. Other sources are acknowledged by explicit references.

Signed: *R. Adams*

Date: *August 9, 2022*

Statement 3

I hereby give consent for my thesis, if accepted, to be available for photocopying and for inter-library loan, and for the title and summary to be made available to outside organisations.

Signed: *R. Adams*

Date: *August 9, 2022*

Acknowledgements

I would like to acknowledge the people, who without this PhD would not have been possible. Firstly, my sincere thanks goes to Peter Theobald and Shwe Soe. From my undergraduate dissertation to postgraduate thesis, you have both been a source of continued encouragement, guidance and support.

Next, I would like to thank my colleagues in w/1.09 who I shared the highs and the lows of postgraduate study. Whilst there have been many of you over the years, Scott Townsend, Ben Hanna and Michael Robinson have provided notable help, advice, and contributions to the work presented in this thesis.

I would also like to thank my collaborators. Ian King and Richard Thomas, who provided technical assistance during testing at Cardiff University. Rafeal Celleghini, for providing access to high strain rate testing facilities. And lastly, Michael Gilchrist, for the use of the University College Dublin Brain Trauma Model.

Finally, I would like to thank the financial support of Charles Owen and therefore the contributions of Matthew Stewart and the late Roy Burek. Roy's interest in head injury transcended his commercial interests, which distinguished him from many others.

Contents

List of Figures	xiii
List of Tables	xxii
1 Introduction	1
1.1 General	1
1.2 Research aim	2
1.3 Thesis structure	2
2 Literature review	5
2.1 Introduction	5
2.2 Head injury	6
2.2.1 Anatomy of the head	6
2.2.2 Injury mechanisms	9
2.2.3 Common cycling injuries	9
2.2.4 Injury metrics	12
2.3 Helmet design	15
2.3.1 Functional requirements	15
2.3.2 Components	17

2.3.3	Design for impact mitigation	19
2.3.4	Impact test protocols	24
2.3.5	Emerging technologies	27
2.4	Prismatic cellular structures	30
2.4.1	Topology	31
2.4.2	Mechanical properties	33
2.4.3	Numerical modelling	38
2.4.4	Manufacturing methods	40
2.5	Polymer Additive Manufacturing	42
2.5.1	Process definitions	42
2.5.2	Laser sintering mechanics	44
2.5.3	Manufacturing artefacts	46
2.5.4	Available materials	49
2.6	Research Focus	51
2.7	Conclusion	54
3	Experimental Characterisation and Numerical Material Model Calibration of a Laser Sintered Elastomer	56
3.1	Introduction	57
3.2	Materials & Methods	58
3.2.1	Laser Sintered Elastomer	58
3.2.2	Strain Rate and Build Orientation Sensitivity	59
3.2.3	Characterisation for Material Model Calibration	62
3.2.4	Material Model Callibration	65
3.2.5	Finite Element Analysis	66

3.2.6	Experimental Material Model Validation	69
3.3	Results	71
3.3.1	Strain Rate and Build Direction Sensitivity	71
3.3.2	Hyperelastic Material Model Calibration	72
3.3.3	Linear Viscoelastic Material Model Calibration	76
3.3.4	Finite Element Validation	76
3.4	Discussion	80
3.5	Conclusion	83
4	Experimental and Numerical Analysis of Elastomeric Honeycomb Mechanical Behaviour	84
4.1	Introduction	85
4.2	Materials & Methods	86
4.2.1	Honeycomb Structure	86
4.2.2	Honeycomb Fabrication	88
4.2.3	Experimental Characterisation	89
4.2.4	Performance Parameters	89
4.2.5	Finite Element Model	90
4.3	Results	92
4.3.1	Review of Fabricated Honeycombs	92
4.3.2	Experimental Quasi-Static Compression	95
4.3.3	Experimental Impact Loading	97
4.3.4	Experimental Rate Dependant Behaviour	100
4.3.5	Experimental Multi-Loading Behaviour	101
4.3.6	Finite Element Mesh Independence	103

4.3.7	Finite Element Quasi-Static Compression	105
4.3.8	Finite Element Impact Loading	107
4.3.9	Finite Element Parameter Sweep	108
4.4	Discussion	110
4.5	Conclusion	114
5	Structural Optimisation of an Additively Manufactured Elastomeric Honeycomb Structures	116
5.1	Introduction	117
5.2	Materials & Methods	118
5.2.1	Honeycomb Structural Bounds	118
5.2.2	Finite Element Analysis	119
5.2.3	Optimisation	120
5.2.4	Experimental Validation	124
5.3	Results	125
5.3.1	Optimisation PTA as objective function	125
5.3.2	Optimisation HIC as objective function	130
5.3.3	Experimental Validation	133
5.3.4	Repeat Loading Behaviour	135
5.4	Discussion	137
5.5	Conclusion	141
6	Traumatic Brain Injury Assessment of the Optimised Honeycomb Helmet Liner	143
6.1	Introduction	144
6.2	Material & Methods	145

6.2.1	Helmet Contact Area Approximation	145
6.2.2	Optimisation	146
6.2.3	Helmet Finite Element Model	147
6.2.4	Impact Conditions	151
6.2.5	Traumatic Brain Injury Finite Element Model	153
6.3	Results	154
6.3.1	Optimisation	154
6.3.2	Full Scale Honeycomb Helmet Model	156
6.3.3	Comparison to Elastomeric Foam for Direct Impact	157
6.3.4	Comparison to Elastomeric Foam for Oblique Impact	159
6.3.5	Traumatic Brain Injury Assessment	164
6.4	Discussion	168
6.5	Conclusion	171
7	Conclusion	173
7.1	Summary	174
7.2	Further work	177
7.3	Academic contributions	180
8	Appendix 1	181
8.1	Material Model Coefficients	181
9	Reference List	182

List of Figures

2.1	Sectional view of the scalp, skull, and brain. Adopted from [20]	7
2.2	Illustration of the brain, identifying the frontal, parietal, temporal and occipital lobes. Adopted from [24].	8
2.3	Classification of skull fractures, linear (left), depressed (centre) and diastatic (right)	10
2.4	Cross-sectional view of the human head, illustrating a haematoma.	11
2.5	Exemplar behaviour of a crushable material used for impact mitigation. Adopted from [76]	20
2.6	The influence of material selection when the equivalent magnitude of energy is absorbed. Adopted from [59]	21
2.7	Free body diagram of a helmeted undergoing an oblique impact, giving rise to simultaneous components of normal and tangential force components	23
2.8	Comparison of impact test conditions for guided and free fall. Adopted from [85]	26
2.9	CEN WG11 proposal of test methods for direct and oblique impacts	27
2.10	Slip liner technologies, MIPS (a), SPIN (b), and ODS (c), available within cycling helmets.	28
2.11	Collapsible structure technologies, WaveCel (a) and Koroyd (b), available within cycling helmets	29
2.12	WaveCel deformation mechanisms under axial buckling and cell folding. Adopted from [95]	30

2.13	Illustration of a hexagonal honeycomb unit cell (top) and an array (bottom)	32
2.14	Definition of honeycomb orientations	33
2.15	Honeycomb out-of-plane compressive response, characterised by typical stretch dominated behaviour.	35
2.16	Influence of relative density on the honeycomb mechanical behaviour. Adopted from [76]	36
2.17	Honeycomb under combined compression shear loading, adopted from [117]	37
2.18	Illustration of different buckling phenomena, folding plastic hinges (a) and elastic buckling (b), observed in honeycombs under out-of-plane compression	38
2.19	Several conventional manufacturing methods for honeycombs including expanding, slotting and corrugation & joining. Adopted from [130]	41
2.20	Illustration of the sintering particles giving rise to a liquid phases which coalesce and form a solid upon cooling. Adopted from [140]	44
2.21	Illustration of the sintering process. Adopted from [144]	45
2.22	Identification of orange peeling artefact on the sintered part. Adopted from [148]	46
2.23	Examples of distortion due to laser sintering, curling (a) and warping (b). Adopted from [149]	47
2.24	Illustration of sintering showing (a) the development of necking between particles in a single vector, (b) necking between parallel vectors and (c) necking between different layers. Adopted from [143]	48
2.25	Illustration of the build orientations aligned with the x, y and z axis of the build bed. Adopted from [157]	48
2.26	Classification of laser sintering materials according to the pyramid of polymer materials. Adopted from [163]	50
2.27	Distribution of material properties relative to elongation and Young's modulus for laser sintered polymers.	51

3.1	Illustration of orthogonal build orientations for a tensile coupon aligned with the x, y and z axis.	60
3.2	Illustration of tensile coupon variants for material anisotropy and rate sensitivity tests for low (left), intermediate (centre) and high (right) strain rate. Coupon gauge length is provided in text. . . .	60
3.3	Intermediate strain rate test setup including universal testing machine (A), DIC camera (B), data acquisition (C) and LED light sources (D).	61
3.4	High strain rate test setup including twin rail falling mass (A), DIC camera (B), test sample (C) and LED light source (D). . . .	62
3.5	Uniaxial tension test setup including non-slip grips (A), strain gauge markers (B) and test coupon (C). Where U_z denotes the direction of the applied displacement.	63
3.6	Planar tension test setup including non-slip boundary (A), strain gauge markers (B) and test coupon (C). Where U_z denotes the direction of the applied displacement.	64
3.7	Equibiaxial tension test setup including clamps (A), test coupon (B), strain gauge markers (C). Where U_r denotes the radial direction of the applied displacement.	65
3.8	Experimental setup for the quasi-static honeycomb compression including LED light source (A), video camera (B), load cell (C), platens (D) and honeycomb structure (E).	70
3.9	Experimental setup for honeycomb impact loading including LED light source (A), high speed camera (B), load cell (C), carriage weight (D), platen (E), honeycomb (F) and ruler (G)	70
3.10	Mechanical response of Luvosint under uniaxial tension at different strain rates subject to changing build orientation for xy (a), xz (b), zy (c) orientation as well as combined plot for comparison (d). . .	72
3.11	Luvosint mechanical behaviours under uniaxial, planar and equibiaxial tension.	73
3.12	Comparison of hyperelastic material model and their capacity for predicting the mechanical behaviours of Luvosint for uniaxial (a), planar (b) and equibiaxial (c) tension.	74

3.13	Comparison of relative difference to experimental data and number of coefficients for each hyperelastic model.	75
3.14	Comparison of experimental data to calibrated material for deformation states uniaxial, planar and equibiaxial tension. Material model coefficients are available in table 8.1 of Appendix 1.	75
3.15	Normalised stress relaxation test data and Prony representation. Material model coefficients are available in table 8.2 of Appendix 1.	76
3.16	Validation of hyperelastic and linear viscoelastic material model for an isolated deformation mode, comparison of high strain rate tensile (100 /s) loading data against simulation.	77
3.17	Comparison of mechanical behaviour of experimental and simulation honeycomb quasi-static compression to validate hyperelastic model under mixed deformation conditions.	78
3.18	Comparison of deformation mechanisms of experimental and simulation honeycomb quasi-static compression to validate hyperelastic model under mixed deformation conditions.	78
3.19	Comparison of mechanical behaviour of experimental and simulation of honeycomb impact loading to validate hyperelastic and linear viscoelastic model under mixed deformation conditions.	79
3.20	Comparison of deformation mechanisms of experimental and simulation honeycomb impact to validate hyperelastic and linear viscoelastic model under mixed deformation conditions.	79
4.1	Annotated circular honeycomb (2x2) illustrating the geometric parameters of the unit cell	87
4.2	Variation in pre-buckled honeycomb design subject to changing aspect ratio.	87
4.3	The fabrication method for the optimal honeycomb design including digital design, laser sintering overview and final part. Scanning electron imagery of Luvosint powder has been adopted from [168]	88
4.4	Finite element model of the honeycomb for quasi-static and impact conditions.	91

4.5	Location of nodal zero displacement boundary conditions for the honeycomb periodic BC model (upper and lower plates removed for clarity).	92
4.6	Fabricated honeycomb samples subject to changing aspect ratio, $e = 1.0$ (left), $e = 0.8$ (centre), and $e = 0.6$ (right).	94
4.7	Identification of sintered rib artifact proliferated through the z -axis height of honeycombs with an aspect ratio of $e = 1.0$ (straight walled honeycombs).	95
4.8	Engineering stress-strain curves for honeycomb variants subject to changing aspect ratio $e = 1.0$ (a), $e = 0.8$ (b) and $e = 0.6$ (c), under quasi-static uniaxial compression.	96
4.9	Photographic stills of the honeycomb variants subject to changing aspect ratio $e = 1.0$ (top-row), $e = 0.8$ (middle-row) and $e = 0.6$ (bottom-row) under quasi-static compression.	97
4.10	Engineering stress-strain curves for honeycomb variants subject to changing aspect ratio $e = 1.0$ (a), $e = 0.8$ (b) and $e = 0.6$ (c), under uniaxial compression impact loading	98
4.11	Photographic stills of the honeycomb variants subject to changing aspect ratio $e = 1.0$ (top-row), $e = 0.8$ (middle-row) and $e = 0.6$ (bottom-row) under uniaxial compression impact loading.	99
4.12	Comparison of strain rate behaviour for yield stress (a) and energy absorbed (b) under quasi-static and impact uniaxial compression.	100
4.13	Comparison of multi-loading energy absorbed for quasi-static (a) and impact (b) loading uniaxial compression.	101
4.14	Variation in simulated mechanical behaviour of honeycombs with changing aspect ratio $e = 1.0$ (a), $e = 0.8$ (b) and $e = 0.6$ (c) under quasi-static uniaxial compression subjected to increasing mesh density	103
4.15	Comparison of the experimental quasi-static compression mechanical behaviour to the full and periodic BC finite element simulation result for various aspect ratio $e = 1.0$ (a), $e = 0.8$ (b), and $e = 0.6$ (c).	105

4.16	Comparison of the experimental impact compression mechanical behaviour to the full and periodic BC finite element simulation result for various aspect ratio $e = 1.0$ (a), $e = 0.8$ (b), and $e = 0.6$ (c).	107
4.17	Variation in dynamic honeycomb mechanical behaviour yield stress (a), energy absorbed (b) and efficiency (c) relative to changing wall thickness and aspect ratio.	109
5.1	Identification of search area through examination of performance maps subject to behaviour limits.	118
5.2	The finite element model of the pre-buckled honeycomb, comprising two unit cells positioned between an upper and lower rigid plate. The upper plate is assigned a pre-impact velocity and point mass, whilst the lower is fixed.	119
5.3	The optimisation steps for construction of the surrogate response used by the search algorithm for an increasing number of sampled finite element simulations including, (a) random sampling, (b) surrogate construction, (c) merit function analysis, (d) the best point simulated, (e) surrogate model updated and (f) final surrogate model approximation.	121
5.4	The outline of the computational procedure indicating the software used during each step of the optimisation (oval = start/end, parallelogram = input/output, rectangle = process, diamond = decision).	123
5.5	The variation in the objective function, peak translational acceleration, for each function evaluation relative to a threshold of 250g.	125
5.6	Variation in honeycomb mechanical behaviour, translational acceleration – time (a), and engineering stress – strain (b) relative to iteration number 1, 14 and 56	126
5.7	Visualised deformation with respect to time relative to iteration number 1, 14 and 56.	127
5.8	The variation in peak translational acceleration and head injury criterion at each function evaluation.	128
5.9	The comparison of impact response and mechanical behaviour of iteration 11 and 136.	129

5.10	The variation in peak translational acceleration relative to wall thickness and aspect ratio when the objective function is set to PTA. Each function evaluation is indicated by a black point. . . .	130
5.11	The variation in the objective function, head injury criterion, for each function evaluation relative to a threshold of 1574.	131
5.12	The variation in head injury criterion relative to wall thickness and aspect ratio when the objective function is set to HIC. Each function evaluation is indicated by a black point.	132
5.13	Comparison of mechanical behaviour translational acceleration – time (a) and engineering stress – strain (b) for optimal honeycombs based on an objective function of PTA and HIC.	132
5.14	Manufactured honeycomb variant exhibiting a build defect	133
5.15	Experimental data of single impact loading for PTA (a) and HIC optimised solutions (b)	134
5.16	Validation simulation with comparison to experimental datasets of the optimal configurations for PTA (a) and HIC optimised solutions (b)	135
5.17	Experimental comparison of repeat impact loading behaviour for PTA (a) and HIC optimised solutions (b), as well as a comparison when considering the values of PTA (c) and HIC (d) recorded for all experiments.	137
6.1	Side helmet cross-section to illustrate and approximate contact area geometry and with a flat surface, reconstructed from [220] . .	146
6.2	Construction of the finite element model including liner, shell, headform and retention strap (modelled as an axial connector). . .	149
6.3	Comparison of calibrated material model to experimental data for foam with density of 125 kg/m ³ and 183 kg/m ³	150
6.4	Mapped meshing of honeycomb unit cells into hexahedral guide mesh.	151
6.5	Orientation and boundary conditions of direct and oblique impacts for foam and honeycomb liner helmets	152

6.6	Annotated finite element head model with components of translational and rotational acceleration depicted as inputs to the centre of gravity.	153
6.7	The variation in the objective function, peak translational acceleration, for each function evaluation relative to the threshold of 250g	155
6.8	The variation in the objective function, head injury criterion, for each function evaluation relative to the threshold of 1574	155
6.9	The resultant acceleration time behaviour for a full scale honeycomb helmet impact subject to the impact conditions of EN1078	156
6.10	Comparison of translational acceleration subject to the direct impact for the full scale honeycomb helmet and vinyl nitrile foam	158
6.11	Comparison of severity metrics, PTA and HIC, subject to a direct impact for the full scale honeycomb helmet and vinyl nitrile foam	158
6.12	Snapshots of direct impact finite element simulation for vinyl nitrile and honeycomb up to the point of densification	159
6.13	Comparison of translational acceleration subject to the oblique impact for the full scale honeycomb helmet and vinyl nitrile foam	160
6.14	Comparison of translational severity metrics, PTA and HIC, subject to an oblique impact for the full scale honeycomb helmet and vinyl nitrile foam	161
6.15	Comparison of rotational acceleration subject to the oblique impact for the full scale honeycomb helmet and vinyl nitrile foam	162
6.16	Comparison of translational severity metrics, PRA and RIC, subject to an oblique impact for the full scale honeycomb helmet and vinyl nitrile foam	162
6.17	Comparison of combined, translational and rotational, severity metrics, GAMBIT and HIP, subject to an oblique impact for the full scale honeycomb helmet and vinyl nitrile foam	163
6.18	Snapshots of oblique impact finite element simulation for vinyl nitrile and honeycomb helmets up to the point of densification.	163

6.19	Comparison of TBI severity metrics, 95 th percentile MPS and CSDM _{0.25} , subject to direct impact conditions for the full scale honeycomb helmet and vinyl nitrile foam	164
6.20	Comparison of the distribution of MPS within the finite element head model when subject to direct impact conditions for the full scale honeycomb helmet and vinyl nitrile foam	165
6.21	Comparison of TBI severity metrics, 95 th percentile MPS and CSDM _{0.25} , subject to oblique impact conditions for the full scale honeycomb helmet and vinyl nitrile foam	166
6.22	Comparison of the distribution of MPS within the finite element head model when subject to oblique impact conditions for the full scale honeycomb helmet and vinyl nitrile foam	167

List of Tables

- 2.1 Description of additive manufacturing processes and their relevant technologies 43
- 3.1 Luvosint TPU X92A-1 NT physical and mechanical properties. Adopted from [171]. 59
- 3.2 Luvosint TPU X92A-1 NT recommended processing parameters. Adopted from [171]. 59
- 3.3 Hyperelastic material models available within Abaqus classified as phenomenological, mechanistic and hybrid. 66
- 3.4 Abaqus boundary conditions used in quasi-static isolated deformation testing. 68
- 4.1 Structural parameters cell width, wall thickness, aspect ratio and number of folds of the manufactured honeycombs 88
- 4.2 Recorded dimensions of manufactured honeycomb samples. Variants were labelled from A, B and C representing honeycombs with an aspect ratio of $e = 1.0$, $e = 0.8$, and $e = 0.6$ respectively. 93
- 4.3 Average performance parameters yield stress, absorption efficiency and energy absorbed for changing aspect ratio of each honeycomb variant under quasi-static uniaxial compression. Standard deviation in parentheses, CV =coefficient of variation. 97
- 4.4 Average performance parameters yield stress, absorption efficiency and energy absorbed for changing aspect ratio of each honeycomb variant under impact uniaxial compression. Standard deviation in parentheses, CV = coefficient of variation. 100

4.5	Computed performance parameters and relative error subject to increasing mesh density for each structural variant.	104
4.6	Comparison of the experimental quasi-static compression mechanical behaviour to the full simulation and periodic BC model result for various aspect ratios	106
4.7	Computed performance parameter error when compared to experimental data for impact uniaxial compression full and periodic BC model.	108
5.1	Structural and performance parameters for the optimal configurations of each objective function	131
5.2	Manufactured optimal honeycomb samples dimensions	134
6.1	Equation 6.4 coefficients for vinyl nitrile foam with densities 125 kg/m ³ and 183 kg/m ³ used as comparison to the state of the art.	150
6.2	Structural and performance parameters for the optimal configurations of each objective function	156
6.3	Comparison of PTA and HIC values for the prediction of the periodic BC model used in the optimisation and full scale helmet model. Percentage difference between the two cases is reported in brackets.	157
8.1	Hyperelastic material model, Ogden N=5, coefficients for implementation in Abaqus.	181
8.2	Linear viscoelastic material model, Prony series, coefficients for implementation in Abaqus.	181

Nomenclature

Uppercase Latin letters

A	Project cross sectional area
A_c	Impact contact area
E	Absored energy
E	Modulus
E_{re}	Energy absorbed relative error
F	Force recorded by load cell
F_n	Normal force
F_o	Oblique force
F_t	Tangential force
$I_{headform}$	Headform inertia
I_{helmet}	Helmet inertia
I_{total}	Total inertia
I_{xx}	Moment of inertia along x axis
I_{yy}	Moment of inertia along y axis
I_{zz}	Moment of inertia along z axis
J_{calc}	Objective function calculated value

J_{crit}	Objective function critical threshold
P	Applied force
P_n	Equation coefficients for elastomeric foam strain rate dependant behaviour
R	Headform radius
R_d	Relative density
RF_z	Reaction force along z axis
T	Impact pulse duration
U	Displacement
U_r	Applied displacement along z axis
U_r	Applied radial displacement
V_r	Volume ratio
V_z	Velocity along z axis
V_{hc}	Honeycomb volume
V_{ref}	Volume of unit cell extremities

Lowercase Latin letters

a	Translational acceleration
a_g	Global accceleration due to gravity
a_x	Translational acceleration along x axis
a_y	Translational acceleration along y axis
a_z	Translational acceleration along z axis
a_{cr}	Critical translational acceleration value for GAMBIT equation
a_{max}	Maximum value of translational acceleration

d	Diameter of coupon strain region
d	Helmet liner thickness
e	Honeycomb cell aspect ratio
e	Honeycomb cell number of folds
g	Proney series coefficient
h	Honeycomb cell height
i_{max}	Iteration limit
m	Mass
m_f	Mass scale factor
n_{var}	Number of structural paramters
r_1	Honeycomb cell minor axis
r_2	Honeycomb cell major axis
r_d	Relative difference
r_s	Helmet shell thickness
r_x	Elipsoid radii along x axis
r_y	Elipsoid radii along y axis
r_z	Elipsoid radii along z axis
t	Coupon thickness
t	Honeycomb wall thickness
t	Time
t_{avg}	Average honeycomb wall thickness
u_x	Displacement along x axis
u_y	Displacement along y axis

u_z	Displacement along z axis
w	Coupon width
w	Honeycomb cell width
x	Honeycomb array width
x_d	Structural parameter array
y	Honeycomb array breadth

Uppercase Greek letters

ν	Poisson ratio
-------	---------------

Lowercase Greek letters

α_{cr}	Critical value of rotational acceleration for BRIC equation
α_{cr}	Critical value of rotational acceleration for GAMBIT equation
α_{max}	Maximum value of rotational acceleration
α_x	Rotational acceleration along x axis
α_y	Rotational acceleration along y axis
α_z	Rotational acceleration along z axis
μ_{global}	Global friction
ν	Energy absorption efficiency
ω	Rotational velocity
ω_{cr}	Critical value of rotational velocity for BRIC equation
ω_{max}	Maximum rotational velocity
ρ	Proney series coefficient
σ	Engineering stress
σ_0	Initial engineering stress

σ_{equ}	Equibaxial engineering stress
σ_{exp}	Experimental engineering stress
σ_{mod}	Model engineering stress
σ_{pla}	Planar engineering stress
σ_{pl}	Plateau stress
σ_{uni}	Uniaxial engineering stress
$\sigma_{yield,rel}$	Yield stress relativ error
σ_{yield}	Yield stress
τ	Proney series coefficient
τ	Strain rate
ε	Engineering strain
ε_d	Densification engineering strain
ε_{max}	Maximum engineering strain
ε_{min}	Minumum engineering strain

Acronyms & Abbreviations

ABS	Acrylonitrile butadiene styrene
AM	Additive Manufacturing
ANSI	American National Standards Institute
ASTM	American Society of Testing and Materials
BC	Boundary Condition
BrIC	Brain Injury Criterion
BS	British Standards
CAD	Computer Aided Design

CEN	European Committee for Standardisation
CG	Centre of gravity
CPU	Central Processing Unit
CSA	Canadian Standards Association
CSDM	Cumulative Strain Damage Measure
CSDM _{0.25}	Volume fraction of the brain exceeding a maximum principal strain of 0.25
CSPC	Consumer Product Safety Commission
GAMBIT	Generalised Acceleration Model for Brain Injury Threshold
HIC	Head Injury Criterion
HIC _{opt}	Optimal solution that minimises head injury criterion
ISO	International Organization for Standardization
LS	Laser Sintering
MIPS	Multidirectional Impact Protection System
MPS	Maximum Principal Strain
MPS ₉₅	95 th percentile maximum principal strain
ODS	Omnidirectional Protection System
PA	Polyamide
PBC	Periodic Boundary Condition
PBHC	Pre buckled honeycomb
PRA	Peak Rotational Acceleration
PTA _{opt}	Optimal solution that minimises peak translational acceleration
RIC	Rotational Injury Criterion

s.t.	Subject To
SI	Severity Index
SPIN	Shear Pads Inside
STAR	Summation of Tests for the Analysis of Risk
STL	Standard Tessellation Language
TBI	Traumatic Brain Injury
TC	Technical Committee
TfL	Transport for London
TPU	Thermoplastic Polyurethane
UCDBTM	University College Dublin Brain Trauma Model
VMS	von Mises stress
VN	Vinyl Nitrile
WG	Working Group
WSTC	Wayne State Tolerance Curve
XY	Through thickness direction
XZ	Through width direction
ZY	Through length direction

Chapter 1

Introduction

1.1 General

Use of a bicycle is a popular method of transport or active exercise, with the number of cyclists increasing steadily since 2009 [1]. It is estimated that in the United Kingdom alone, over 40% of people have access to a bicycle, whilst over 30% have been cycling in the last year [2]. Consequently, pedal cyclist traffic has increased by 16% between 2009 and 2019 [3]. Further interest in cycling has occurred more recently too; since the COVID-19 pandemic, weekday and weekend cycling has seen increases of 100% and 200% respectively compared to pre-COVID-19 levels [3]. Whilst cycling is associated with several environmental [4], social [5] and economic benefits [6], the growing interest in cycling is, however, paralleled by increases in related injuries [7]. Cyclists are among the most at-risk road user. When switching transport mode, the reported injury risk is 29 times greater for cyclists compared to car occupants [8]. Furthermore, recent Transport for London (TfL) reports indicate that between 2017 – 2020 cyclists represented 16% of all casualties by mode of travel [9]. Of all types of injury sustained to a cyclist, a blow to the head is the most significant as impacts to the head can lead to the development of traumatic brain injury (TBI), a notable cause of mortality and morbidity [10].

A critical strategy in TBI mitigation in cycling accidents is the use of a protec-

tive helmet [11] and is strongly advocated by The World Health Organisation [12]. The prevalence of TBI of any severity has been reported to be higher in non-helmeted accidents when compared to helmeted accidents [13]. Furthermore, the likelihood of sustaining a TBI is reduced (18%) when wearing a helmet compared to non-helmet cyclists (48%) [14]. Current bicycle helmets are designed to protect the user by deforming to mitigate the impact energy and reduce the resultant acceleration. Due to the onset of permanent deformation within the helmet following an impact, its protective capacity is diminished. Consequently, they do not provide adequate performance when subject to a history of loading, such as multiple or consecutive impacts [15]. Indeed, it is common to wear a previously damaged helmet despite contrary advice. Current multi-hit solutions are derived from elastomeric foams which have been applied in several other sporting helmets. These materials, however, suffer from a lack of development in recent years. Furthermore, they have limited geometric freedom, which precludes optimisation. Advances in computational modelling and additive manufacturing (AM) now poses an alternative route to developing novel alternative helmet liners that could exceed contemporary materials' performance. Therefore, there is growing motivation in identifying a new multi-hit solution.

1.2 Research aim

This work aims to improve head protection by exploiting the mechanical benefits of cellular structures and elastomeric materials, by use of finite element analysis, numerical optimisation and additive manufacturing.

1.3 Thesis structure

In this thesis, an approach is established to enabling the optimisation of an elastomeric honeycomb structures for impact mitigation by use of experimental and computational methods. The motivation for this is the development of new, higher performing helmet liners which benefit from the use of elastomers to be able to sustain a series of impacts for improved user safety. Material model calibra-

tion was carried out based on extensive characterisation data to enable numerical analysis. The design and optimisation of these structures are carried out using finite element analysis and implementation of an intelligent search algorithm. The manufacture of these structure is facilitated through additive manufacturing from elastomeric materials and subject to experimental testing for validation of a multi-impact solution. The full scale behaviour of the optimisation honeycomb helmet was numerically investigated under direct and oblique conditions. The performance of the proposed liner was compared to contemporary elastomeric foams via calculation of tissue-based and kinematic-based severity metrics. The structure of this thesis is as follows.

Chapter 2 establishes an overview of the key topics of this work: head injury, helmets, prismatic cellular structures and additive manufacturing. The availability of elastomeric materials and design freedom afforded by laser sintering motivates the development of prismatic cellular structures (i.e., honeycombs) to create an improved helmet liner, when compared to the shortcomings of current materials. This chapter culminates in the identification of the research focusses of this thesis. Namely, additively manufactured helmets, honeycombs with variable energy absorption and finite element based optimisation.

Chapter 3 begins the investigation with a detailed inspection and characterisation of an additively manufactured thermoplastic elastomer realised through selective laser sintering. A finite element material model suitable for quasi-static and dynamic explicit simulation is calibrated before being validated through comparison to experimental data. The influence of manufacturing build orientation is established with respect to the resultant mechanical behaviour.

Chapter 4 introduces an exemplar circular honeycomb structure with a pre-buckled design feature as a candidate structure for helmet applications. Laser sintering is utilised to manufacture samples before being subjected to uniaxial compression under quasi-static and impact conditions. The calibrated material model, developed in chapter 3, is then used as part of the development of an equivalent finite element model. A full-scale finite element model is established prior to developing a computationally efficient periodic boundary condition model which enables approximation of the full-scale model. Both models are closely compared to the experimental data, building confidence in the validity of the models for

subsequent investigations. Lastly, the periodic boundary condition models are used to investigate the geometric parameters with respect to yield stress, energy absorption and efficiency under dynamic conditions. The validated periodic boundary condition model provides the foundation for exclusive, simulation-based investigation in the following chapter, whilst the parametric sweep enables identification of suitable bounds and limits for future optimisation.

Chapter 5 identifies a computational procedure for the design and optimisation of parametrically defined cellular structures, subject to loading conditions and performance thresholds of the bicycle helmet design standard EN1078. In this study, the pre buckled honeycomb, introduced in chapter 4, is used as an exemplar. Effectiveness of the procedure, and associated mechanical behaviour of the honeycomb, is investigated relative to changing performance objective functions. The optimal design for each objective function is then manufactured and experimentally tested under the design standard loading conditions for single impact and repeat impact conditions. This investigation serves as a validation for the proposed procedure before application to the helmet design envelope.

Chapter 6 leverages the computational optimisation procedure reported in chapter 5. The design envelope of the helmet is considered and anticipated contact area under impact is identified to inform the structural geometric bounds. Following optimisation, the incumbent design is then propagated through a helmet liner volume. The prototype helmet is compared to a contemporary foam liner, derived from Vinyl Nitrile, under direct and oblique impacts conditions, where the resultant acceleration time histories, as well as kinematic-based severity metrics are compared. Lastly, a validated human head finite element model is utilised to establish the risk of traumatic brain injury by comparing tissue-based severity metrics for each case.

Chapter 7 reports the conclusions relative to the research objectives of the thesis, describing the findings of chapters 3, 4, 5 and 6. Further work is described to inform future research, so this work may be continued. Lastly, academic contributions to the literature, by means of journal publications, are listed.

Chapter 2

Literature review

2.1 Introduction

This chapter first provides an overview of the four core topics of the study:

- 1 Head injury
- 2 Helmet design
- 4 Prismatic cellular structures
- 4 Additive manufacturing

Together, these form a basis for a more detailed description of the research focuses:

- 5 Additively manufactured helmets
- 6 Tailorable honeycomb behaviour
- 7 Finite element-based optimisation

2.2 Head injury

This section describes the literature that was reviewed concerning head injury. In particular, the anatomy of the head is described relative to their intrinsic protective features. Furthermore, injury mechanisms are discussed and common cycling injuries identified. Lastly, injury metrics are reviewed in terms of kinematic and tissue-based metrics.

2.2.1 Anatomy of the head

To aid the development of helmets, an understanding of the anatomy of the human head is important. In particular, the intrinsic mechanisms which serve to protect the brain have provided the inspiration for present head protection solutions previously. Whilst the individual characteristics of the brain such as morphology and material properties vary as a function of age, health, and sex, the broader anatomy is similar for all humans and will be discussed generally in the section.

The human head is the most complex system within the body. Structurally, the various layers of the head work as protective barriers for the brain and are illustrated by figure 2.1. Considering the outermost layer first, the scalp covers the bony structure of the skull bordering the front of the face and neck. The word SCALP itself is a mnemonic which describes its component layers, termed: skin, connective tissue, aponeurosis, loose areolar connective tissue and periosteum [16]. The thickness of the scalp is subject to age and location and can vary between 3 mm to 8 mm from children to adults [17]. Whilst serving to provide an immunological barrier and thermal insulation, the scalp clearly also plays a role in head impact mechanics. It has been reported that the scalp absorbs and distributes external forces by sliding freely over the skull. This was examined experimentally, where cadaveric testing demonstrated the impact force imparted to the head is 35% higher than without the presence of the scalp [18]. Moreover, the presence of the scalp on a headform reduces the magnitude of translational and rotational acceleration as much as 70% under oblique head impacts [19].

Below the scalp, the skull forms the head and supports the structure of the face

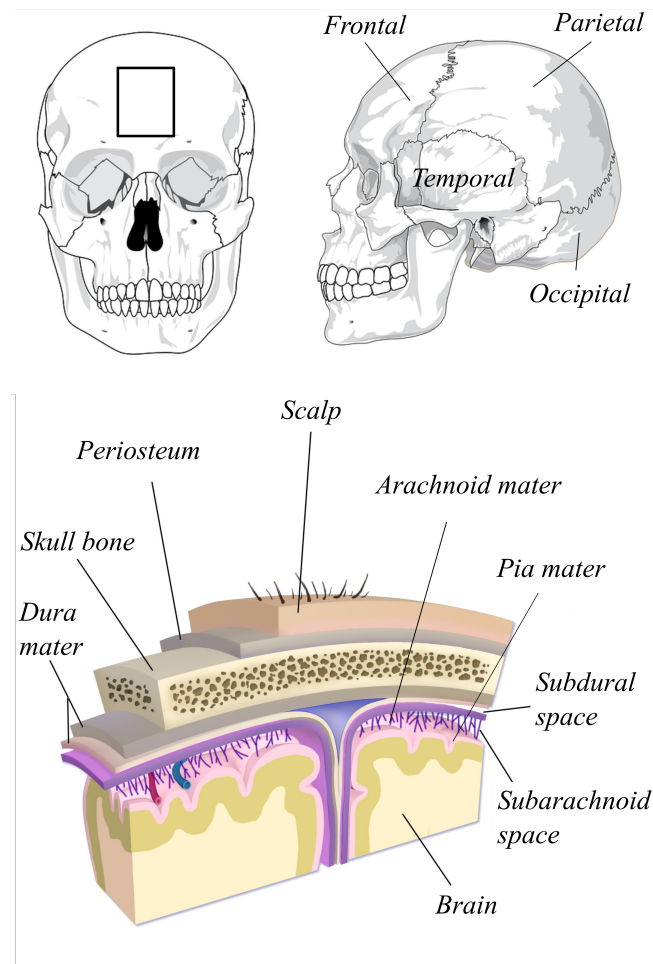


Figure 2.1: Sectional view of the scalp, skull, and brain. Adopted from [20]

and cavity for the brain (cranium). The skull is a complex geometric structure comprised of 22 fused bones, 14 of which form the facial bones, whilst the remaining 8 form the cranium. The thickness and curvature, varies across the surface of the cranium. Notably, the frontal and occipital bones are thicker with a high curvature than the upper temporal and side parietal regions [21]. Consequently, thicker sections are likely to fracture rather than elastically bend when subject to deforming forces [22]. The varying regional differences in strength of the skull ultimately influences the energy transfer under impact, suggesting the potential need for variable protection within head protection.

The internal surface of the skull bone is characteristically irregular, encompassing several protrusions and acute geometric features. The incidence of brain injuries because of these features, however, are largely mitigated by the presence of tough

meninges. The meninges consist of three layers: the dura mater, arachnoid and pia mater. The dura mater is a tough and fibrous membrane which is directly connected to the skull and reflects the negative of the protrusions. Moving inwards, the arachnoid membrane has a spider-like structure that provides a cushioning effect. Lastly, the pia mater is a delicate membrane which is directly connected to the outer surface of the brain [23]. Within this region, termed the subarachnoid space, cerebrospinal fluid (CSF) is present, buoyantly suspending the brain relative to the cranium. This anatomical arrangement serves to provide relative degrees of freedom from the motion of the head whilst cushioning impact loads. It is important to note, however, that even with the presence of these protective features, the movement of the brain inside the skull can lead to strain within the brain tissue that result in injury.

The brain is connected to the spinal cord and is responsible for a range of functions, from breathing and sleeping to co-ordination and balance. Consequently, interruption to this system can prove debilitating. The brain itself is a complicated assembly of grey and white matter as well as blood vessels, membranes, fissures, and voids surrounded by the CSF. As illustrated by figure 2.2, it is made up of the frontal, parietal, temporal and occipital lobes. Each lobe is made up of subsections which control different functions of the brain. Consequently, injury to different regions within the brain results in loss or diminished use of function controlled by that region.

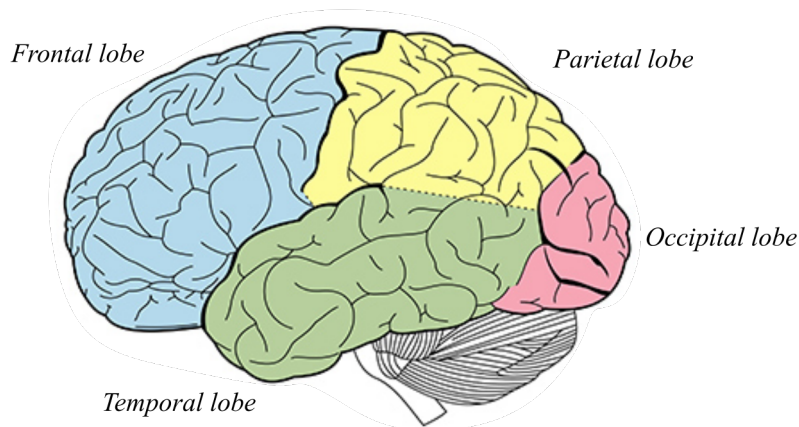


Figure 2.2: Illustration of the brain, identifying the frontal, parietal, temporal and occipital lobes. Adopted from [24].

2.2.2 Injury mechanisms

Head injuries are defined as damage to regions of the scalp, skull and brain occurring when energy is transferred to the head and is not effectively attenuated. Consequently, structures of the head may undergo changes in terms of shape and strain beyond a recoverable limit [25]. These injuries can be classified as skull fracture, vascular injury, focal injury or axonal injury.

The major mechanisms of brain injury are defined by one or a combination of skull fracture, bending of the skull, translational motion, as well as rotational motion of the skull [10]. These mechanisms of injury may occur during contact loading where the head is struck by an object, or by inertial loading where the head is not necessarily in contact but undergoes a regime of acceleration or deceleration. As the head is subjected to these loading conditions, positive pressure, negative pressure, and shear due to the presence of pressure gradients or relative motion of the brain with respect to the skull occurs. Positive pressure, arises due to compressive pressure at the impact site. This is further accentuated by the in-bending deformation of the skull. In contrast, negative pressure develops at the opposing region of the impact site. This can lead to either tensile loading or cavitation, where compressive loading arises due to the collapse of vapour bubbles formed under negative pressure. Lastly, shear is attributed to pressure gradients as well as the relative motion of the brain inside the skull. As previously discussed, the CSF serves to largely mitigate the prominence of the injury mechanism, however, excessive shear leads to contusions on the surface of the brain and diffuse straining within. These mechanisms are largely attributed to the prominence of rotational acceleration, since the brain tissue is nearly incompressible, and its bulk modulus is orders of magnitude greater than its shear modulus the brain has a propensity to deform under these conditions.

2.2.3 Common cycling injuries

Compared to other commuters, cyclists are at an elevated risk of injury due to the unpredictable nature of traffic collisions. The most common areas of the human body injured following a cycling accident are the upper limb, lower limb head and facial regions. Since this thesis relates to the development of new helmet

liners, the following section shall focus exclusively on head injuries. Notably, skull fracture (86%), brain contusions (73%), acute subdural haematoma (43%) and diffuse axonal injury (17%) are among some of the most common injuries sustained to the head and brain following a cycling accident that required surgical intervention [26]. Interestingly concussion was not reported, however, this shall be described too due to its prominence as an injury during helmet impacts [27].

Skull fractures are classified as focal injuries and arise due to contact loading where the resultant force exceeds the failure criterion of the cranium [28]. These fractures are by the nature of the break as either linear, depressed, diastatic or basilar, as illustrated by figure 2.3. Linear fractures are thin line breaks which occur at points remote from the impact site. Depressed fractures result from when an object penetrates the skull, and the bone protrudes inwards into the brain. Lastly, diastatic fractures occur when the fracture liner traverses one or more sutures, resulting in widening of the suture.

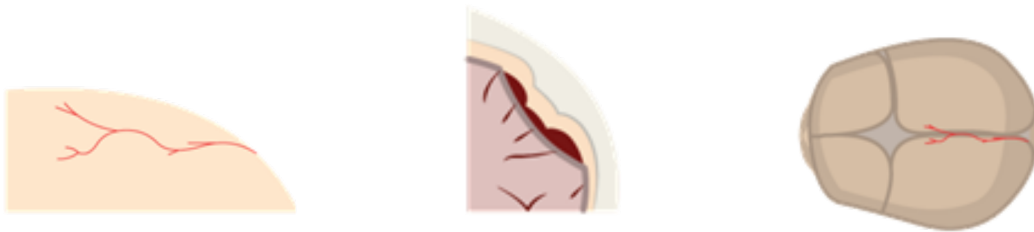


Figure 2.3: Classification of skull fractures, linear (left), depressed (centre) and diastatic (right)

A contusion is where the brain tissue is bruised focally, associated with microhaemorrhage of the blood vessels [29]. Contusions are categorised as coup or contrecoup. Coupe contusions manifest at the site of the impact as the skull flattens and deforms or depresses the underlying brain, as the brain moves around the skull bone fragments may thrust into the brain. Conversely, contrecoup contusions, are caused by the brain rebounding after the initial impact and deforming against the opposing skull wall.

A haematoma is characterised as a focal volume of blood that develops near the surface of the brain due to damage to the vasculature, as described by figure 2.4. Haematoma are further classified by their location above (epidural), or below

(intracranial) the dura layer. Epidural haematomata are most commonly caused by large contusions that bleed, developed by a fracture to the skull, whilst intracranial haematoma are caused by tearing of the bridging veins [30]. Tearing of bridging veins commonly result from high magnitude rotational acceleration. It has been reported that purely translation movement alone cannot induce such tearing [31], hence why the minimisation of rotational acceleration during an impact is an important consideration.

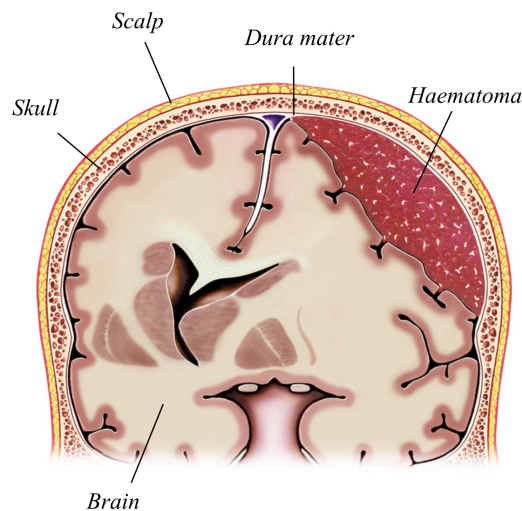


Figure 2.4: Cross-sectional view of the human head, illustrating a haematoma.

Diffuse Axonal Injury (DAI) is disruption of neurons within the white matter of the brain, either through stretching, pulling or tearing. Neurons are composed of two different constituents, the cell body and axon. Owing to the disparity in mass and density, under impact loading which involves rotational acceleration each constituent moves at a different velocity which can ultimately shear the axon from the cell body [32]. The proliferation of shearing disrupts communication throughout the brain [33]. Moreover, the damaged cells result in further swelling and bleeding within the brain. Concussion is a milder form of diffuse axonal injury. Similar to DAI, concussion is predominantly caused by impact loading that undergoes rotational acceleration in combination with linear acceleration loading. It has been reported that diffuse stresses and strain development in the brain tissue result in minor stretching of axons. Both DAI and concussion, however, are difficult to detect because abnormalities are not registered by standing imaging techniques.

2.2.4 Injury metrics

Metrics can be used to assess the severity of an impact sustained to the head, whilst also providing helmet designers with an objective for optimal design. These injury metrics can be categorised as kinematics-based, relating to peak kinematic values and equations, or tissue-based criteria obtained from finite element models [34].

Simple analysis of the 6 degree of freedom acceleration-time history recorded from the centre of gravity of a test headform can be undertaken to report peak translational acceleration (PTA) and peak rotational acceleration (PRA) providing an indication of behaviour during an impact. PRT and PRA are the maximum values of the vector magnitude for translational and rotational acceleration time vector, respectively. A criticism, however, of using peak values is that it does not account for the duration dependence of the impact event. As such, the Wayne State Tolerance Curve (WSTC) [35] was developed from frontal impacts to animals and cadavers to identify a relationship for translational acceleration, duration of exposure and the likelihood of head injury [36]. These initial findings were then used to develop the Severity Index (SI) [37], as illustrated by equation 2.1:

$$SI = \int_0^T |a(t)|^{2.5} dt \quad (2.1)$$

Where $|a(t)|$ is the resultant translational acceleration time history recorded from the centre of gravity of the head (recorded in g) and T is the impact pulse duration. A nominal injury limit of 1000 was set for the solution of the formula.

An extension of the SI was proposed to account for the sensitivity of large acceleration in short intervals, and small accelerations over long intervals. Hence, the Head Injury Criterion (HIC) [38] was reported as:

$$HIC = \max \left[\frac{1}{t_2 - t_1} \int_{t_1}^{t_2} a(t) dt \right]^{2.5} (t_2 - t_1) \quad (2.2)$$

Again, $a(t)$ is the resultant translational acceleration time history recorded from the centre of gravity of the head (recorded in g). The time interval, $t_2 - t_1$, should

be chosen such that the solution of the equation is maximised.

It is widely accepted that the human head is in fact more susceptible to rotational kinematics [32], where these loading conditions are linked to traumatic brain injury [39]. Hence, the formula for HIC can be modified for the Rotational Injury Criterion (RIC) [40].

$$RIC = \max \left[\frac{1}{t_2 - t_1} \int_{t_1}^{t_2} \alpha(t) dt \right]^{2.5} (t_2 - t_1) \quad (2.3)$$

Where α is the resultant rotational acceleration time history recorded from the centre of gravity.

Whilst HIC and RIC serve to analyse the impact response in terms of the translational and rotational components in isolation, they are limited by the fact that a real-world impact achieves multi-axial loading. Thus, both translational and rotational accelerations are simultaneously present. The Generalised Acceleration Model for Brain Injury Threshold (GAMBIT) [41] serves to incorporate both translational and rotational acceleration by normalising the peak values of PRT and PRA by critical thresholds. Hence, GAMBIT is reported as:

$$GAMBIT = \sqrt{\left[\left(\frac{a_{max}}{a_{cr}} \right)^2 + \left(\frac{\alpha_{max}}{\alpha_{cr}} \right)^2 \right]} \quad (2.4)$$

Where the critical values for a_{cr} and α_{cr} are 250 g and 10000 rad/s² respectively.

Another important consideration and therefore limitation of the discussed metrics so far as is that the head is sensitive to the direction of loading [42]. Head Impact Power (HIP) suggests that the rate of change of translational and rotational kinetic energy can be used as a biomechanical assessment tool for brain injury [43].

$$\begin{aligned} HIP = & ma_x \int a_x dt + ma_y \int a_y dt + ma_z \int a_z dt \\ & + I_{xx} \alpha_x \int \alpha_x dt + I_{yy} \alpha_y \int \alpha_y dt + I_{zz} \alpha_z \int \alpha_z dt \end{aligned} \quad (2.5)$$

Where m is the mass of the headform and helmet, a is the component of translational acceleration, α is the component of rotational acceleration and I is the moment of inertia along each axis of the headform.

Currently, the discussed metrics have only considered the components of translational and rotational acceleration that are transmitted to the head. Since acceleration changes during the impact, so does the velocity. It has been proposed that rotational velocity can be better correlated to mild traumatic brain injuries than angular acceleration [44]. Hence, the Brain Injury Criterion (BrIC) was proposed as defined by equation 2.6.

$$BrIC = \sqrt{\left(\frac{\omega_x(t)}{\omega_{x,c}}\right)_{max}^2 + \left(\frac{\omega_y(t)}{\omega_{y,c}}\right)_{max}^2 + \left(\frac{\omega_z(t)}{\omega_{z,c}}\right)_{max}^2} \quad (2.6)$$

Where ω_x , ω_y , and ω_z are the components of rotational velocity and $\omega_{x,c}$, $\omega_{y,c}$, and $\omega_{z,c}$ are the critical values of rotational velocity 66.25, 56.45 and 42.87 rad/s respectively [45].

It should be noted that the metrics described so far only provide an indication of injury as a function of the kinematic response of the head. To better understand how these kinematics yield brain injury, tissue-based criteria should be used. Tissue-based criteria are captured using finite element models of the human head, which are then inertially loaded using the 6 degrees of freedom acceleration time history recorded during the impact [46].

Established models within the literature include the Global Body Model Consortium [47], the Imperial College model [48], the Royal Institute of Technology (KTH) model [44], the Total Human Model for Safety [49] and the University College Dublin Brain Trauma Model (UCDBTM) [50]. These models have been used in an extensive number of studies including the development of injury metrics [51], accident reconstruction [52] and assessing the effectiveness of helmets [53].

Maximum principal strain (MPS) has commonly been used as tissue-based criteria for injury prediction [54]. Defined as the elongation of a tissue along one of its principal axes relative to its original length, MPS is used in brain injury

biomechanics due to its correlation to mechanical failure in anatomical testing. The limitation, however, of MPS is that it accounts for the largest elongation and therefore may not be representative of the mechanism of injury which is spread across a region of the brain [55]. Another tissue based criteria, von Mises stress (VMS), is equally eminent as MPS [54]. The computation of VMS is used to represent a threshold or yield criteria. This is particularly useful for prediction of brain injury because it accounts for different directions of stress acting on a volume. Cumulative Strain Damage Measure (CSDM) [56] is another tissue based criterion which is more suited for prediction of diffuse brain injury [57], that occurs over a large region of the brain. It is calculated by measuring the volume of the brain that experiences strain above an established threshold. This measurement is based on the theory that diffuse brain injury occurs due to the exposure of a volume of tissue to injurious levels of strain. Given CSDM considers a volume of brain tissue exposed to a certain level of strain, it may provide some advantages over the limitations of measuring strain in one element, as is the case for MPS. Consequently, it is important to assess the resultant brain injury severity using finite element models to identify the performance of new helmet designs.

2.3 Helmet design

This section describes the literature that was reviewed concerning helmet design. In particular, current functional requirements of helmets, their construction, and the role each subcomponent's play are reported. Furthermore, the principles of design for impact mitigation are discussed before expansion on impact test protocols. Lastly, emerging technologies are critically reviewed in terms of their efficacy and their mechanisms for impact mitigation.

2.3.1 Functional requirements

Wearing a helmet is an effective strategy for reducing the likelihood of sustaining a head injury during an impact. There is extensive literature supporting the evidence for helmet efficacy and the overwhelming benefits versus not wearing a helmet [58]. Owing to the diverse applications within which a helmet is worn,

the functional requirements differ based on application. For example, bicycle helmets, motorcycle and equestrian helmets are designed to mitigate a single impact whilst American football, ice hockey and combat helmets serve to mitigate against a series of impacts. Furthermore, the anticipated severity of the administered impact may vary as a function of the increased elements of speed and height present in the sport, e.g., motorcycle helmet's protective capacity exceed that of soccer [59]. Application specific loading conditions inform helmet design too. Equestrian and motorcycle helmets both include rigidity and penetration tests to mitigate against the likelihood of crushing under high static loads or impact involving sharp objects, whilst softball and combat include ball and fist shaped impactors respectively [60]. Other practical concerns also dictate helmet design. For example, if a helmet is to be worn for a long period of time, the helmet should have good thermal management and be well ventilated [61]. This, however, is often a conflicting requirement for motorcycling and equestrian, which require full coverage to provide sufficient penetration cover and rigidity [62]. In contrast, bicycle helmets, which do not have these additional requirements, easily include unique geometries to facilitate thermal comfort as well as aiding aesthetic designs. Some helmets have other protective elements too, such as visors, goggles, or face cages, which ultimately requires consideration of how they are fixed to the helmet without reducing or inhibiting performance. Therefore, when designing a helmet, the following functional requirements are considered. The helmet must:

1. Attenuate the energy of the impact.
2. Reduce the translational acceleration exposed to the head.
3. Reduce the rotational acceleration exposed to the head.
4. Remain fixed to the head during the impact.
5. Prevent penetration during the impact.
6. Prevent crush during the impact.
7. Cover the head without hindering vision.
8. Be mechanically and thermally easy to wear.

Principally, these tenets of design inform the choice of material and construction of the helmet.

2.3.2 Components

The components of modern helmets have remained relatively unchanged in recent years, typically consisting of a hard external shell which houses an impact mitigating liner followed by a comfort liner positioned immediate to the user's head [59]. Certain designs include the addition of a slip liner, or other technology, which aid rotational mitigation [53], although this will be described further in later sections. While the aforementioned components are synonymous across a variety of sporting helmets, the materials used in their construction differ to suit the needs of the application. A distinction, therefore, can be made between helmets for single-hit applications (e.g., cycle, motorcycle, and equestrian) and multi-hit applications (e.g., American football, ice-hockey, and combat) where the latter requires the ability to recover to efficiently manage a history of successive loading compared to the former which is only required to mitigate a single impact [63]. As such, the impact mitigating liner and shell varies between helmet type, whilst comfort liner remains largely generic.

The comfort liner consists of a thin layer of low-density of elastomeric foam which serves to improve user comfort between the denser impact mitigating liner and the head. Positioned inferior and secured to the impact mitigating liner, the soft and malleable nature of the comfort liner, bottoms-out upon compression and provides minimal effect to the overall impact performance. Of note, however, finite element simulations have demonstrated that the frictional interplay between the head and comfort liner is important where high friction can yield increases in rotational components of acceleration [64], therefore the friction of the comfort liner is important.

The primary role of the shell serves to provide a large contact area over which to engage the impact mitigating liner, thus distributing the force of the impact and reducing local stress. The secondary role of the shell can be considered application specific but includes penetration resistance [65], maximising sliding friction between the impact surface and shell [66], resistance to crush [62] or in-

creased thermal comfort [61]. The helmet shell is commonly either derived from thermoplastic polymers, such as polyvinyl chloride, polycarbonate, or acrylonitrile butadiene styrene (ABS) which can either be injection moulded as well as in-moulded during liner manufacture. Or, derived from alternative materials include carbon, Kevlar and glass fibre composite impregnated with resins which are laid up in moulds and cured by heat or chemical reaction. Helmets for multi-impact applications exclusively use polymer shells, whilst single-hit applications use both polymers and composites.

Under impact, the shells act differently based on their material composition. For example, polymer shells deform, demonstrating elastic bending and viscoelastic dissipation. Due to the relatively low modulus, however, it has been reported that load distribution is in fact determined by the impact object and minimal impact attenuation is achieved [67]. The benefit, however, of polymer shells are in their ease of manufacture and low cost, as well as their ability to undergo repeat impacts without incurring significant damage. In contrast, composite shells not only attenuate the impact by buckling but also through damage mechanisms like delamination, fibre breakage and matrix failure [68]. Moreover, composite materials have notably greater stiffness when compared to polymer shells leading to better load distribution and more effective impact mitigation under high velocity impacts, albeit at the expense of low velocity performance [69]. Leveraging damage mechanisms, however, makes them an unsuitable candidate material for multi-hit applications. At the time of writing, the literature is limited on the development of helmet shells in comparison to that of helmets liners for improved rider safety. Nevertheless, examples do exist whereby topology optimisation [70], application of novel resins [71] and composites [72] have been applied to aid lateral crush resistance and enhance energy absorption under impact respectively.

The primary role of the impact mitigating liner is to attenuate the energy of the impact, and reduce the transmitted force to the head below a sub-injurious level. During the impact, forces acting on the head give rise to translational and rotational acceleration, which is transmitted to the head and must be minimised to ensure that likelihood of injury is reduced. This is nominally achieved through use of lightweight, crushable materials which can undergo large regimes of deformation at a near constant stress [63]. Liners for single-hit helmets are routinely manufactured from rigid polymeric foams, such as expanded polystyrene, and

leverage non-recoverable deformation mechanisms, such as plasticity and fracture, to facilitate high volumetric energy absorption under impact. In contrast, multi-hit liners are derived from elastomeric foams such as polypropylene, polyurethane and vinyl nitrile which are nominally denser than their single-hit counterparts. Unlike, single-hit liners, these materials exhibit lower volumetric energy absorption due to their exclusive use of non-permanent deformation mechanisms such as viscoelastic dissipation and elastic buckling.

Clearly an ideal impact mitigating liner would be multi-hit capable as the onset of permanent deformation will diminish helmet performance. This would be particularly beneficial to cycling and motorcycling, where instances of secondary impacts through interactions with a car and then the ground occur frequently [73]. Moreover, it is common for a user to unknowingly wear a previously damaged helmet via seemingly innocuous drops, or by virtue of resistance to replacing the helmet following an impact despite contrary advice [15]. The use of a multi-hit materials are limited by mass, volume, and manufacturing constraints, necessitating a design choice and ultimately limiting them to the applications that truly require it. Whilst elastomeric foams are well established as impact mitigating materials for helmets, they have progressed minimally. Small improvements have been reported in manufacturing optimisation [63] and the use of advanced materials [74], however, an obvious step change has not been achieved. Consequently, there is a growing motivation to develop multi-hit liners which can replace elastomeric or ultimately rigid polymeric foams.

2.3.3 Design for impact mitigation

The design for impact mitigation of a helmet focuses on identifying the ideal design parameters which satisfy the objective of protection prescribed by a design standard. In this case, protection refers to impact mitigation. It can, and does, refer to the other aspects of helmet design that have previously been mentioned, although the primary focus shall be impact mitigation within this thesis. During an impact, the kinetic energy is defined by the sum total of mass of the head¹

¹It is important to note that the body contributes to the impact energy, where the presence of the body increases the helmet liner crushing distance. Headforms with up to a 40% increase in mass, yielding an equivalent increase in impact energy, have been proposed to capture this influence [75], however, this has not been adopted within the present investigation as it is not currently reflected in the design standards tests.

and velocity. Initial contact with the impact surface gives rise to a contact force which opposes the motion, causing it to deform. Energy is stored in the contacted material in the form of strain energy due to the deformation. The velocity of the head will decrease from its initial value due to the opposing contact force until it reaches zero. A restoring force then reverses a portion of the force causing rebound, leaving the impact surface.

The typical strategy to minimise the transmission of force and resultant acceleration exposed to the head is to use a deformable structure which attenuates the energy at a permissible stress [59]. To deform a structure, however, an energy expenditure is required. This energy expenditure is a product of the reactive force and extent of deformation, which can be visualised by the area beneath a force-displacement, or similarly, stress-strain curve where the area is in fact volumetric energy absorption.

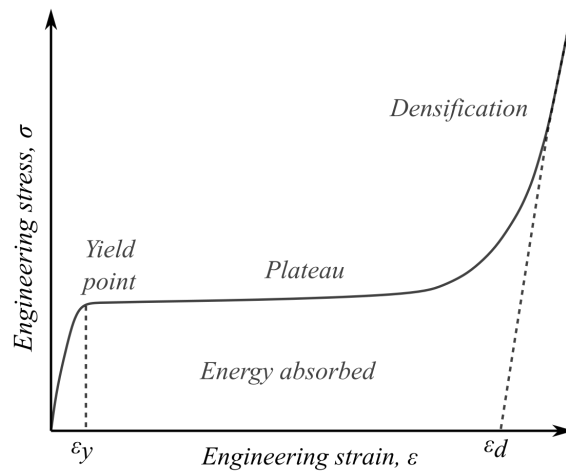


Figure 2.5: Exemplar behaviour of a crushable material used for impact mitigation. Adopted from [76]

As illustrated by figure 2.5, for an exemplar crushable material such as a polymeric foam, a large proportion of energy absorption occurs beyond the point of yielding within a long plateau phase [76]. Considering the simple case of pure compression arising from a direct helmet impact with a flat anvil, which for the sake of simplification shall be analogous to the crushing of material between rigid plates. When the work done by the restoring force via deformation of the structure is equal to the kinetic energy of the impact energy, the motion of the impact either stops in the case of a perfectly plastic impact or reverses in the case of

elastic recovery. Consequently, consideration of static properties such as strength and stiffness are not sufficient for the selection of helmets materials. Rather yield stress, plateau behaviour, densification strain and volumetric energy absorption are more informative, as well as the overall thickness of the liner section.

The impact absorption capability of common helmets can be tuned by balancing the thickness and, for the case of foam materials, the density used in the liner [77]. Increasing thickness² promotes greater capacity for absorbing energy by extending the distance available to mitigate the impact via compression, however, it is at the expense of helmet size and therefore user comfort. Increasing foam density increases the yield stress which enables a greater magnitude of energy to be absorbed, however, exposes the user to a greater peak acceleration as a result. A dilemma therefore arises, whereby a compromise between the maximum acceleration transmitted to the head and the helmet liners mechanical properties must be selected for a given thickness [59]. This is further limited by a low number of design parameters to achieve this optimally.

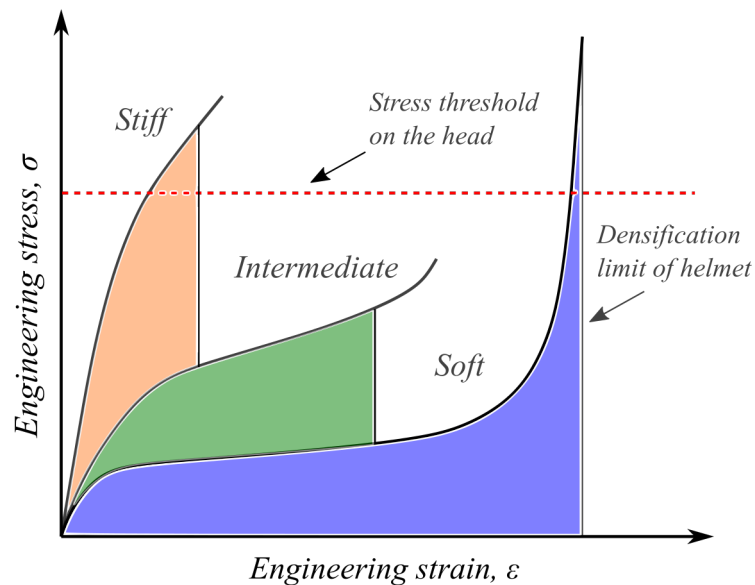


Figure 2.6: The influence of material selection when the equivalent magnitude of energy is absorbed. Adopted from [59]

As illustrated by figure 2.6, a spectrum of different liner material behaviours can be used within a helmet, which ultimately yield varied responses when subject

²Increasing thickness of the liner also has an implication on the development of rotational acceleration which shall be discussed later in this section

to an impact of equivalent energy. A softer material results in a reduced initial contact force and therefore acceleration level, however, is likely to densify before suitably mitigating the entirety of the impact energy. As a result, the densification will be reached, yielding a high acceleration level which might exceed the permissible limit on the head. Conversely, adopting a stiffer material, which yields at a high force, results in less deformation and exposes the user to an intolerable level of acceleration. The ideal scenario, as depicted here, is the intermediate response where a force limiting strategy is used, keeping the force exposure at an almost constant level whilst avoiding densification.

The impact mitigation strategy described so far considers only the case of direct helmet impacts that yield pure compression. This results in minimising translational acceleration without consideration of rotational acceleration. There is limited information on how the effect of material selection influences the behaviour under oblique conditions. This, however, is contrary to the fact that most helmet impacts are oblique in nature [78], which leads to loading of the liner under a combination of compression and shear [79]. This loading condition leads to simultaneous components of tangential and normal forces acting on the head. The normal force can act through the centre of gravity, giving rise to translational acceleration, or act off-set from the centre of gravity, giving rise to both translation and rotational acceleration. The tangential force acts perpendicular to the helmet surface and causes a moment which rotates the head. It is the presence of the tangential force, as well as the off-centre normal force [80], which gives rise to components of rotational acceleration.

Considering figure 2.7 (overleaf), by resolving moments about the headform centre of mass, equation 2.7 demonstrates that rotational acceleration is a function of the normal and tangential force, their distance from the centre of gravity (i.e., the lever arm) and the total sum of head and helmet inertia.

$$F_T(R + t) + F_N(h) = (I_{headform} + I_{helmet})\alpha = I_{total}\alpha \quad (2.7)$$

Where F_T and F_N are the components of normal and tangential force, R is the head form radius, t is the liner thickness, h is the off-set distance of the normal force from the centre of gravity, I_{total} is the total inertia and α is rotational

acceleration.

Since headform inertia and the normal force off-set distance is not a design variable, there are two strategies to minimising the rotational acceleration. First, reducing the overall thickness of the helmet liner, ultimately reduces the lever arm. This, however, has a competing effect on the performance of the liner in mitigating the normal component of force, as there is a reduced distance over which to decelerate the impact. Secondly, reducing the magnitude of tangential force transferred to the head can reduce rotational acceleration. This can be achieved by choosing a liner with greater shear compliance, or one which facilitates enhanced decoupling between the helmet and head rotation.

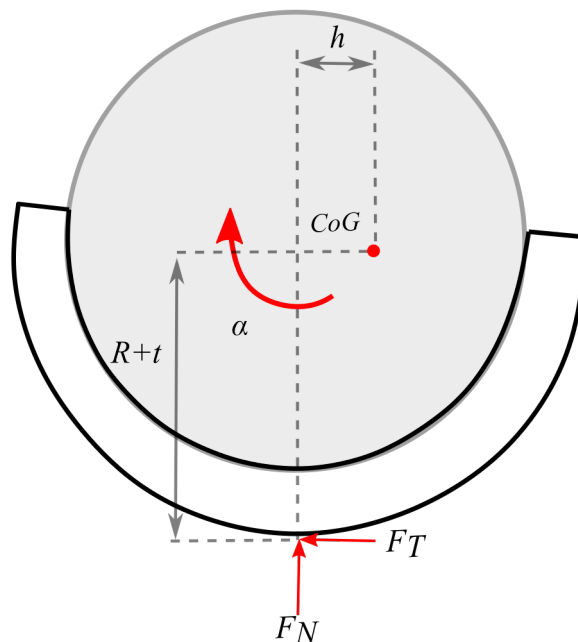


Figure 2.7: Free body diagram of a helmeted head undergoing an oblique impact, giving rise to simultaneous components of normal and tangential force components

Based on the earlier discussions, a helmet's impact mitigating liner should therefore provide sufficient stiffness and deformation such that the impact energy is attenuated without a stress and acceleration arising that exceeds a permissible threshold (e.g., skull fracture) whilst preventing densification. The issue, however, with this approach is that the materials adopted to facilitate this (e.g., polymeric and elastomeric foam) are ultimately too stiff under shear [81] leading to high tangential force and ultimately rotational acceleration. It has been reported that the use of anisotropic materials are better suited for helmet impact mitigation

under oblique conditions [82]. This is due to the combination of high out-of-plane and low in-plane stiffness which, when subjected to oblique conditions, yields a greater shear compliance whilst still sustaining high compression resistance. One such exemplar anisotropic structure, the honeycomb, shall be discussed in the future sections.

2.3.4 Impact test protocols

Whilst the previous discussions have remained broad, incorporating functional requirements, components, and impact mitigation strategies for both single-hit and multi-hit helmets, the following section shall focus on the route for certification of a cycling helmet and the impact test protocols used when evaluating helmet performance.

In order to commercialise a helmet for cycling, it must be subjected to a series of standardisation tests, which take the form of the design standards. Design standards evaluate the helmet performance specifying construction requirements, as well as a minimal level of acceptable performance under a range of testing relative to its field of vision, retention, coverage and shock absorption³. Since cycling is a global endeavour, there are distinct standards set within each territory including the Canadian Standards Association (CS), the U.S. Consumer Product Safety Commission (CSPC), the American National Standards Institute (ASNI), the American society of Testing and Materials (ASTM), the Snell Memorial Foundation, the European Committee for Standardisation (CEN) and the International Organization for Standardization (ISO). Of particular interest to this thesis, shock absorption testing demonstrates a large variability across the testing bodies. In particular, the use of varying impact conditions, human head test surrogates, assessment criteria and thresholds demonstrate there is a lack of harmonisation [60]. Notably, the expected impact energy for a flat impact varies from 55 J to 110 J, arising from impact velocities equivalent to 4.7 m/s and 6.63 m/s respectively. The associated permissible acceleration thresholds for these tests also range from 250 g to 300 g. The consequence of this is that a helmet that passes one standard may not necessarily pass another. In fact, helmet

³Within this thesis shock absorption is synonymous with impact mitigation

standards do not differentiate performance between models [83]. It is only since the inception of the STAR (Summation of Tests for Analysis of Risk) evaluation system that informed consumer choice has been enabled [84].

Further disparities are observed within the experimental setup and therefore boundary conditions of the test, which have a knock down effect on helmet performance. All tests use a rigid headform, either EN960 or ISO6220, however, there is distinction between guided fall and free fall test configurations as illustrated by figure 2.8. In a guided impact setup, as used by the CSA, CSPC, ASTM and Snell, the impact headform is aligned and restrained by a rigid metallic arms such that only translational motion in the vertical direction is permitted in response to an impact with the anvil. In contrast, the free fall setup used by CEN allows headform motion in three-dimensional space following an impact. The lack of restraint allows for rotation, however, these kinematics are not considered in the pass / fail criteria of the standard. Comparison of the two methods under equivalent impact conditions has revealed that the free fall method is a less severe condition, reporting that the presence of rotation facilitates re-direction of impact energy to rotational kinetic energy whilst minimising peak translational acceleration [85]. Therefore, without consideration of all kinematics, there is a danger that helmet manufacturers could inadvertently exploit rotation to facilitate improved translational kinematics.

Currently, the review has focused on impact test protocols used within the current design standards. Notably, these adopt direct impacts, which yield translational kinematics without consideration of rotation. There is a significant body of research that shows rotational kinematics are in fact the key determinant of brain deformation and subsequent damage to the tissues [10]. Oblique testing which yields rotational kinematics should therefore be included in future test standards. Whilst this disparity exists within the certification standards, various testing protocols have been developed within the scientific literature and third party test houses, that enable measurement of rotational kinematics as a result of an oblique impact. Early examples included a guided helmeted headform dropped onto a moving sled [80]. In this setup, an oblique impact is achieved by the horizontal motion of the sled. Newer protocols achieve an oblique impact through an angled anvil, which helps to reduce the complexity of the setup and space required [86]. In addition to these setups, increased biofidelity and more physi-

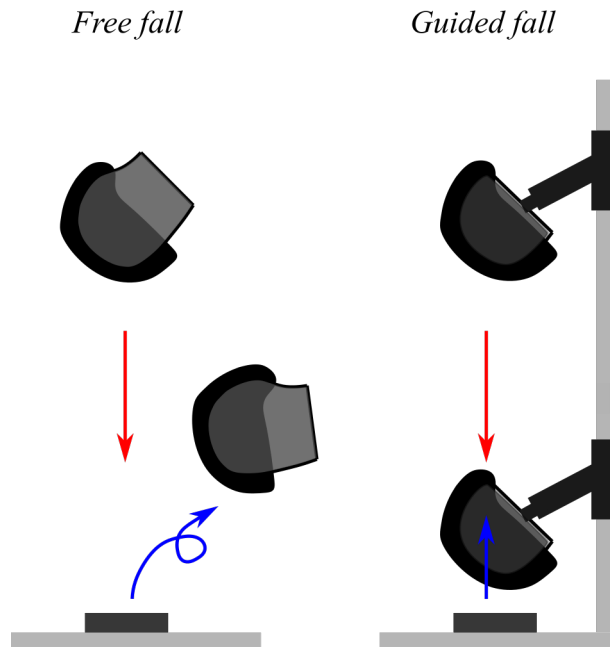


Figure 2.8: Comparison of impact test conditions for guided and free fall. Adopted from [85]

ological loading has been achieved through the inclusion of neck surrogates [84] and the body [75]. The presence, however, of the neck for helmet impact testing is contested. It is well known that the Hybrid III neck is far too rigid in flexion and is not designed for extension, lateral flexion or torsion. Moreover, for short impacts the influence of the neck is negligible as peak values are similar for case with and without the neck for the first 10 ms [87]. Since cycle helmet impacts typically occur over 5 - 10 ms the omission of the neck is generally acceptable for helmet testing.

Guided by the current literature, the CEN working group 11 (CEN/TC158/WG11) has recently suggested a new method for inclusion in the next generation of standards. As illustrated by figure 2.9, modification has been made to the current EN1078 free-fall protocol, which now includes a vertical drop towards a 45 degree anvil to enable measurement of rotational kinematics. Furthermore, a newly developed headform with biofidelic inertia [88] and surface coefficient of friction [19] has also been suggested for use in addition to the impact surface being finished with rough grinding paper to better represent the impact surface friction.

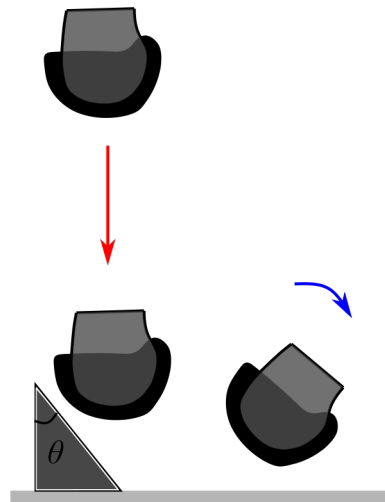


Figure 2.9: CEN WG11 proposal of test methods for direct and oblique impacts

2.3.5 Emerging technologies

As previously discussed, common bicycle helmets employ a liner of rigid polymeric foam which serves to attenuate the impact energy, reducing the impact force and in turn minimising the translational and rotational head acceleration. Recently, emerging technologies that are aimed at improving the safety performance of a helmet have been introduced to helmet designs. These systems can take various approaches, either using a slip liner, collapsible or inflatable⁴ structures.

The recent developments in emerging technologies for bicycle helmet designs are promising for the future of cycling safety and injury prevention. Overall, the introduction of these technologies provides a performance benefit [90]. For low velocity impacts (4.2 m/s), PTA and PRA are reduced by 20.2% and 21.8% respectively when compared to a conventional polymeric foam liner. Moreover, when considering the injury severity metric, GAMBIT, the relative reduction was 52.6%. For high velocity impacts (5.9 m/s), the reduction, however, is less notable. For PTA, PRA and GAMBIT, the relative reduction was 5.6%, 6.6% and 17.6%. This is likely due to the test velocity exceeding the design standard velocity (5.42 m/s) which will have informed the design rationale.

⁴Inflatable structures have been omitted from the review as they are not subject to the same design volume constraints as contemporary helmets or helmets with slip liners and collapsible structures. For a more in-depth review, refer to [89].

Multi-directional impact protection system (MIPS) [91], is an established slip liner technology which aims to improve the protective capacity of helmets by introducing a low-friction layer between the foam liner and head (figure 2.10a). Under impact the foam manages the normal forces which results in translational acceleration whilst the slip liner improves the decoupling of the head and helmet rotation yielding a reduction in tangential force and thus rotational acceleration [91]. It is important to note, however, that the efficacy of the system may be limited by both the tightness of fit and shape of the head, which may inhibit relative movement in certain orientations [53]. Nevertheless, the value of this technology is that it can be installed in addition to newer, more advanced liners and therefore its use is not prohibitive of different liners designs.

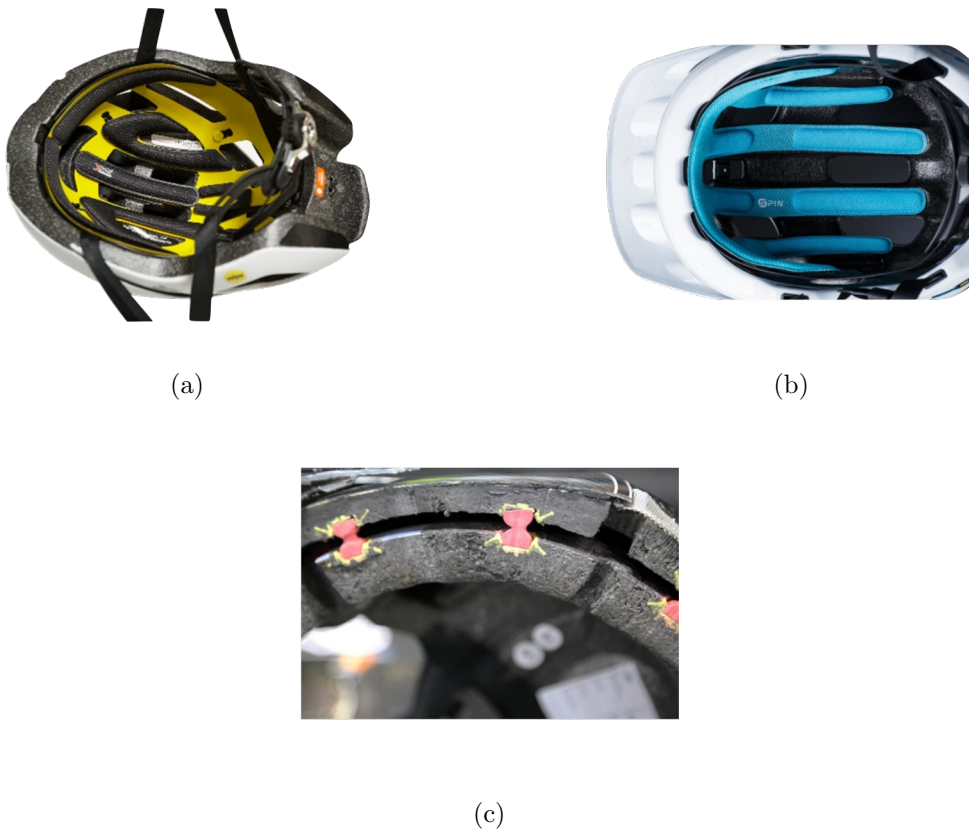


Figure 2.10: Slip liner technologies, MIPS (a), SPIN (b), and ODS (c), available within cycling helmets.

Similarly, shear pads inside (SPIN), is another example of a slip liner which also serves to improve rotational mitigation of helmets [92] (figure 2.10b). Comprising a pad which contains low friction silicone, the pad shears during oblique

conditions, improving the decoupling of the head and helmet rotation. The last example of a slip liner system is omnidirectional suspension (ODS) (figure 2.10c). ODS comprises a dual EPS liner connected by an array of elastomeric hour-glass shaped dampers. The unique geometry improves the decoupling of the upper EPS liner and shell which is in contact with the ground and the lower EPS liner in contact with the head.



Figure 2.11: Collapsible structure technologies, WaveCel (a) and Koroyd (b), available within cycling helmets

WaveCel is an example of a collapsible structure which takes the form of a polymeric auxetic honeycomb embedded within a foam liner [93] (2.11a). This serves as an alternative strategy to introducing a slip liner to achieve a similar effect in terms of rotational acceleration mitigation. The collapsible structure is designed such that there is a distinct mechanism of mitigation for the tangential force. Specifically, each cell has a transverse crease to initiate organised cell buckling deforming in-plane as illustrated by 2.12 (overleaf). This is also in addition to the impact mitigation achieved by the foam liner, however, this has a reduced capacity as the liner thickness is reduced to house the structure therefore the collapsible structure must also provide additional normal force mitigation.

Koroyd is another example of a collapsible structure [94] (figure 2.11b). Comprised of a hexagonally packed circular honeycomb liner which is either used in its entirety through the helmet liner or sits within a recess of a pre-existing foam liner. The specific mechanisms for reducing tangential force is unclear, however, it is claimed that this technology reduces translational acceleration which also reduces angular acceleration, regardless of the impact direction. It may however be

due to the anisotropic nature of the honeycomb as to why a reduction is observed, although limited analysis exists.

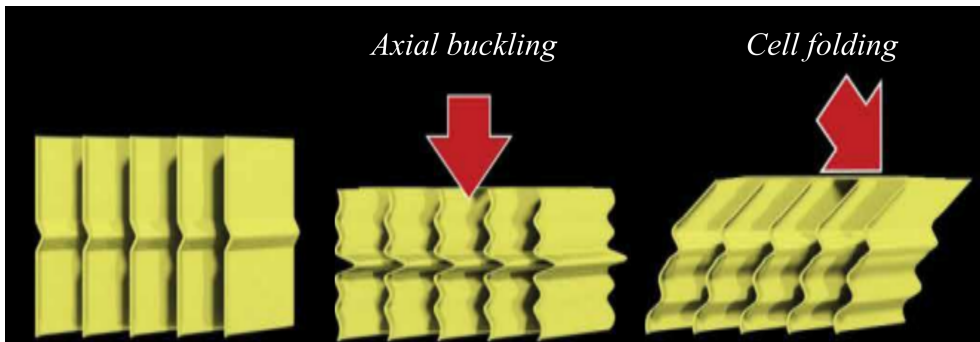


Figure 2.12: WaveCel deformation mechanisms under axial buckling and cell folding. Adopted from [95]

Both types of emerging technologies improve the protective capacity. In addition to the performance benefits of collapsible structures, however, other advantages such as light weight, high heat transfer rate and airflow permeability makes liners derived from prismatic cellular structures, or other cellular structures, a good potential to replace conventional foam liners. Either derived from a polymer for single-hit applications or, elastomers for multi-hit, there is potential to improve rider safety. These could be further augmented with a slip liner technology to combine the performance benefits of both.

2.4 Prismatic cellular structures

This section describes the literature that was reviewed concerning prismatic cellular structures. In particular, the topology and mechanical properties are described. Furthermore, numerical methods are identified and reviewed. Lastly, manufacturing methods are described.

2.4.1 Topology

Prismatic cellular structures are one of three groups used to classify cellular structures, the others being foams and lattices [76]⁵. Prismatic cellular structures, hereafter referred to simply as honeycombs, are denoted as two-dimensional shapes extruded in the third dimension. The most obvious example of these structures is the hexagonal honeycomb which occurs in nature, however, outside of nature, the use of honeycombs have been widely adopted for use in several industries such as aerospace, transportation, build construction and sporting equipment [96]. Owing to the intrinsic simplicity, other topological variations may be formed from 2D shapes such as circular [97], triangular [98], and square [99] to name but a few. As illustrated by figure 2.13, these single unit cells, nest together to fill a plane and form an array.

The parameters which describe the unit cell topology of a honeycomb are cell size, depth, and wall thickness. Cell size is defined as the distance between the top and bottom edge, if these are equal then the unit cell is considered regular. The depth of the honeycomb is the extrusion distance of the 2D shape, whilst the wall thickness equates to the thickness of material from which the honeycomb is constructed.

Honeycombs can be differentiated from the solid material which they are derived from by consideration of the relative density. Relative density, R_ρ represents the ratio between the volume encompassed by the honeycomb core and the unit cell extremities, as reported by equation 2.8.

$$V_f = \frac{V_{honeycomb}}{V_{reference}} \quad (2.8)$$

Where $V_{honeycomb}$ is the volume of the honeycomb and $V_{reference}$ is the volume defined by the unit cell extremities.

Owing to the construction of honeycombs, relative density can be simplified as the area ratio of the cross-section. Equations 2.9-2.12, list various relative density

⁵It can be argued that in fact there are only two groups, honeycombs and foams, where a lattice is classified as an open-cell foam.

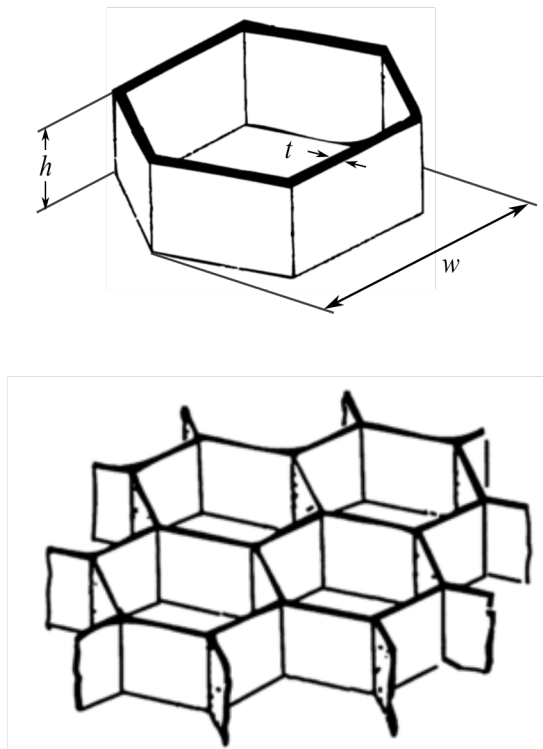


Figure 2.13: Illustration of a hexagonal honeycomb unit cell (top) and an array (bottom)

relationships based on the topology of common unit cells [100].

$$[R_\rho]_h = \frac{2t_h}{s_h} \quad (2.9)$$

$$[R_\rho]_s = \frac{2t_s}{s_s} \quad (2.10)$$

$$[R_\rho]_t = \frac{2\sqrt{3}t_t}{s_t} \quad (2.11)$$

$$[R_\rho]_c = \frac{\pi t_c}{s_c} \quad (2.12)$$

Where t is the wall thickness and s is the unit cell width, for which it is assumed that the unit cell is regular. Superscript h , s , t and c denotes the hexagonal, square, triangular, and circular topology respectively.

2.4.2 Mechanical properties

Honeycomb mechanical properties are commonly described relative to three directions termed 'W', 'L' and 'T', as illustrated by figure 2.14. 'W' and 'L' refer to the in-plane behaviour, whilst 'T' refers to the out-of-plane behaviour [101]

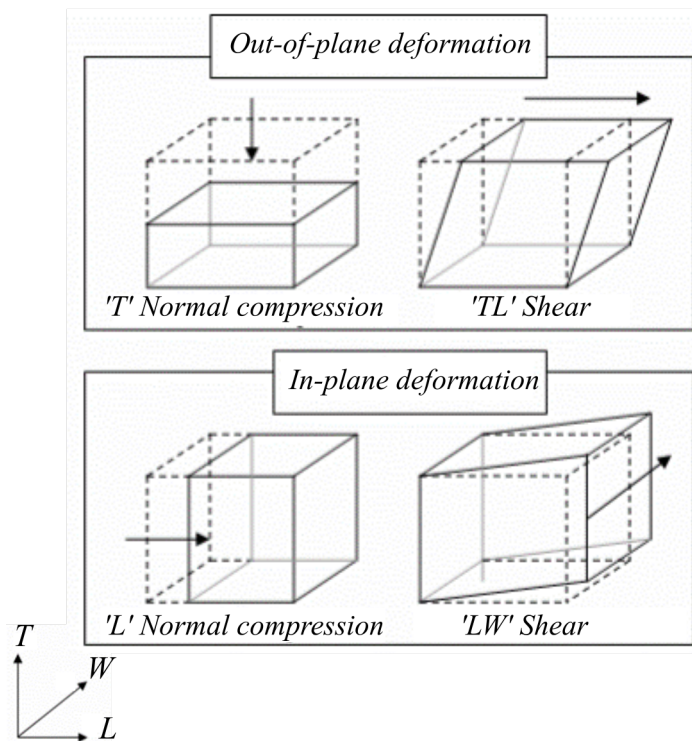


Figure 2.14: Definition of honeycomb orientations

Honeycombs have distinctly different in-plane and out-of-plane response. Consequently, they are anisotropic and depending on the construction, they can be either orthotropic or transversely isotropic [76]. The in-plane response is soft and spring-like, dominated by bending and the collapse of the cell walls. The out-of-plane response is stiffer, as the walls must be compressed and resist buckling as a hollow tube. As such, the out-of-plane orientation is commonly adopted for engineering applications that require impact resistance and mitigation by lever-

aging the intrinsic high specific energy absorption [102]. Despite this, in-plane behaviour has been extensively studied experimentally [76] and numerically [103] with respect to its structural parameters [104], loading conditions [105] and strain rate [106]. This is due to the fact that honeycomb manufacturers commonly omit this information. Nevertheless, the out-of-plane orientation remains the most suited for helmet applications where protection from multi-directional loading is required [107]. Hence, this section and the remainder of the thesis shall focus on the mechanical behaviour in the out-of-plane orientation exclusively.

Out-of-plane loading is defined by the component of stress acting parallel to the axis of the cells. The stress is reported using equation 2.13.

$$\sigma = \frac{P}{A} \quad (2.13)$$

Where σ is the out-of-plane stress, P is the applied force and A is the projected cross-sectional area of the honeycomb array extremities.

Under compressive out-of-plane loading, honeycomb structures demonstrate typical stretch-dominated behaviour which is defined by initial high stiffness with a post-yield softening and non-monotonic plateau stress as illustrated by figure 2.15 (overleaf). This behaviour can be further divided into five phases which are termed linear elastic (1), non-linear elastic (2), softening (3), plateau (4) and densification (5) [108].

Phase 1 is defined by an initially linear elastic response where, for increasing strain, the stress rises. As the cell wall begins to deform axially, this behaviour is truncated by phase 2 where cell wall buckling gives rise to a non-linear response. The end of the non-linear phase is defined by the point at which the local stress in the cell wall exceeds the yield stress of the base material. This is characterised by a peak in stress value. Following, phase 3 occurs, which is characterised by a sharp drop in the stress value as the cell walls buckle and the load bearing capacity of the honeycomb is reduced. Accordingly, the structure collapses, giving rise to deformation in the cell walls. Here phase 4 begins as the stress plateaus and progressive buckling continues for increasing strain. As the strain increases, the progressive buckling results in densification indicated by a sharp increase in stress

where the honeycomb is fully compressed, and the response is equivalent to that of the base material. Entering densification indicates that the honeycomb can no longer absorb energy effectively.

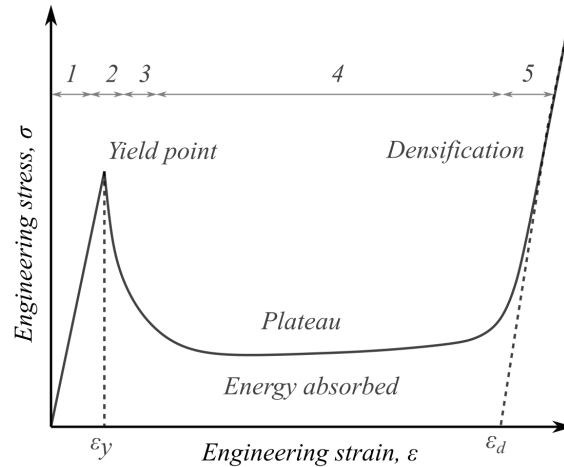


Figure 2.15: Honeycomb out-of-plane compressive response, characterised by typical stretch dominated behaviour.

The effect of relative density on compressive out-of-plane mechanical behaviour is shown in figure 2.16. As illustrated by the previously discussed equations 2.9 - 2.12, the relative density for a set cell size is proportional to the wall thickness. Therefore, under normal compressive loading, the initial response reflects the solid modulus of the base material scaled by the load-bearing area section. Consequently, there is a direct dependence of compressive behaviour to relative density [76]. Furthermore, the modulus of elasticity, yield and plateau stress increases with increasing relative density, whilst the length of plateau and the strain at the onset of densification decreases [109]. This is attributed to increased wall thickness resisting buckling and consequently the neighbouring cells walls touching earlier.

The applied strain rate also affects the compressive out-of-plane behaviour. Typically the behaviour under increased strain rate is characterised by increased stress at yield and energy absorption capability when compared to quasi-static conditions. This behaviour can be attributed to four phenomena namely, strain rate sensitivity of the base material [110], entrapped air contributions [111], as well as inertial stabilisation and plastic wave propagation [112]. Base material rate dependence is exclusively due to the adopted material, where honeycombs man-

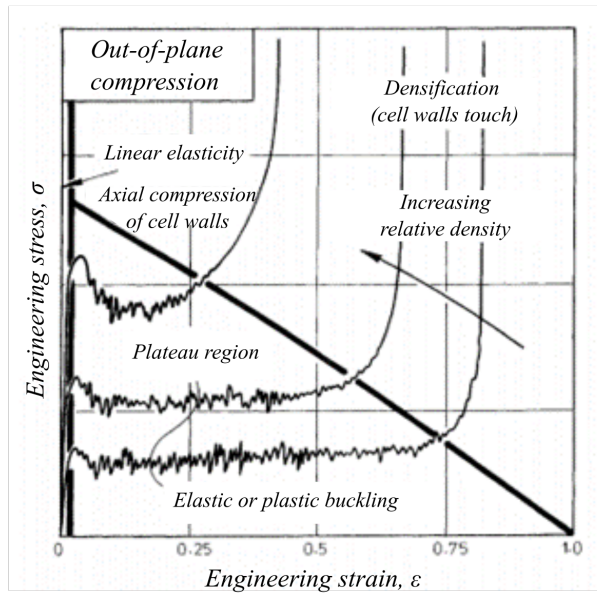


Figure 2.16: Influence of relative density on the honeycomb mechanical behaviour.
Adopted from [76]

ufactured from polymeric and composite materials present greater strain rate sensitivity than metals. The compression of entrapped air within the unit cells causes pressure changes which yield enhanced dynamic stiffness, although this requires a seal between the supported and impact faces, otherwise the air escapes. Inertial stabilisation gives rise to rate dependence due to the activation of high order buckling modes, whilst further enhancements are unlocked via plastic wave propagation. The last two phenomena, however, occur at dynamic velocity of 30 m/s and greater than 50 m/s respectively. Therefore, it is unlikely these conditions will be met, or leveraged, for the application of helmet design. Rather, rate-dependence may be leveraged through adopting materials which have notable rate-dependence, such as elastomers [113].

Whilst most applications ensure that the out-of-plane behaviour is orientated towards the anticipated loading direction such that normal compression is achieved, it is unlikely that this can always be ensured. As such, a honeycomb may be subjected to combinations of normal compression and shear loading [114] relative to the 'TL' and 'TW' orientation, as illustrated by figure 2.14. The effect of combined loading regimes has a notable effect on the mechanical behaviour of the honeycomb [115]. As illustrated by figure 2.17, deviation from the classical normal compressive response is observed with a reduced yield and diminishing

plateau [116]. This is further influenced by the loading angle and orientation [117]. Furthermore, the shear response presents an initial yield followed by a regime of negligible stress as the cell walls buckle in-plane. This is attributed to the anisotropy of the structure, where the out-of-plane response is stiffer than the in-plane response. Notably, the ratio of shear to compressive stress yields a nominal value of between 0.15 - 0.30. When compared to equivalent conditions, other commonly used impact mitigating materials such as vinyl nitrile, expanded polypropylene and expanded polystyrene report ratios of 0.50 [81], 0.80 [118] and 0.4 [119] respectively. Hence, for conditions which incur combined loading regimes such as an oblique impact in a helmet, a honeycomb could transmit proportionally less force in shear than in compression compared to existing foams.

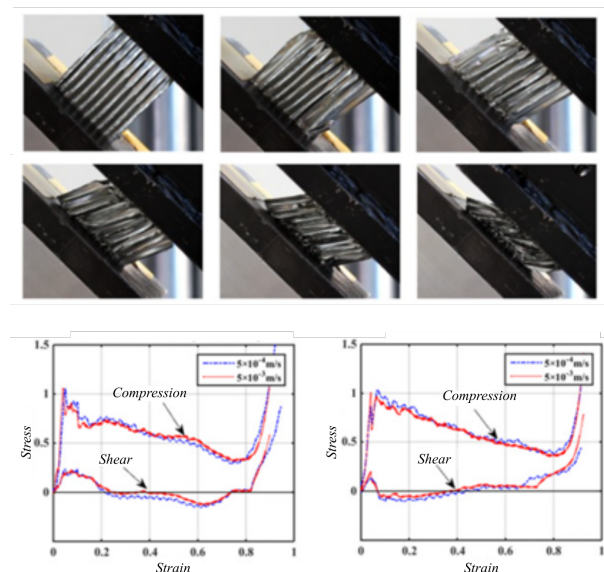


Figure 2.17: Honeycomb under combined compression shear loading, adopted from [117]

Currently, the description of behaviour has focused on metallic honeycombs. Whilst metallic honeycombs have been adopted with success for use in a helmet either as localised reinforcement [120], exclusive use [121], or a hybrid system of foam and honeycombs [122], providing superior performance relative to a monolithic equivalent. In all cases, the principal mechanisms leveraged to mitigate the impact energy are plastic deformation and material fracture. These solutions are unsuitable for applications with potential for multiple (or consecutive) impacts however, as the onset of permanent deformation will diminish helmet

performance [15] Therefore, adopting robust materials such as elastomers may enable a honeycomb structure capable of repeat impact mitigation [123].

Changing the material, however, has a notable effect on the mechanical behaviour [110]. Honeycombs manufactured from elastomers deform elastically and are recoverable, whilst metal and rigid polymer, deform plastically resulting in permanent deformation and fracture. The mechanism of buckling also changes, from buckling plastically at folding hinges as illustrated by figure 2.18a, to elastic buckling as illustrated by figure 2.18b. This results in a change in the stress strain profile, where the period of stress softening is greater, the non-linear profile of buckling is more pronounced and the plateau region is diminished [124].

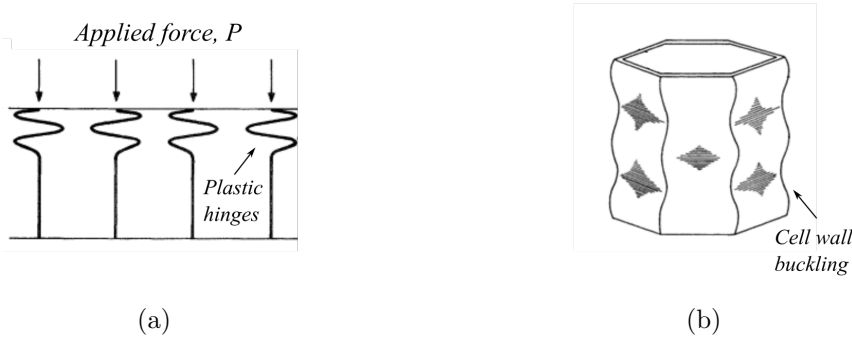


Figure 2.18: Illustration of different buckling phenomena, folding plastic hinges (a) and elastic buckling (b), observed in honeycombs under out-of-plane compression

2.4.3 Numerical modelling

The mechanical behaviour of a honeycomb can be explored using analytical approaches [76], numerical simulations [125] and experimental techniques [126]. Whilst experimental approaches can provide accurate results as true to reality as possible, they are, however, time-consuming and expensive to run over successive, iterative design cycles. Analytical approaches can enable analysis of simple honeycomb topologies, such as circular, rectangular in terms of their elastic modulus, although are limited in the representation of novel topologies. Furthermore, they fail to accurately predict the shear behaviour and progressive collapse of honeycomb cells. Numerical simulation based on finite element analysis can be

adopted to predict the behaviour of structures under a wide range of loading conditions, strain rates and facilitates exploration of complicated geometries otherwise unobtainable using analytical approaches.

Finite element has been used extensively to analyse the mechanical behaviour of honeycomb structures. This is motivated by unlocking the potential of these structures for improved bending and impact resistance as well as energy absorption. Depending on the application, honeycomb arrays can be comprised of hundreds of cells under loading. As each cell has a nominally small wall thickness, the resultant mesh will comprise thousands of elements. Consequently, this comes at high computational expense. To reduce the computational cost of running these simulations, an established strategy is taking advantage of symmetry through representative area or volume elements with periodic boundary conditions applied [127]. These reduced periodic boundary condition models consist of one, or a few, unit cells which are restrained by pairs of opposing boundaries. This results in identical deformation, thus creating a scenario where edge or boundary effects are eliminated. The rationale for this approach assumes that a system comprised of a large number of repeating cells will deform similarly to an infinite system. In this system, the ratio of boundary units to internal units is very low, and therefore the overall behaviour is determined by deformation of the internal units. This represents an ideal strategy for design optimisation, increasing the number of design cycles by reducing the computational expense of each finite element simulation.

Within the finite element solver, there are various approaches to modelling the geometry of a honeycomb structure. Previous investigations have adopted a variety of element types including brick [124], shell [120], and beam [128]. Brick elements are recommended for large deformation analysis as they are computationally efficient and accurate, however, require hourglass control and high element counts to prevent shear locking which can lead to spurious results under bending conditions [129]. Shell elements require fewer computations when compared to brick elements due to the reduction in nodes, and are suited to applications where the shell thickness is significantly smaller than the other dimensions. Beams elements are simpler still and more computationally efficient. Whilst adopting shell elements for honeycomb analysis is common practise [102] when compared to the response of brick element and beam elements under equivalent conditions, hon-

eycombs meshed with brick elements best match experimental data sets [128]. Hence, this approach will be leveraged within the methodology of this thesis.

2.4.4 Manufacturing methods

Since the inception of commercialised manufacture of honeycombs, several manufacturing methods have been developed. These include expansion, slotting and corrugation joining which comprise several steps, as illustrated by figure 4.6, and are exclusive to certain materials and wall thicknesses [130]. Expansion forming is suited to honeycombs with thin walls derived from metals, as well as composites, and is characterised by the stacking of material along offset bond lines. After being cut to the appropriate thickness, they are expanded to form a honeycomb. Whilst compatible with similar materials to expansion, slotting is best achieved by thick strips of material. Slotting, is the interlocking and bonding by brazing or adhesive of individual strips. This is best represented by an interlocking square formation, although other topologies can be realised. Lastly, corrugation is compatible with intermediate wall thickness, where sheets are corrugated between rollers prior to stacking and bonding. Polymeric honeycombs are compatible with expanding and slotting manufacturing methods, although this doesn't extend to the use of elastomeric materials. Elastomeric honeycombs can be manufactured using casting [131], although this ultimately requires manufacture of moulds, which limits the design freedom afforded by the process.

The issue associated with these manufacturing methods is that they result in a flat, planar section. When a honeycomb is wrap into a curved volume, such as a dome, or the curvature of the head, the resultant curvature is anticlastic [132]. Modern manufacturing methods can now facilitate curved volumes by use of thermal welding (such is the case for fabricating Koroyd [133]). At present, however, these new techniques do not allow for changes in out-of-plane profile (e.g., folds) which can enable tailorable energy absorption [124]. Additive manufacturing presents both the geometric freedom to enable fabrication throughout a curved volume whilst retaining the ability for fine features.

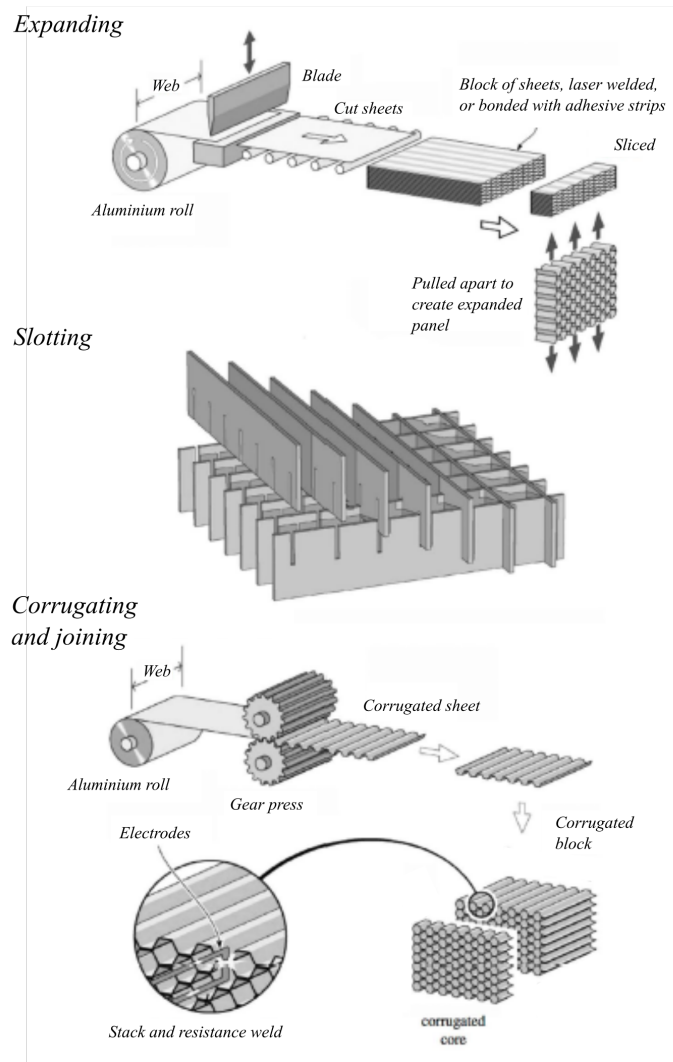


Figure 2.19: Several conventional manufacturing methods for honeycombs including expanding, slotting and corrugation & joining. Adopted from [130]

2.5 Polymer Additive Manufacturing

This section describes the literature that was reviewed concerning polymer additive manufacture. An initial overview and definitions are provided relating to additive manufacturing and its various processes available for manufacturing polymers, before focusing on laser sintering. Next, further descriptions are provided referring to the manufacturing mechanics and artefacts which arise due to laser sintering and how they influence the sintered mechanical behaviour. Lastly, currently available materials are established and reviewed relative to the mechanical properties.

2.5.1 Process definitions

Additive manufacturing (AM) is the process of building parts through controlled deposition or binding, of material rather than conventional means such as subtractive (e.g., machining) and formative (e.g., injection moulding) methods which use a tool to form a part. This therefore enables manufacturing structures which would otherwise be unobtainable based on conventional manufacturing restraints and costly tooling overheads. This can facilitate topology optimisation in the pursuit of lightweight structures [134], as well as low-cost geometric freedom to enable user-specific customisation of components [135]. Consequently, AM has been applied to several industries such as construction, prototyping, biomedical, sportswear and protective equipment [136].

ASTM international has consolidated and characterised AM technologies into 7 broad categories which include: Material Extrusion, Material Jetting, Binder Jetting, Sheet Lamination, Vat Photopolymerisation, Direct Energy Deposition and Powder Bed Fusion [137]. Table 2.1, lists each category, providing a description of the process and examples of technology available. Of note, however, Direct Energy Deposition has been omitted from the review as it cannot facilitate polymer manufacturing. For more information relating to detailed description of the technologies, refer to [138].

Table 2.1: Description of additive manufacturing processes and their relevant technologies

Process definition	Description	Technologies
Material Extrusion	Continuous extrusion of build material through a nozzle or orifice onto a build platform where it subsequently solidifies.	Fused Deposition Modelling (FDM).
Material Jetting	Analogous to conventional 2D inkjet printing whereby liquid material is deposited from the printhead onto a platform, either on demand or continuously, which is then subsequently solidified through photopolymerization.	Multi-jet Modelling (MJM), Three Dimensional Printing (3DP).
Binder Jetting	Uses two materials, a powder-based material and a binder. The binder acts as an adhesive between powder layers.	Binder Jetting.
Sheet Lamination	Cut sheets of material are stacked to form a 3D object and then joined either using an adhesive or heat source.	Laminated Object Manufacturing, Ultrasonic Consolidation.
Vat Photo-polymerisation	Radiation curable liquid resins (photopolymers) are irradiated, enabling a chemical reaction to occur, causing solidation of the resin.	Stereolithography, Digital Light Processing.
Powder Bed Fusion	Sequentially stacked layers of powder are sintered using a thermal source (e.g., laser) to fuse the powder particles together.	Laser Sintering

From the perspective of selecting a process for the development of a helmet liner, some technologies discussed in table 2.1 are prohibitive. To develop a continuous liner, which takes the form of a prismatic cellular structure within a doubly-convex volume, the process must:

1. Be self-supporting to achieve a conformal geometry.
2. Achieve fine detail on the scale of a mm.
3. Have equivalent material properties to established polymer processes.
4. Be able to process elastomeric materials.

Considering these requirements, the use of binder jetting was deemed inappropriate due to the material characteristics not being suitable for structural parts. Sheeting lamination was also excluded as it is unable to create complex geometries. Material jetting is known to exhibit fatigue over multiple loading cycles, so was not considered. Material extrusion and Vat Photopolymerisation both have a large array of materials available, can yield fine detail and achieve near equivalent material properties to injection moulded parts, however, cannot achieve conformal geometries without additional supports. Hence, powder bed fusion, in particular laser sintering, was adopted for use within this thesis. As such, the remainder of the section shall focus on process mechanics, artefacts of manufacturing and currently available materials relevant to laser sintering.

2.5.2 Laser sintering mechanics

Sintering refers to coalescing of powder material into a solid by means of heating without liquefaction. Laser sintering is therefore achieved by selective fusing of powder via application of a laser. This occurs over successive layers of 2D slices, which represents a 3D geometry.

As illustrated by figure 2.20, thermal energy supplied in heating of the powder and application of the laser raises the temperature of the powder beyond its melting point. Following, sintering begins where the outer region of the powder particles melt first, giving rise to necks at the contact points between adjacent particles. The evolution of the liquid phase from the solid phases begins and coalesces around the particle core, which commonly remains solid [139]. Following removal of the laser, the regions where melting occurred cool and return to their solid state.

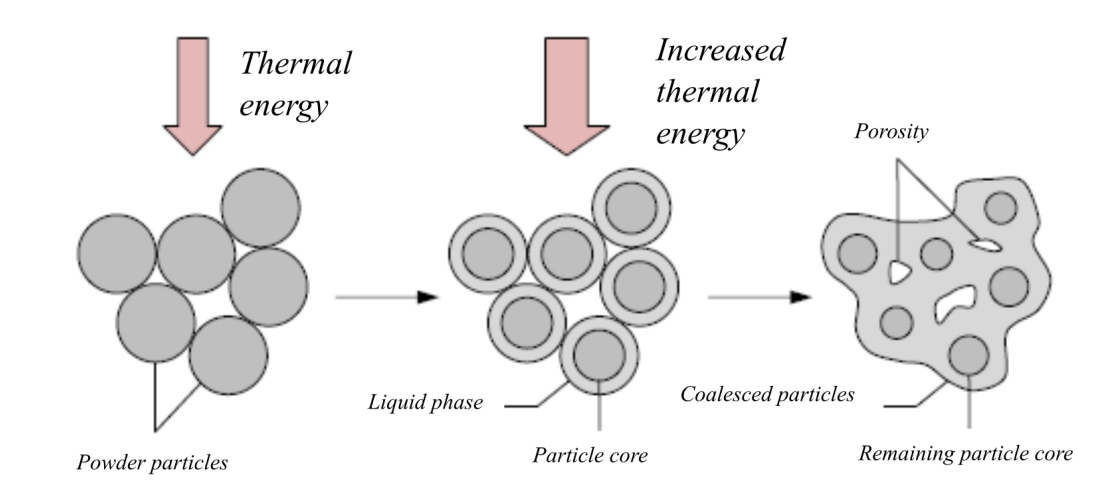


Figure 2.20: Illustration of the sintering particles giving rise to a liquid phases which coalesce and form a solid upon cooling. Adopted from [140]

As illustrated by figure 2.21, the laser sintering process includes several steps. Firstly, powder is distributed over the build bed via a roller fed from powder reservoirs. This powder is heated to a point just below the polymer powders melting point, such that melting can be triggered easily by the laser. Following, a laser is then used to fuse the first layer of the cross-section of the model. The build platform is then lowered, and powder is re-distributed using a roller to cover the sintered layer. Further layers are subsequently fused and added. The

process then repeats until the entire model is created. Loose, unfused powder remains in position, supporting the model until it's removed upon completion of the build during the post-processing. The powder that is not sintered during manufacturing can be used during subsequent builds, however, repeat thermal cycling of the material eventually degrades the material characteristics [141]. The consequences of this shall be discussed in the later section.

The quality of the build is subject to operational parameters. Whilst default operational parameters are provided by powder manufacturers, there is inherent variability across machines. Consequently, this requires optimisation [142]. Notably, the processes parameters that have an influence on the laser sintering process are laser power, fill scan spacing, beam speed, scan count, part heater set point and powder layer thickness [143]. Manufacturing artefacts can arise from improper selection of these parameters, leading to compromising mechanical properties.

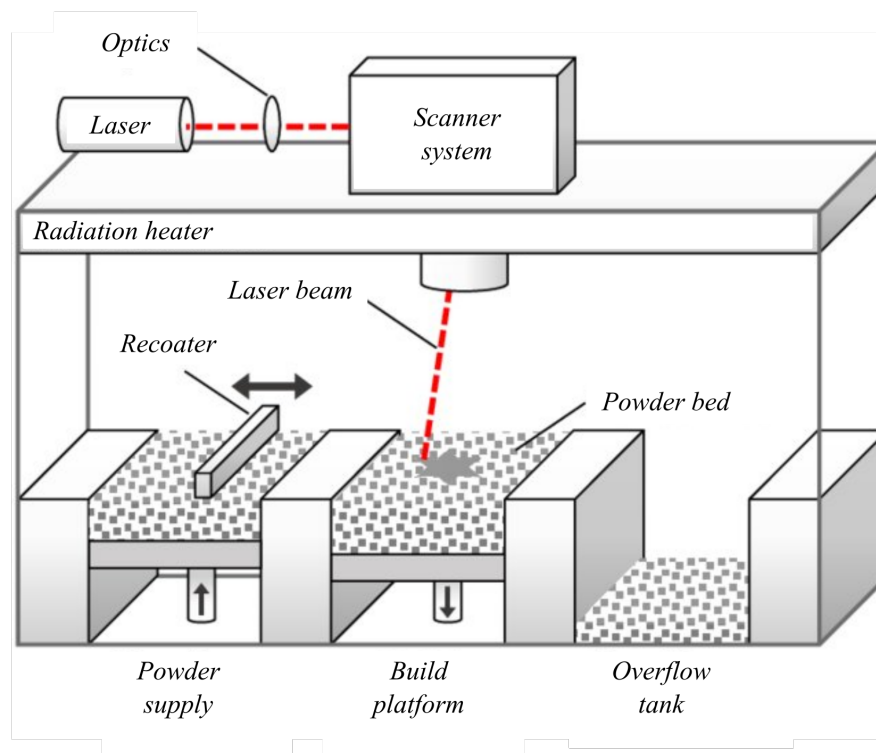


Figure 2.21: Illustration of the sintering process. Adopted from [144]

2.5.3 Manufacturing artefacts

Parts fabricated using laser sintering distinguish themselves from other AM processes. Notably, laser sintering allows for a wide range of thermoplastic materials with high performing mechanical properties to be leveraged. As such, laser sintered parts are durable enough to be used in applications whereby they are subjected to mechanical loads. Despite this, they often exhibit artefacts which inhibit mechanical behaviour. In this instance, comparison is typically drawn to part fabricated using injection moulding as a benchmark for quality [145].

As previously mentioned, repeat heating cycles of unsintered powder gives rise to changes in its mechanical characteristics. Whilst laser sintering aims to recycle unsintered powder, the thermal history and ratio of virgin to used powder can be detrimental to the manufactured mechanical properties. Notably, whilst tensile strength can in fact be improved in builds using the same powder (for a low number of cycles), in subsequent builds it can decrease notably [141]. Moreover, this can also affect the elongation at break [146]. The influence of these phenomena can also be observed visually, where so-called “orange peeling”, as illustrated by figure 2.22, develops as surface roughness [147].

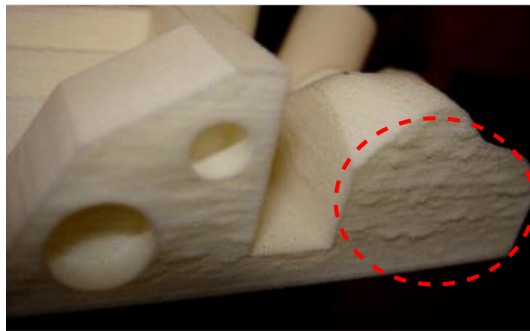


Figure 2.22: Identification of orange peeling artefact on the sintered part. Adopted from [148]

Warping and curling are features of distortion which occur due to the forces which arise due to the contraction of cooling material during laser sintering polymers and give rise to poor quality parts [149]. Curling is associated with the deformation of a localised section of the geometry, most prevalent at the base section (see figure 2.23a). Warping is the distortion of a whole part [150], such that the effect is global (see figure 2.23b). The distinction between the two phenomena is that

material is lost from the geometry because of curling, however, distortion can be managed with thermal treatment.

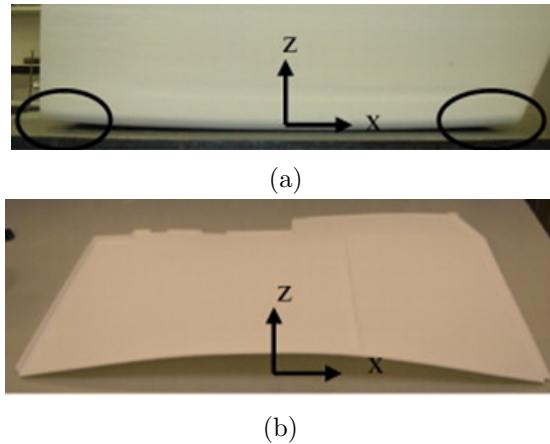


Figure 2.23: Examples of distortion due to laser sintering, curling (a) and warping (b). Adopted from [149]

The density, also known as porosity, of laser sintered parts is known to influence the overall mechanical properties [151]. For example, laser sintered PA12 reports on average a density of 0.95 kg/m^3 which is less than the 1.04 kg/m^3 reported for equivalent compression moulded PA12 [152]. Consequently, considerably lower tensile strength is reported, however, compression properties remain similar. This is likely due to the ease of crack propagation through the inclusion of voids. Similarly, the fatigue performance is notably influenced by the inclusion of unfused powder particles, which give rise to the initiation of cracks and damage [153]. Poor part density arises from inadequate energy [154] or very high-energy levels [155] provided by the laser during the manufacturing. In the latter case, polymer pyrolysis occurs (i.e., thermal degradation), giving rise to a porous structure. The former, however, represents a strategy to achieving variable mechanical properties throughout a build volume [156].

Anisotropy caused by the build orientation and placement within the build volume is a feature of laser sintering process due to the layer-by-layer process [157]. This is similar to other processes such as fused material extrusion [158] and jetting [159]. As illustrated by figure 2.24, as the laser scans across the powder, necks arise between particles. Subsequent parallel laser vectors give rise to similar necks, as the previous scan will have cooled and subsequently contracted. As the layer height increases, fresh powder is spread over each sintered layer, meaning the bond

between particles is different and is further reduced. The weakest properties are therefore experienced when the applied stress is perpendicular to the layer-to-layer bonding.

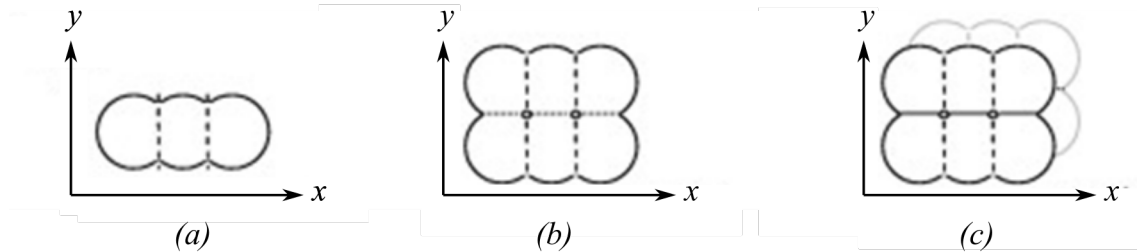


Figure 2.24: Illustration of sintering showing (a) the development of necking between particles in a single vector, (b) necking between parallel vectors and (c) necking between different layers. Adopted from [143]

Anisotropy, on the material scale, is not a desirable feature within laser sintering as it leads to variable mechanical behaviour unlike traditional methods like compression and injection moulding. There is a distinct hierarchy in magnitude of behaviour for each orientation, whereby parts build in the z-axis report less favourable tensile and compressive modulus compared to the y-axis and x-axis respectively (refer to figure 2.25) [157]. The development of anisotropy for polymeric laser sintered materials is well documented [160], however, less information is available regarding elastomeric materials.

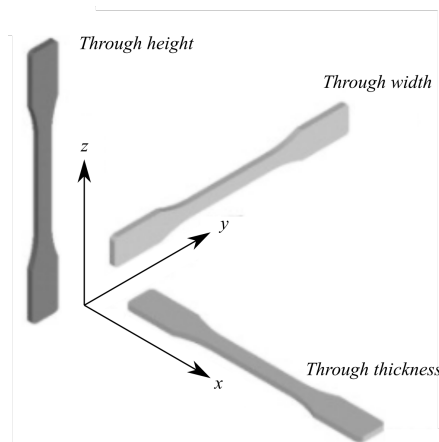


Figure 2.25: Illustration of the build orientations aligned with the x, y and z axis of the build bed. Adopted from [157]

2.5.4 Available materials

Laser sintering has the potential to process a large array of materials with vastly different bulk properties. The polymeric powders used can be derived from amorphous and semi-crystalline polymers. Amorphous polymers (e.g., polycarbonate, PC) do not exhibit a distinct melting temperature. When heated above their glass transition temperature, they gradually soften, eventually reaching a liquid state with no clear transition. Typically, these materials are processed by preheating the part bed surface to a temperature just below the glass transition temperature, with the laser adding enough energy to initiate sintering above the glass transition temperature. Only partial consolidation and significant residual porosity occurs, meaning that parts suffer from low strength compared to traditionally processed counterparts [143]. Consequently, their functional application is limited. One advantage of amorphous polymers is that they exhibit minimal shrinkage upon cooling, which enables the manufacture of components with high dimensional accuracy [161]. In contrast, semi-crystalline polymers do not gradually soften, but change rapidly from a solid to a viscous liquid at a defined melting temperature [162]. Processing involves preheating the part bed surface to a temperature just below T_m , with the laser adding enough energy to enable complete melting. Semi-crystalline polymers can be processed to produce near-full density parts exhibiting mechanical properties comparable to injection moulded equivalents [160]. However, significant levels of shrinkage upon cooling (3 – 4%) [161], with a notable step-change in volume as the material cools through the melting temperature [149].

The availability of commercialised polymer powders for laser sintering is scant in comparison to other AM processes [163]. This is due to the complexity of material development. Challenges include fabrication of a polymer powder with an appropriate particle size, size distribution and morphology [164], as well as identifying polymers with a wide thermal processing window [160]. Nevertheless, companies such as 3D systems [165] and EOS [166] supply a variety of polymer materials. These materials are predominantly polyamide-based thermoplastics, which represent an overwhelming proportion of the laser sintering market; however, elastomers are becoming more widely available. In comparison to injection moulding, the availability of processable materials is notably limited. For ex-

ample, several thousands of materials exist for injection moulding, however, less than 50 are available for laser sintering [163]. Increasing research interest is being carried out on the development of laser sintering materials, although the main focus of this is the inclusion of additives such as resin [167], fibre and carbon particles [143] within a polyamide matrix.

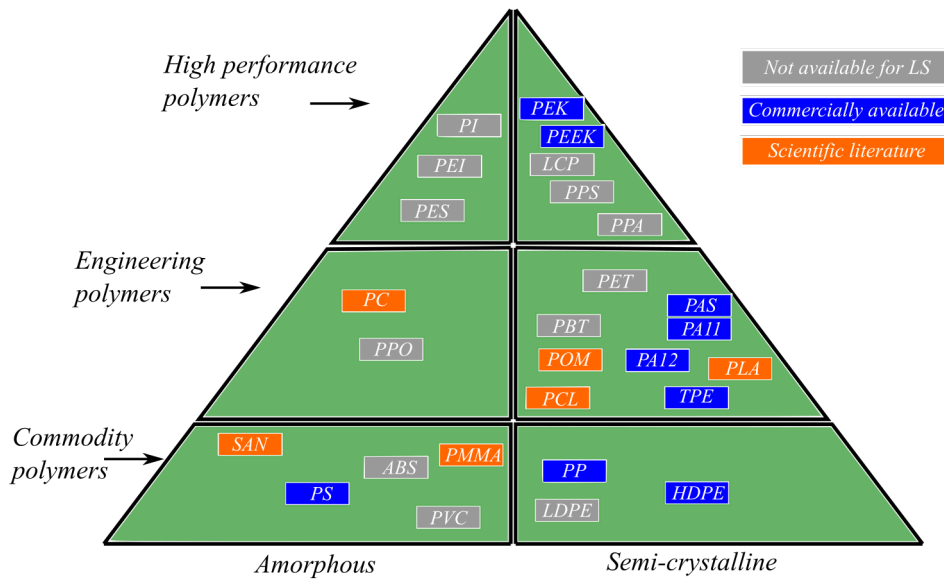


Figure 2.26: Classification of laser sintering materials according to the pyramid of polymer materials. Adopted from [163]

A review of commercially available materials is illustrated by figure 2.27⁶. Notably, the available range in modulus lies over several orders of magnitude from less than 10 MPa to 1000 MPa, with the associated range in engineering strain ranging from 6 mm/mm to 0.05 mm/mm. Despite a narrow academic focus on elastomer laser sintering materials to-date [168], especially on understanding the range of physical properties required for optimum sintering within the process, there are a few thermoplastic elastomers available [169]. Nevertheless, laser sintered elastomers have been developed and adopted within functional designs [170]. One such example, Luvosint, has been adopted for made-to-measure shoe mid-soles [171], robotic actuators [172] and in the development of cellular structures [173]. Therefore, it stands to reason to be adopted as a candidate material within this thesis.

⁶Whilst the figure is not exhaustive of every variant offered, it covers all main polymer types available.

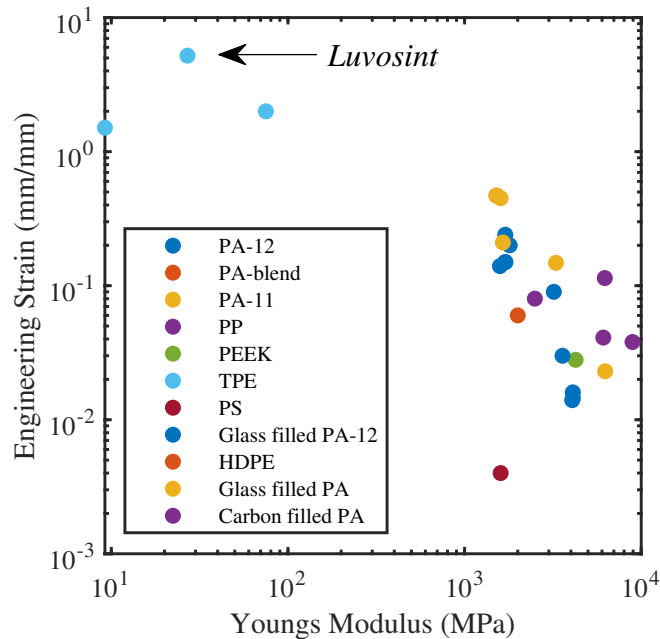


Figure 2.27: Distribution of material properties relative to elongation and Young's modulus for laser sintered polymers.

2.6 Research Focus

Within this section, the research focuses associated with this thesis shall be presented, these include additively manufactured helmets, tailorable honeycomb behaviour and finite element based optimisation.

Additive manufacturing processes are finding an increasing range of design applications. One such application garnering attention is the design and development of helmet liners. In this application, AM offers a number of advantages compared to traditional fabrications routes. A primary focus of this study is to exploit the capabilities of additive manufacturing to create an improved helmet liner derived from a prismatic cellular structure for impact protection.

Additively manufactured cellular structures have previously been evaluated with respect to the loading conditions of a helmet impact. For example, Soe et al. numerically explored the use of an ordered lattice structure for impact mitigation within the volume of a helmet liner [174], demonstrating that tailorable energy absorption and thus impact mitigation can be achieved through structural changes.

This concept has since been expanded by Khosroshahi et al., who investigated lattice grading schemes [175] and relative density on resultant head injury severity [176]. Clough et. al fabricated micro lattice impact attenuators, which afforded greater specific stiffness and densification strain, resulting in a reduction in peak linear acceleration under impact versus stochastically architecture foams [177]. The greater geometric freedom means architected cellular structures hold a notable advantage over stochastic cellular structures [178]. Architected cellular structures with tailorable mechanical properties, therefore, represent a viable route to improving helmet liner performance by identifying optimal configurations to ultimately head protection.

Outside of academic research, these concepts have been translated to commercial reality. Hexr [179] have developed the first user specific, laser sintered cycling helmet. Comprised of a continuous honeycomb array and fabricated from Polyamide-11 using laser sintering, it has been reported to lower risk of brain injury compared with a foam helmet by 26%, as well as reducing other severity metrics, such as rotational and translational acceleration by 30%. Other companies such as KAV [180], Kupol [181] and Rheon [131] have leveraged similar technologies to achieve a performance benefit versus contemporary foams. This suggests that there is a viable commercial route to leveraging these structures as an alternative material.

Honeycomb structures can undergo large regimes of compressive strain, making them ideal structures for energy absorption. A typical honeycomb mechanical behaviour is characterised by an initial high peak stress, followed by a relatively flat plateau and densification. Such a response typically results in low energy absorption efficiency, as the initial peak absorbs little energy, though incurs a very high stress level [182]. The consequence of which, when discussing materials for helmet liners, would be exposing the head to a large resultant acceleration. Nevertheless, the remarkable stiffness-to-weight ratio of honeycombs loaded out-of-plane and comparatively reduced in-plane behaviour makes them a viable alternative to current helmet liner materials. A primary focus of this study is to exploit this class of structure as an alternative helmet liner.

An established methodology for minimising the prominence of the high peak stress observed during honeycomb out-of-plane compression is the adoption of

pre-crushing or built-in imperfections [67]. These, however, can only be facilitated in planar sections manufactured using contemporary methods. Strategic material and geometry selection represents an effective method to tailor a honeycomb's mechanical behaviour. For example, Bates et al. reported that hexagonal honeycombs manufactured from thermoplastic polyurethane achieved recoverable and repeatable behaviour under cyclic compression [123]. Furthermore, the behaviour of these structures could be tailored by changing the unit cell geometry [183]. Park et al. investigated personal protective equipment by leveraging additive manufacturing, demonstrating the efficacy of elastomeric honeycombs at mitigating impact loads associated with falls [184]. A design strategy now garnering research attention is the introduction of folds in axially compressed structures. Townsend et al. investigated the energy absorption ability of elastomeric origami-inspired honeycombs [124]. Through inclusion of a pre-buckled feature (i.e., a fold), it was reported that it is feasible to retain the characteristic stiffness-to weight ratio of honeycombs, whilst removing the undesirable stress-softening phenomena. Outside of origami, however, fold patterns have been implemented which approximate the higher order buckling modes of honeycombs, thus providing the theoretical grounding, to modify current honeycombs with a pre-buckled feature. The same crush mode is reported in circular tube-like structures [185] and therefore informs the choice of geometry for this study. Hence, there is good potential to tune the mechanical behaviour of elastomeric pre-buckled structures for repeat, impact mitigating applications that are subject to variable, application-specific loading regimes which would not otherwise be effectively mitigated by elastomeric foams.

Finite element analysis is a useful and effective tool for design, development, and application of mechanical structures subject to dynamic loading. By facilitating the ability to run simulations equivalent to in-situ loading conditions, optimal configurations can be identified without lead times associated with manufacturing and running physical experiments. Moreover, when coupled with intelligent search algorithms this can facilitate iterative, virtual prototyping enabling design optimisation relative to an objective function. A primary focus of this study is to establish a computational approach for design and optimisation of cellular structures for application in helmet liners.

Limited literature exists on the computational design optimisation of helmets,

and rarely is an optimisation route, or best practises, presented. Shuaeib et al. performed single objective optimisation on a motorcycle helmet to determine foam density, foam thickness and shell thickness to minimise the peak acceleration [77]. Tinard et al. applied manual modifications to a motorcycle helmet based on modal analysis in order to reduce severity metrics [186]. Soe et al. [174] and Khosoroshi [176] carried out investigation on lattice structures within a full-scale helmet, however, this was limited to a single parameter sweep which couldn't be leveraged for more complicated structures with multiple design parameters. Furthermore, exploring novel structures requires finer meshing which can take as long as 48 hours to complete, for a single simulation, [187]. Thus, full scale iterative design optimisation is computational prohibitive. Caccese et al. are one of few authors describing design optimisation using intelligent search algorithms to develop optimal elastomeric honeycomb structures for head impact mitigation [188]. Adopting a simplified genetic search algorithm, minimum unit cell depth could be identified to achieve a reduced peak acceleration. Here, a several simplifications were made, including symmetric periodic boundary conditions, to facilitate expeditious finite element analysis whilst retaining equivalence to in-situ loading conditions. This, however, was not validated by comparison to the full-scale model to identify how effective the predictions were, nor was it undertaken at an impact velocity equivalent to design standard testing. Hence, this will be further investigated in this thesis.

2.7 Conclusion

Despite continued effort in the head protection sector, head injury remains a persistent problem. Investigating new materials and structures for helmets is therefore of significant social importance. Whilst current solutions for cycle helmets serve to mitigate the impact load under a singular impact, they are unsuitable for applications with potential for multiple (or consecutive) impacts. Furthermore, limiting the likelihood of consumers wearing a previously damaged helmet by identifying a multiple impact solution adds further motivation. Currently, solutions to this problem include multi-hit capable materials such as expanded polypropylene and vinyl nitrile foams, however, they are limited in terms of their geometric freedom so prohibit optimisation.

Honeycomb structures are versatile and have previously found application within helmets, however, when manufactured from materials which plastically deform, such as metals and polymers, these solutions only serve to mitigate a single impact. Furthermore, recent advances have demonstrated that architected honeycombs can attain variable stress-strain responses that exceed contemporary materials. A honeycomb structure manufactured from an elastomeric material is therefore an ideal candidate due to their recoverable specific energy absorption. Furthermore, these structures can now routinely be additively manufactured, facilitating rapid design exploration of novel geometries otherwise not possible through conventional methods. Continued development of additive manufacturing technologies has made possible new exotic materials such as polyurethane powders within laser sintering. Polyurethane materials can undergo large regimes of elastically recoverable deformation. This now unlocks a feasible route to a manufacturing method which can realise architected honeycombs from recoverable elastomeric materials within the doubly convex profile of a helmet. Several barriers, however, have been identified before a pathway for design optimisation of elastomeric additively manufactured honeycomb structures for helmet impact mitigation can be established. These are :

1. A lack of material behaviour relating non-linear, rate dependant and anisotropic material behaviour to inform finite element models.
2. A honeycomb structure with a mechanism to achieve tailorable energy absorption.
3. A numerical approach for optimising the structure in a computationally efficient manner subject to user specified boundary conditions.

These barriers will be investigated, and the culmination of this thesis aims to establish a pathway for efficient design and optimisation, including the best practises using computational approaches, of new materials and structure for enhanced head protection.

Chapter 3

Experimental Characterisation and Numerical Material Model Calibration of a Laser Sintered Elastomer

Sections of this chapter have been published as:

R. Adams et al. A novel pathway for efficient characterisation of additively manufactured thermoplastic elastomers. *Materials and Design* (2019), article number: 107917.

3.1 Introduction

As described in the literature review, Additive Manufacturing (AM) serves as a feasible route to fabrication of a helmet liner based on a cellular structure design. In particular, laser sintering boasts both the capability to achieve fine-scale structural features that are self-supporting, and the capacity for utilising elastomeric materials that can undergo large regimes of elastically recoverable deformation. This makes laser sintering an excellent candidate manufacturing process, however, material information and experimental data for mechanical behaviour is scant and therefore cannot accurately inform a numerical material model for finite element simulation which captures non-linearity and rate dependence. Moreover, since parts can be manufactured under different orientations using laser sintering, it is unclear how the build orientation influences the mechanical performance of manufactured components. Consequently, the route for leveraging this material for future design optimisation using finite element analysis is limited.

This chapter aims to address two specific issues that restrict the design for optimisation capability of laser sintered elastomers. Firstly, further understanding is required regarding the development of anisotropy as a function of the build orientation. This will highlight the limitations in mechanical behaviour when designing for manufacture. Secondly, non-linearity and rate dependence of the sintered elastomer will be investigated to calibrate a material model for finite element simulation under quasi-static and impact conditions. The real behaviour of elastomers under deformation is complex. Specifically, the material behaviour demonstrates non-linearity as well as rate dependence. Previously, investigations have been enabled through the assumption of linear elasticity, however, this is inappropriate since it cannot predict the discussed material behaviours.

This chapter is organised as follows. Firstly, to assess the material's strain-rate and build orientation sensitivity, tensile coupons were sintered in orthogonal build orientations and tested under different strain rates. Secondly, to calibrate a numerical material model suitable for use in finite element analysis, quasi-static uniaxial, planar and equibiaxial tension deformation state experimental data were collected to define the non-linear elastic behaviour, whilst single step relaxation data were collected to define the rate-dependant behaviour. The suitability of each native hyperelastic material model within Abaqus, a finite element software,

was then assessed for the ability to robustly predict both the single and combined deformation state. The selected hyperelastic model was then augmented with a linear viscoelastic model to predict rate-dependence. Finally, comparison is drawn between experimental and simulation data of the characterisation tests, high strain rate tensile testing, quasi-static and impact loading of a honeycomb structure to assess the accuracy of the calibrated model. The culmination of this chapter provides a validated approach for characterising newly developed elastomers. Furthermore, it will enable further numerical investigation using the material model in subsequent chapters.

3.2 Materials & Methods

3.2.1 Laser Sintered Elastomer

The commercially available laser sintered thermoplastic polyurethane powder, Luvosint TPU X92A-1 NT (Lehmann Voss Co; Germany), hereafter to referred to as Luvosint, was adopted for use within this investigation. Luvosint was identified within the literature review and was deemed suitable for use in the development of a new helmet liner. Luvosint material properties are reported in table 1, however, they are insufficient to calibrate an accurate numerical material for use in finite element analysis.

In the following study, mechanical test coupons and a circular honeycomb were modelled using computer aided design software (Solidworks, Dassault Systemes, France), exported as standard tessellation language (STL) files and provided to a third party for manufacture (FKM, Germany). The recommended processing parameters, as provided by the manufacturer, are presented in table 2. since manufactured was subcontracted, however, the exact processing parameters are confidential.

Table 3.1: Luvosint TPU X92A-1 NT physical and mechanical properties. Adopted from [171].

Property	Value	Units
Specific gravity	1.2	g/cm ³
Shore hardness	92	A
Poisson ratio	45	-
Elongation	5.0-5.2	mm/mm
Tensile Strength	16-20	MPa
Compressive Strength	33-40	MPa
Compressive Modulus	33-40	MPa

Table 3.2: Luvosint TPU X92A-1 NT recommended processing parameters. Adopted from [171].

Paramter	Value	Units
Powder bed temperature	94	°C
Laser power	2 x 55	W
Scanning speed	12.5	m/s
Heater output limit	30	%
Layer height	0.1	mm
Fill scan spacing	0.15	mm

3.2.2 Strain Rate and Build Orientation Sensitivity

Uniaxial tension tests were performed at three strain rates, low, intermediate and high equivalent to 0.05 /s, 5 /s and 100 /s respectively. These strain rates were selected as they represent the spectrum of strain rates expected in the application of personal protective equipment. Coupons were manufactured in three orthogonal build directions, with sintered layers lying through thickness (xy), width (xz) and length (zy) per previous investigations [157], as illustrated by figure 3.1. As described by figure 3.2, the coupon gauge lengths were dependent on the testing strain rates, where 0.05 /s = 33 mm, 5 /s = 5 mm and 100 /s = 100 mm, which is equivalent to previous tests in the literature [189]. The area of analysis within the gauge length was limited to mitigate against any potential stress concentrations that may arise from the internal corners of the specimen tabs. It is important to note, that for this section the experimental procedure was undertaken by Dr. Rafael Celeghini Santiago, adjunct professor, at Federal University of ABC (Brazil) in collaboration with Cardiff University facilitated by a Royal Society Newton International Exchange award. Data sets were provided to the

author, who analysed them within this chapter.

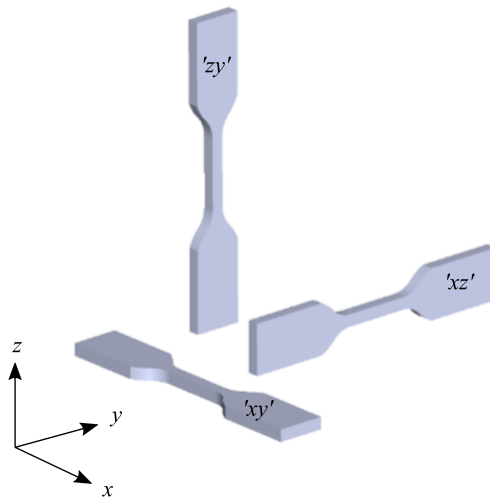


Figure 3.1: Illustration of orthogonal build orientations for a tensile coupon aligned with the x, y and z axis.

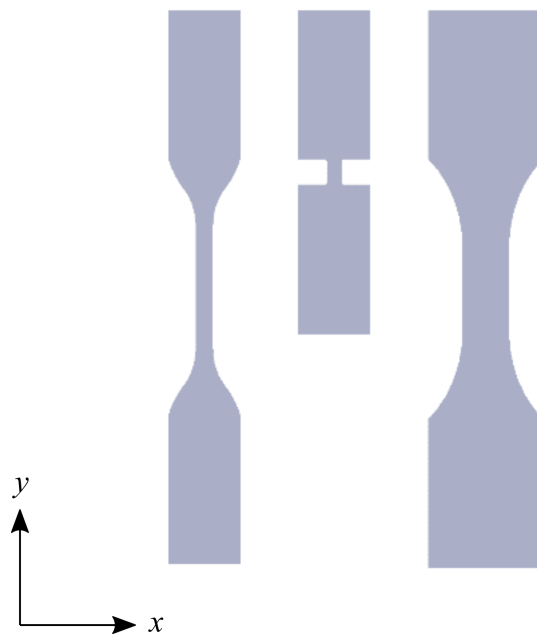


Figure 3.2: Illustration of tensile coupon variants for material anisotropy and rate sensitivity tests for low (left), intermediate (centre) and high (right) strain rate. Coupon gauge length is provided in text.

Low strain rate testing was performed using a universal testing machine (Instron 3369, Instron, US), with each coupon loaded in uniaxial tension. The reaction

force was recorded using the in-built load cell, whilst specimen strain was measured with video extensometry system (VIC-2D, Correlated Solutions Inc, US).

Intermediate strain testing was performed using another universal testing machine (ElectroPulse E100, Instron, US), whilst high strain rate testing used an in-house twin rail rig that achieved deformation of the sample through reaction of a falling mass where the reaction force was recorded using a 50 kN load cell (Type: 9532A, Kistler, Switzerland) [189].

Samples had a high-contrast black and white speckle pattern applied to the surface prior to testing to enable strain measurements via digital image correlation using a high speed camera (APX-RS, Photron, Japan) at a frame rate of 10,000 fps. For further information, relating to the application of the speckle pattern and setup, refer to [189, 190] Annotated figures 3.3 and 3.4 illustrate the experimental setup adopted for the intermediate and high strain rate tests. All experiments were performed at ambient room temperature ($18 \pm 2^\circ\text{C}$).

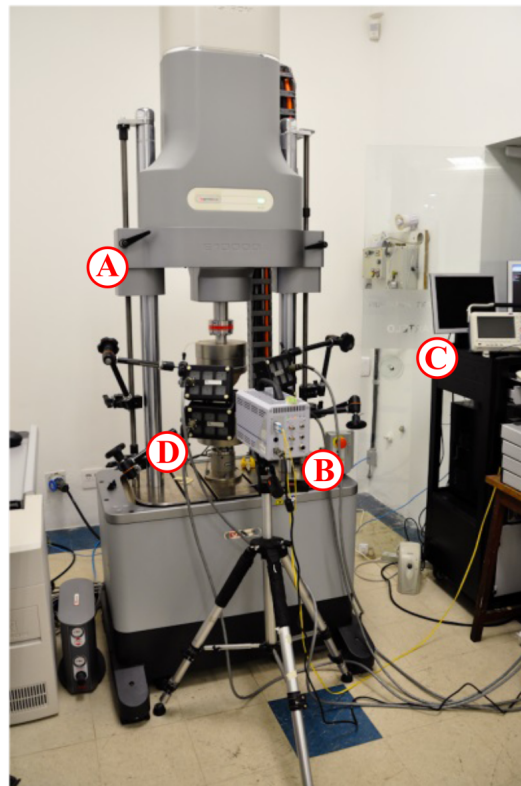


Figure 3.3: Intermediate strain rate test setup including universal testing machine (A), DIC camera (B), data acquisition (C) and LED light sources (D).

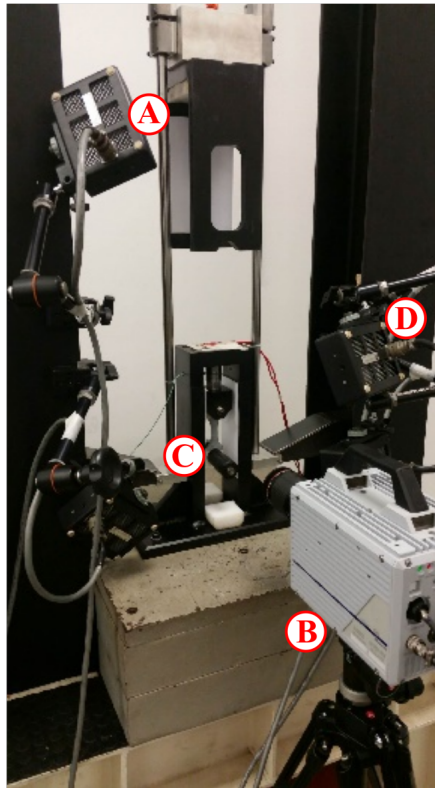


Figure 3.4: High strain rate test setup including twin rail falling mass (A), DIC camera (B), test sample (C) and LED light source (D).

3.2.3 Characterisation for Material Model Calibration

Quasi-static uniaxial, planar and equibiaxial tension data within the range of 0 mm/mm to 0.4 mm/mm [113] was collected to define the hyperelastic behaviour, whilst uniaxial tension stress relaxation data was collected to define the strain-rate behaviour. The data collected for material model calibration is representative of the material printed in the 'xy' build orientation. All experiments were performed at ambient room temperature ($18 \pm 2^\circ\text{C}$).

As illustrated by figure 3.5, uniaxial tension testing was performed using a universal testing machine (Zwick Z50, Zwick, Germany) fitted with non-slip grips at a crosshead speed of 100 mm/min as per previous investigations [113]. An oil-based ink was used to mark discrete strain markers within the gauge length. A video extensometry system (iMetrum, UK) was used to enable relative strain measurement of the markers under deformation. Coupon dimensions were measured

at multiple positions across the gauge length using a vernier caliper (Mitutoyo, Japan) and averaged.

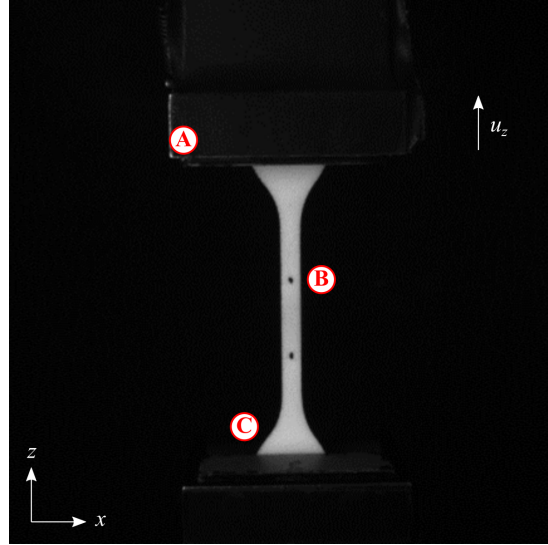


Figure 3.5: Uniaxial tension test setup including non-slip grips (A), strain gauge markers (B) and test coupon (C). Where U_z denotes the direction of the applied displacement.

The reaction force was recorded using the in-built load cell and the tensile engineering stress developed within the gauge length was defined as:

$$\sigma_{uni} = \frac{f}{wt} \quad (3.1)$$

Where f is the recorded force by the load cell, w and t are the measured width and thickness of the coupon.

As illustrated by figure 3.6, planar tension testing, equivalent to pure shear, was performed [191]. A jig was designed to enable application of a wide load across a sheet of material, achieving a 10-fold width-to-height gauge area ratio, at a crosshead speed of 100 mm/min. Flat $60 \times 200 \times 2$ mm coupons were manufactured and $20 \times 200 \times 2$ mm strips of aluminium were affixed across the top and bottom using epoxy, which provided a non-slip boundary and enabled an even clamping pressure when mounted within the jaws of the jig.

An oil-based ink was used to mark discrete strain markers within the gauge length. Video extensometry enabled strain measurement within the gauge length at three locations across the width. The reaction force was recorded using the in-built load cell and planar engineering stress was calculated using equation 3.1.

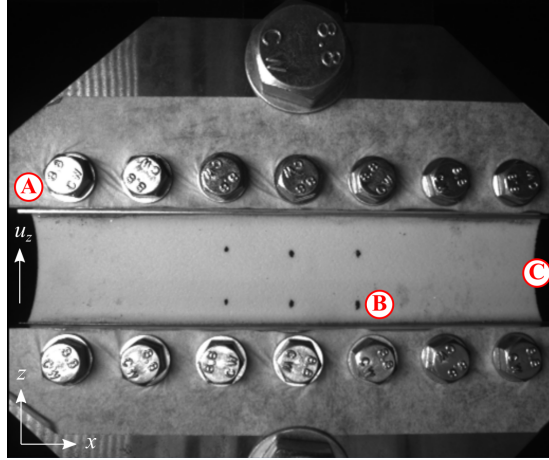


Figure 3.6: Planar tension test setup including non-slip boundary (A), strain gauge markers (B) and test coupon (C). Where U_z denotes the direction of the applied displacement.

As illustrated by figure 3.7, equibiaxial tension testing, equivalent to pure compression, was performed using an in-house jig [192]. The jig was designed to achieve multi-axial loading. Circular test coupons, $d = 60$ mm and $t = 2$ mm, with a perimeter comprising 16 clamping tabs were manufactured. A series of cuts and radii edges around the perimeter of the coupons ensured a homogeneous circular strain area, reducing the contribution of the stress concentrations and mitigating premature failure. Non-contact video extensometry was used to measure the specimen strain across 4 distinct pairs of strain locations.

The reaction force was recorded using the in-built load cell and equibiaxial engineering stress was defined as:

$$\sigma_{equi} = \frac{f}{\pi dt} \quad (3.2)$$

Where f is the force recorded by the load cell, d is the diameter of the gauge area and t is the thickness of the coupon.

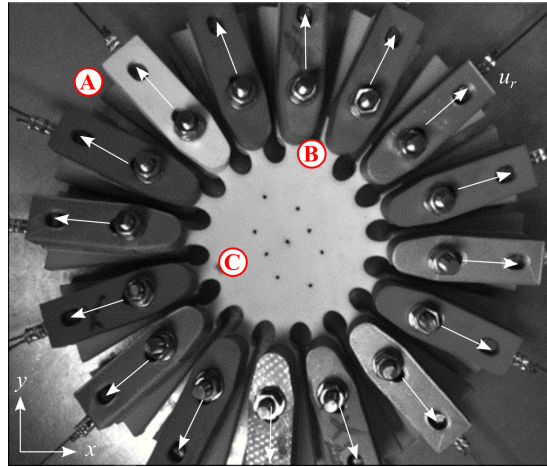


Figure 3.7: Equibiaxial tension test setup including clamps (A), test coupon (B), strain gauge markers (C). Where U_r denotes the radial direction of the applied displacement.

Single step stress relaxation testing was performed using identical test setup and coupons as the uniaxial tension testing. Stress relaxation requires instantaneous straining of a material followed by a period of relaxation at a constant strain, therefore the maximum loading rate of the machine was used to achieve a strain of 0.4 mm/mm followed by an 100 s relaxation period. During testing, video extensometry enable strain measurement in the gauge length. The reaction force was recorded using the in-built load cell and normalised stress was defined as:

$$\bar{\sigma} = \frac{\sigma}{\sigma_o} \quad (3.3)$$

Where σ is the stress calculated during testing, σ_o is the initial stress at the point of instantaneous strain. Due to normalisation this can be simplified to the applied force.

3.2.4 Material Model Calibration

Hyperelastic material model calibration was performed within the Abaqus finite element solver (Dassault Systèmes, France) using the uniaxial, planar and equibiaxial tension data collected in section 3.2.3. The in-built solver was used to run a non-linear least squares curve fitting algorithm which calculated the coefficients

for the material model. The material models considered during this analysis are listed in table 3.3

Table 3.3: Hyperelastic material models available within Abaqus classified as phenomenological, mechanistic and hybrid.

Class	Material model
Phenomenological	Mooney-Rivlin
	Ogden
	Polynomial
	Yeoh
	Marlow
Mechanistic	Arruda-Boyce
	Neo-Hookean
Hybrid	Van der Waals

Rate-dependant material model calibration was performed within the Abaqus finite element solver using the single step stress relaxation data in section 3.2.3. Data was treated and back extrapolated using the procedure reported in [193]. Unlike the previous hyperelastic model calibration there is only one viscoelastic model available within the solver – the linear viscoelastic model, therefore, this model was adopted. The linear viscoelastic model is defined by a Prony series, which is the sum of exponential terms as described by equation 3.4. The in-built solver was used to perform a curve fitting procedure, utilising a non-linear least squares fit, which calculated the coefficients of the model.

$$g_r(t) = 1 - \sum_{i=1}^N \bar{g}_i^P (1 - e^{-\frac{t}{\tau_i^G}}) \quad (3.4)$$

Where t is time, and \bar{g}_i^P and τ are constants of the Prony series expansion.

3.2.5 Finite Element Analysis

Hyperelastic models are effective at predicting the behaviour of elastomeric materials, however, they are limited by the fact that they cannot predict strain rate effects. A simple approach to extending the predictive capacity of the model is to augment it with a linear viscoelastic model. Since the proposed material model

is a function of multiple data sets, the steps to validating the model are now multi-faceted. The proposed series of tests for validation are as follows:

1. Quasi-static isolated deformation
2. Dynamic isolated deformation
3. Quasi-static mixed deformation
4. Dynamic mixed deformation

This section outlines the finite element simulations undertaken to assess the predictive capability of the newly calibrated model, whilst the following section, section 3.2.6, describes the experimentation that validates the simulation tests.

To test under isolated quasi-static deformation, a single element approach was adopted to assess each candidate material model [129]. The single element approach utilises a cube of unit dimensions, an established strategy for analysing material models without enabling deformation in an isolated state without edge effects [194]. The single eight-node element was of hexahedron shape type, the Abaqus explicit solver enabled consideration of large deformation effects. To simulate deformation, a ramp deformation-time history was applied, which yielded a strain of 0.4 mm/mm. This strain level was selected as it has been previously reported to be the local strain of the cells walls during compression of a honeycomb [113]. Force was extracted, and engineering stress was calculated as per equation 3.1 and 3.2. The boundary conditions adopted to achieve isolated deformation is detailed in table 3.4

In order to compare the suitability of each model, the area under the curve for each model was assessed and compared in terms of the relative difference between the model output and experimental data (equation 3.5). The relative difference metric was calculated for each individual deformation condition as well as combined pairs of each. The most appropriate model was defined as that which minimised the total relative difference

$$r_d = \frac{\int_{\varepsilon_{min}}^{\varepsilon_{max}} |\sigma_{mod} - \sigma_{exp}| d\varepsilon}{\int_{\varepsilon_{min}}^{\varepsilon_{max}} \sigma_{exp} d\varepsilon} \quad (3.5)$$

Table 3.4: Abaqus boundary conditions used in quasi-static isolated deformation testing.

Deformation	Boundary conditions
Uniaxial tension	$u_x = U$
	$u_y = free$
	$u_z = free$
Planar tension	$u_x = U$
	$u_y = fixed$
	$u_z = free$
Equibiaxial tension	$u_x = U$
	$u_y = U$
	$u_z = free$

Where σ_{exp} and σ_{mod} are stress for experimental and material model data, respectively, and ε is the applied engineering strain.

Once the most appropriate hyperelastic model was identified, the model was augmented with the linear viscoelastic model to extend the predictive capability into the dynamic regime. Again, a single element approach was used within Abaqus. Uniaxial tension was achieved by applying the boundary condition specified in table 3.4. To simulate high strain rate conditions ($\dot{\varepsilon} = 100$ /s), the deformation-time history from the experimental testing (section 3.2.2) was applied to the upper face by means of an amplitude boundary condition. Force was summed across the face and engineering stress was calculated for comparison to experimental data.

To assess the predictive capacity of the hyperelastic model in a mixed deformation condition, quasi-static compression of a circular honeycomb was simulated. The circular honeycomb was adopted due to its potential application to personal protective equipment, a theme which will be explored later in the thesis. For this analysis, the linear viscoelastic model was not applied such that rate dependence effects were isolated. Uniaxial compression of the honeycomb structure results in bending and buckling of the cell walls. Consequently, this is a challenging deformation condition for the proposed model to accurately predict. The structure was positioned between two analytically rigid plates which were assigned a ramp deformation boundary condition which achieved a strain of 0.6 mm/mm. An eight node brick element, with hexahedron shape type, reduce integration (C3D8R) and hourglass control was utilised. Mesh size was selected to be half that of the wall thickness, and a global friction value of $\mu_{global} = 1.0$ [124] was

adopted. The force deformation history was extracted from a reference node at the centre of the upper rigid plate. Engineering stress and strain were calculated for comparison against experimental data.

To assess the predictive capacity of the hyperelastic model augmented with the linear viscoelastic model in mixed deformation condition under dynamic conditions, impact loading of the circular honeycomb was simulated. A similar simulation setup was used as before, where the honeycomb was positioned between two analytically rigid plates, however, the upper plate was assigned a point mass of 6.1 kg, representing the total mass of the experimental setup, and prescribed a pre-impact velocity of 2.5 m/s which is equivalent to a strain rate of 100 /s. The kinetic energy (i.e. mass) of the impactor was chosen such that densification of the structure was achieved. Force and displacement history were extracted from a reference node at the centre of the upper rigid plate and converted to engineering stress and strain, respectively. It is important to note that in this chapter, the circular honeycomb is utilised as a tool to validate the capacity of the material model to analyse mixed deformation state. Further description of the finite element model and analysis of the circular honeycomb and its geometric parameters, relative to mechanical behaviour, will be investigated in the forthcoming chapters. For a more detailed description of the finite element model setup, refer to Chapter 4.

3.2.6 Experimental Material Model Validation

To validate the proposed material model, additional experimental data was collected that emulated the finite element simulation conditions. Quasi-static uniaxial compression testing was performed using a universal mechanical tester (Z50, Zwick, Germany), as illustrated by figure 3.8. The specimen was placed between two horizontal, rigid plates fitted. The upper platen was translated vertically at a rate of 100 mm/min, until a strain of 0.6 mm/mm. Force was measured using a load cell and displacement was recorded using the in-built measurement system. A video capture system (iMetrum, UK) was used to record the deformation mechanisms. All specimens were compressed out-of-plane, aligned with the build orientation. All experiments were performed at ambient room temperature ($18 \pm 2^\circ\text{C}$).

Impact tests were performed using a spring-loaded linear impactor (Dynatup 9250 HV, Instron, US) as illustrated by figure 3.9. The carriage and flat platen attachment had a total mass of 6.1 kg. The carriage was guided by two solid rails onto the honeycomb, which was taped to the lower platen positioned beneath the impactor. The sample was subjected to an initial impact velocity of 2.5 m/s equivalent to a strain rate of 100 /s. A load cell measured the reactive force during the impact, whilst a light gate measured the inbound velocity. A high-speed video camera (Edgertronic SC1, Sanstreak Corp, US) was used to record the deformation mechanisms. All experiments were performed at ambient room temperature ($18 \pm 2^\circ\text{C}$).

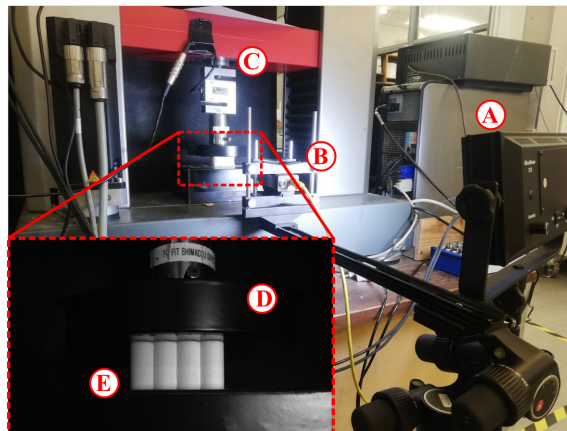


Figure 3.8: Experimental setup for the quasi-static honeycomb compression including LED light source (A), video camera (B), load cell (C), platens (D) and honeycomb structure (E).

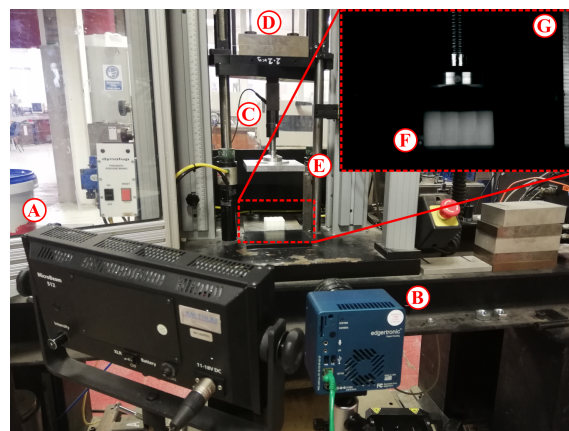


Figure 3.9: Experimental setup for honeycomb impact loading including LED light source (A), high speed camera (B), load cell (C), carriage weight (D), platen (E), honeycomb (F) and ruler (G)

3.3 Results

3.3.1 Strain Rate and Build Direction Sensitivity

The influence of build orientation and strain rate was investigated through uniaxial tension testing under three distinct strain rates using coupons sintered in three orthogonal orientations. Figure 3.10a - 3.10d, illustrates the mechanical behaviour under the experimental conditions.

Across several decades of strain rate, the magnitude of stress-strain behaviours increases. For increasing strain rates, higher values of engineering stress are observed for equivalent engineering strains. For example, at an engineering strain of 0.4 mm/mm, values of engineering stress for intermediate and high strain rate testing are 49 - 51 % and 107 - 122 % greater than low strain rate testing. Furthermore, this is also reflected in the initial modulus, which was 33 - 47 % and 117 - 103 % greater, respectively.

It is evident that the build orientation of Luvosint has a significant effect on overall mechanical performance. In figure 3.10d, notable build direction sensitivity is observed relative to mechanical performance. Trends vary across build orientation, with a clear hierarchy observed. Build orientation 'xy' exhibits superior performance 'xz' and 'zy'. For high strain rates, ultimate tensile strain ranged from 0.56 - 0.42 mm/mm for 'xy', 'xz' and 'xy' respectively. For low and intermediate strain rate conditions, tensile failure was only achieved by the 'zy' orientation for a strain of 0.41 - 0.82 mm/mm respectively. Tensile failure was not achieved for the other orientations, due to limitations of the test facilities.

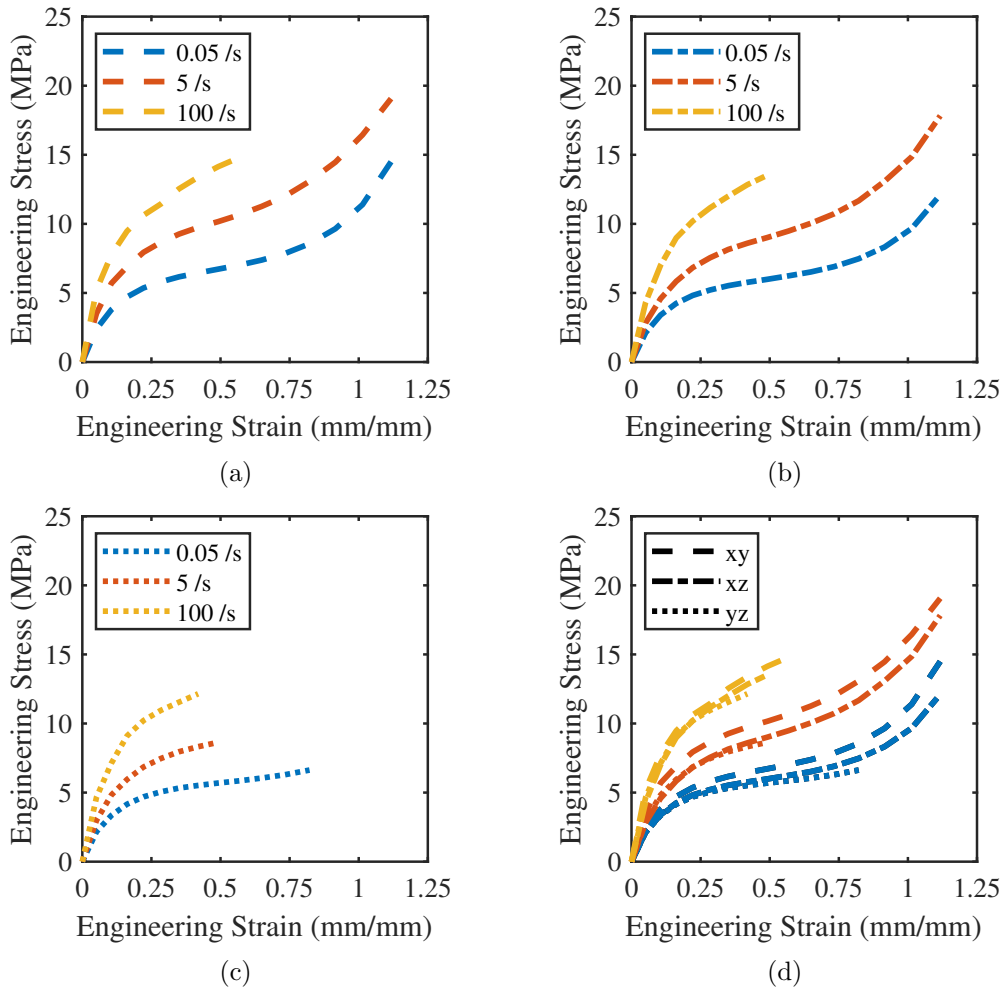


Figure 3.10: Mechanical response of LuvoSint under uniaxial tension at different strain rates subject to changing build orientation for xy (a), xz (b), zy (c) orientation as well as combined plot for comparison (d).

3.3.2 Hyperelastic Material Model Calibration

The influence of deformation state relative to the mechanical behaviour was investigated by undertaking uniaxial, planar and equibiaxial tension testing. Figures 3.11 illustrates engineering stress strain behaviour under the experimental conditions. Under monotonic deformation, each state yields behaviours that are characteristically linear in the range of 0 – 0.1 mm/mm, after which, notable non-linearity is observed. No upwards progression is observed in the stress-strain curves, signifying that there was no yielding; therefore, plasticity wasn't considered for material modelling in the strain range. This is intuitive, since ther-

moplastic elastomers demonstrate recoverable elasticity. The initial modulus for uniaxial, planar and equibiaxial tension was calculated as 30.86 MPa, 37.13 MPa and 49.58 MPa respectively. Relatively, the planar and equibiaxial modulus is greater than the tensile modulus by 20.3 and 60.7 % respectively. At an engineering strain of 0.4 mm/mm, uniaxial stress was 5.92 MPa, planar stress was 6.97 MPa and equibiaxial stress was 7.43 MPa.

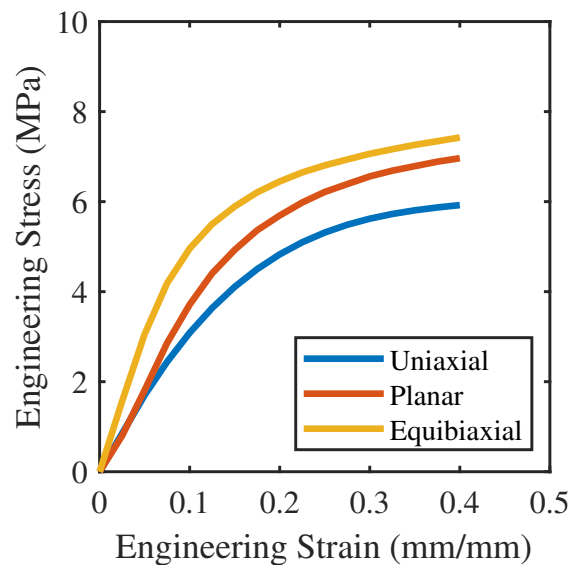


Figure 3.11: Luvsint mechanical behaviours under uniaxial, planar and equibiaxial tension.

Figure 3.12a - 3.12c compares each model to the experimental data used for calibration. The Drucker stability criterion was considered to ensure that the models would be well-suited to numerical analysis [195]. The suitability of each hyperelastic material model relative to the mechanical behaviour was investigated using finite element analysis. Consequently, fewer models are illustrated in this figure than were initially considered. Models that did not satisfy the criterion were omitted from further analysis. The calibrated models that satisfied the criterion were: Ogden $N = 1$ and $N = 5$, reduced polynomial $N = 3$ (Yeoh), Van Der Waals and Aruda Boyce.

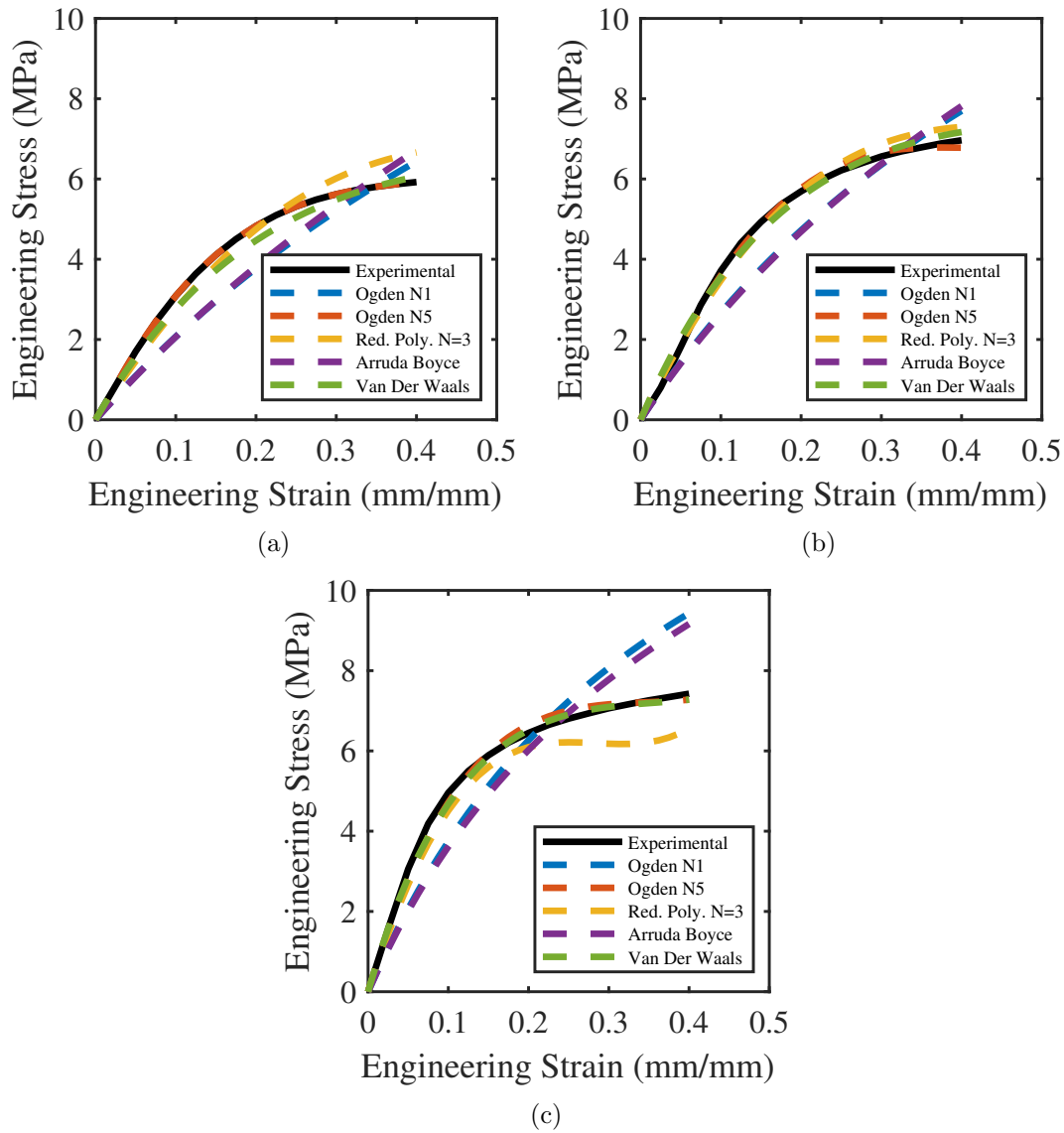


Figure 3.12: Comparison of hyperelastic material model and their capacity for predicting the mechanical behaviours of Luvsint for uniaxial (a), planar (b) and equibiaxial (c) tension.

Figure 3.13 presents the analysis of each candidate model. Varying degrees of agreement are observed. Relative difference and number of material model coefficients, inferred as computational expense, was assessed. The relative difference was calculated for each independent deformation state and coupled deformation states, to determine efficacy at assessing deformation loading scenarios which combined more than one state. In both cases, the Ogden $N = 5$ model presented the best fit to experimental data, with a relative error of 0.048 and 0.095 respectively. The Ogden $N = 5$ model is presented in figure 3.14 where comparison is

drawn to the experimental data used for calibration.

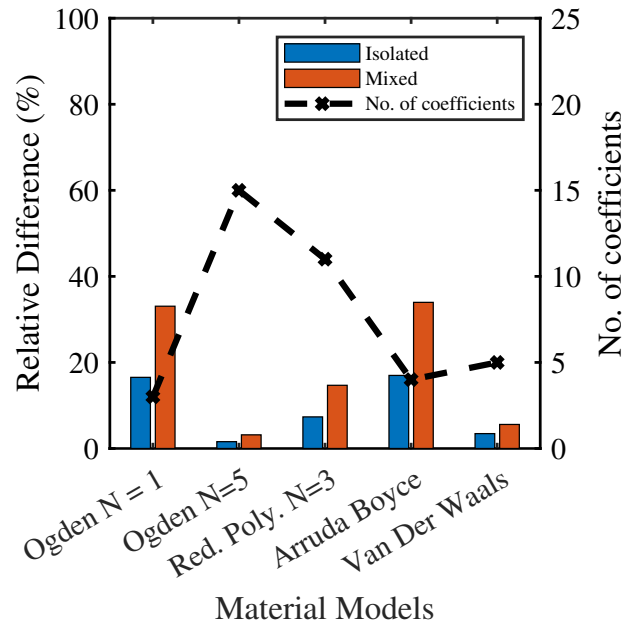


Figure 3.13: Comparison of relative difference to experimental data and number of coefficients for each hyperelastic model.

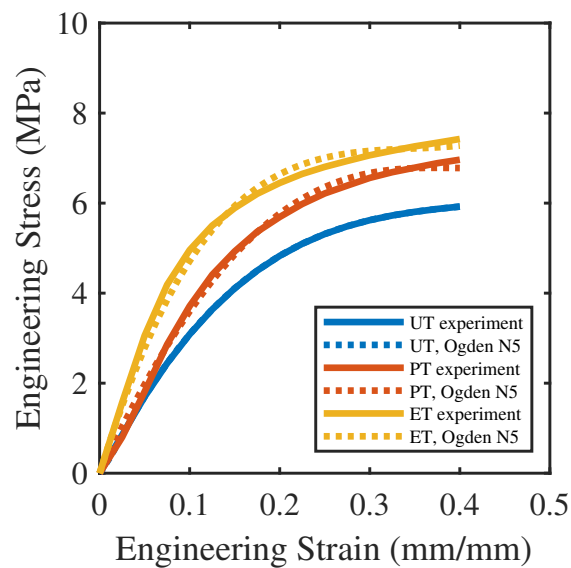


Figure 3.14: Comparison of experimental data to calibrated material for deformation states uniaxial, planar and equibiaxial tension. Material model coefficients are available in table 8.1 of Appendix 1.

3.3.3 Linear Viscoelastic Material Model Calibration

Figure 3.15 illustrates the experimental normalised single-step relaxation data compared to the calibration linear viscoelastic model (Prony series). The model is closely calibrated due to the low root-mean-square error prescribed by the solver. Inspecting the presented viscoelastic behaviour, the normalised long term modulus is calculated as 0.5.

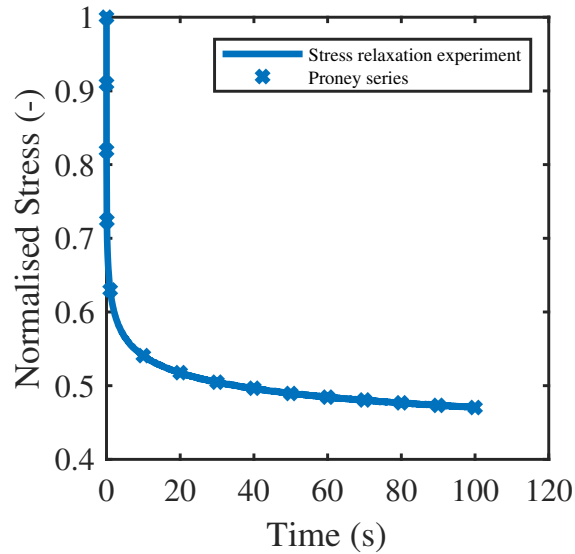


Figure 3.15: Normalised stress relaxation test data and Prony representation. Material model coefficients are available in table 8.2 of Appendix 1.

3.3.4 Finite Element Validation

To validate the proposed material model, a sequential approach including several simulations and comparison to experimental data sets was undertaken. Firstly, simulation in an isolated state of deformation under dynamic conditions was carried out. Next, simulation in a mixed state of deformation under quasi-static conditions was carried out. Lastly, simulation in a mixed state of deformation under dynamic conditions was carried out, which was achieved through impact loading.

Figure 3.16 illustrates the results of the experimental and simulation investigation described in section 3.2.5 and 3.2.2 for dynamic uniaxial tension tests. In this case,

the hyperelastic and linear viscoelastic material model was used under an isolated deformation condition. The result of the numerical analysis match well with the experimental data collected. The stress-strain behaviour favourably represents the high strain-rate behaviour. At a strain of $\varepsilon = 0.1$ mm/mm, the numerical prediction of stress is $\sigma = 5.6$ MPa whilst at a strain of $\varepsilon = 0.4$ mm/mm, stress is $\sigma = 10.8$ MPa. For these points, the calculated values of error are 10% and 7% respectively.

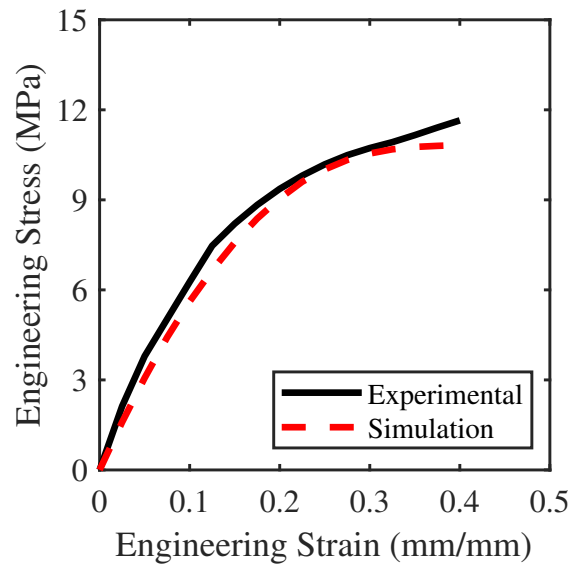


Figure 3.16: Validation of hyperelastic and linear viscoelastic material model for an isolated deformation mode, comparison of high strain rate tensile (100 /s) loading data against simulation.

Figure 3.17 and 3.18 illustrates the results of the experimental and simulation described in section 3.2.5 and 3.2.6 for quasi-static uniaxial compression of the honeycomb. In this case, under a mixed deformation condition, the hyperelastic material model is used in isolation. The results of the numerical analysis match well with the experimental data collected. When compared to the experimental results, the non-linear mechanical response of the honeycomb is well represented by the simulation. For the stress at yield, the numerical value was 47% greater than the experimental result. Nevertheless, the prediction of total energy absorbed by the structure was 13%. When comparing the video captured during the experiment to snapshots of the simulation, a good degree of comparability is observed, specifically, location and mode of buckling.

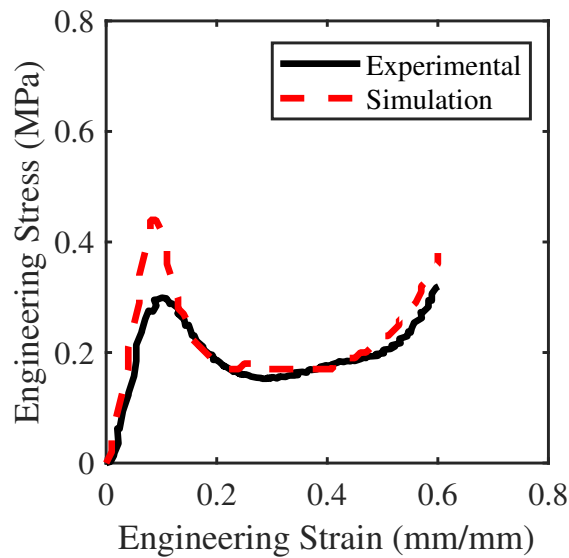


Figure 3.17: Comparison of mechanical behaviour of experimental and simulation honeycomb quasi-static compression to validate hyperelastic model under mixed deformation conditions.

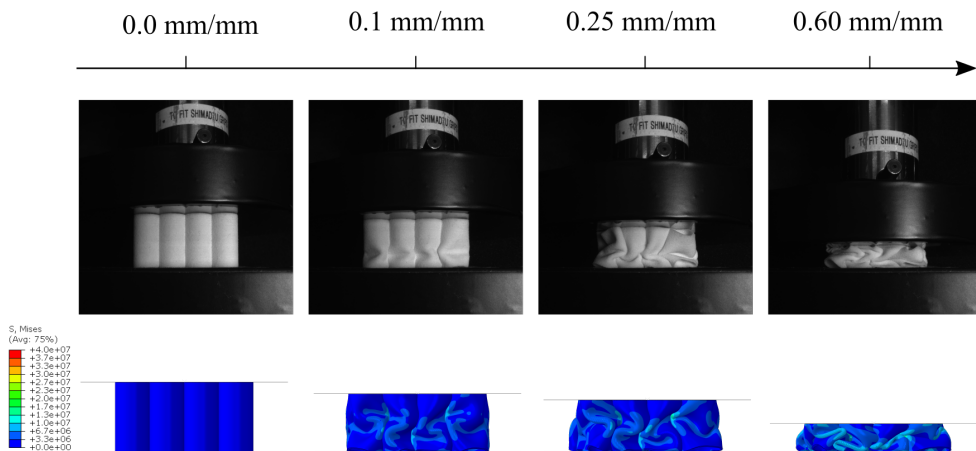


Figure 3.18: Comparison of deformation mechanisms of experimental and simulation honeycomb quasi-static compression to validate hyperelastic model under mixed deformation conditions.

Figure 3.19 and 3.20 illustrates the result of the experimental and simulation described in 3.2.5 and 3.2.6 for impact loading of the honeycomb. Both the hyperelastic and linear viscoelastic model were adopted for the mixed deformation mode case. The results of the numerical analysis match well with the experimental data collected. When compared to the experimental results, the non-linear mechanical behaviour is well represented by the simulation, except for the stress at yield. The reported numerical value was 48% greater than the experimental

result. Notably, this is similar to the quasi-static case, too. Nevertheless, the prediction of total energy absorbed by the structure before densification was within 11%. When comparing the video captured during the experiment to snapshots of the simulation, a good degree of comparability is observed, specifically, location and mode of buckling.

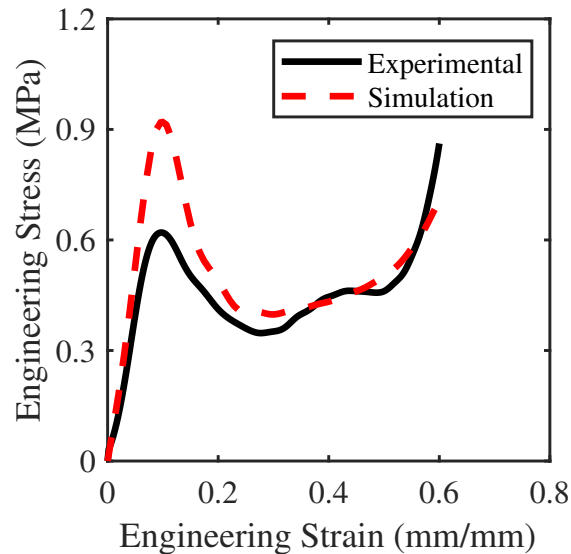


Figure 3.19: Comparison of mechanical behaviour of experimental and simulation of honeycomb impact loading to validate hyperelastic and linear viscoelastic model under mixed deformation conditions.

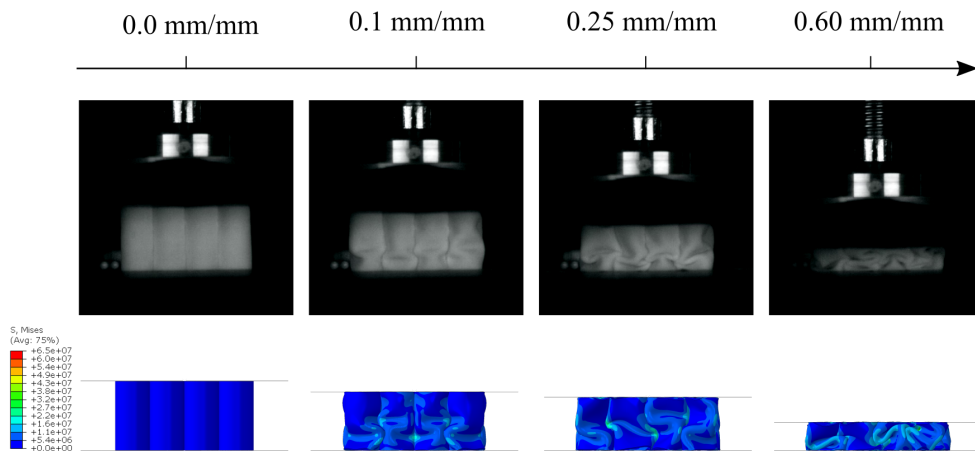


Figure 3.20: Comparison of deformation mechanisms of experimental and simulation honeycomb impact to validate hyperelastic and linear viscoelastic model under mixed deformation conditions.

3.4 Discussion

The aim of this chapter was to address two specific issues that restrict the design for optimisation capability of laser sintered elastomers. Principally, these are anisotropy, as a consequence of the manufacturing build orientation, and the lack of mechanical behaviour provided by manufacturers that precludes the calibration of a material model for use in finite element analysis. Consequently, a pathway was established which enabled identification of material model coefficients directly from experimental data for laser sintered elastomer LuvoSint. The calibrated material model was validated through comparison to isolated and mixed deformation cases under quasi-static and impact loading conditions.

The mechanical behaviour of LuvoSint was reported with respect to build orientation, strain rate and deformation condition. Classically, highly non-linear elastomer-like behaviour was reported [191]. For uniaxial tension under a large monotonic deformation regime, a small period of linear elastic behaviour was followed by a softening region, under large strain. This demonstrates similarity between an isotropic elastomer, achieved through injection moulding, and an additively manufactured alternative. The mechanical behaviour was sensitive to build orientation. Specifically, a notable hierarchy in behaviour was observed, where parts build in the 'xy' direction exhibit superior performance versus 'xz' and 'zy'. This trend is consistent with other studies investigating laser sintered materials, including elastomer [196] as well as other sintered materials [197]. Furthermore, this also aligns with the behaviour observed for elastomers manufactured from other AM processes [159]. The variation in behaviour observed demonstrates the weakness underpinning the AM process. Notably, when attempting to economically pack a build volume, parts may be subject to re-orientation from the intended design plane, perhaps yielding parts which have variable mechanical behaviour [157].

Advanced characterisation techniques, planar and equibiaxial tensile testing were employed to obtain sufficient data that calibrates a robust material model. The observed behaviour was notably different between each deformation mode, whereby the magnitude of equibiaxial tension was greater than planar and uniaxial tension. The response is analogous with similar materials, indicating that a hyperelastic material was required to model the behaviour [113]. Moreover, this

model would require augmentation with a linear viscoelastic material, to accurately mimic the rate sensitivity too [193].

This study captured the time-dependent behaviour for linear viscoelastic calibration using stress relaxation experiments. Stress relaxation experiments cannot achieve an instantaneous step input and will always include an initial loading ramp, as well as inertial effects from the test equipment loading. This is, however, compensated for by analysing the data and back-calculating to a theoretical instantaneous load point, an approach which demonstrated favourable results here and in a previous study [113]. An alternative method is to utilise resonance methods, e.g., Dynamic Mechanical Analysis [159], which also captures the viscoelastic behaviour for strain-rates in a range near that of the impact. It is, however, equally susceptible to the incorporation of user and/or analytical error, due to the utilisation of shift factors [198].

The Abaqus solver enabled comparison of different constitutive material models using the same experimental data input. The conditions of a simple hyperelastic model were considered to aid in selecting the most appropriate model [199], whilst the predictive capability in isolated and mixed deformation modes was assessed through relative difference when comparing models. The Ogden N=5 model is known to be easy to calibrate when using data from multiple tests [200]. As such this model presented the least total relative difference versus the other models, however, it is computationally expensive [201]. The Van Der Waals model utilised few coefficients, whilst demonstrating the second most favourable fit from the experimental data. The high degree of accuracy afforded by the Ogden N=5 provides the foundation for investigation with the dynamic regime when undergoing large deformation, therefore was used for the rest of the thesis. The low RMS error requirement applied to the linear viscoelastic model solver implemented by Abaqus, results in the Prony series strongly agreeing with the experimental data. Simulation using the material model coefficients compared accurately to experimental behaviour for a given strain range, therefore, it is anticipated similar accuracy would be found within a dynamic regime in the same range for both isolated and mixed deformation modes.

Strong comparability was evident between the experimental and simulation data in isolated deformation under dynamic conditions, demonstrating the efficacy of

the proposed material model. The calculated engineering stress relative to the applied strain was accurately predicted. For mixed deformation mode testing (i.e., honeycomb uniaxial compression), under quasi-static and impact loading, good comparison was achieved. The total energy absorbed was within an acceptable error tolerance as observed in similar finite element studies [192]. The stress at the on-set of buckling, however, was markedly different from the observed experimental results. This is due to the prominence of curling which resulted in a tapered cross-section through the wall thickness, which is an artefact of the sintering process [149]. Strategies to account for discrepancies between the design and manufactured specimen including CT scanning to develop an accurate mesh to better inform the finite element model [202], however, this would require higher computational cost due to the anticipated mesh element size on the scale of a micron to account for the fault.

The quantification of mechanical behaviour as function of build orientation and layer-by-layer fabrication was not included within the finite element model. Despite being adopted for other investigations [203], this was not adopted to the higher computation computational cost for marginal improvement in accuracy. Moreover, experimental studies have demonstrated that the behaviour is recognised to be less sensitive to anisotropy when exposed to compressive loads [159], as compared to the uniaxial tensile results of this study. Since honeycombs are commonly loaded in compression, this simplification was deemed acceptable.

3.5 Conclusion

This chapter presents experimental data that characterises the mechanical behaviour of the laser sintered elastomer Luvosint. Furthermore, a finite element material model was calibrated and validated. Establishing this behaviour lays the foundation for subsequent investigations, which adopt this material for design optimisation using finite element analysis. A list of conclusions is presented below:

1. Anisotropy was observed with respect to build orientation. Superior mechanical performance was achieved in coupons build in the ‘xy’ direction compared to ‘xz’ and ‘zy’. Consequently, subsequent investigations will adopt the ‘xy’ build direction.
2. Luvosint demonstrated non-linear and rate-dependant mechanical behaviour – necessitating fit of a hyperelastic material model augmented with a linear viscoelastic model.
3. Hyperelastic (Ogden $N=5$) and rate-dependant (linear viscoelastic) materials models were calibrated, where coefficients were reported for use in future studies.
4. The material model was systematically validated under isolated and mixed deformation state for quasi-static conditions, yielding good comparison.
5. The material model was systematically validated under isolated and mixed deformation state for dynamic conditions, yielding good comparison.

Chapter 4

Experimental and Numerical Analysis of Elastomeric Honeycomb Mechanical Behaviour

The contents of this chapter has recently been published as:

R. Adams et al. Mechanical behaviour of additively manufactured elastomeric pre-buckled honeycombs under quasi-static and impact loading. *Materials and Design* (2022), article number 110368.

4.1 Introduction

Laser sintering of elastomers is a highly promising approach to manufacturing impact mitigating structures for use in helmets. Chapter 3 described the mechanical behaviour of a laser sintered elastomer, Luvosint, which culminated in a calibrated and validated finite element model. This material, when used to manufacture cellular structures, such as honeycombs, may leverage a performance benefit for head protection when compared to contemporary materials. The route to optimising a candidate cellular structure using finite element analysis, however, is limited by the unknown cellular structure behaviour relative to its parametric design space. Moreover, owing to the scale and topology of typical cellular structures it is likely each structural variant will necessitate a fine mesh, made up of thousands of elements. Consequently, computational cost will be high, where a high throughput of design variants may be analysed, leading to an inefficient optimisation process.

This chapter aims to employ two strategies to improve the design optimisation route for cellular structures such as honeycombs. Firstly, a periodic boundary condition (BC) model shall be constructed to enable approximation of the full-scale model under quasi-static compression and impact loading. This model shall be validated relative to a full-scale model as well as additional experimental data. Secondly, using the proposed periodic BC model, the design space of the proposed structure shall be interrogated and analysed relative to its structural parameters and performance metrics to limit the search space of future optimisation studies.

This chapter is organised as follows. Firstly, the candidate structure is presented, a circular pre-buckled honeycomb, and its structural parameters are highlighted and discussed. Secondly, a series of honeycomb variants are laser sintered from Luvosint. Specimens are tested under quasi-static compression and impact loading. Performance metrics yield stress, energy absorption and efficiency are reported under initial loading as well as secondary and tertiary loading. Next, parametric full-scale finite element models are developed for each honeycomb variant and validated relative to experimental data. Following, periodic BC models are developed for each honeycomb variant, the efficacy of which is established relative to the experimental test data and the aforementioned full-scale models. Lastly, the periodic BC models are used to undertake a full-factorial, design of experiment, parameter sweep and rich performance maps are developed. The culmination

of this chapter provides the foundation for numerical optimisation by establishing a validated periodic BC finite element models, to understand the structural parameters relative to energy absorption and to determine a suitable geometry bounds.

4.2 Materials & Methods

4.2.1 Honeycomb Structure

A circular pre-buckled honeycomb was selected as an exemplar structure for use within this thesis. It is an ambition of this thesis, however, that the optimisation design route is generic such that any additively manufactured structure can be analysed using these principles. As illustrated by figure 4.1, the circular honeycomb topology unit cell is defined by geometric parameters: cell size (w), wall thickness (t), and depth (h). The pre-buckled design feature, characterised as a smooth cosine curve propagated through the z axis, is defined by geometric parameters: aspect ratio ($e = \frac{r_1}{r_2}$) and number of folds (f).

Computer-aided design (CAD) models were generated using an in-house software written in python code. As illustrated by figure 4.2, the honeycomb with an aspect ratio of $e = 1.0$ retrieves a basic circular cross-section and straight walls in the z -direction. As e reduces, the tube cross-section becomes more elliptical, and the pre-buckled feature becomes more pronounced. As such, e controls both the ratio of side lengths in the cross-section and the angle in the z -direction.

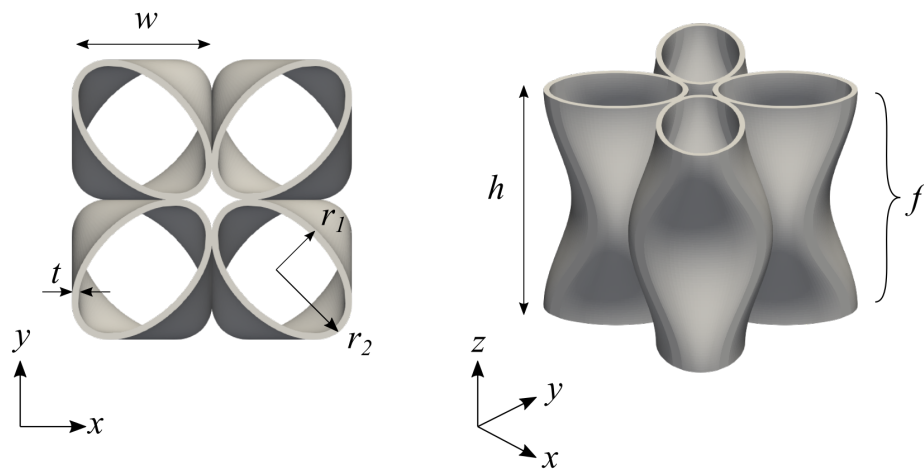


Figure 4.1: Annotated circular honeycomb (2x2) illustrating the geometric parameters of the unit cell

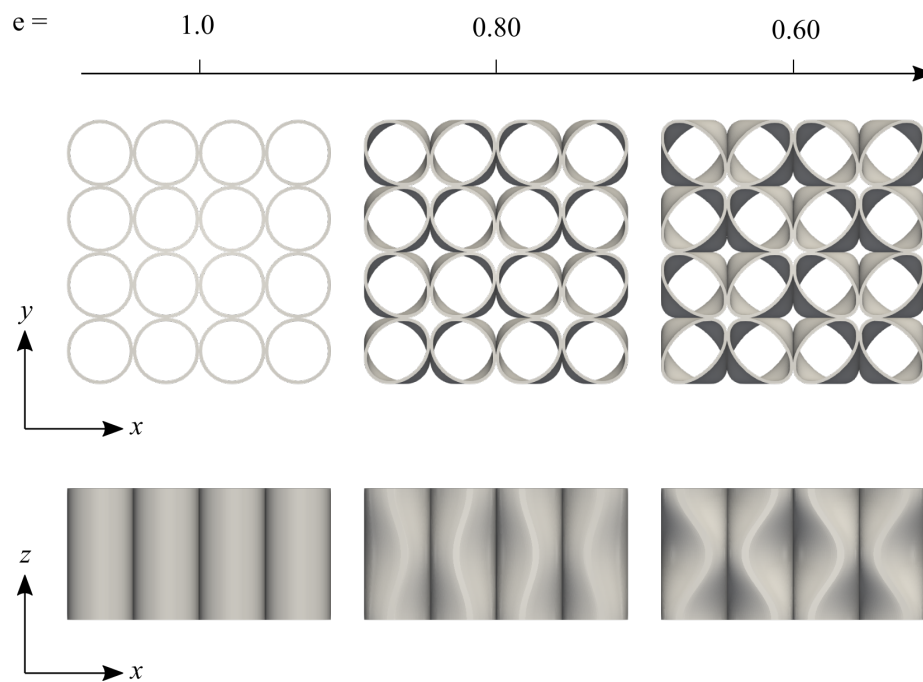


Figure 4.2: Variation in pre-buckled honeycomb design subject to changing aspect ratio.

4.2.2 Honeycomb Fabrication

The circular honeycomb used in the experimental testing was manufactured from Luvosint using selective laser sintering, as depicted by figure 4.3. As previously discussed, manufacturing was outsourced to a third party. For more information, refer to Chapter 3.

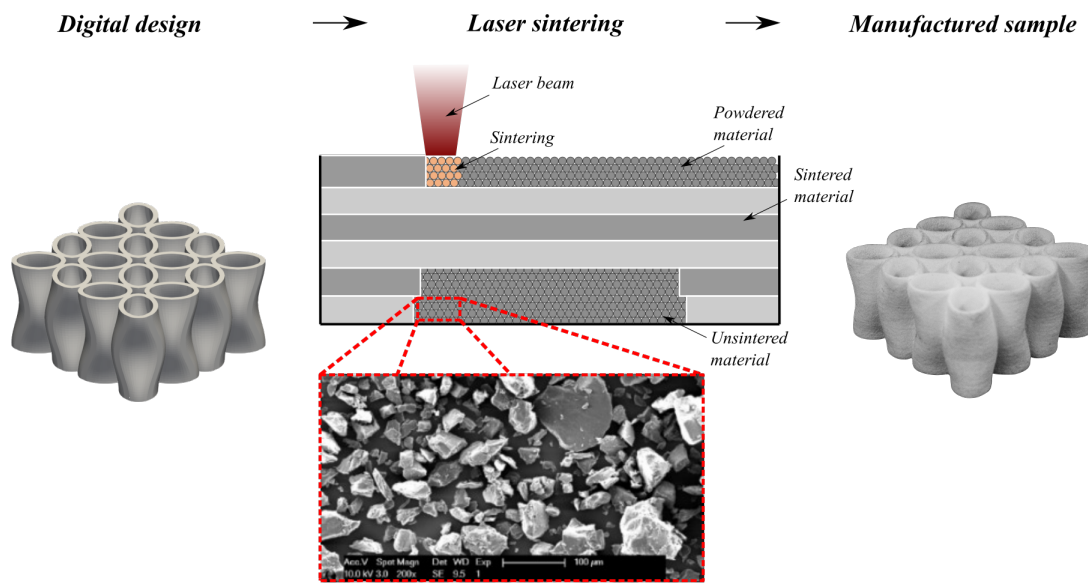


Figure 4.3: The fabrication method for the optimal honeycomb design including digital design, laser sintering overview and final part. Scanning electron imagery of Luvosint powder has been adopted from [168]

Three structural variations, comprised of 16 cells (4 x 4 array), were manufactured with geometric properties described by table 1.

Table 4.1: Structural parameters cell width, wall thickness, aspect ratio and number of folds of the manufactured honeycombs

Cell width, w (mm)	Wall thickness, t (mm)	Aspect ratio e (-)	Number of folds, f (-)	Relative density, R_d (-)	Density, ρ (kg/m^3)
12.5	0.60	1.00	1	0.14	168
12.5	0.60	0.80	1	0.14	168
12.5	0.60	0.60	1	0.14	168

4.2.3 Experimental Characterisation

Quasi-static uniaxial compression testing was performed with a universal mechanical tester, the details of which are described in Chapter 3. The specimen was placed between two horizontal, rigid platens fitted with a 50 kN load cell; the upper platen was translated vertically at a rate of 100 mm/min until the onset of densification. Force was measured using the load cell and displacement was recorded using the in-built measurement system. All specimens were compressed out-of-plane, aligned with the build orientation. Three specimens of each structural design were tested, for statistical analysis. All testing was performed in ambient conditions as per previous characterisation testing.

Impact tests were performed using a spring-loaded linear impactor, the details of which are described in chapter 3. Each honeycomb struck with an impactor, which had a total mass of 6.1 kg. Each sample was subjected to an initial impact velocity of 2.5 m/s (equivalent to 100 /s). The honeycomb was taped across the out-of-plane face of the lower anvil to prevent it from jumping out of the impact area of each strike, which could lead to the anvils striking one another and damaging the equipment. All specimens were compressed out-of-plane to the build orientation. Three specimens were again tested for each structural design for statistical analysis. All testing was performed in ambient conditions as per previous characterisation testing.

An aim of this thesis was to achieve a structure which could mitigate a loading history. Therefore, specimens were subjected to subsequent repeat under the previously discussed quasi-static and impact conditions. The virgin response was captured and then, after an hour, testing was repeated. Testing was then repeated the following day. Repeat testing was performed to capture the recoverable behaviour of the manufactured honeycomb.

4.2.4 Performance Parameters

To assess the energy absorption capacity of each honeycomb variant, the following performance parameters were used: yield stress, energy absorption and absorption efficiency. Yield stress was defined as the peak load during initial yield (nominally

between 0 – 0.2 mm/mm). Energy absorption was defined as the cumulative work done by the structure until densification, as per equation 4.1

$$E = \int_0^{\varepsilon_d} \sigma d\varepsilon \quad (4.1)$$

Where E is the energy absorbed, σ is the engineering stress, ε is engineering strain and ε_d is the densification strain.

Lastly, energy absorption efficiency (equation 4.2), was defined as the ratio of cumulative absorbed energy up to densification strain, divided by the peak stress.

$$\eta = \frac{\int_0^{\varepsilon_d} \sigma d\varepsilon}{\sigma_{peak}} \quad (4.2)$$

Where η is the energy absorption efficiency and σ_{peak} is the peak stress.

4.2.5 Finite Element Model

Finite element models of the honeycomb structure were developed, to establish a route for optimisation in future studies. Abaqus was utilised leveraging the material model from Chapter 3. The honeycomb structure was modelled using the geometric parameters measured from the manufactured specimens to account for the discrepancy in digital design versus the as-built configuration that can occur due to thermal expansion during the sintering process [204].

Figure 4.4 presents the quasi-static compression finite element model. It is important to note that although in this investigation the quasi-static response is analysed, the explicit dynamic solver in Abaqus was utilised to access the general contact algorithm, as this enables better representation of the behaviour during post-buckling and densification. The honeycomb structure was positioned between two analytically rigid plates. The lower plate was assigned an encastre boundary condition, whilst the upper plate was assigned a ramp deformation boundary condition, achieving a strain of 0.75 mm/mm in the z-direction. An eight-node brick element, with hexahedron shape type, reduced integration and

hourglass control was utilised (C3D8R). Mesh size was identified through an independence study, where an average element size of 0.3 mm was sufficient, with a finer mesh yielding better results, however, dis-proportionality greater computational run-time. A global friction value of 1.0 was adopted as per the previous chapter. Reaction force and displacement was extracted from a reference point at the centre of the upper plate. Engineering strain was calculated by dividing the displacement of the upper plate by the honeycomb height. Engineering stress was calculated by dividing the recorded force by the projected area of the honeycomb.

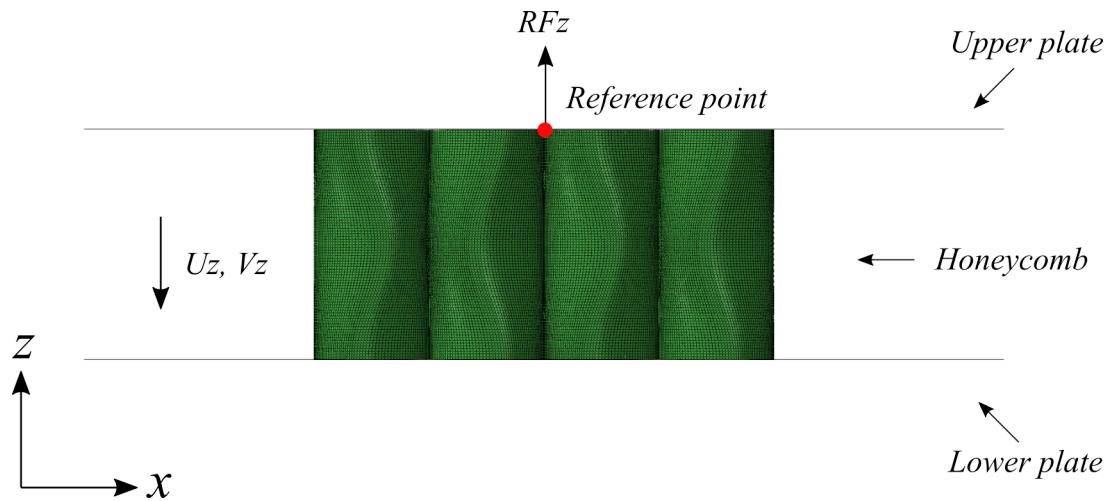


Figure 4.4: Finite element model of the honeycomb for quasi-static and impact conditions.

The impact compression model was constructed analogous to the quasi-static model. The lower plate was assigned an encastre boundary condition, whilst the upper plate was assigned a 6.1 kg point mass and prescribed a pre-impact velocity of 2.5 m/s.

In addition to the previously discussed finite element models, hereafter referred to as the full-scale models, two computationally efficient models for quasi-static and impact conditions were developed, termed periodic boundary condition (BC) models. As illustrated by figure 4.5, these were achieved by taking advantage of the symmetry in the X and Y plane and utilising zero displacement boundary conditions around the perimeter of the unit cell.

In the quasi-static model, a 2 x 2 honeycomb configuration was modelled with zero displacement in the X and Y axes prescribed along the perimeter nodes. The

displacement conditions of the upper and lower plates were identical to the previous model. The impact model adopted a similar boundary condition approach. The lower plate boundary conditions remained the same, whilst the upper plate point mass was scaled by 25%, which is proportional to the kinetic energy, to account for load distribution over a quarter of the projected area.

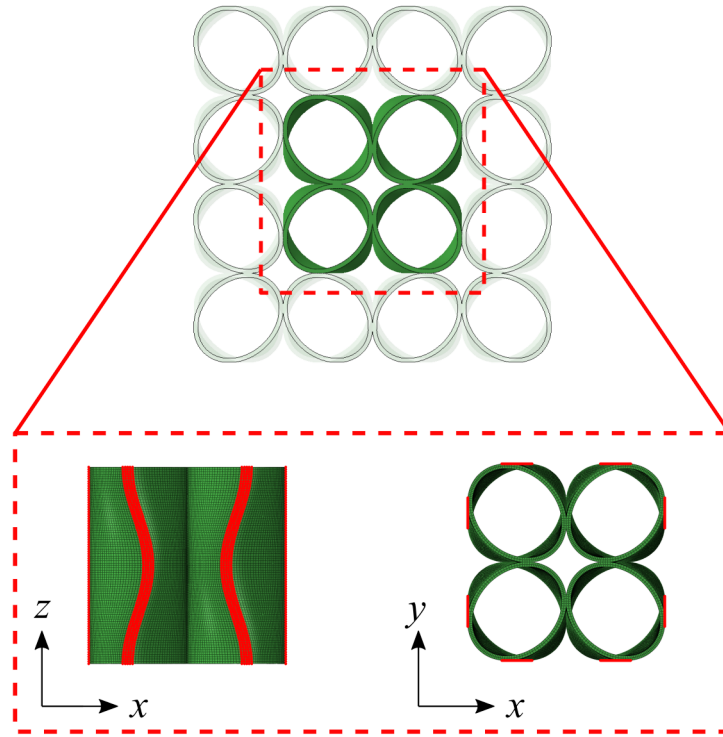


Figure 4.5: Location of nodal zero displacement boundary conditions for the honeycomb periodic BC model (upper and lower plates removed for clarity).

4.3 Results

4.3.1 Review of Fabricated Honeycombs

The manufactured honeycombs are illustrated by figure 4.6. Prior to testing, individual mass and dimensions of all specimens ($N = 18$) were recorded using digital scales and a Vernier Caliper. Table 4.2 reports the mass, length, width, depth and average wall thickness for each sample. Length, width, and depth varied about the design value by 0.76 mm, 0.62 mm, and 0.19 mm respectively,

when compared to the CAD models, for all structural variations. For samples with an aspect ratio of $e = 1.0$, wall thickness exceeded the design value by 0.23 mm. For samples with an aspect ratio of $e = 0.8$ and 0.6 , the variation was 0.17 mm and 0.16 mm respectively.

Table 4.2: Recorded dimensions of manufactured honeycomb samples. Variants were labelled from A, B and C representing honeycombs with an aspect ratio of $e = 1.0$, $e = 0.8$, and $e = 0.6$ respectively.

Aspect ratio, e (-)	Specimen name	Mass (g)	Width, x (mm)	Breadth, y (mm)	Depth, h (mm)	Average wall thickness, t_{avg} (mm)
1.0	A-1	10.51	49.44	49.78	24.98	0.71
	A-2	11.22	49.51	49.75	25.01	0.76
	A-3	11.84	49.56	49.88	25.08	0.81
	A-4	12.64	50.04	49.89	24.99	0.83
	A-5	11.15	49.24	50.10	25.02	0.76
	A-6	11.73	49.88	49.91	24.89	0.77
0.8	B-1	11.85	49.89	49.88	24.96	0.77
	B-2	10.83	49.87	49.93	24.92	0.71
	B-3	10.21	49.95	49.68	25.01	0.68
	B-4	10.51	49.58	49.48	25.12	0.68
	B-5	10.74	49.53	49.38	24.92	0.72
	B-6	11.23	49.67	49.73	24.81	0.74
0.6	C-1	9.83	49.82	49.67	25.01	0.68
	C-2	11.46	49.96	49.70	24.94	0.74
	C-3	11.83	49.75	49.83	24.89	0.76
	C-4	10.75	49.61	49.83	24.89	0.71
	C-5	11.33	49.84	49.78	24.93	0.75
	C-6	11.18	49.54	49.83	24.93	0.72

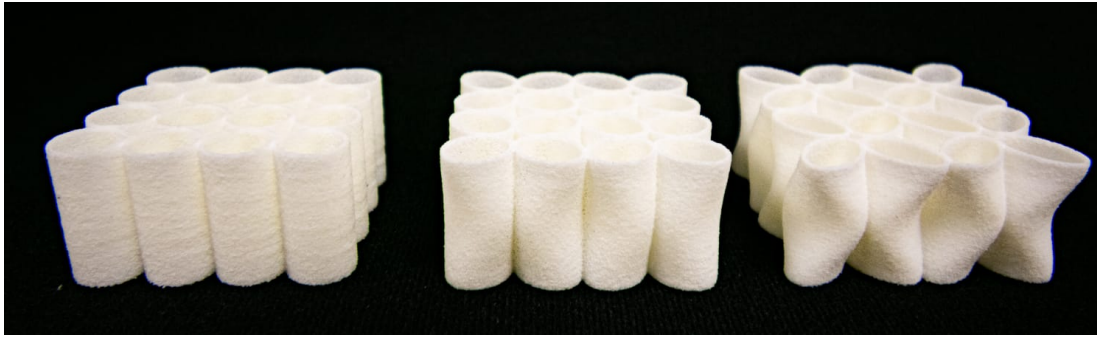


Figure 4.6: Fabricated honeycomb samples subject to changing aspect ratio, $e = 1.0$ (left), $e = 0.8$ (centre), and $e = 0.6$ (right).

Visual inspection identified artefacts of the sintering process in certain samples. As highlighted in figure 4.7, samples with an aspect ratio of $e = 1.0$, had a series of ribs distributed throughout the build axis. . At these locations, localised curling has occurred due to a raised area of powder on the build layer. During the following build layer, the raised area limits the deposition of new powder directly on top of the sintered layer, instead being pushed outward causing the rib feature. This feature occurs multiple times throughout the build height due to variation in the bed temperature profile of the build. This feature is not observed in samples with an aspect ratio of $e = 0.8$ or $e = 0.6$, because the fold provides a moving cross-sectional area through the z -axis, meaning the material is not sintered normal to the subsequent layer, mitigating the phenomena.

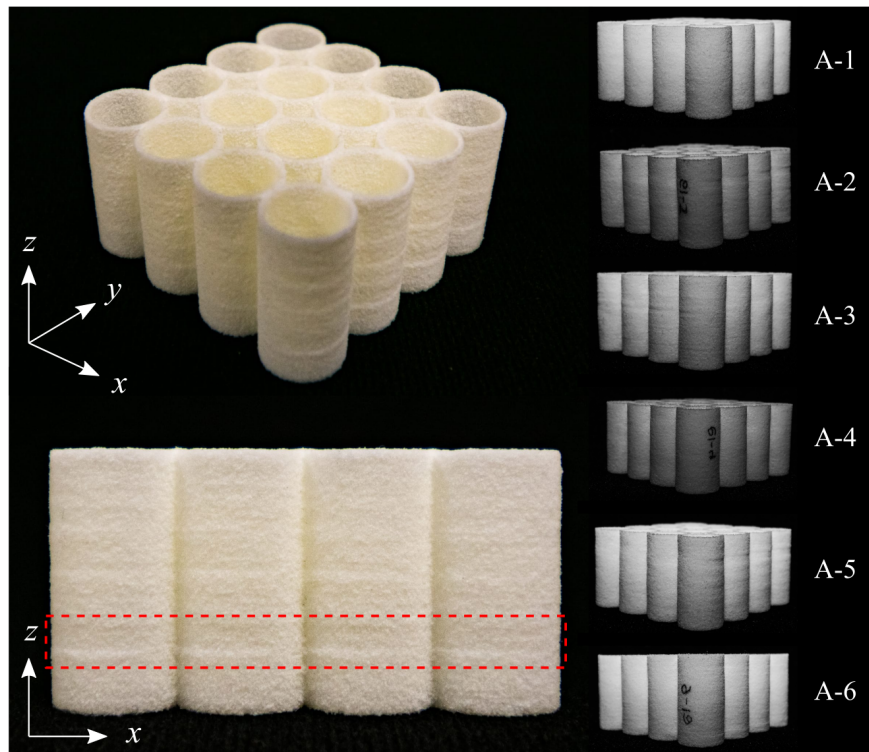


Figure 4.7: Identification of sintered rib artifact proliferated through the z-axis height of honeycombs with an aspect ratio of $e = 1.0$ (straight walled honeycombs).

4.3.2 Experimental Quasi-Static Compression

Quasi-static uniaxial compression was undertaken for each honeycomb variant, with stress-strain curves reported in figure 4.8a - 4.8c. For completeness, all data sets ($n = 9$) for each variant ($n = 3$) are reported here. Video snapshots are reported 4.9 to illustrate the deformation mechanisms.

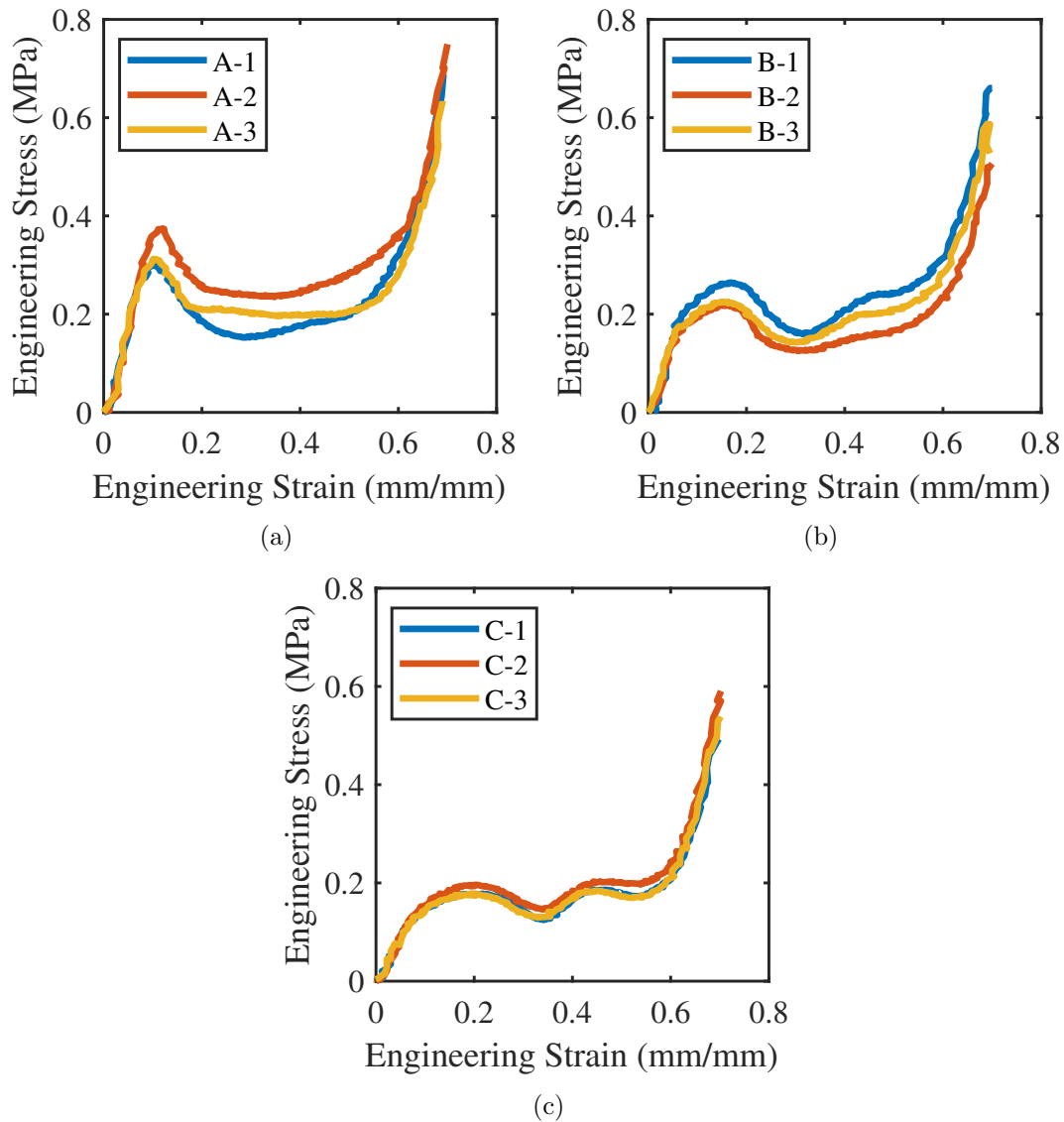


Figure 4.8: Engineering stress-strain curves for honeycomb variants subject to changing aspect ratio $e = 1.0$ (a), $e = 0.8$ (b) and $e = 0.6$ (c), under quasi-static uniaxial compression.

As reported by table 4.3, for an aspect ratio of $e = 1.0$, the average yield stress was 0.33 MPa whilst at $e = 0.8$ and $e = 0.6$, the average value was 0.24 MPa and 0.18 MPa, respectively. For decreasing aspect ratio, the energy absorbed decreases, yielding 8.72 J, 6.20 J and 5.17 J respectively. Conversely, the energy absorption efficiency increases to 0.41, 0.43 and 0.46.

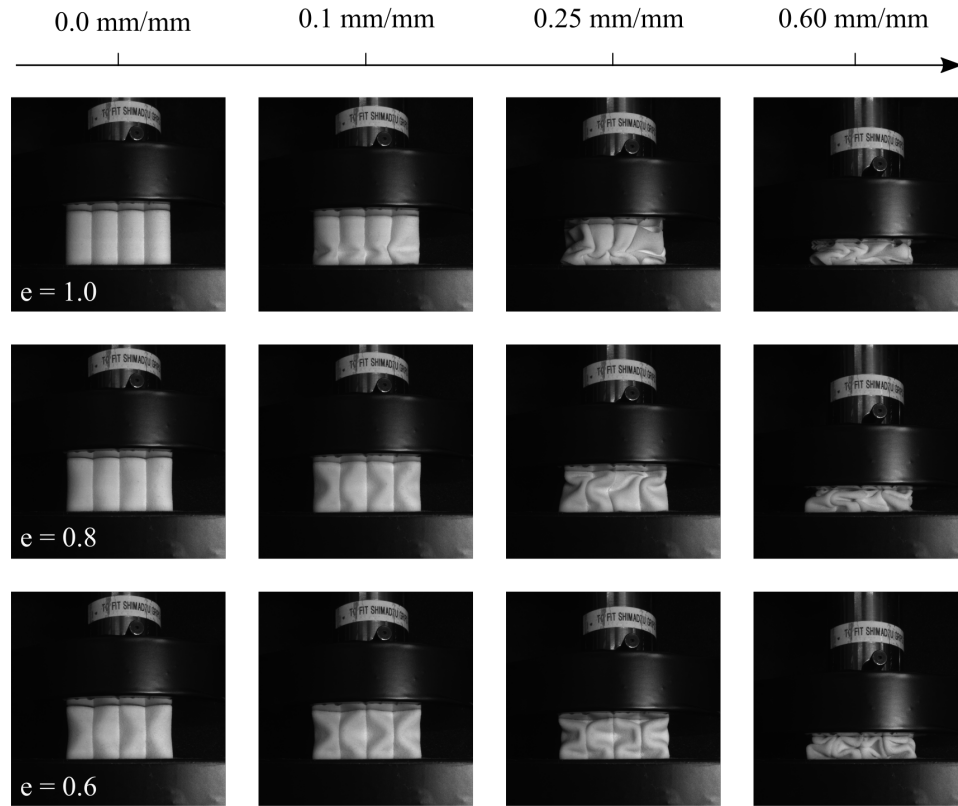


Figure 4.9: Photographic stills of the honeycomb variants subject to changing aspect ratio $e = 1.0$ (top-row), $e = 0.8$ (middle-row) and $e = 0.6$ (bottom-row) under quasi-static compression.

Table 4.3: Average performance parameters yield stress, absorption efficiency and energy absorbed for changing aspect ratio of each honeycomb variant under quasi-static uniaxial compression. Standard deviation in parentheses, CV = coefficient of variation.

	Aspect Ratio	$e = 1.0$	$e = 0.8$	$e = 0.6$
σ_{yield} (MPa)	Mean	0.33 (0.04)	0.24 (0.02)	0.18 (0.01)
	CV (%)	12.08	10.34	5.86
E (J)	Mean	8.72 (1.53)	6.20 (0.53)	5.17 (0.06)
	CV (%)	17.56	8.49	1.12
η	Mean	0.41 (0.03)	0.43 (0.01)	0.46 (0.01)
	CV (%)	6.39	1.07	1.46

4.3.3 Experimental Impact Loading

Impact tests were performed for each honeycomb variant, with stress-strain curves reported in figure 4.10a - 4.10c. For completeness, all datasets ($n = 9$) for each variant ($n = 3$) are reported here. Video snapshots are reported 4.11 to illustrate

the deformation mechanisms.

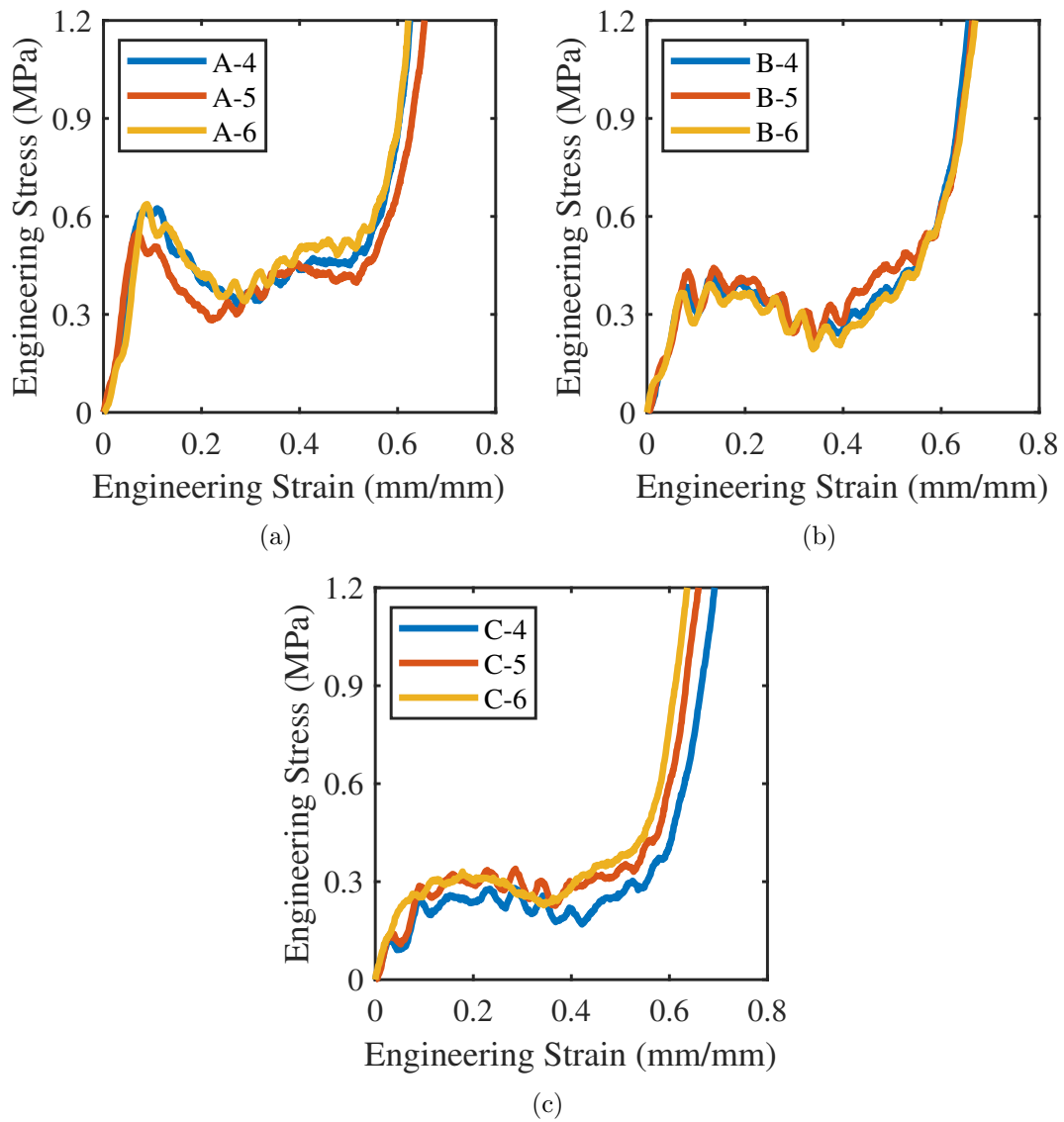


Figure 4.10: Engineering stress-strain curves for honeycomb variants subject to changing aspect ratio $e = 1.0$ (a), $e = 0.8$ (b) and $e = 0.6$ (c), under uniaxial compression impact loading

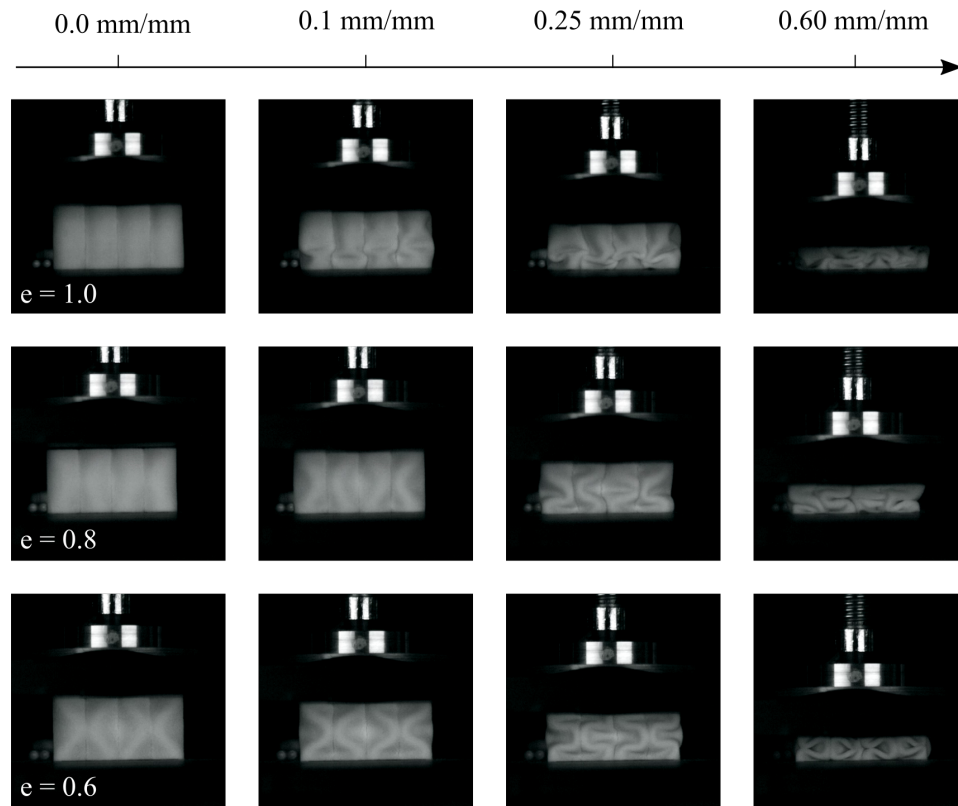


Figure 4.11: Photographic stills of the honeycomb variants subject to changing aspect ratio $e = 1.0$ (top-row), $e = 0.8$ (middle-row) and $e = 0.6$ (bottom-row) under uniaxial compression impact loading.

As reported by table 4.4, for an aspect ratio $e = 1.0$, the average yield stress was 0.58 MPa, whilst at $e = 0.8$ and $e = 0.6$ the observed yield stress were 0.38 MPa and 0.29 MPa, respectively. In all cases, densification was achieved for the impact, thus enabling calculation of energy absorption efficiency and energy absorbed. In a similar trend to yield stress, values for energy absorbed decreased to 14.69 J, 10.04 J and 8.31 J for decreasing aspect ratio. For energy absorption efficiency the results were 0.39, 0.40 and 0.41 for decreasing aspect ratio.

Table 4.4: Average performance parameters yield stress, absorption efficiency and energy absorbed for changing aspect ratio of each honeycomb variant under impact uniaxial compression. Standard deviation in parentheses, CV = coefficient of variation.

	Aspect Ratio	e = 1.0	e = 0.8	e = 0.6
σ_{yield} (MPa)	Mean	0.58 (0.05)	0.38 (0.02)	0.29 (0.04)
	CV (%)	8.66	5.42	12.37
E (J)	Mean	14.69 (0.90)	10.04 (1.39)	8.31 (0.92)
	CV (%)	6.15	13.81	11.03
η	Mean	0.39 (0.02)	0.40 (0.01)	0.41 (0.01)
	CV (%)	4.40	2.06	2.95

4.3.4 Experimental Rate Dependant Behaviour

Comparison of the static and impact test results enables identification of the rate-dependant behaviour. Figure 4.13a and 4.13b, reports the change in energy absorption with respect to aspect ratio for both the quasi-static and impact conditions. The honeycomb structures are sensitive to loading regime. Structures with an aspect ratio of $e = 1.0$ yield an increase in energy absorption by 69 % between the static and impact regime. As the aspect ratio decreases to $e = 0.8$ and $e = 0.6$, the associated rate effects decrease and energy absorption is only 62% and 61% greater than the static case, respectively.

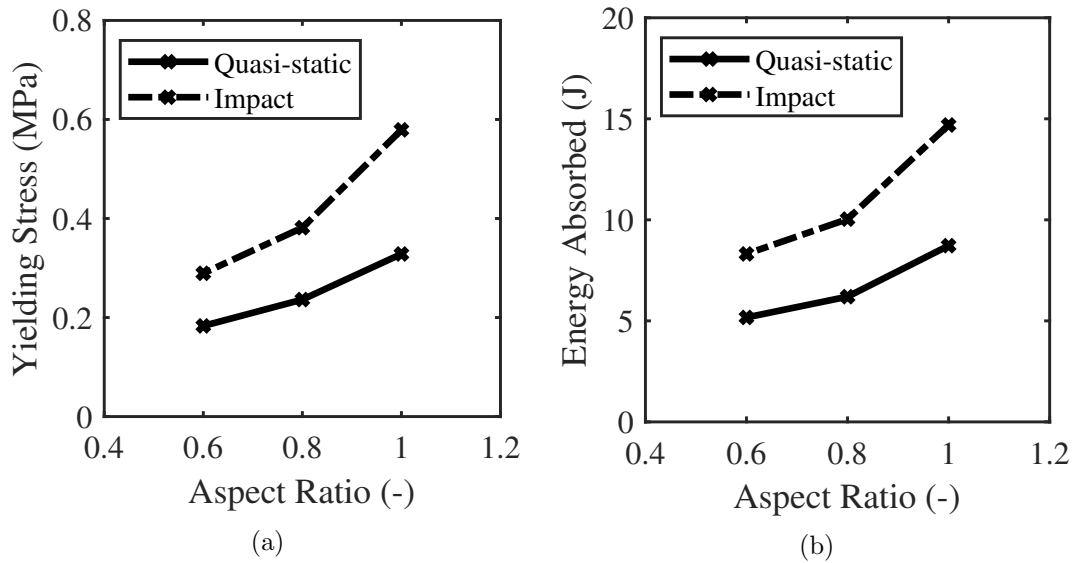


Figure 4.12: Comparison of strain rate behaviour for yield stress (a) and energy absorbed (b) under quasi-static and impact uniaxial compression.

The relative increase in yielding stress and energy absorbed is due to the rate dependence of the base material. This aligns with the uniaxial tension results of Chapter 3 whereby a similar relative increase in magnitude of behaviour was observed. The similarity in increase suggests that the rate-dependence observed in this study is due to the base material rate dependence and not structural dependence, such as inertial stabilisation and plastic wave propagation, which can only be attained at higher strain rates.

4.3.5 Experimental Multi-Loading Behaviour

Following initial tests, each sample was subjected to secondary (1 hour after the initial test) and tertiary (24 hours after the secondary test) testing under identical conditions, to identify the multiple loading behaviour of the additively manufactured honeycomb structure. Fig. 4.13a and 4.13b reports change in energy absorption with respect to aspect ratio for quasi-static and impact conditions for each repeat.

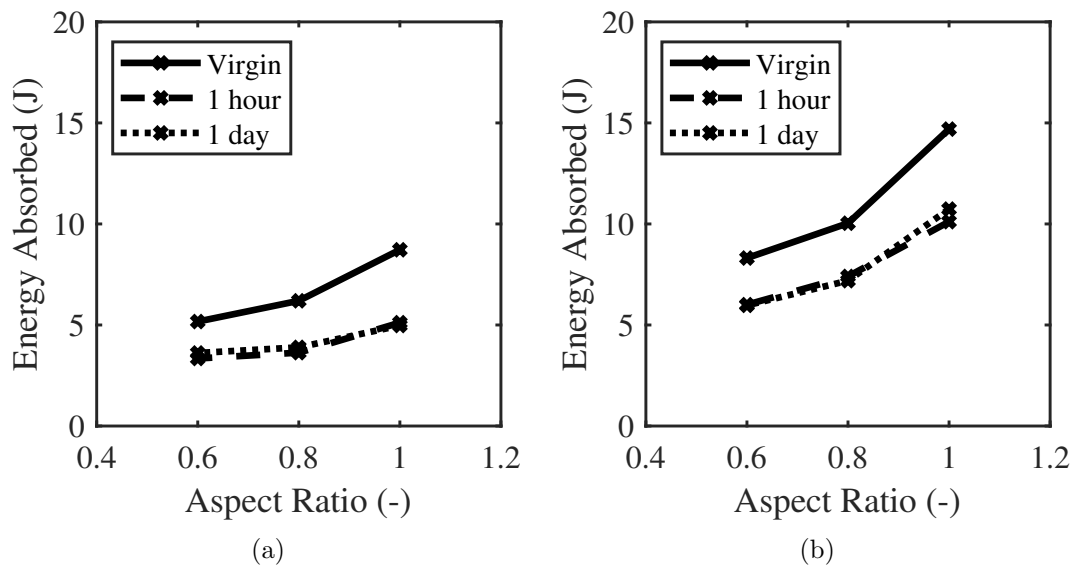


Figure 4.13: Comparison of multi-loading energy absorbed for quasi-static (a) and impact (b) loading uniaxial compression.

For quasi-static conditions, the average energy absorbed was greatest for the virgin compression. A subsequent compression performed an hour later reported a decrease in total energy absorbed of 41 %, 40 % and 35 % for decreasing aspect ratio. The final, tertiary compression occurred 24 hours after the secondary test. The calculated energy absorbed during these tests reported a reduction, when compared to the initial response, of 43 %, 38 % and 30 %. In a similar trend to quasi-static conditions, the calculated energy absorbed under impact testing was greatest for the virgin impact. Secondary loading yielded a reduction in total energy absorbed of 31 %, 21 % and 28 % for decreasing aspect ratios. The calculated energy absorbed during the tertiary tests reported a reduction, when compared to the initial response, of 27%, 28 % and 28 %.

Under initial compression, the base material undergoes both elastic and plastic deformation, characterised by base material stress softening (i.e., Mullins effect [191]), this is confirmed by the stress reduction in the secondary compressive cycle. During the secondary loading cycle, the base material undergoes exclusively elastic deformation, representing a relaxed state. The relaxed state is present in the subsequent compression cycle, where the values of yield stress and energy absorbed are consistent with one another. The magnitude of relative decrease in energy absorption, over successive compressive cycles, is markedly greater for quasi-static than impact testing. This is attributed to the viscoelastic stress relaxation of the bulk material attaining a greater degree of relaxation. Repeat successive loading was not carried out after 24 hours due to a stabilised response, as well as the change in sample height recording less than 2.0% of the overall initial recorded height, suggesting that minimal plasticity had occurred. The behaviour reported in this investigation, aligns with others which investigated laser sintered elastomer cellular structures [205], suggesting it is feasible to achieve a recoverable energy absorbing structure.

4.3.6 Finite Element Mesh Independence

The influence of mesh size on the honeycomb mechanical behaviour was investigated by simulating quasi-static conditions for models with different number of elements through the wall thickness of the honeycomb, as reported by table 4.5 and figures 4.14a - 4.14c.

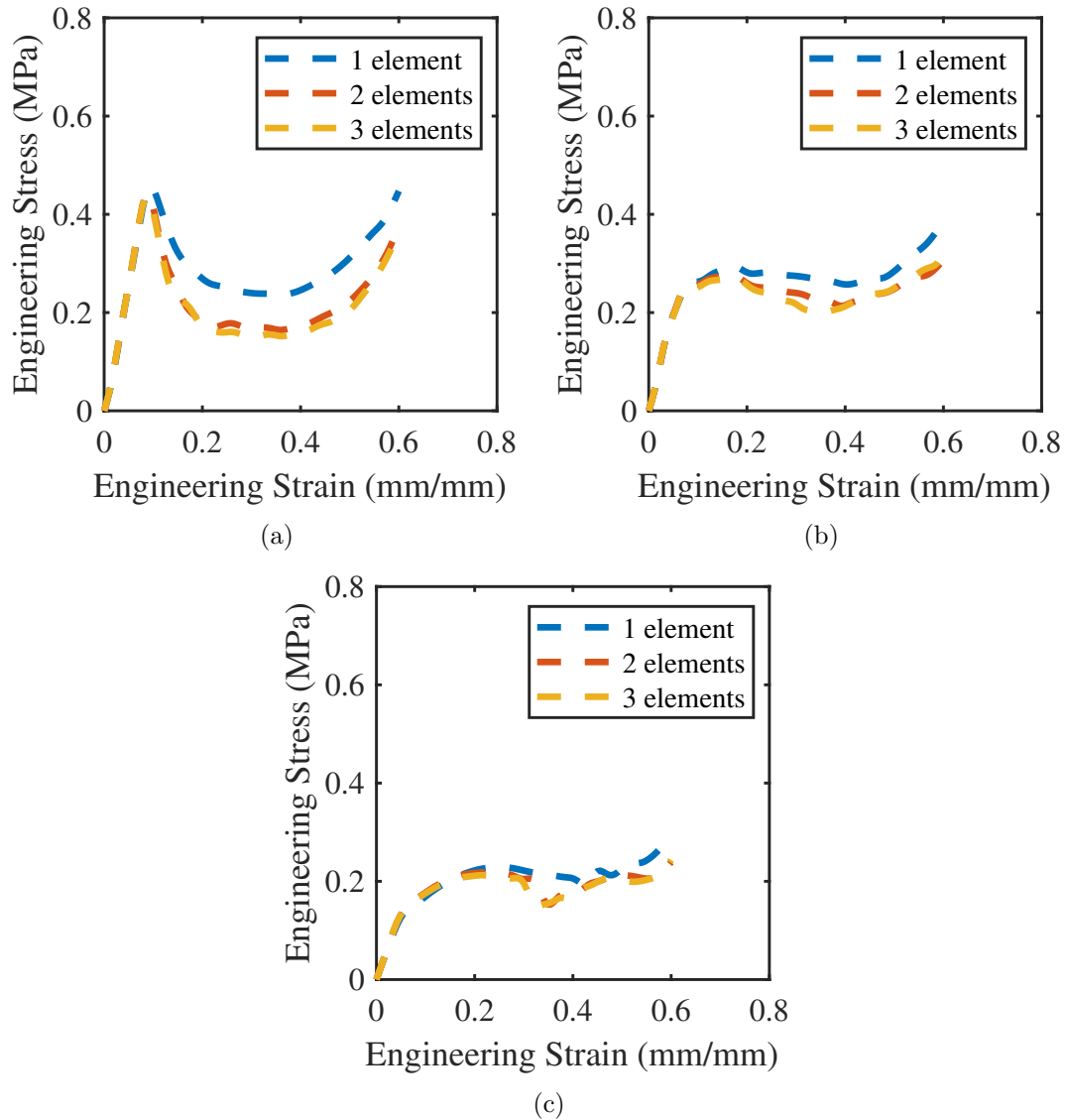


Figure 4.14: Variation in simulated mechanical behaviour of honeycombs with changing aspect ratio $e = 1.0$ (a), $e = 0.8$ (b) and $e = 0.6$ (c) under quasi-static uniaxial compression subjected to increasing mesh density

It is clear that as the number of elements increases from 2 to 3, the change in stress-strain behaviour becomes less significant, however, computational cost increases considerably. The computational cost of utilising a mesh with 3 elements, in combination with increased structural complexity necessitating fine meshing, would otherwise make further studies impractical. As previously stated, the difference in yield stress and energy absorbed recorded between structures with 2 and 3 elements is small, therefore, for the rest of this study a mesh with 2 elements through the wall thickness was adopted.

Table 4.5: Computed performance parameters and relative error subject to increasing mesh density for each structural variant.

Aspect ratio, e	No. elements	Yield stress, σ_{yield} (MPa)	Yield stress relative error, $\sigma_{yield,re}$ (%)	Energy absorbed, E (J)	Energy absorbed relative error, E_{rd} (%)
1	1	0.46	-	8.29	-
	2	0.44	3.48	6.67	24.3
	3	0.44	1.35	6.39	4.42
2	1	0.29	-	7.40	-
	2	0.28	6.10	6.83	8.32
	3	0.27	2.72	6.62	3.17
3	1	0.22	-	5.47	-
	2	0.22	2.68	5.26	4.01
	3	0.22	2.63	5.11	2.86

4.3.7 Finite Element Quasi-Static Compression

To validate the quasi-static full model of the honeycomb structure, uniaxial compression was simulated and compared to the experimental data. Moreover, the periodic BC model was also simulated to determine how well it approximates experimental data. The results of both simulations are combined and compared to the experimental data as seen in figure 4.15a - 4.15c.

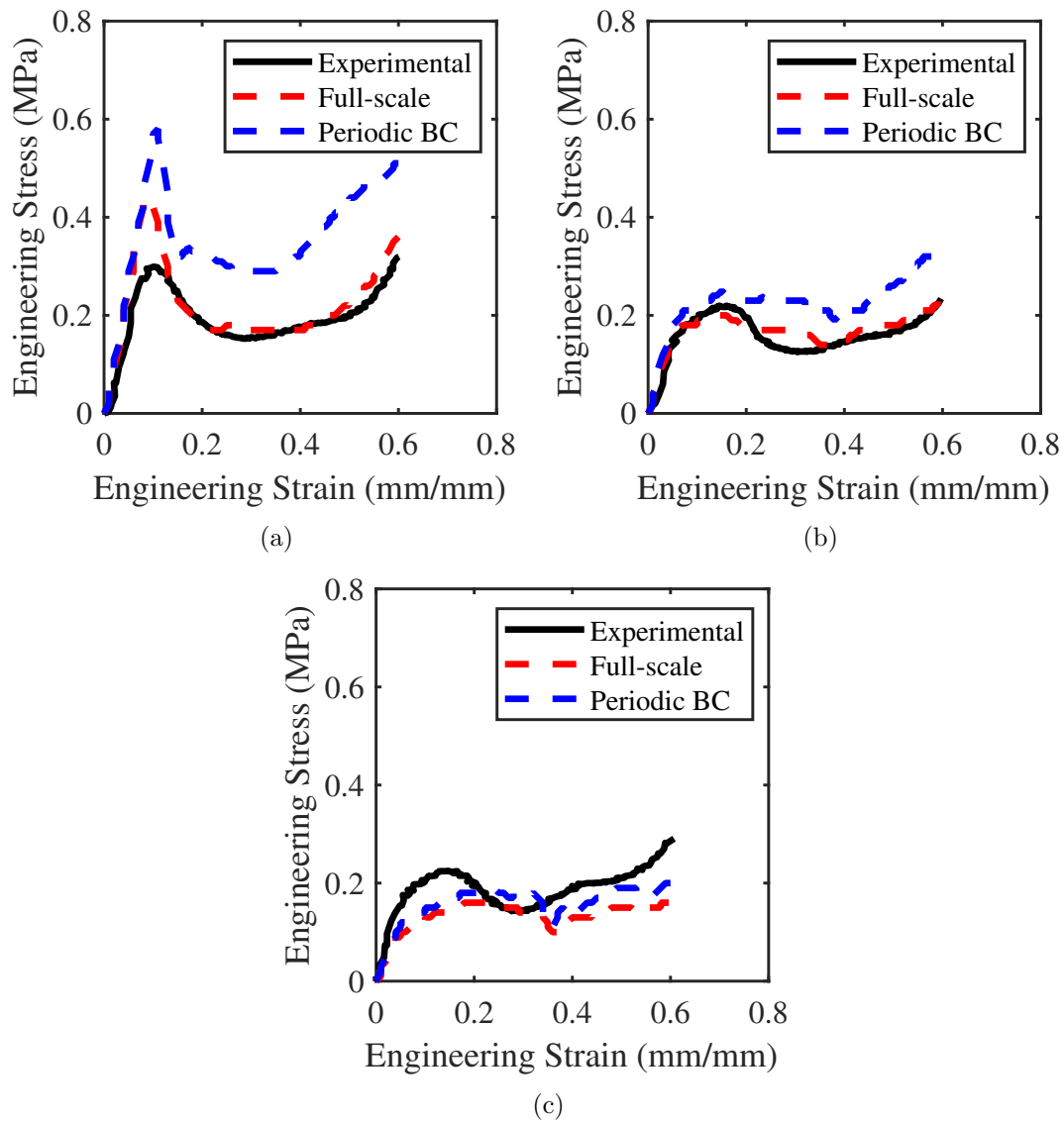


Figure 4.15: Comparison of the experimental quasi-static compression mechanical behaviour to the full and periodic BC finite element simulation result for various aspect ratio $e = 1.0$ (a), $e = 0.8$ (b), and $e = 0.6$ (c).

The reduction in CPU run-time, when comparing the full-scale to the periodic BC model, was between 70.39% – 70.63%. Calculated error values for yield stress and energy absorption, when compared to the experimental data, are reported in table 4.6. The full model reports good agreement when compared to the experimental data. Generally, the non-linear profile is best represented for the model with an aspect ratio of $e = 1.0$, where decreasing aspect ratio yields a fair approximation to the stress-strain profile. Yield stress was over-reported by 46.01 %, yet the prediction of the total energy absorbed was within 7.50 %. For decreasing aspect ratio, the full model error reported for peak stress was between 10.55 % – 13.30 % and energy absorbed was 0.77 % – 12.28 %. The periodic BC model reports fair agreement when compared to the experimental data. For an aspect ratio of $e = 1.0$, the yield stress was over-reported by 94.17 % and energy absorbed by 31.24 %. For decreasing aspect ratio, the periodic BC model error reported for peak stress is between 19.58 % – 27.83 % and energy absorbed by 2.14 % – 15.70 %.

Table 4.6: Comparison of the experimental quasi-static compression mechanical behaviour to the full simulation and periodic BC model result for various aspect ratios

Aspect ratio, e (-)	Finite element Model	Yield stress error, $\sigma_{yield,re}$ (%)	Energy absorbed error, E_{re} (%)
1.0	Full	46.01	7.38
	Periodic BC	94.17	31.24
0.80	Full	10.55	12.28
	Periodic BC	19.58	2.14
0.60	Full	13.30	0.77
	Periodic BC	27.83	15.70

4.3.8 Finite Element Impact Loading

Full-scale and periodic BC model impact simulations were performed and compared to the collected experimental data to determine their predictive capacity. The results of both simulations are combined and compared to the experimental data as seen in figure 4.16a - 4.16c.

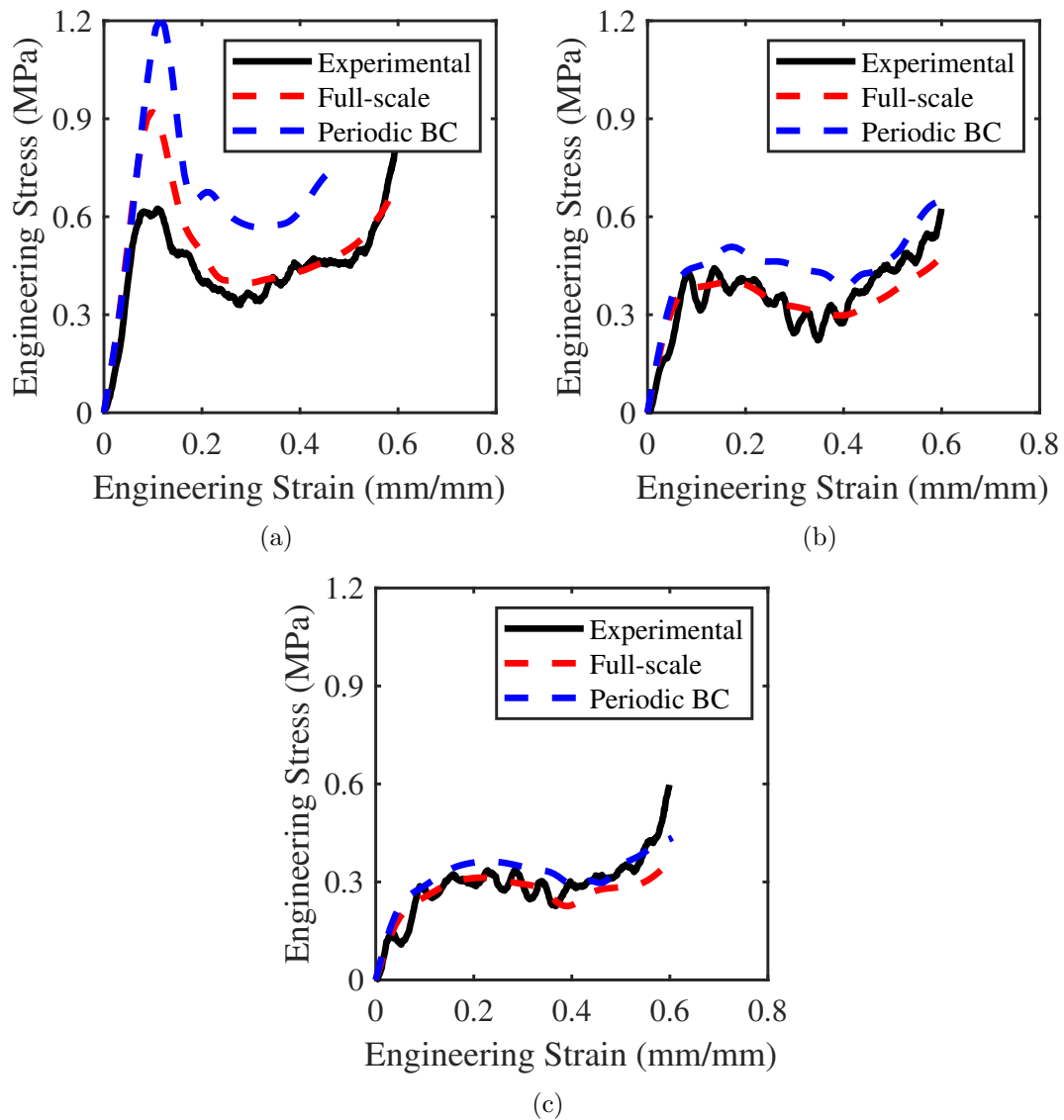


Figure 4.16: Comparison of the experimental impact compression mechanical behaviour to the full and periodic BC finite element simulation result for various aspect ratio $e = 1.0$ (a), $e = 0.8$ (b), and $e = 0.6$ (c).

The reduction in CPU run-time, when comparing the full-scale to the periodic BC model, was between 75.77 % – 76.15%. Calculated error values for yield stress and energy absorption, when compared to the experimental data, are reported in table 4.7. The full-scale finite element models report good agreement when compared to the experimental data. Generally, the non-linear profile is well represented for all models. In a similar trend to the quasi-static full model, the yield stress was over reported by 48.70%, whilst the prediction of energy absorbed was within 23.56 %. For decreasing aspect ratio, the error reported for peak stress was between 0.36 % – 1.91 % and energy absorbed was 2.86 – 6.29 %. The periodic BC model also achieved good agreement with the experimental data, except for the structure with an aspect ratio of $e = 1.0$, where yield stress was over-reported by 93.36 % and energy absorption by 62.01 %. For decreasing aspect ratio, the periodic BC model error reported for yield stress was between 17.40 % – 26.5 % and 11.94 % – 25.50% for energy absorption. For the case of $e = 1.0$, analysis was limited to $\varepsilon = 0.4$ mm/mm because the periodic BC model simulation did not yield densification

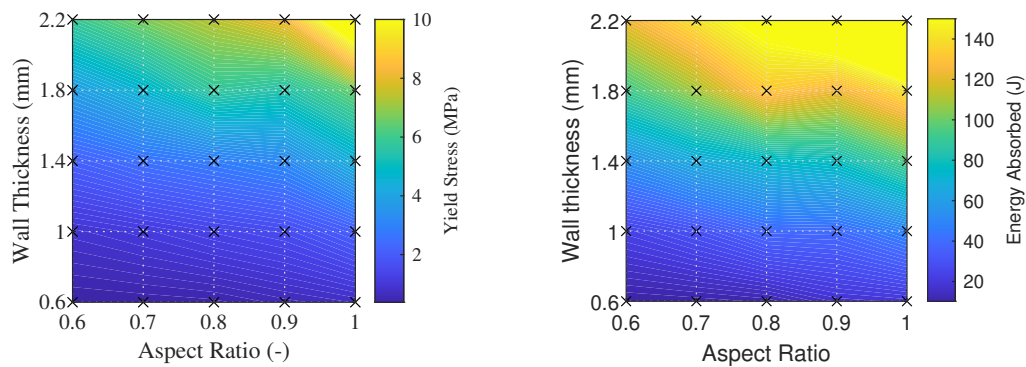
Table 4.7: Computed performance parameter error when compared to experimental data for impact uniaxial compression full and periodic BC model.

Aspect ratio, e (-)	Finite element Model	Yield stress error, $\sigma_{yield,re}$ (%)	Energy absorbed error, E_{re} (%)
1.0*	Full	48.70	23.56
	Periodic BC	94.36	62.01
0.80	Full	0.36	2.86
	Periodic BC	26.5	25.5
0.60	Full	1.91	6.29
	Periodic BC	17.40	11.94

4.3.9 Finite Element Parameter Sweep

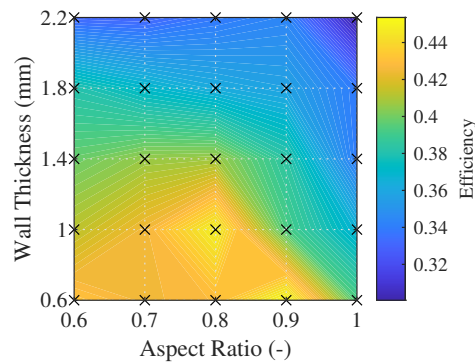
To understand the relationship between the aspect ratio and wall thickness under impact conditions, the periodic BC model under a constant strain rate conditions was leveraged to undertake a full factorial parameter sweep. Analysis was limited to the dynamic regime, since the anticipated loading conditions in a helmet application is impact loading. This approach combined the quasi-static modelling, dynamic material properties and a constant strain rate equivalent to the previous impact loading. This approach was adopted such that each simulation achieved

densification, enabling calculation of energy absorption and absorption efficiency. The validity of adopting this approach compared to impact loading was assessed and did not yield a notable difference. Yield stress, energy absorption and efficiency were calculated for each simulated response. The results were assembled into contour plots, as illustrated in figures 4.17a - 4.17c. The overlaid black crosses indicate each simulation point. Energy absorption and efficiency were calculated up to densification strain.



(a)

(b)



(c)

Figure 4.17: Variation in dynamic honeycomb mechanical behaviour yield stress (a), energy absorbed (b) and efficiency (c) relative to changing wall thickness and aspect ratio.

Figure 4.17a and 4.17b exhibit similar trends, where yield stress and energy absorbed increase towards the right-hand corner of the plot. Values reported range from 0.37 MPa – 11.82 MPa and 10.20 J – 222.0 J respectively, representing an increase of several orders of magnitude. The area of maxima corresponds to a traditional honeycomb, e.g., wall thickness, $t = 2.2$ mm, and aspect ratio, $e = 1.0$. Figure 4.17c reports a range of energy absorption efficiency between 0.30 and 0.45. Unlike figure 4.17a and 4.17b, a broad region of maximum values is observed and positioned in the lower left-hand region. This region of maximum values corresponds to a honeycomb of varying structure and is defined by values of wall thickness, $t = 0.6$ – 1.2 mm, and aspect ratio, $e = 0.6$ – 0.9 .

4.4 Discussion

The aim of this chapter was to improve the finite element based design optimisation route of cellular structures. The issues that currently inhibit an effective design optimisation of these materials for design applications are the computational expense in running full scale finite element models, and, establishing suitable bounds for the design space. Consequently, a periodic BC, representative of full-scale simulations, were established and validated relative to experimental data. These were further leveraged to undertake a full-factorial parameter sweep to establish relationships between energy absorption, yield stress, efficiency and geometries parameters. This will enable informed selection of geometric bounds subject to anticipated in-situ loading conditions and injury thresholds in future design optimisations in the later chapters.

A circular honeycomb was selected as candidate structure for this investigation and was additively manufactured using laser sintering. A review of the as-built part dimensions identified that thin features, such as the walls of the honeycomb, are particularly susceptible to thermal distortion because of the sintering process. This aligns with studies that have utilised sintering, although with other polymers, and observed that the print quality was subject to operation parameters that must be calibrated to achieve acceptable results [206]. To account and mitigate for these phenomena, adopting linear or non-linear scaling factors along the principal axis is suggested [150]. It is well known that the mechanical behaviour

of traditional honeycombs is proportional to the cell wall thickness, for a fixed cell size [76]. The ability to achieve desired, and consistent thin wall features is therefore particularly important when manufacturing honeycomb structure. This becomes increasingly important when optimising for a specific mechanical response in a mass-sensitive application such as a helmet. The implication of overly thickened cell walls will yield a suboptimal response when subjected to impact loading, resulting in high resultant accelerations.

Visual inspection identified artefacts of the sintering process were prevalent in certain samples. Samples with an aspect ratio, $e = 1.0$, had a series of ribs distributed throughout the build axis. At these sections localised curling had occurred which yields a raised area of material on the layer [149]. Consequently, during the subsequent build layer, the curled edge limits the deposition of new powder directly on the top of the sintered layer. Instead, the new powder is pushed outward, causing the ribbed feature. Accordingly, this feature is not observed in samples with an aspect ratio of $e = 0.8$ or $e = 0.6$ because of the prevalence of the fold, which has a moving cross-sectional area through the z-axis, necessitates that material is not sintered normal to the subsequent layer.

When tested experimentally, the axially compressed honeycomb samples demonstrated various mechanical behaviours. For an aspect ratio $e = 1.0$, typical honeycomb behaviour is observed, where there is an initial linear response. Continued strain introduces stress non-linearity. Buckling occurs once the walls of the honeycomb cells are axially deformed beyond a critical yield point. The period of buckling is associated with stress softening. In contrast to metallic, polymeric, or paper honeycombs, honeycombs derived from elastomeric materials present softening for a greater period of compression. The onset of buckling reduces the stiffness of the structure; however, the deformation mechanism is characterised by bending of the cell walls rather than folding at plastic boundaries [124]. Consequently, the non-linear region of buckling is more pronounced, and the plateau region is diminished. In contrast, the introduction of an aspect ratio less than 1.0 yields atypical honeycomb behaviour, achieving a reduction in yield stress and prolongation of the non-linear buckling region. Moreover, characteristic stress softening, which is a limiting factor of traditional honeycombs, is less prominent. As the aspect ratio is decreased, the buckling mode becomes more controlled as axial crushing is guided by the introduction of the fold. The overall response

tends towards a square shape, mimicking the response seen in conventional elastomeric foams. This results in an improvement in energy absorption efficiency, where the maximum value observed was 0.45 which exceeds the values observed for other additively manufactured elastomeric honeycombs ($\eta = 0.37, R_d = 0.18$) [123], polymeric foams ($\eta = 0.40, R_d = 0.03$) [207] and rival elastomeric foams [81]. Given the versatility of absorption behaviours observed, the pre buckled honeycomb structure holds excellent potential for applications requiring tailored energy absorption profiles, such as multi-hit helmets.

Variability in the quasi-static response was identified through the examination of standard deviation and coefficient of variation. The variance observed is attributed to the prominence of slipping at the upper and lower faces, which changes the characteristic response of the structure. This is most notable with structures that have an aspect ratio of $e = 1.0$. The prevalence of slipping is due to a lateral force that develops as each cell buckles, overcoming the friction at the upper and lower face. As the aspect ratio decreases, the introduction of the fold facilitates a reduction in the lateral force and therefore preserves the true response of the honeycomb. Reduced values of standard deviation and coefficient of variation in impact testing suggest the prevalence of a lateral force overcoming friction at the impact interface is less significant. Previous authors have utilised design modifications such as a solid boss at the upper and lower face [113], constrained by adhesive tape at the platen. This restraint isolates the buckling response of the honeycomb; however, it was not achievable in this present investigation as it would trap a volume of un-sintered powder.

Finite element analysis highlighted the importance of mesh element density on the resultant mechanical behaviour of the honeycomb. Adopting a coarse mesh, where a single element represented the wall thickness, achieved artificially high stress-strain behaviour. This erroneous behaviour is otherwise known as shear locking. Linear brick elements are particularly susceptible to these phenomena in bending dominated conditions [208], where zero stress modes are characterised by inverted elements, which can result in terminated simulations. To mitigate against this, finer meshes were examined. Accordingly, meshes with two and three elements noted deviation when compared to the initial result, although reported similarity when compared to one another. Based on diminishing returns, a mesh with two elements through the wall thickness was adopted, aligning with previous

studies[124].

Full scale finite element models were developed which represented the experimental setup. Greater comparability was obtained for energy absorbed than was for yield stress. Failure to accurately predict the yield stress is associated with two features of the experimental data which the finite element failed to model. Firstly, the prevalence of fault lines throughout the mid-section of the honeycomb structure yields a taper in wall thickness, which contributed to a reduction in stress during yield. Including this taper within the model would have been infeasible due to the reduction in mesh size required to attain such a feature, necessitating greater computational cost. Secondly, a standard value for metal to rubber friction ($\mu_{global} = 1.0$ [209]) was used in the global formulation used in the Abaqus solver. This, however, may not have been wholly representative of the experimental conditions for Luvosint which may attain different frictional values due to its surface roughness [210]. Adopting a surface-to-surface tie at the upper and lower face could have proved a more suitable method as per [205] as it would have isolated the buckling mechanism, however, it may not have represented in-situ boundary conditions.

A series of periodic boundary condition models were developed to approximate the response of the full-scale models whilst alleviating the associated computational cost. Adopting symmetry enabled a reduction in elements utilised for each simulation by 75% when compared to a full-scale model. In general, the results of the periodic BC models over-approximates the response, in terms of yield stress and energy absorbed, of the honeycomb structure. The over-approximation is due to utilisation of zero deformation nodal constraints at the perimeter. As has been previously discussed, as the structure compresses and ultimately buckles, a lateral force is generated around the perimeter of the structure. Due to the presence of zero deformation nodal constraints, the structure's perimeter is restrained from this. Consequently, the reduction in stress is less prominent, thus yielding an overly stiff response. As was seen during experimental testing, the presence of a fold and decreasing aspect ratio reduces the phenomena. Nevertheless, for decreasing aspect ratio, the periodic BC model remains an over approximation of the true result. Whilst it is an over approximation of the true result, it represents an effective route to optimisation. The reduction in element count will enable a higher throughput of simulations, when compared to adopting the full-scale

model, in future optimisation studies.

The performance maps developed through the parameter sweeps enable closer inspection of the variation in energy absorption relative to the geometric design envelope. Within the context of this thesis, they are examined by establishing boundaries of acceptable behaviour as follows, based on a helmet application. Firstly, the energy absorption of the structure should be equal to, or greater than, the potential energy of the impact defined by the design standard, e.g., EN1078 = 55J (size J headform) [60]. This limits the performance maps to only consider structures which have the potential to effectively mitigate the impact load. Secondly, the stress of the structure under yield shall not exceed 2.4 MPa. This ensures that the structure's response is limited to a magnitude of stress which will not incur a skull fracture [63]. Lastly, the energy absorption efficiency shall be maximised. This ensures a square response which is most effective at impact mitigation. By applying these limits, the design envelope can be considerably reduced, enabling a more effective search of the design space.

4.5 Conclusion

This chapter presents the mechanical behaviour of a circular pre-buckled honeycomb structure through use of experimental and numerical data. Numerical data was realised through computational efficient finite element periodic boundary conditions models which are equivalent to full-scale models and experimental data. Adopting the periodic BC models in future studies will alleviate the computational cost when running iterative multi-parameter design optimisations. A list of conclusions is presented below:

1. Honeycomb samples were sensitive to manufacturing process. Inaccuracies between intended and actual design, as well as visual sintering artefacts, affect the mechanical behaviour.
2. Introduction of the pre-buckled design feature improved the mechanical behaviour of honeycombs aligning with previous results in the literature.
3. Base material rate dependence influences the mechanical behaviour of the

honeycomb for impact loading regime when compared to the quasi-static response.

4. Subject to multiple compressive loading cycles, the structure recovers and offers good potential to be used as an alternative to traditional impact mitigating materials.
5. Numerical full-scale models accurately predict the mechanical response of the honeycomb structure under quasi-static and impact compression.
6. Numerical periodic boundary condition models provide an approximation of the mechanical response of the honeycomb structure whilst alleviating computational expense.
7. Rich performance maps were developed to inform future optimisation studies by enabling indication of suitable parameter bounds relative to specified limits such as impact energy and injury thresholds.

Chapter 5

Structural Optimisation of an Additively Manufactured Elastomeric Honeycomb Structures

The contents of this chapter has recently been published as:

R. Adams et al. Finite element-based optimisation of an elastomeric honeycomb for impact mitigation in helmet liners. *International Journal of Mechanical Sciences* (2022), article number: 106920.

5.1 Introduction

Additively manufactured elastomeric honeycombs are a highly promising alternative to contemporary materials used in helmet liners. Chapter 4 investigated the energy absorbing properties of a candidate structure, the circular pre-buckled honeycomb, utilising a validated finite element model which enabled approximation of the honeycomb response in a computationally efficient manner. The optimal form of the proposed structure, however, is currently unknown due to changing expected boundary conditions such as impact velocity, mass and contact area which are subject to change due to user attributes as well as design specification. This is further exacerbated by a complex structure including several parameters, which challenges the designer to make an informed decision. Hence, there is a requirement to be able to rapidly develop new structures to see if they can satisfy the design standards, assessing various design permutations, in a time effective manner. Numerical optimisation, driven by intelligent search algorithms, represents a viable solution to parameter identification. Coupled with a computationally simplified and efficient finite element model, this approach may prove an effective pathway for helmet liner development.

This chapter aims to leverage numerical optimisation for expeditious design and development of the previously discussed additively manufactured pre-buckled circular honeycomb when subject to user specified boundary conditions, restraints and objective functions equivalent to the impact conditions of a helmet liner. Moreover, the geometric complexity of the proposed structure is such that exclusive experimental testing methods, would make this process impractical experimentally and unsustainable economically. Consequently, numerical optimisation is performed using the periodic boundary condition model developed and validated in Chapter 4.

This chapter is organised as follows. Firstly, the computational procedure is outlined establishing the user defined inputs such as loading conditions, geometric bounds, optimisation variables and objective function. Moreover, the sequence of mesh and finite element model generation, as well as results analysis, is discussed for the finite element model. Next, optimisation is undertaken. A comparison of varying objective function is performed and the associated change in honeycomb behaviour discussed. Lastly, the optimal geometries are manufactured and subject

to experimental conditions to provide a basis of validation. The culmination of this chapter is a validated approach to rapidly developing additively manufactured structures suitable for adoption in helmet liners.

5.2 Materials & Methods

5.2.1 Honeycomb Structural Bounds

The design and topology of the circular pre-buckled honeycomb has previously been described and discussed (refer to Chapter 4). The performance maps, constructed in chapter 4, can now be used to identify the optimisation design envelope. A constraint was applied to the parameter range of $e \leq 0.8$ to exclude the spurious artificial stiff response identified in Chapter 4 for straight walled honeycomb using the periodic BC model. Another constraint $E \leq 55$ J, which represents the anticipated energy of the impact, was applied to form a bounding box around the design envelope, as illustrated by figure 5.1

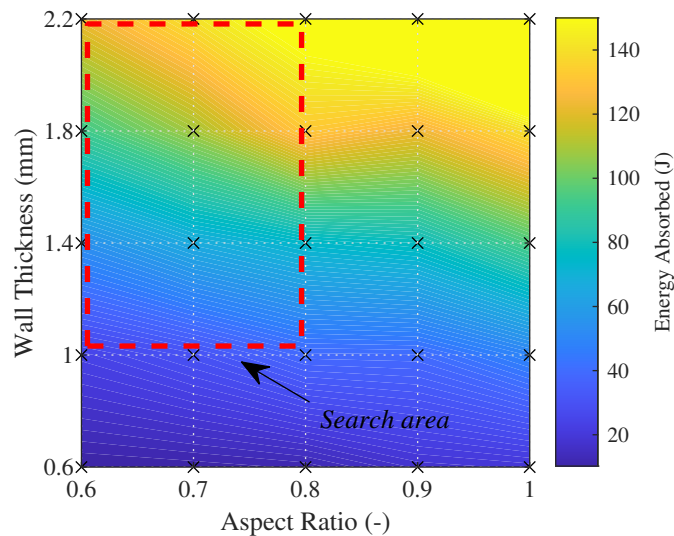


Figure 5.1: Identification of search area through examination of performance maps subject to behaviour limits.

5.2.2 Finite Element Analysis

To replicate the shock absorption test from a helmet design standard, the impact conditions from EN 1078 were used and applied to the finite element model. The material model utilised for the base material was calibrated and validated in chapter 3, whilst the periodic BC model was validated in chapter 4. The periodic BC model was used to mimic the behaviour of the full-scale model as close as possible, whilst reducing computational run time for each evaluation by 75%. The explicit dynamic solver was utilised to enable a general contact algorithm, whilst a global friction coefficient of 1.0 was used [209]. Mesh generation was carried out such that there were two elements across the wall thickness to prevent shear locking. The model comprised of deformable honeycomb cells comprising 4 cells, whose symmetry make up a single unit cell, positioned between two analytically rigid plates, as illustrated by figure 5.2.

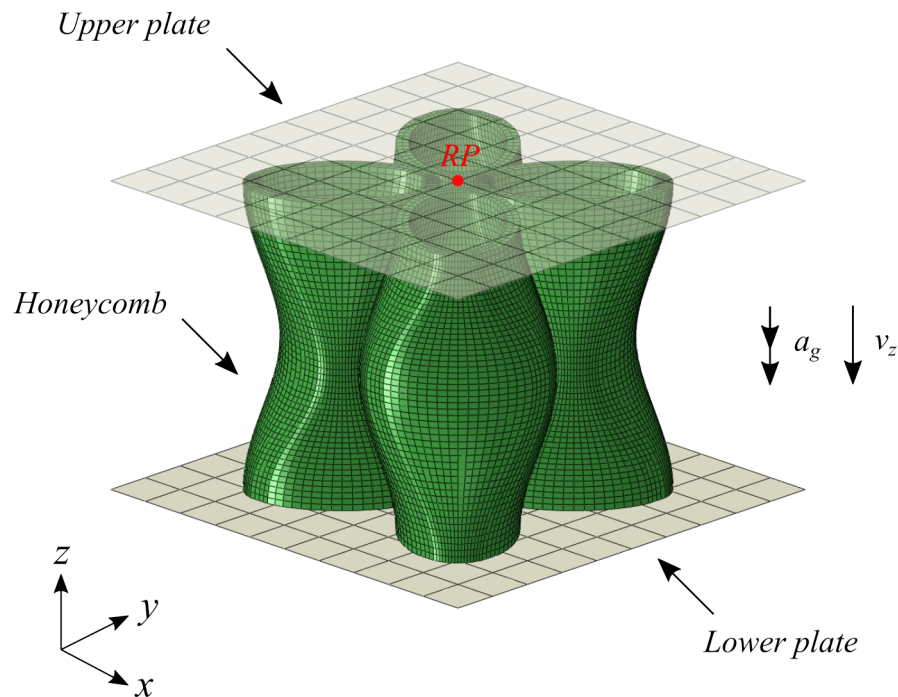


Figure 5.2: The finite element model of the pre-buckled honeycomb, comprising two unit cells positioned between an upper and lower rigid plate. The upper plate is assigned a pre-impact velocity and point mass, whilst the lower is fixed.

The lower plate was assigned an encastre boundary condition and the upper plate a point mass of 4.7 kg, equivalent to a size J headform. Pre-impact velocity of $v_z = 5.42 \text{ ms}^{-1}$ was adopted from the design standard, whilst global acceleration due to gravity, $a_g = 9.81 \text{ ms}^{-2}$ was assigned to the entire model. This represents the experimental setup, refer to section 5.2.4, enabling validation of the numerical outcome, whilst simplifying the anticipated crushing between the head and the liner under impact.

A 15 ms simulation time was used to sufficiently capture the entirety of the impact event. Reaction force, translational acceleration, and velocity, as well as displacement in the Z-axis were recorded with respect to time and extracted from the reference point located on the upper surface. This was then used to calculate the dynamic engineering stress and strain at the reference point. Engineering stress was calculated by dividing the reaction force by the projected cross-sectional area (defined by the maximum width and breadth), and strain by normalising the plate displacement by the honeycomb height. The recorded data was further treated with a low pass Butterworth filter that had a 1000 Hz cut-off frequency, a commonly used approach to treating helmet impact data [211]. Head injury criterion (HIC) was also calculated, using equation 2.2, to establish the relative severity of the resultant acceleration. Since there were no rotational kinematics induced during the impact, rotational severity metrics were not considered.

5.2.3 Optimisation

To identify the ideal honeycomb parameters for impact mitigation, numerical optimisation was performed based on a finite number of simulations using the surrogate optimisation algorithm available in Matlab's Optimisation Toolbox (MathWorks, United States) [212]. The surrogate optimisation algorithm, which is based on a radial basis function [213], was adopted over other search algorithms available in Matlab, such as genetic, particle swarm or simulated annealing due to its capability of accurately modelling arbitrary functions, handling scattered training points in multiple dimensions and requiring fewer iterations [214]. Moreover, since it is a non-gradient based solver, it is more appropriate for problems that include discontinuities due to self-contact. Lastly, it is more suited to time-consuming objective functions, such as finite element problems, as it is proven to

converge to a global optimum for bounded problems.

The surrogate optimisation algorithm occurs over multiple steps, as illustrated by figure 5.3.

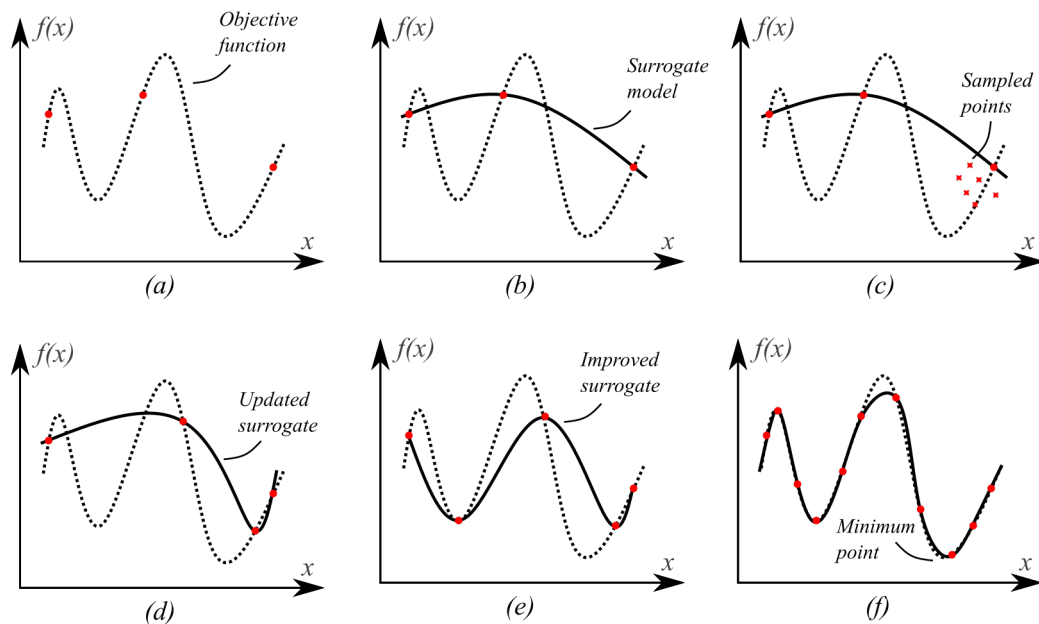


Figure 5.3: The optimisation steps for construction of the surrogate response used by the search algorithm for an increasing number of sampled finite element simulations including, (a) random sampling, (b) surrogate construction, (c) merit function analysis, (d) the best point simulated, (e) surrogate model updated and (f) final surrogate model approximation.

Initially, quasi-random points are sampled throughout the design space (a), with the objective function evaluated following each successful design point simulation. The surrogate, which approximates the relationship between each design point and the objective function, is then constructed by interpolating a cubic spline with a linear tail through the sampled points (b). Next, the algorithm searches for the minimum. New values are sampled within the design space around the incumbent value (c). A merit function is evaluated subject to the surrogate model values at these points, as well as the distance between them and the points where the objective function has already been evaluated. The best point, based on its merit function, is simulated and the objective function evaluated. The surrogate model is then updated to reflect the new information (d). This cycle repeats for a finite number of iterations, where the fidelity of the surrogate model improves

(e). Upon convergence, the surrogate model is reset, and new random samples selected to ensure the design space is fully explored. Once the maximum number of iterations is reached, the minimum point can be identified (f).

The objective function used in this optimisation was adopted from the bicycle helmet design standard too, which defines an acceptable shock absorption threshold. The standard mandates that, for a singular impact, the resultant translational acceleration shall not exceed 250g. Consequently, the objective function was defined by equation 5.1. It is assumed that the acceleration reported by the periodic boundary condition model is equivalent to the expected behaviour of the full-scale helmet liner.

$$f(x_d) = \frac{J_{calc}}{J_{crit}} \quad (5.1)$$

Where $f(x_d)$ is the objective function, x_d is the structural parameters array, J_{calc} is the calculated objective function recorded during the simulation, normalised by J_{crit} a critical threshold value. The optimisation problem is therefore defined by the number of structural parameters, the constructed surrogate model and subjected to the limits described as follows:

$$\begin{aligned} \min_{t,e} \quad & f(x_d) = \frac{J_{calc}}{J_{crit}} \\ \text{s.t.} \quad & w = 12.5 \\ & h = 25.0 \\ & 1.0 \leq t \leq 2.2 \\ & 0.6 \leq e \leq 0.8 \\ & f = 1.0 \end{aligned} \quad (5.2)$$

Where w is the unit cell width, h is the unit cell height, t is the wall thickness, e is the aspect ratio and f is the number of pre-buckled folds. The lower limit of aspect ratio was selected based on the lower bound of the performance maps, whilst the upper bound was selected to avoid the prominence of the spuriously stiff response reported in Chapter 4.

To utilise the optimisation approach, a computational procedure was developed. As illustrated by figure 5.4, Matlab, Python and Abaqus, were utilised to execute the structural optimisation.

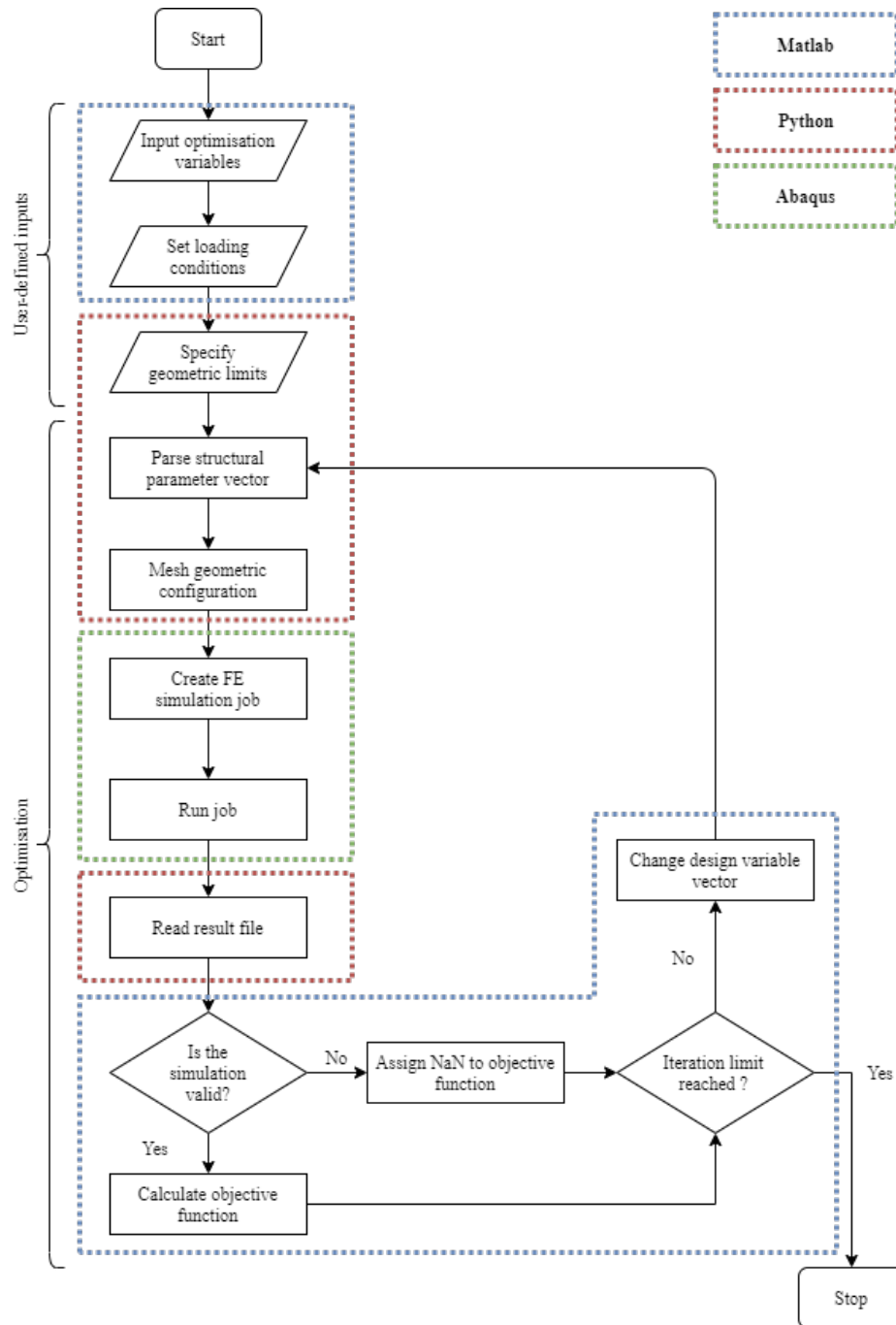


Figure 5.4: The outline of the computational procedure indicating the software used during each step of the optimisation (oval = start/end, parallelogram = input/output, rectangle = process, diamond = decision).

Initially, user-specified inputs such as maximum number of iterations, loading conditions (mass and velocity) and structural parameter limits were set. The optimisation search algorithm was then initiated using Matlab. The structural parameter vector was parsed, and a Python script was called that meshed the structure. A secondary script consisting of indigenous Abaqus macros imported the newly meshed configuration, applied boundary conditions and wrote the simulation job file.

Once the new job file was written, Matlab executed the job. Upon completion of the simulation, the result file was automatically analysed and filtered using another Python script, before being imported into Matlab which calculated the objective function. This procedure was then repeated where the structural parameter vector changes with respect to the calculated objective function. Once the user prescribed iteration limit, as described by equation 5.3, was reached, the procedure ends.

$$i_{max} = 75n_{var} \quad (5.3)$$

Where n_{var} is the number of design variables in the vector x_d . For this study there were 2 parameters, hence the iteration limit was 150.

5.2.4 Experimental Validation

In order to validate the results of the design optimisation procedure, the optimal honeycomb configurations were manufactured in a 4×4 array (equivalent to $50 \times 50\text{mm}$) from Luvosint as per the previous chapters, and subjected to impact loading.

Impact loading was performed using a spring-loaded linear impactor, the details of which are described in chapter 3. Each honeycomb was taped to the lower platen of the anvil and struck with an impactor, which had a total mass of 4.7 kg. Each sample was subjected to an initial impact velocity of 5.42 m/s, validated through use of a light gate). All specimens were compressed out-of-plane to the build orientation. Three specimens of each structural design were tested

for statistical analysis. All testing was performed in ambient conditions. Following initial impact loading, repeat impact loading was undertaken to establish performance degradation.

5.3 Results

5.3.1 Optimisation PTA as objective function

Initial optimisation was undertaken to establish the validity of the proposed method. Figure 5.5 reports the variation in the objective function, peak translational acceleration (PTA), for each evaluation relative to the acceptable 250g limit during the optimisation.

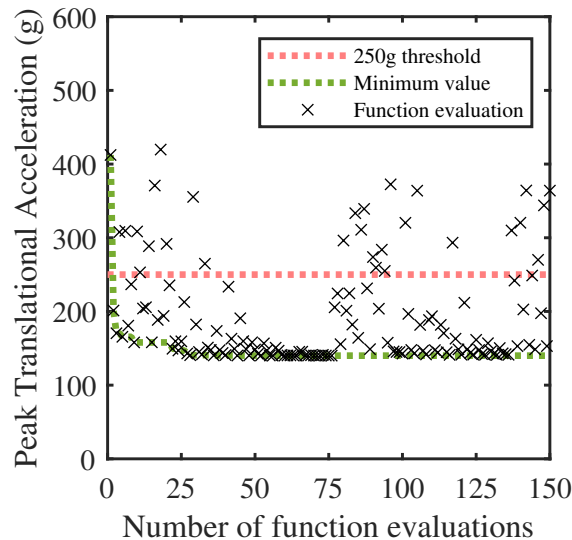


Figure 5.5: The variation in the objective function, peak translational acceleration, for each function evaluation relative to a threshold of 250g.

The optimisation procedure successfully satisfied the objective function, yielding a response less than 250 g. The first 20 evaluations are randomly sampled, yielding a variation in objective function between 419.7 g and 158.0 g. The minimum value reported in the random sample was at iteration 9. This represents a relative reduction in the objective function by 36.8%. The optimal solution was identified during the first surrogate, within the adaptive sampling phase between iterations

20 and 75. The minimum solution reported was 140 g at the 56th evaluation, representing a further reduction by 11.4% compared to the best point of the random sample. To ensure that the current best point was the global minimum, the surrogate model was reset after the 75th iteration and random sampling was undertaken to construct a new surrogate. The surrogate reset failed to achieve an improvement on the best point from the first surrogate. Similarly, a third and final reset (started at the 125th iteration) also failed to achieve an improvement, although the procedure was terminated prior to reaching adaptive sampling as the maximum number of iterations had been exceeded ($i_{max} = 150$).

Figure 5.6a - 5.6b illustrates the changing resultant acceleration and mechanical behaviour of the honeycomb during the optimisation procedure. Comparison is made to the acceptable shock absorption threshold of the design standard, as well as the failure criterion for skull fracture.

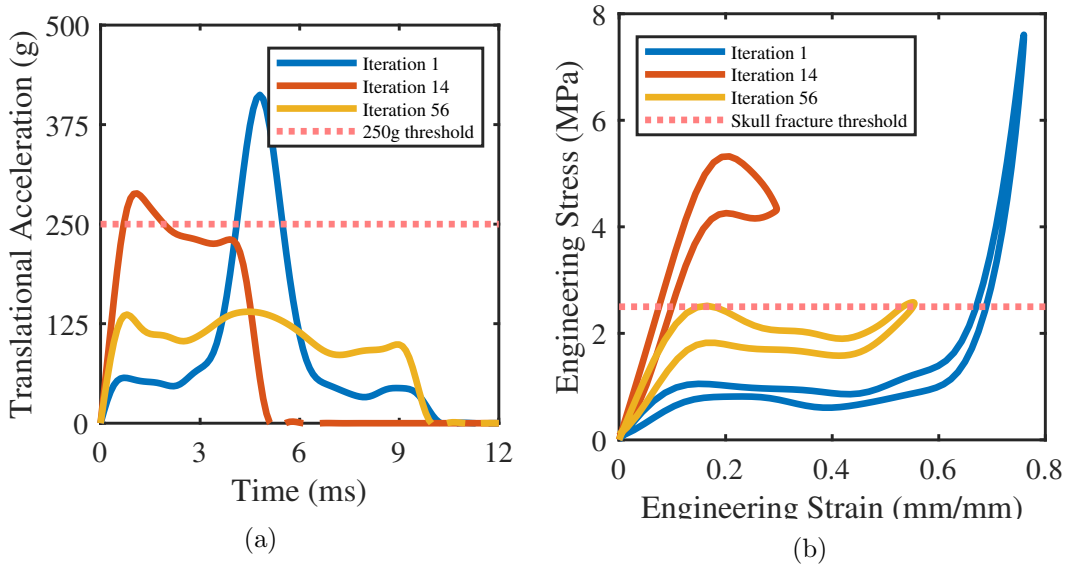


Figure 5.6: Variation in honeycomb mechanical behaviour, translational acceleration – time (a), and engineering stress – strain (b) relative to iteration number 1, 14 and 56

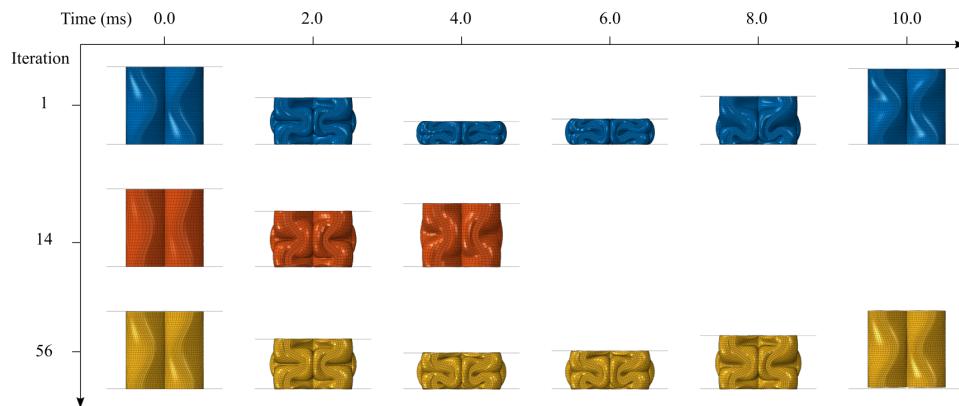


Figure 5.7: Visualised deformation with respect to time relative to iteration number 1, 14 and 56.

Iterations 1, 14 and 56, of the first surrogate model, are reported as they demonstrate two characteristic behaviours and the optimal result. Iteration 1 represents an overly compliant response. As the structure begins to deform, buckling occurs at a relatively low stress, initially resulting in a low acceleration. As the structure proceeds through the plateau region, the structure fails to sufficiently mitigate the kinetic energy of the impactor. Consequently, the structure begins to densify yielding a large and rapid increase in acceleration, exceeding the acceptable threshold, as the impact is mitigated through compression of the base material. The duration of the impact occurs over 9 ms, reaching a PTA of 412 g, and a peak stress of 7.6 MPa. Conversely, iteration 14 represents an overly stiff response. The structure deforms at a high stress, yielding a high initial acceleration, which exceeds the permissible threshold. By the time the structure buckles, entering the non-linear region before the plateau phase, the kinetic energy of the impact has been mitigated leading towards a response which is over in less than 6 ms reaching a PTA of 288 g, and a peak stress of 5.3 MPa. Iteration 56 represents the optimal solution. The response effectively mitigates the kinetic energy prior to reaching the onset of densification, without exceeding the 250 g threshold. Buckling occurs at a stress that is below the acceptable threshold; whilst structural stress-softening is observed, acceleration remains nearly constant throughout.

Figure 5.8 further examines the data recorded in the optimisation procedure. In addition to PTA, HIC was calculated at each function evaluation; the variation in PTA and HIC is reported at each function evaluation. The data features two

trends constructed in a slanted ‘V-shape’. Firstly, the left-hand side trend ranges between 140 to 412g, within which the value for HIC varies between 1129 and 3024. Conversely, for a similar PTA range, the associated right-hand HIC values range from 1129 to 5658. These two trends meet at a point of intersection located at the bottom left-hand corner. The density of function evaluations in this region, compared to the others, is indicative of the location of the identified minimum. The ‘V-shape’ formulation of data reports an interesting feature, where points of equivalent PTA have markedly different HIC.

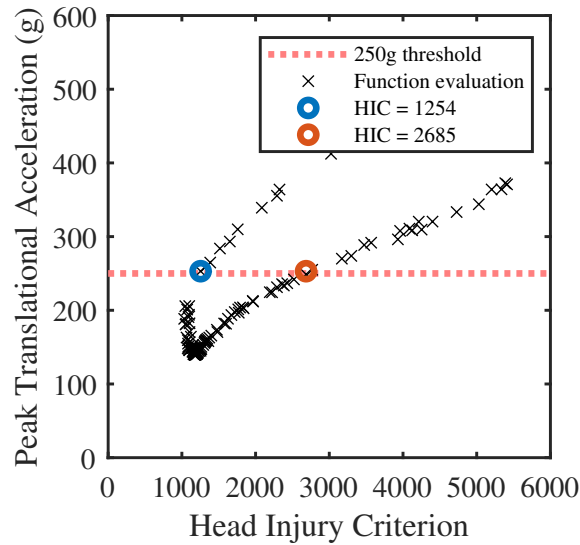


Figure 5.8: The variation in peak translational acceleration and head injury criterion at each function evaluation.

One such instance is reported in figure 5.9a and 5.9b, which compares the mechanical behaviour of these two points. Similar behaviour to that observed in figure 5.6a and 5.6b is observed, i.e., a stiff structure that mitigates the kinetic energy prior to reaching the plateau, versus a compliant structure that mitigates kinetic energy by deforming within the plateau and densification region. Interestingly, the search algorithm qualifies both results equally based on the PTA reported, however, the calculated HIC values are markedly different. Notably, the HIC value for the stiff structure is 114.1% greater than the compliant structure. Since the search algorithm examines these two responses equally, a greater number of iterations is required to attain the optimum solution. In both cases the requirement of the design standard ($PTA \leq 250$ g), and thus objective function have been satisfied; however, owing to the significance of HIC as an injury sever-

ity metric, it is prudent for further optimisation to consider HIC as the objective function.

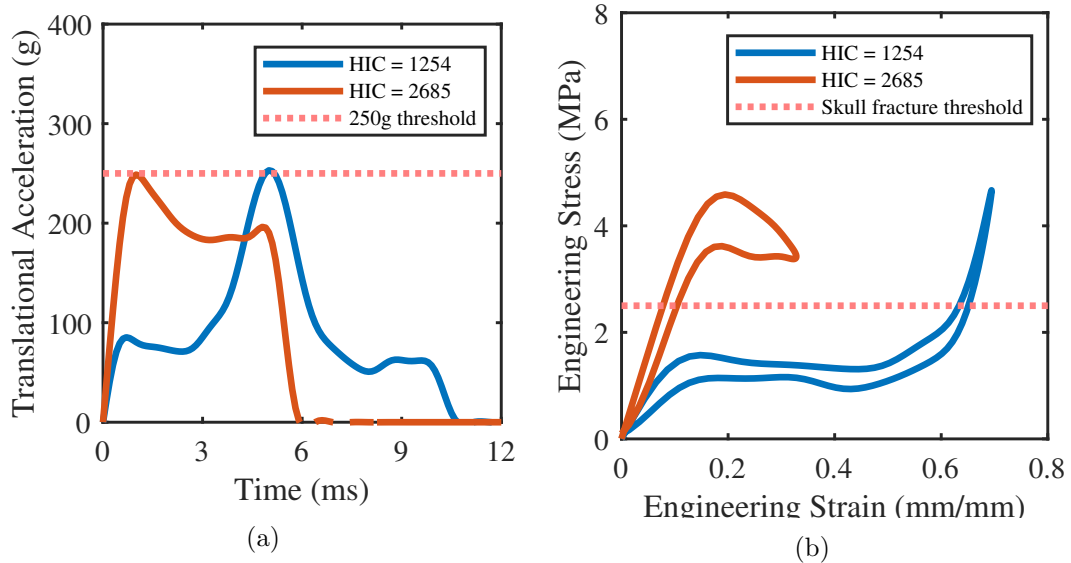


Figure 5.9: The comparison of impact response and mechanical behaviour of iteration 11 and 136.

Figure 5.10 compares the objective function, peak translational acceleration, relative to the structural parameters, wall thickness and aspect ratio.

The contour plot illustrates a band of minimum peak translational acceleration, neighbored equally either side by areas of increasing values, indicating that the results are forming a valley shape where the minima are located within the gully. The two localised clusters of function evaluations are representative of the completed adaptive sample phases. The optimal values found for each surrogate were within 1% of each other. This suggests that for the pre-buckled honeycomb structure, there is a band of optimal values for various combinations of wall thickness and aspect ratio, as indicated by the dashed lines. Within this band of near contact performance for decreasing aspect ratio, an increase in wall thickness is required to mitigate the impact. Hence, to minimise mass, the design variant with the lowest wall thickness should be selected.

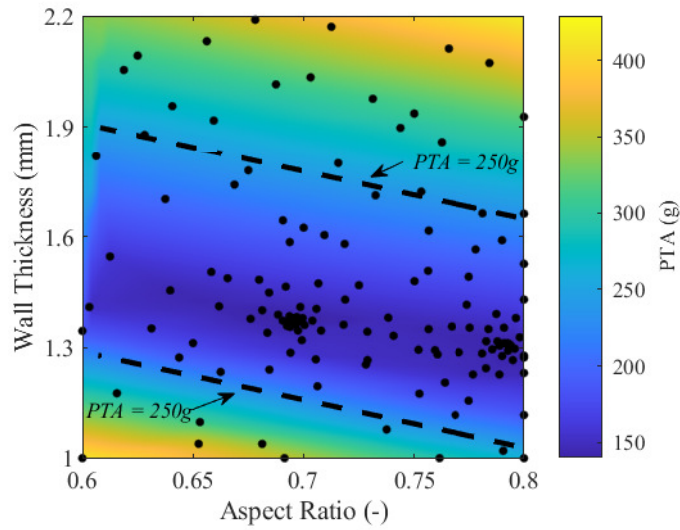


Figure 5.10: The variation in peak translational acceleration relative to wall thickness and aspect ratio when the objective function is set to PTA. Each function evaluation is indicated by a black point.

5.3.2 Optimisation HIC as objective function

To examine the influence of objective function, HIC was used in a secondary optimisation. The head injury criterion was calculated and normalised by a value of $HIC = 1574$, equivalent to an abbreviated injury score (AIS) of 4 which has been as indicative of a serious injury [215], whilst all other optimisation and structural parameters remained the same. Figure 5.11 reports the variation in objective function, HIC, for each evaluation relative to the new acceptable threshold during the optimisation. The optimisation procedure successfully satisfied the objective function, yielding a response with a HIC less than 1574. The first 20 evaluations are randomly sampled, yielding a variation in HIC between 5412 and 1050. The minimum value reported in the random sample was at iteration 7. This represents a reduction in the objective function by 33.3%. The minimum solution was identified during the adaptive solution between iterations 20 to 85. The minimum solution reported was 1029 at the 48th evaluation, representing a reduction of 2.0 % compared to the best point of the random sample. Subsequent function

evaluations do not yield an improved result. After the 90th function evaluation the surrogate model is reset and random sampling occurs again to construct the surrogate model, however, this search does not attain improvement.

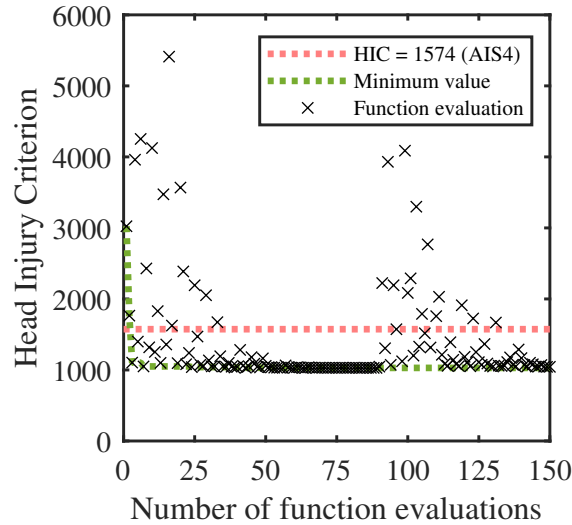


Figure 5.11: The variation in the objective function, head injury criterion, for each function evaluation relative to a threshold of 1574.

Figure 5.12 compares the objective function, HIC, relative to the structural parameters of wall thickness and aspect ratio. The contour plot illustrates a similar trend to figure 5.10.

Figure 5.13a and 5.13b compares the optimal results from the PTA and HIC optimisation, hereafter referred to as PTA_{opt} and HIC_{opt} respectively. The objective function has a notable influence on the resultant mechanical response of the honeycomb. Specifically, the PTA_{opt} favours a higher yield and plateau stress than HIC_{opt} . Conversely, HIC_{opt} favours a lower yield stress and takes advantage of densification. The reported PTA and HIC values for each optimal are reported in table 5.1

Table 5.1: Structural and performance parameters for the optimal configurations of each objective function

Objective function	Cell width, w (mm)	Wall thickness, t (mm)	Aspect ratio, e (-)	Number of folds, f (-)	PTA (g)	HIC	Relative density, R_d	Density, ρ , (kg/m^3)
PTA	12.5	1.37	0.70	1.0	140.0	1174	0.31	367.1
HIC	12.5	1.11	0.80	1.0	193.2	1029	0.25	305.7

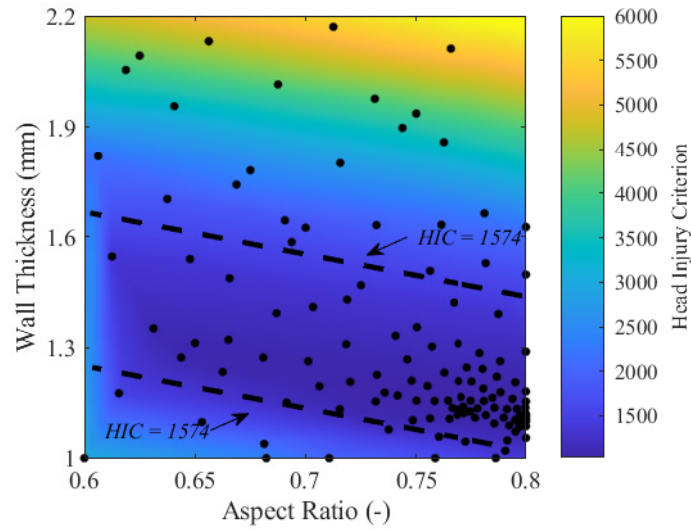


Figure 5.12: The variation in head injury criterion relative to wall thickness and aspect ratio when the objective function is set to HIC. Each function evaluation is indicated by a black point.

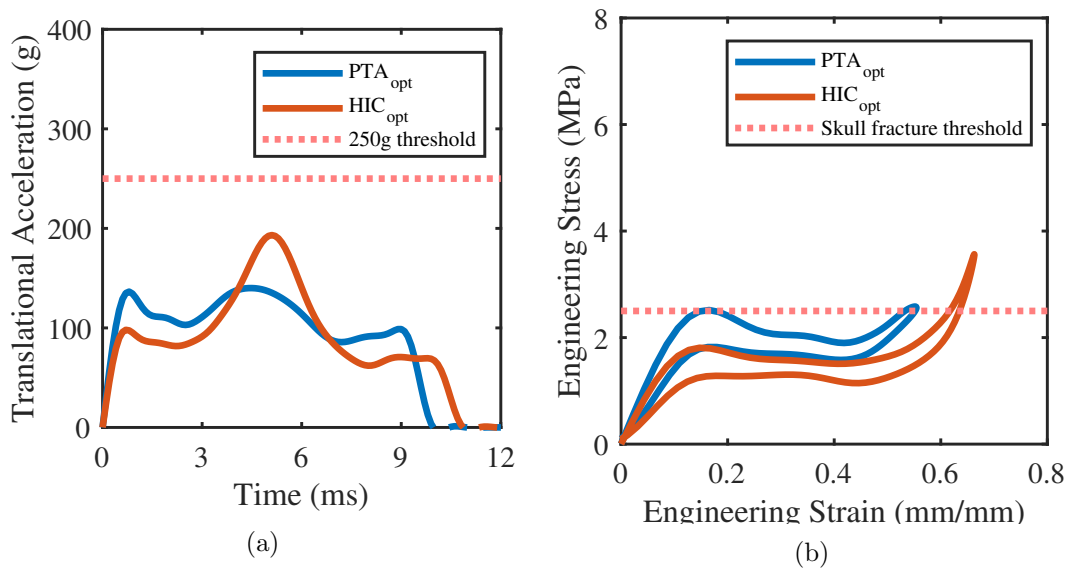


Figure 5.13: Comparison of mechanical behaviour translational acceleration – time (a) and engineering stress – strain (b) for optimal honeycombs based on an objective function of PTA and HIC.

5.3.3 Experimental Validation

This section presents the results of the experimental validation. Manufactured parts were reviewed before being subjected to experimental impact tests. The findings of this investigation will be used to validate the optimisation process. Prior to testing, individual mass and dimensions of all specimens ($N = 3$) for each variant ($N = 2$) were recorded.

Figure 5.14 identifies artefacts associated with the laser sintering process. The grid pattern highlights neighbouring cells of varying density. This is attributed to poor sintering which is a function of several factors such as localised curling (previously discussed in chapter 4) incomplete binding due to poor powder distribution or laser scanning strategy.

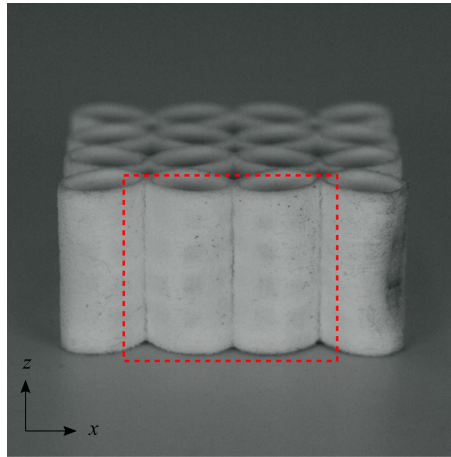


Figure 5.14: Manufactured honeycomb variant exhibiting a build defect

Table 5.2, reports individual mass, length, width, depth and average wall thickness for each sample. Through comparison to the CAD models, it was identified that both the PTA_{opt} and HIC_{opt} group's overall dimensions (e.g., length, width and depth) were accurate. Accordingly, for PTA_{opt} length, width and depth varied from the true value by +0.05 mm (0.1%), +0.06 mm (0.12%) and +0.04 mm (0.16%), whilst the HIC_{opt} varied by +0.23 mm (0.46%), +0.67 mm (1.34%) and +1.08 mm (4.32%). Moreover, wall thickness, which was identified as being susceptible to thermal distortion leading to notable deviation from the design value in chapter 4, yielded a deviation of +0.048 mm (3.50%) and -0.049 mm (-4.42%) for PTA_{opt} and HIC_{opt} respectively.

Table 5.2: Manufactured optimal honeycomb samples dimensions

Objective function	Aspect ratio, e (-)	Specimen name	Mass (g)	Width, x (mm)	Breadth, y (mm)	Depth, h (mm)	Average wall thickness, t_{avg} (mm)	Relative density, Rd	Density, ρ (kgm^{-3})
PTA	0.7	PTA-2	23.99	50.05	50.02	25.04	1.42	0.32	382.70
		PTA-3	22.28	49.97	50.06	24.04	1.41	0.31	370.50
HIC	0.8	HIC-1	14.92	49.62	49.32	26.08	1.06	0.20	233.77
		HIC-3	15.91	50.23	49.33	25.93	1.06	0.21	247.62

Impact loading was undertaken for the manufactured honeycombs to demonstrate that the optimisation process yields structures which satisfy their objective functions. Figure 5.15a and 5.15b reports the acceleration-time data for the PTA_{opt} and HIC_{opt} . The PTA_{opt} solution satisfies its objective function, yielding a PTA value ranging from 186.3 g - 232.2 g, representing a relative decrease of 7.1 % - 25.5% compared to the threshold value. Moreover, the PTA_{opt} solution also satisfies the HIC objective function yielding values ranging from 804.1 - 1274, representing a relative decrease of 19.1 % - 48.9%. The HIC_{opt} solution also satisfies its objective function, yielding a HIC value ranging from 1085 to 1519 which is a relative decrease of 3.5 and 31.1% compared to the threshold value, respectively. The HIC_{opt} solution, however, did not satisfy the PTA_{opt} threshold. The recorded PTA was 258.6 g - 316.3 g which exceeds the threshold value by 3.4% - 26.5%.

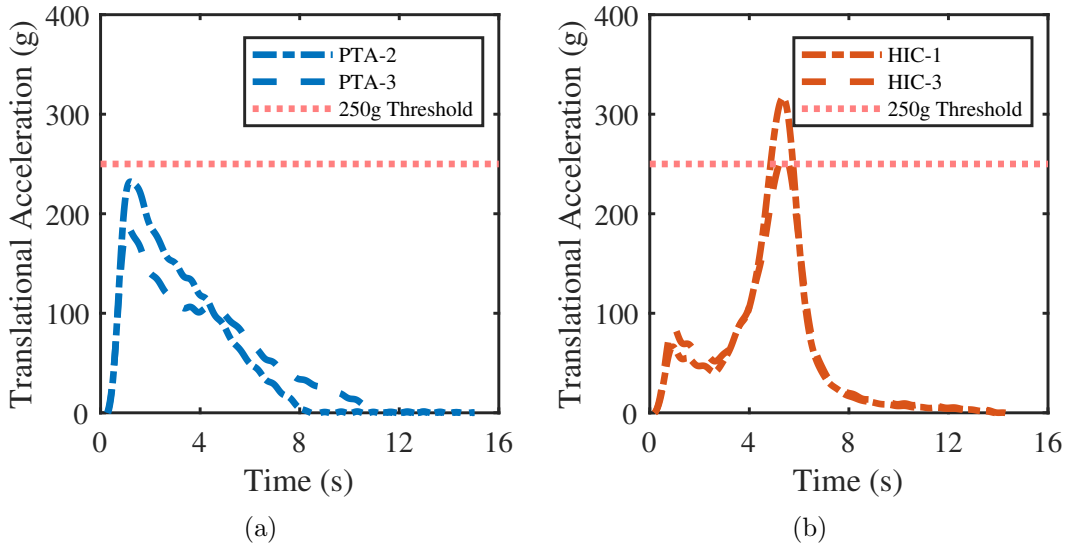


Figure 5.15: Experimental data of single impact loading for PTA (a) and HIC optimised solutions (b)

Additional simulation was undertaken for the configurations identified through the optimisation sequence and compared to the experimental dataset to provide

a basis for validation. Figure 5.16a and 5.16b reports the acceleration-time data for the simulation relative to the experimental dataset. The results of the analysis match well with the experimental dataset, whilst both simulations underreport the acceleration, for the PTA optimal simulation the percentage error for acceleration at the point of restitution is 9.6% whilst for the HIC optimal simulation the error reported was 18%.

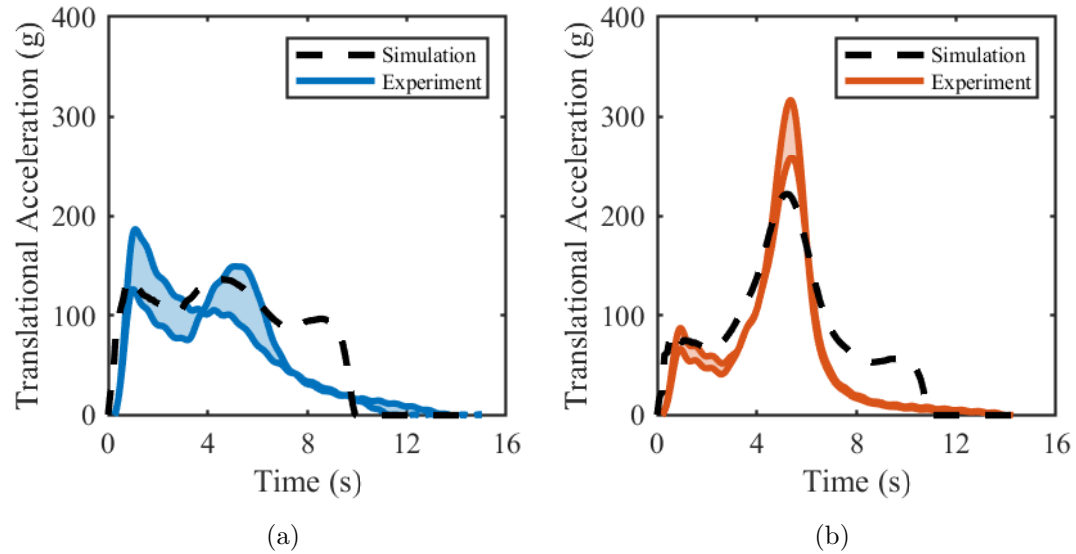


Figure 5.16: Validation simulation with comparison to experimental datasets of the optimal configurations for PTA (a) and HIC optimised solutions (b)

5.3.4 Repeat Loading Behaviour

Following the initial single impacts, each sample was subjected to 4 additional repeat impacts at 1-hour intervals to characterise the multiple loading behaviour of the optimal structures. Figure 5.17a and 5.17b reports the acceleration-time data for samples of PTA_{opt} and HIC_{opt} with respect to the first, third and fifth repeat impact. Moreover, figure 5.17c and 5.17d reports the PTA and HIC values reported with respect to the number of repeat impacts.

The PTA_{opt} solution was optimised with respect to an objective function threshold of $PTA \leq 250$ g. The previous analysis demonstrated that the PTA_{opt} solution recorded a PTA less than the threshold for a single impact. Following the second

impact, the PTA recorded was 172.3 g representing a relative reduction of 25.8 %. For an increasing number of impacts, an improvement in performance was observed. For impacts 3 – 5, a successive relative reduction of 8.5 %, 1.8 % and 2.5 % is observed. Moreover, repeat impacts 4 and 5 represent a stabilised response when compared to impacts 1 – 3 which yields less variation and a more predictable response. Comparing the performance of the final impact (number 5), the reported value is 39.6 % less than the objective function threshold $PTA = 250$ g. The PTA_{opt} results also satisfies the HIC_{opt} objective function for repeat impacts. Similar to the PTA trends, the reported HIC values decreased for increasing number of impacts. For a single impact, the reported HIC value was 1274. Following the second impact, the HIC value recorded was 945 representing a relative reduction of 25.8%. For impact 3 – 5, a successive reduction of 3.5 %, 2.0 % and 1.0 % was observed. Comparing the performance of the final impact (number 5), the reported value was 29.9% less than HIC_{opt} objective function threshold.

The HIC_{opt} solution was optimised with respect to an objective function of $HIC \leq 1574$. The analysis of the single impact behaviour demonstrated that the HIC_{opt} solution recorded a HIC less than the critical value for a single impact. Following the second impact, the HIC recorded was 2723 representing a relative increase of 150.1%. For an increasing number of impacts, a common trend of deteriorating performance is observed. For impacts 3-5, a successive increase of 32.6%, 12.1% and 8.9 is reported. Comparing the performance of the final impact (number 5), the reported value is 306.0% greater than the critical value. As previously discussed in the analysis of single impact behaviour, the HIC_{opt} solution does not satisfy the PTA_{opt} objective function. For the first repeat impact, the PTA recorded was 446.2 g representing an increase of 72.5%. For an increasing number of impacts, a common trend of deteriorating performance is observed. For impacts 3 – 5, a successive increase of 19.8%, 7.3% and 5.2% of PTA is reported. Comparing the performance of final impact (number 5), the reported value is 141.3% greater than the critical value.

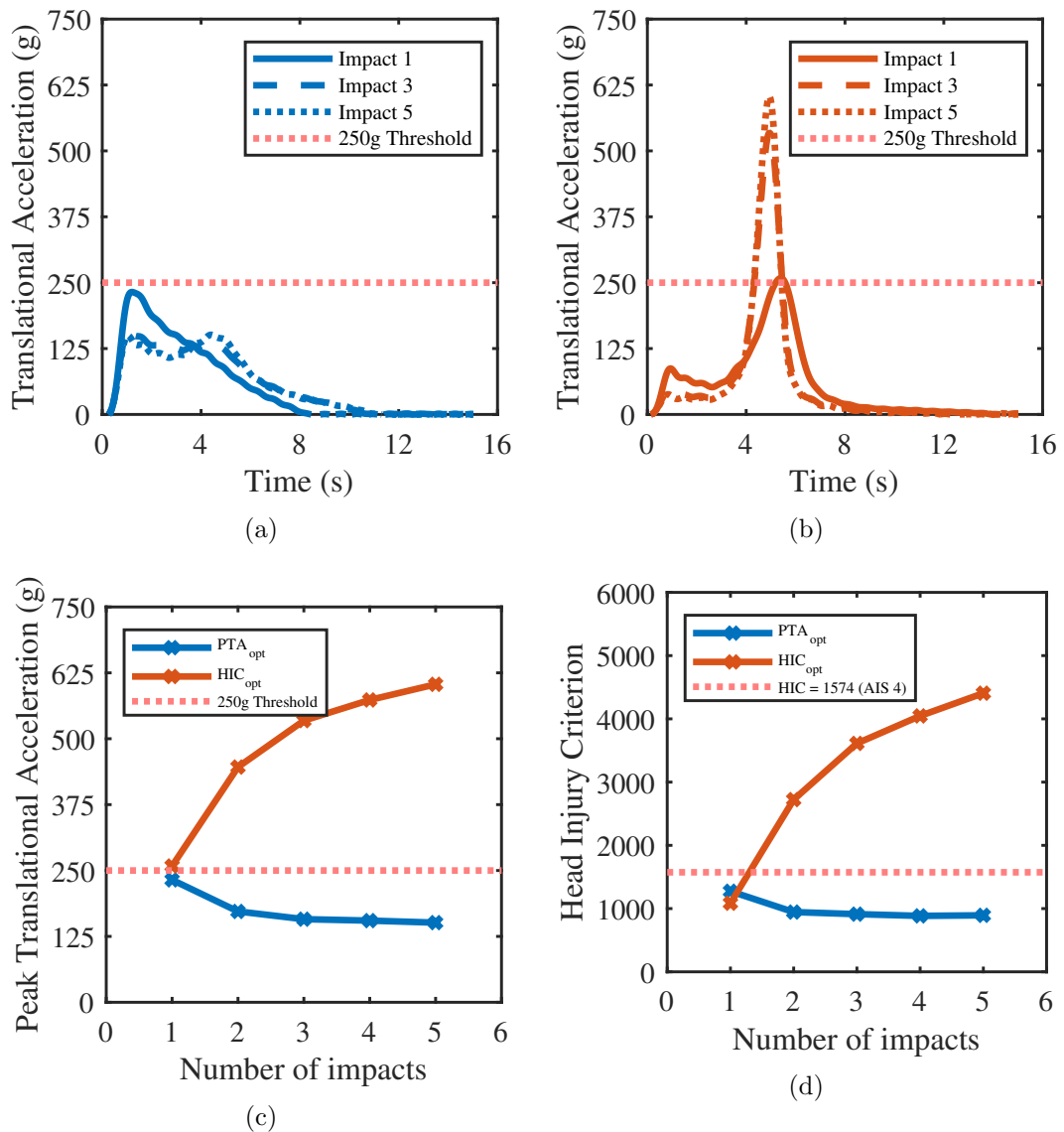


Figure 5.17: Experimental comparison of repeat impact loading behaviour for PTA (a) and HIC optimised solutions (b), as well as a comparison when considering the values of PTA (c) and HIC (d) recorded for all experiments.

5.4 Discussion

In this study, a numerical route to optimising parametrically defined cellular structures when subjected to impact conditions and differing objective functions associated with helmet performance was established and investigated.

Finite element simulations were employed to obtain the resultant acceleration of

the parametrised pre-buckled honeycomb structure when subject to impact loading. The surrogate optimisation algorithm from the MATLAB toolbox was used to analyse the results of FE simulation response relative to the design space. It was shown that the pre-buckled circular honeycomb design can minimise PTA and therefore satisfy the requirements of the design standard, but this was achieved at the expense of the HIC value. Varying the objective function from PTA to HIC resulted in notable differences in honeycomb response. The PTA optimal favoured a high yield and plateau stress, ensuring that the impact energy had been mitigated prior to entering densification, avoiding the characteristic large and rapid increase in acceleration. This is known as a force limiting approach [59]. In contrast, the HIC optimal favoured a lower yield and plateau stress, resulting in densification of the structure. Since the structure yields at a lower comparative stress, the resultant acceleration is reduced in comparison to the PTA optimal. Once the structure densifies, however, the resultant acceleration exceeds that of the PTA optimal. This reduces the time of exposure to injurious levels of acceleration.

Appropriate selection of the objective function effects the optimisation procedure and results. This is particularly important when optimising structures which can have large variation in response due to small changes in geometric parameter value. A notable benefit of HIC versus PTA as an objective function was demonstrated in this study. In particular, honeycomb behaviour was reported which the optimiser ranked as equal due to equivalent PTA values, although their HIC values were notably different. Since PTA fails to consider the time of exposure, the optimiser stalls, requiring a greater number of function evaluations to come to an optimal solution. The use of either PTA or HIC as a metric for head injury in isolation is generally contested, rather, it is favourable to use a combination [107]. When rotational kinematics are developed, these should be considered too. This, however, is challenging for optimisation investigations as it is unclear how they should be ranked or weighted. Within the design standards, PTA has historically been used [60]. In comparison, HIC is used scantily, featuring only in motorcycle design standards [215]. Importantly, the prevalence of HIC as an injury criterion should not be dismissed and its inclusion in the design standards should be considered as it will aid in the selection of new helmet designs rather than using PTA. The resistance to HIC in the design standards may be due to a

lack of consensus on an acceptable threshold.

Experimental testing aimed to validate the numerically identified optimal configurations. Both structures, when tested experimentally, satisfied their respective objective function, however, the reported results did not match the numerical analysis. The HIC_{opt} configuration adopts a low yield stress, which results in a reduced translational acceleration for a large proportion of the impact. It, however, takes advantage of the densification region to mitigate residual impact force for short periods at high acceleration. Consequently, there is a small operational window with which this structure works optimally. Variance in performance is therefore anticipated, subject to variation in structural parameters. In this case, variation in wall thickness, as reported by table 5.2, led to an overly compliant structure, meaning the structure was unable to sufficiently mitigate the impact. The negative performance was compounded over successive impacts, yielding a larger spike in acceleration as an increasing proportion of kinetic energy was mitigated within the densification region. Conversely, the wall thickness for the PTA_{opt} configuration exceeded the design value. Over successive impacts, the performance, however, improved. In both cases, repeat impact loading causes the base material to transition into its relaxed state due to cyclic stress softening, known as the Mullins effect [191]. In the polymer's relaxed state, the resultant stress is lower for the same strain compared to the initial response. Considering the experimental PTA_{opt} results, the initial response was overly stiff, deforming at high stress and did not densify. The consequence of this was a larger resultant acceleration than that anticipated in the computational result. During the subsequent impacts, the structure deformed at lower stress due to the relaxation of the base material. The structure then proceeded to deform at a lower stress, yielding a reduced resultant acceleration whilst deforming further as characterised by nearly reaching densification. These results align with previous studies and indicates that there is opportunity for helmets to be pre-stressed (cycled / conditioned) to achieve repeatable, consistent behaviour [173]. This structure would be more long living than polymeric foams such as EPS, which tend to either plastically deform or demonstrate permanent set. Consequently, this could benefit the user by reducing the risk of unknowingly wearing a helmet that is already damaged, from an innocuous drop or following an impact.

The present approach to defining and meshing geometries for finite element anal-

ysis leveraged an in-house python code. This enabled novel structures to be explored, such as the pre-buckled honeycomb, within the numerical optimisation finite element procedure. Whilst there are commercially focused software packages, such as nTopology [216], which enable topology optimisation as well as volume filling of cellular structures, this does not have the capability to import custom structures. Moreover, the indigenous finite element solver is limited, offering only static analysis with linear rate-insensitive material models and is incapable of contact analysis. Consequently, this means it is infeasible to adopt the approach for use within the present study. Numerical optimisation was carried out using Matlab's optimisation toolbox. This enabled access to a large array of optimization methods such as the radial basis function algorithm which has been previously used in the design, optimisation, and analysis of safety structures subject to dynamic loading and design standard objective thresholds [217]. Other commercially focused programmes do exist, such as Abaqus' integrated module and iSight [129]. However, they were not adopted for use in this investigation. Whilst they are designed to be generally easy to use and robust, they do not contain a wide range of analysis options to handle real-world problems. Moreover, they are constrained to default settings and do not allow for user modification.

Whilst the optimised configurations satisfied the design standard performance threshold, the sample densities exceeded that of typical elastomeric foams used in helmet liners, 0.011 kg (183 kg/m^3 [81]) by 0.008 kg (305.7 kg/m^3). The sample dimensions, however, used to inform the optimisation may not be representative of the true helmet contact area, and therefore it is likely these structures are overly stiff for the intended loading conditions. For example, the finite element model used in this study consisted of a 2×2 array with a cell width of 12.5 mm , representing a 4×4 array with a total contact area of $50 \times 50 \text{ mm}$ equivalent to 2500 mm^2 . Contact area, however, is likely to change on a user-by-user basis as a function of head and helmet radii [218]. Previous investigations adopted a similar contact area values when investigating impact mitigation materials for helmet applications [178] although there seems to be little justification for this design choice. Moreover, other examples exist where a value as high as 6400 mm^2 has been used for similar impact conditions [219]. Increasing contact area for the same resistive force will yield a reduction in local stress exposed to the user. Therefore, selecting an appropriate contact area is paramount for future

investigations. Analytical expression exists for the anticipated contact area based on helmet and head radius, and liner crush [220]. Considering general values for a size J headform (equivalent to 50th percentile human head), and a nominal liner crush of 0.5 mm/mm for a 25 mm liner, the contact area is in fact 10,000 mm². This exceeds the value used in this study, as well as previous studies, suggesting that an additional performance gain and reduction in sample mass can be achieved through greater consideration of the anticipated contact area.

The performance of the optimised honeycomb was tested in isolation to reduce the computational expense of a full-scale helmet model. In its assembled form, the helmet would consist of other components, such as the shell. Therefore, the model does not account for the contribution of impact mitigation that the polymeric shell provides either through viscoelastic, or hysteresis loading, or cracking and delamination of a composite. Consequently, the optimal solution may be overly stiff, as it is required to mitigate the entirety of the impact load without contributions of other components. Additionally, flat compression of a planar honeycomb was adopted to represent the loading conditions of the linear impact. From an experimental perspective, cellular structures are generally created in planar shapes to enable ease of design and test. In the helmet design application, this is not truly representative of the in-situ boundary conditions, as the head and helmet conform to a doubly convex surface and therefore the contact area changes as the helmet liner is compressed. Consequently, there may be unaccounted deviation between intended design and actual mechanical response. The honeycomb is optimised for flat conditions, as such it must be analysed in a full helmet configuration to examine the influence of this investigative choice.

5.5 Conclusion

This chapter presents a numerical optimisation procedure utilising the finite element model presented in Chapter 4, however, can be applied to any parameterised model. The procedure culminates in an optimal configuration of the honeycomb structure when subjected to user specified boundary conditions, constraints and objective functions equivalent to helmet impact conditions. Adopting this approach proves an efficient route to rapidly generating helmet liners using novel

structures. A list of conclusions is presented below:

1. An effective framework is reported for optimisation of parametrised cellular structures, subjected to boundary and performance thresholds of a helmet design standard.
2. Informed selection of geometric bounds aided effective and efficient identification of optimal configuration.
3. Numerical optimisation revealed the influence of objective function on the impact behaviour for this class of additively manufactured elastomeric honeycomb.
4. For the limits prescribed in the analysis, optimising for peak translational acceleration resulted in a structure that mitigates the kinetic energy of the impact at a stress, which facilitates avoidance of the densification region.
5. In contrast, optimising for head injury criterion results in a structure which yields at a relatively lower yield stress and resultant acceleration, however, densifies thus resulting in a higher peak translational acceleration but for a small duration.
6. Fabrication and experimental testing of the samples provided further insights regarding the impact performance. Both structures satisfied their respective objective function when subjected to experimental testing, therefore providing validity for the numerical procedure and its adoption in future studies.
7. Over repeat impacts, PTA optimised structures reported improved performance and stabilised after the third impact. performance was observed over multiple impacts, stabilizing after the third impact.
8. In contrast, HIC optimised structures reported degrading performance over successive impacts.

Chapter 6

Traumatic Brain Injury Assessment of the Optimised Honeycomb Helmet Liner

6.1 Introduction

Numerical optimisation is a useful and effective tool for identifying designs that can achieve or exceed performance criteria such as those specified in design standards. Chapter 5 described a framework for numerical optimisation, coupled with a finite element model, for rapid optimisation of an exemplar honeycomb structure under impact loading. This approach could be advantageous for developing new helmet liners that are comprised of honeycombs, as well as other parametrically defined cellular structures. Currently, however, this approach optimises for a flat-on-flat impact, and it is unclear whether this approach is equivalent or provides a good indication, of the optimal configuration of a full-scale helmet. Moreover, when designing helmet liners, a single best configuration, or one size fits all approach, is inappropriate since changes in user boundary conditions (e.g., mass and contact area) necessitates different liner mechanical responses to mitigate the impact effectively. This is exemplified in the construction of foam helmet liners, which utilises various densities to achieve impact mitigation throughout size bands. Therefore, the helmet design envelope, e.g., anticipated contact area, should be considered within the current optimisation framework.

This chapter aims to optimise the additively manufactured conformal pre-buckled circular honeycomb for the helmet design envelope by consideration of design standard objectives and the anticipated contact area between the liner and the head. Furthermore, the chapter aims to assess the efficacy of the optimised honeycomb under helmet impact conditions whilst also quantifying the traumatic brain injury mitigation effects compared to a contemporary impact mitigating material.

This chapter is organised as follows. Firstly, the anticipated impact contact area based on headform and liner geometry was calculated. This variable was then introduced into the optimisation procedure. Next, optimisation was undertaken utilising the approach defined in chapter 5 subject to the design standard requirements EN1078. Once the ideal geometry was identified, a helmeted headform model was constructed, where the optimised honeycomb structure was propagated through the volume encompassed by the liner. The full-scale honeycomb helmet model was then subject to two load cases defined as direct and oblique, representative of typical lab-based helmet tests. Lastly, a finite element model of the human head was loaded with the resultant acceleration-time pulses from the

previous full helmet simulations to predict brain response during the impact and assess the resultant severity in terms of tissue-based severity metrics.

6.2 Material & Methods

6.2.1 Helmet Contact Area Approximation

As illustrated by figure 6.1, to identify the anticipated load bearing contact area during an impact between the head, helmet and anvil, equation 6.1 was used. This equation, relates the head and helmet dimensions to identify the circular contact area, assuming that the amount of liner crush is much less than the radius of curvature. For simplification, the helmet was approximated to an ellipsoid shape.

$$A_c = 2\pi Rx \tag{6.1}$$

Where R is the radius of curvature and x is the maximum liner crush (assumed to be 0.5 mm/mm based on the results of Chapter 4).

The helmet model utilised in this thesis (refer to figure 6.2) is approximated to an ellipsoid shape. Consequently, it is defined by three radii, r_x , r_y and r_z . The contact area was calculated using equation 6.1 and the value of r_x as this was the axis coincident with the axis of the impact, yielding a contact area of 9032 mm² for a liner crush of 15 mm. Considering the anticipated contact area is circular in shape, the diameter is 107 mm. The propagation of the honeycomb, however, is achieved along principal axis X, Y and Z, yielding a square configuration. Therefore, the contact width based on an equivalent square ($A_{c,square}$) area was calculated to be 95 mm. Alternative strategies were also identified, including a square area which can be circumscribed within the circular area and a square area which has a width equivalent to the diameter of the circular area. Both of these strategies, however, were not implemented as they would under-approximate and over-approximate the anticipated contact area respectively.

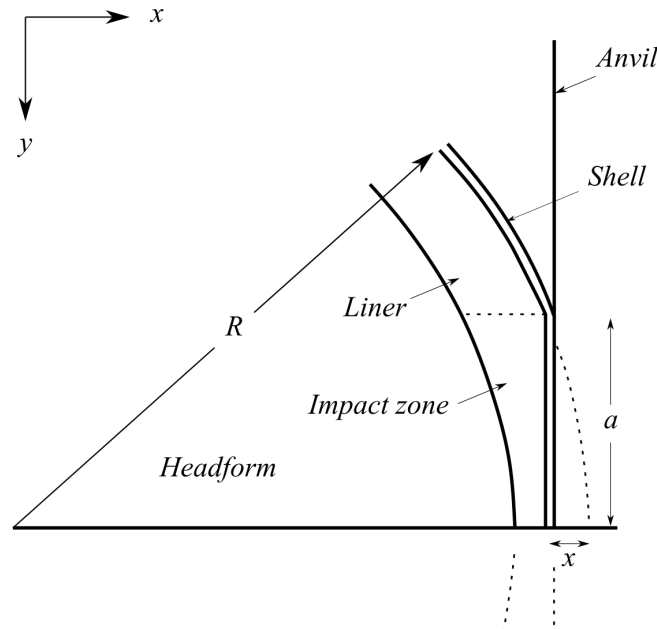


Figure 6.1: Side helmet cross-section to illustrate and approximate contact area geometry and with a flat surface, reconstructed from [220]

6.2.2 Optimisation

To identify the optimal configuration of the honeycomb structure, the structural optimisation methodology, reported in chapter 5 was utilised. Similar to before, boundary conditions representative of the helmet design standard, EN1078, were adopted. Wall thickness (t) and aspect ratio ($e = r_1/r_2$) were set as parameters. The cell width parameter was set to $w = 20.0$ mm, which was half the average size of the guide mesh of the honeycomb helmet liner, refer to figure 6.4. A mass scale factor of 0.18 ($m_f = 40^2/95^2$) was used, which was calculated by normalising the honeycomb contact area with the contact area calculated by equation 6.1 converted to a square area, as described by equation 6.2.

$$m_f = \frac{(2w)^2}{A_{c,square}} \quad (6.2)$$

The optimisation was run twice. Previous investigations identified for a problem with 2 parameters, the random sampling and iteration limit can be reduced. Hence, random samples were set to 25 and the maximum iteration limit (i_{max}) was to 75. The objective function, $f(x_d)$, was set to peak translational acceleration and secondarily as head injury criterion. The limits for the wall thickness were defined as a function of the cell width, where the minimum value yielded a honeycomb with a density of 125 kg/m^3 equivalent to the least dense contemporary foam used in the comparison, whilst the maximum limit yielded a density of 300 kg/m^3 , to ensure an acceptable density limit [221]. The optimisation problem was therefore defined as:

$$\begin{aligned}
 \min_{t,e} \quad & f(x_d) = \frac{J_{calc}}{J_{crit}} \\
 \text{s.t.} \quad & w = 20.0 \\
 & h = 25.0 \\
 & 0.033w \leq t \leq 0.072w \\
 & 0.4 \leq e \leq 0.8 \\
 & f = 1.0 \\
 & m_f = 0.18 \\
 & i_{max} = 75
 \end{aligned} \tag{6.3}$$

6.2.3 Helmet Finite Element Model

To validate the predictive capacity of the optimisation, it was compared to a full scale finite element model. Furthermore, comparison was undertaken to an established multi-hit material, Vinyl Nitrile, to identify whether a performance benefit can be achieved.

Finite element analysis was undertaken using Abaqus explicit solver to generate a helmeted headform impact. As illustrated by figure 6.2, the model comprised several components including: a headform, anvil and helmet (which further comprised of a shell and liner). A BS EN 960 headform (size J) was adopted and utilised for this investigation. The headform was approximated as a surface and considered analytically rigid, as the headform material is several orders of mag-

nitude stiffer than the helmet and therefore does not contribute to impact mitigation. The surface was meshed using a 3-node shell surface element with tetrahedral shape type. A point mass of 4.7 kg was applied and moments of inertia $I_{xx} = 161 \text{ kgcm}^2$, $I_{yy} = 221 \text{ kgcm}^2$, and $I_{zz} = 179 \text{ kgcm}^2$ were applied to its centre of mass. It is important to note that the moments of inertia of the EN960 headform were not used, because they are considered non biofidelic [88]. As such, the Hybrid headform moments of inertia were applied instead.

The helmet shell was approximated to have the shape of a half ellipsoid with principal radii, $r_x = 135.0 \text{ mm}$, $r_y = 120.0 \text{ mm}$ and $r_z = 125.0 \text{ mm}$. The thickness of the shell was set to $t_s = 1.0 \text{ mm}$ equivalent to previous cycling helmet studies [222]. The shell was modelled using linear brick elements with reduced integration and hourglass control options. Two elements were meshed through the thickness to mitigate against shear locking. Elements were assigned a linear elastic material model with a Young's modulus of $E = 7250.0 \text{ MPa}$, Poisson ratio $\nu = 0.3$ and density $\rho = 1200 \text{ kgm}^{-3}$, equivalent to the material properties of polycarbonate [222]. The shell-anvil surface interaction varied between the impact conditions. For direct and oblique impact conditions, the coefficient friction value of 0.2 and 0.5 [223] was used respectively. To simulate the headform helmet interface, a coefficient friction value of 0.16 was used [50].

The retention strap was modelled as an elastic axial connector element which connects a reference node on the head from the chin surface to four points on the helmet. The axial load in the connector element corresponded to tensile behaviour of the retention strap, which produced a primary linear elastic behaviour based on data from the literature [175]. This modelling methodology was deemed appropriate based on other helmet studies adopting a similar approach, enabling a simplification which reduced computational expense [187]

The helmet liner was approximated to have the shape of a half ellipsoid with principal radii, $r_x = 110.0 \text{ mm}$, $r_y = 95.0 \text{ mm}$ and $r_z = 100.0 \text{ mm}$ and a thickness of 25.0 mm [82]. The liner was modelled using linear brick elements with reduced integration and hourglass control options. At least 10 elements were meshed, as per other studies [175] through the thickness to prevent shear locking.

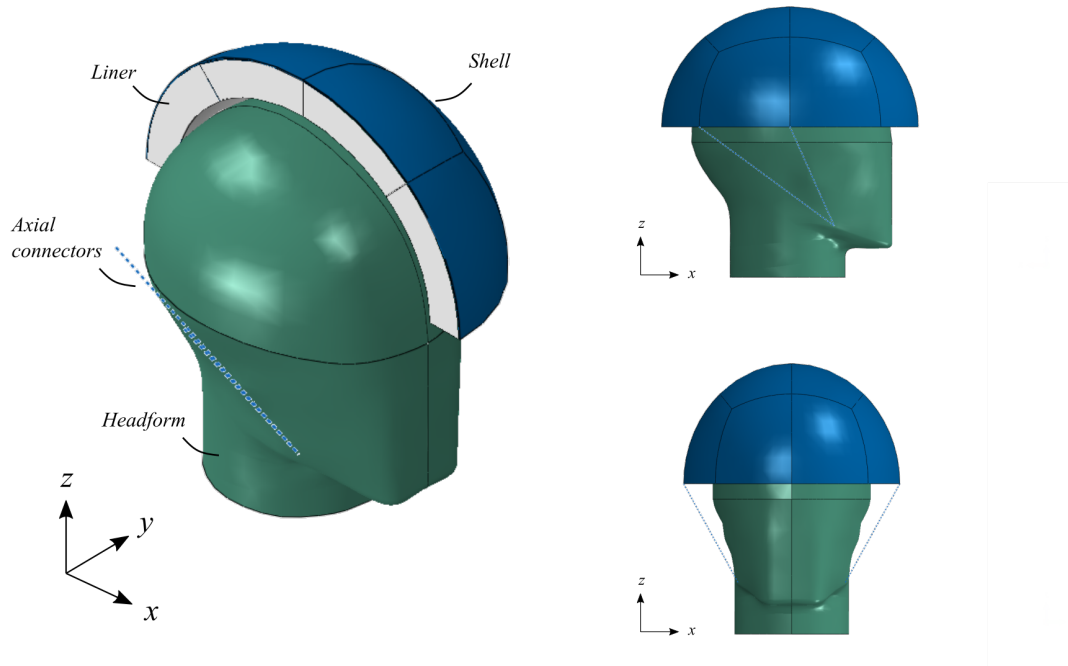


Figure 6.2: Construction of the finite element model including liner, shell, headform and retention strap (modelled as an axial connector).

For the elastomeric foam liner, mechanical behaviour of Vinyl Nitrile obtained from the literature was used to calibrate the material model [81]. Using equation 6.4 and the coefficients reported in table 6.1, the mechanical behaviour can be established at discrete strain rates equivalent to the test impact velocity.

The contemporary foam liner elements were modelled as a hyperelastic material, using the Hyperfoam model available in the Abaqus material library. This model has been previously used for modelling elastomeric foams that present hyperelastic behaviour. It is intended for finite-strain applications, where it can deform elastically up to 80% strain. A 3 term ($N = 3$) polynomial was used with Poisson ratio set to 0. Figure 6.3, illustrates the calibrated material model relative to the data, calculated using equation 6.4.

$$\sigma = P_1 + P_2\tau + P_3\varepsilon + P_4\varepsilon\tau + P_5\varepsilon^2 + P_6\tau\varepsilon^2 + P_7\varepsilon^3 + P_8\tau\varepsilon^3 + P_9\varepsilon^4 + P_{10}\tau\varepsilon^4 + P_{11}\varepsilon^5 \quad (6.4)$$

Where σ is the engineering stress (MPa), ε is the engineering strain (mm/mm), τ is the strain rate (/s) and $P_1 - P_{11}$ are the coefficients of the equation for the strain rate dependant behaviour.

Table 6.1: Equation 6.4 coefficients for vinyl nitrile foam with densities 125 kg/m³ and 183 kg/m³ used as comparison to the state of the art.

Density, ρ (kg/m ³)	Coefficients										
	P_1	P_2	P_3	P_4	P_5	P_6	P_7	P_8	P_9	P_{10}	P_{11}
125	-0.00778	-8.5E-05	17.21608	-0.00916	-115.953	0.100709	326.1629	-0.24255	-410.552	0.173589	193.9375
183	0.020099	-0.0002	23.80014	-0.01559	-163.719	0.236052	475.953	-0.6654	-616.255	0.549516	300.7181

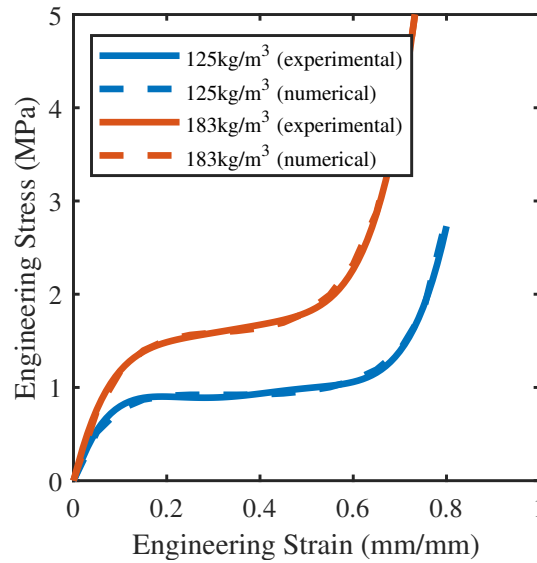


Figure 6.3: Comparison of calibrated material model to experimental data for foam with density of 125 kg/m³ and 183 kg/m³

For the conformal honeycomb liner, the optimised structure was generated using an in-house mapped meshing system, as illustrated by figure 6.4. In this example, a curved section of helmet was isolated and used as the guide mesh. The guide mesh informs the position, orientation and scale of each unit cell. The generated mesh was imported into Abaqus resulting in a curved section of honeycomb liner with the structural parameters identified through the previously discussed optimisation process.

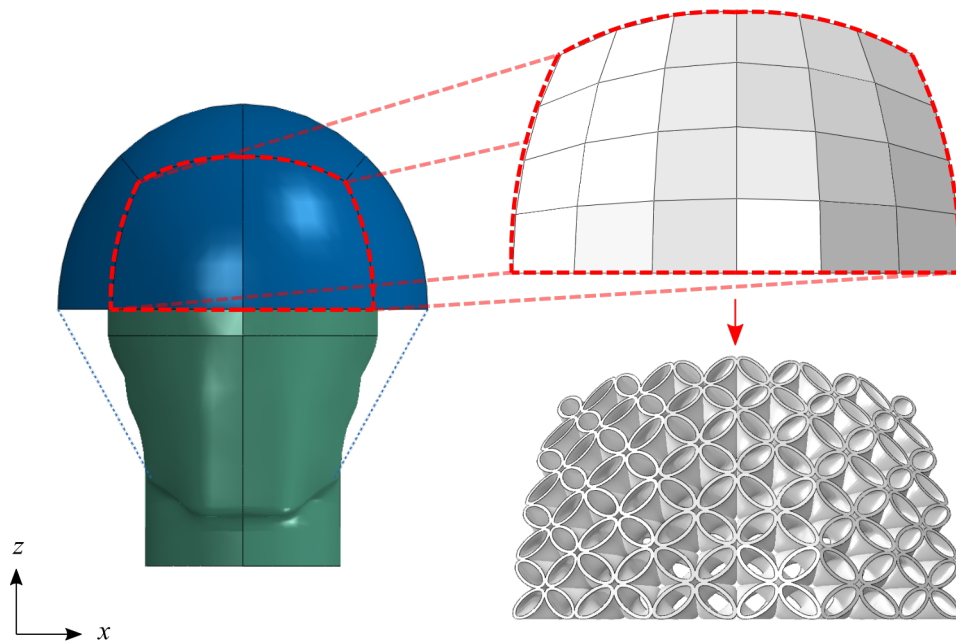


Figure 6.4: Mapped meshing of honeycomb unit cells into hexahedral guide mesh.

6.2.4 Impact Conditions

The helmeted headform was subject to direct and oblique impact loading. The following section describes the details of these impact conditions. As illustrated by figure 6.5, direct impact testing onto a flat anvil was undertaken in accordance with shock absorption test method of EN 1087. The helmeted headform was given an initial velocity of 5.42 m/s. Simulations were performed for 15 ms and the components of translational acceleration were recorded from the headform centre of gravity. Additionally, oblique impact testing onto a 45° inclined flat anvil was undertaken in accordance with typical lab-based testing [83]. The helmeted headform was given an initial velocity of 6.3 m/s. Simulations were performed for 15 ms and components of translational and rotational acceleration were recorded from the headform centre of gravity.

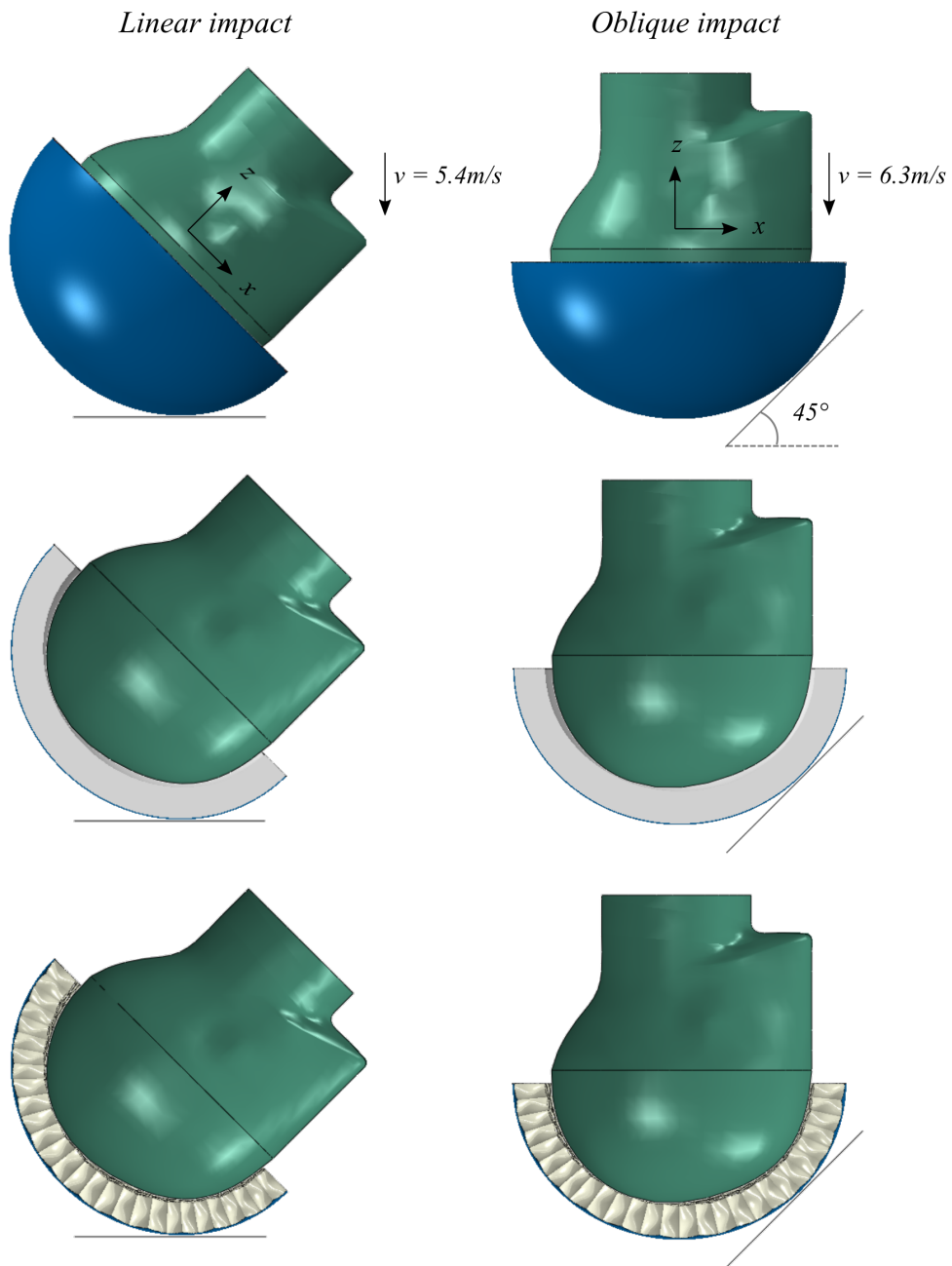


Figure 6.5: Orientation and boundary conditions of direct and oblique impacts for foam and honeycomb liner helmets

6.2.5 Traumatic Brain Injury Finite Element Model

The University College Dublin Brain Trauma Model (UCDBTM) was used to determine the severity of the resultant impacts [21]. The geometry of the model was derived from a male cadaver as determined by Computed Tomography (CT), Magnetic Resonance Tomograph (MRT) and slice contour photographs. The head and brain are comprised of 10 sections including the: scalp, skull, pia, flax, tentorium, cerebrospinal fluid (CSF), grey and white matter, cerebellum and brain stem, however, does not include elements representing the cerebral blood vessels. In total, the model consists of 26,000 elements in which the scalp, falx and tentorium were modelled using shell elements, cortical bone, trabecular bone, CSF, cerebrum, cerebellum and brain stem using brick elements and the dura with membrane elements. A low shear modulus and sliding boundary conditions between the interfaces of the skull, cerebrospinal fluid and brain were used.

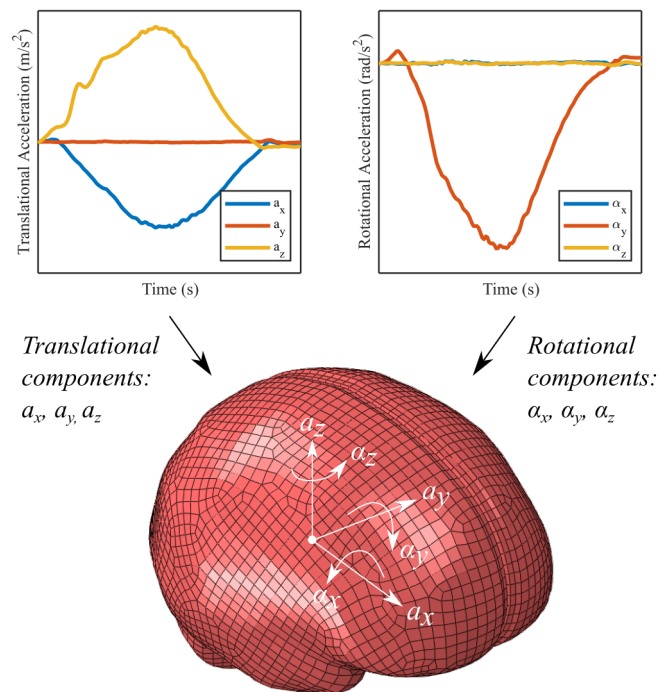


Figure 6.6: Annotated finite element head model with components of translational and rotational acceleration depicted as inputs to the centre of gravity.

The model was validated against intracranial pressure data [224], cadaver impact tests, and brain motion research [225]. Further validations accomplished comparing real world brain injury events to the model reconstructions with good agreement [226]. It is important to note that there are newer and more complex finite elements models than the UCDBTM that have been reported in the literature for head and brain injury research. While not possessing the same refinement and characteristics as some of these models, the UCDBTM benefits from having been used to process a large spectrum of brain injured and non-injured subjects.

In this study, the components of translational and rotational acceleration recorded during the helmeted headform impacts were used as the input to the centre of gravity node of the UCDBTM, refer to figure 6.6. Abaqus enabled calculation of the magnitude of maximum principal strain. Analysis was restricted to the cerebrum, as per other studies [50]. To ensure that the simulation result was valid, mesh integrity analysis was conducted for each simulation to ensure there were no errors as a result of high element aspect ratios exceeding a value of 3.0. In addition, the ratio of artificial energy and internal strain energy of the simulation, associated with the prevalence of hourglassing was monitored, elements exceeding a ratio of 3% were excluded from the analysis

6.3 Results

6.3.1 Optimisation

Numerical optimisation was undertaken to identify the optimal configuration subject to the two objective functions. Figures 6.7 and 6.8 reports the variation in the objective functions, PTA and HIC, for each evaluation. The minimum value is also presented, which represents the minimum objective function value recorded so far at each iteration.

In both cases, the optimisation procedure successfully satisfied the objective function. For the PTA_{opt} , the recorded PTA was 136.5 g and the calculated HIC was

960.7, representing a reduction of 45.4% and 38.9 %, relative to the threshold of values of 250 g and 1574 respectively. For the HIC_{opt} the recorded PTA was 165.9 g and the calculated HIC was 913.4, representing a reduction of 33.6 % and 41.9 % relative to the threshold of values. Of note, these values align with results of chapter 5. Whilst similar performance is achieved, the identified structures have a lower density (refer to table 6.2) as a more representative contact area was used.

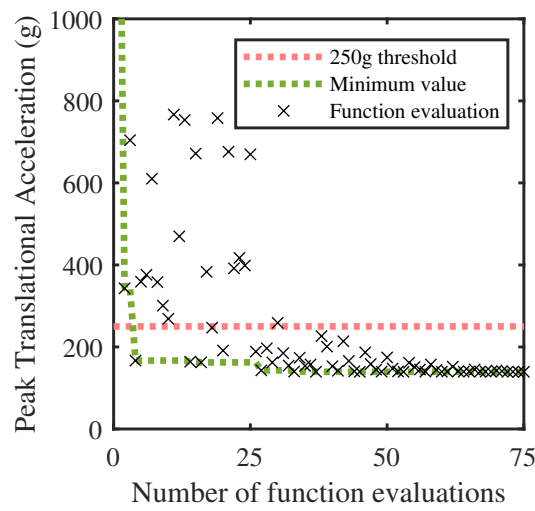


Figure 6.7: The variation in the objective function, peak translational acceleration, for each function evaluation relative to the threshold of 250g

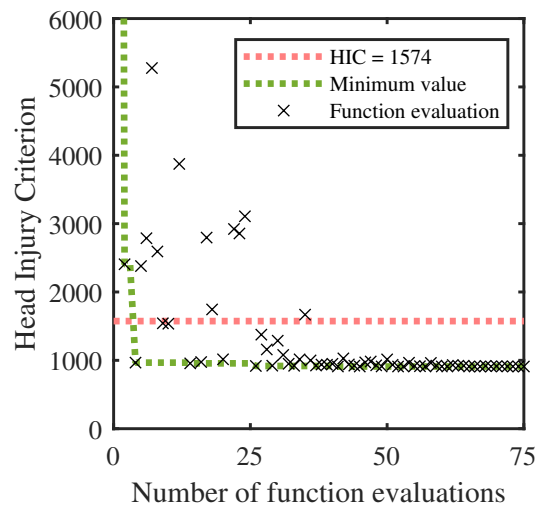


Figure 6.8: The variation in the objective function, head injury criterion, for each function evaluation relative to the threshold of 1574

Table 6.2: Structural and performance parameters for the optimal configurations of each objective function

Objective function	Cell width, w (mm)	Wall thickness, t (mm)	Aspect ratio, e (-)	Number of folds, f (-)	PTA (g)	HIC	Relative density, R_d	Density, ρ , (kg/m^3)
PTA	20.0	1.62	0.60	1	136.5	960.7	0.231	276.9
HIC	20.0	1.11	0.80	1	165.9	913.4	0.165	198

6.3.2 Full Scale Honeycomb Helmet Model

The honeycomb structures, identified through the optimisation procedure, were propagated within the volume of a helmet liner. These helmet liners were subjected to direct impact conditions equivalent to the EN1078 design standard, to assess the predictive capacity of the optimisation sequence when the honeycombs are subject to in-situ loading conditions. Figure 6.9 reports the resultant translational acceleration exposed to the headform during the impact.

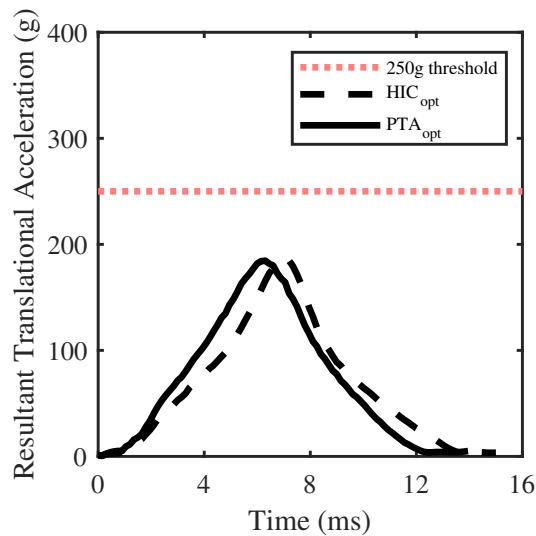


Figure 6.9: The resultant acceleration time behaviour for a full scale honeycomb helmet impact subject to the impact conditions of EN1078

Both helmet liner configurations satisfy the design standard threshold. The profile of the acceleration curve for PTA_{opt} presents marginally higher acceleration during the loading of the helmet liner, when compared to HIC_{opt} up until the point of peak acceleration where PTA is greatest for HIC_{opt} . Peaks in acceleration are observed at 6.3 ms and 7.1 ms for PTA_{opt} and HIC_{opt} respectively. At these points, the calculated PTA was 184.6 g and 186.9 g. The reported duration of each event was 12.5 ms and 13.7 ms, whilst HIC was calculated as 1162.2 and

1012.6.

Table 6.3 compares the results of the periodic boundary condition model used in the optimisation and the full scale helmet model. Percentage difference is reported for both PTA and HIC and is used to assess the predictive capacity of the proposed optimisation sequence. Generally, both PTA and HIC are underreported by the optimisation sequence. For PTA_{opt} , the relative difference was 35.2% and 20.9% for PTA and HIC, respectively. Comparatively, the relative difference reported for HIC_{opt} was less than that of PTA_{opt} , where values of 12.7% and 10.9% were reported.

Table 6.3: Comparison of PTA and HIC values for the prediction of the periodic BC model used in the optimisation and full scale helmet model. Percentage difference between the two cases is reported in brackets.

Objective function	Periodic BC model		Full scale helmet model	
	PTA (g)	HIC	PTA (g)	HIC
PTA_{opt}	136.5	960.7	184.6 (+35.2%)	1162.2 (+20.9%)
HIC_{opt}	165.9	913.4	186.9 (+12.7%)	1012.6 (+10.9%)

6.3.3 Comparison to Elastomeric Foam for Direct Impact

The honeycomb structures were compared against Vinyl Nitrile foam to assess the potential to replace them as a helmet liner. Vinyl Nitrile foam liners were subject to an equivalent direct impact. Figure 6.10 reports the resultant translational acceleration exposed to the headform during each impact. Furthermore, figure 6.11 reports a comparison of severity metrics PTA and HIC.

Comparison to Vinyl Nitrile foam demonstrates that both grades of material, 125 kg/m³ and 183 kg/m³, hereafter referred to as VN125 and VN183 respectively, can satisfy the requirements of the design standard ($PTA \leq 250$ g). The profile of the acceleration curves for each foam report notably different behaviour when compared between themselves as well as to the honeycomb structures. During the loading of the liner (refer to figure 6.12 for visualisation), values for translational acceleration exceed that of the honeycomb liners. Furthermore, at all points during loading, the value of translational acceleration for VN183 foams exceeds

that of VN125. Peaks in acceleration are observed at 5.1 ms and 5.9 ms where the values for PTA are 226.5 g and 177.9 g for VN183 and VN125, respectively. The calculated HIC for VN183 exceeds that of the imposed threshold ($HIC \leq 1574$) by 42.2%, whilst the HIC value for VN125 was 2.1% less than the threshold.

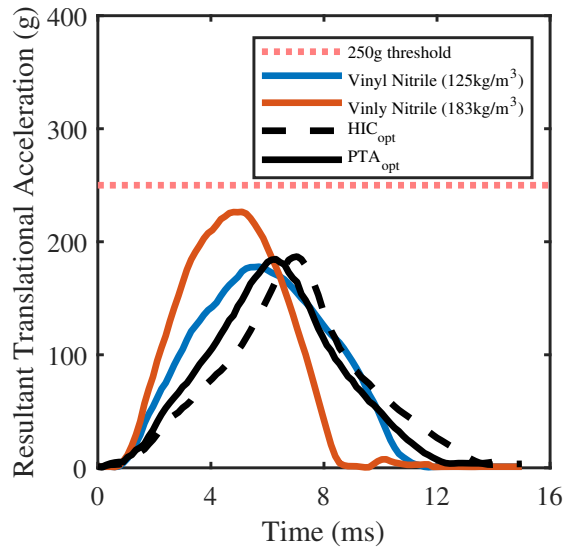


Figure 6.10: Comparison of translational acceleration subject to the direct impact for the full scale honeycomb helmet and vinyl nitrile foam

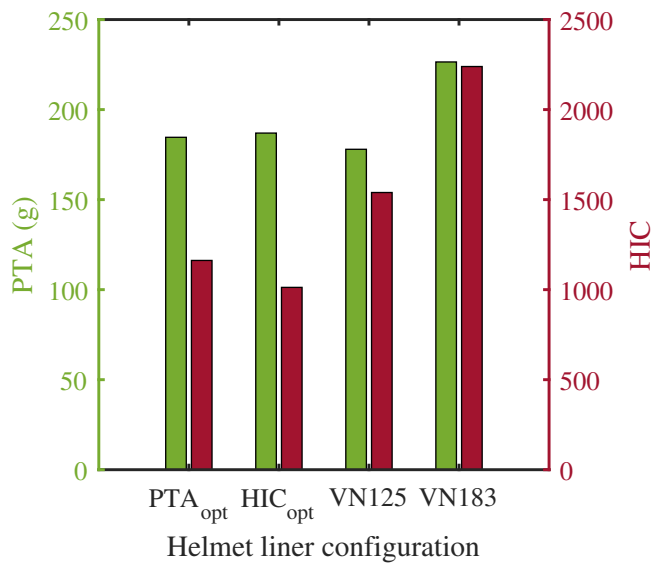


Figure 6.11: Comparison of severity metrics, PTA and HIC, subject to a direct impact for the full scale honeycomb helmet and vinyl nitrile foam

The minimum value for PTA, as recorded during the impact of VN125, was 177.9 which is 3.8% and 5.1 % less than that of the values recorded during the impacts of PTA_{opt} and HIC_{opt} , respectively. When comparing HIC values, however, a more notable difference in performance is observed. The minimum value for HIC, as recorded again during the impact of VN125, was 1540 which is 24.5% and 34% greater than of the values calculated during the impacts of PTA_{opt} and HIC_{opt} , respectively.

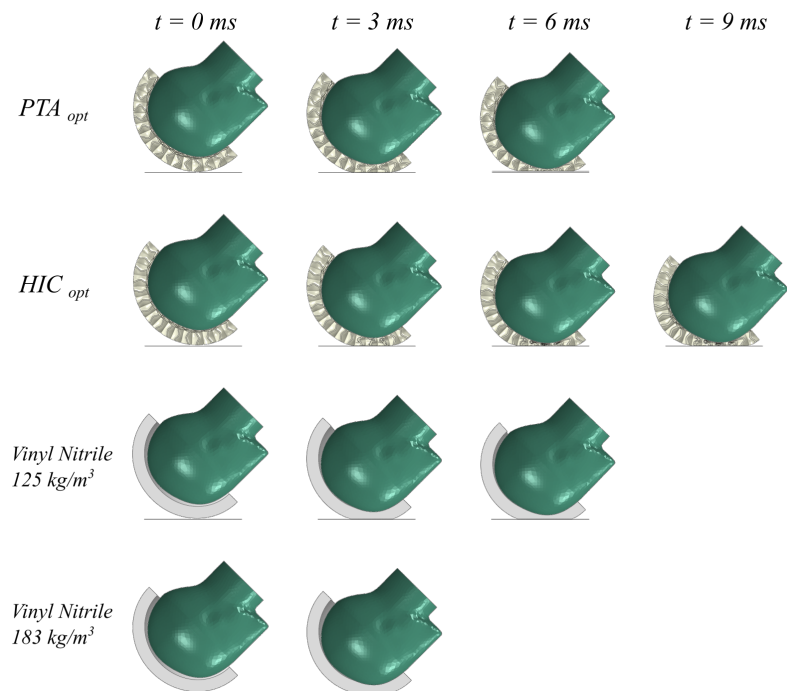


Figure 6.12: Snapshots of direct impact finite element simulation for vinyl nitrile and honeycomb up to the point of densification

6.3.4 Comparison to Elastomeric Foam for Oblique Impact

The four configurations of helmet liner (VN125, VN183, PTA_{opt} and HIC_{opt}) were also subjected to oblique impact conditions, to establish the relative performance. Figure 6.13 and 6.15 reports the resultant translational and rotational acceleration exposed to the headform during the impact, respectively. Furthermore, figure 6.14 compares the translational severity metrics, 6.16 compares rotational severity metrics and lastly 6.17 compares combined metrics.

Figure 6.13 shows that both liners with the pre-buckled honeycomb structure yield reductions in translational acceleration when compared to the foam liners. The profile of each translational acceleration curve reports notably different behaviour. During loading, up until the point of densification (refer to figure 6.18 for visualisation), values for translational acceleration of the foam liners exceed that of the pre-buckled honeycomb liners. Peaks in translational acceleration are observed at 6.3 ms and 4.3 ms for VN125 and VN183, respectively, where the values for PTA are 135.1 g and 170.1 g. In comparison, the peaks in translational acceleration for PTA_{opt} and HIC_{opt} are observed at 6.8 ms and 7.7 ms, respectively. At these points, the values for PTA are 111.7 g and 96.2 g, representing a relative reduction of 17.3% and 28.8% percent when compared to best performing foam (VN125). The impact duration recorded demonstrates a direct relationship to the HIC values calculated. For VN125 and VN183, the impact duration was 11.3 ms and 9.9 ms, whilst the HIC values were 847.4 and 1207.7. Similarly, for PTA_{opt} and HIC_{opt} the impact duration was 12.9 ms and 15 ms, whilst the HIC values were 529.8 and 424.8. Comparatively, this represents a reduction of 37.5% and 49.9%.

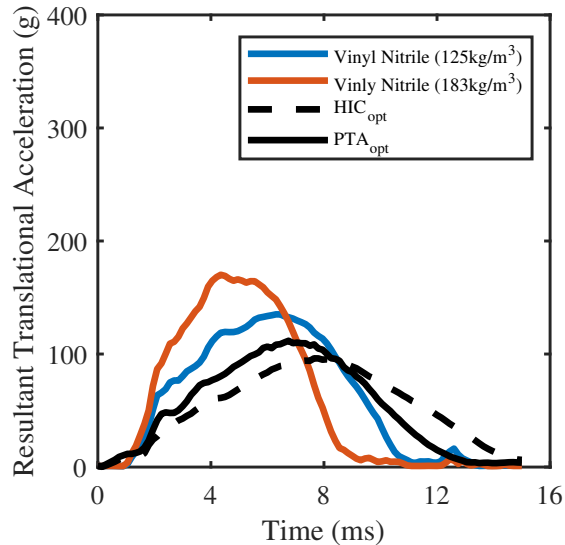


Figure 6.13: Comparison of translational acceleration subject to the oblique impact for the full scale honeycomb helmet and vinyl nitrile foam

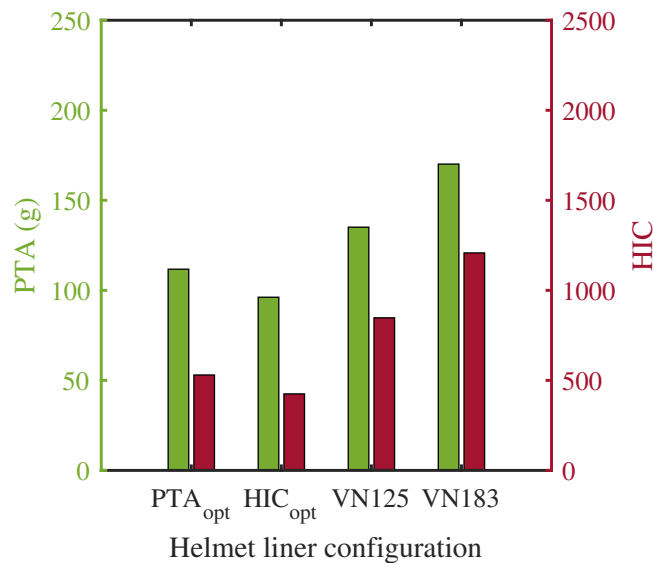


Figure 6.14: Comparison of translational severity metrics, PTA and HIC, subject to an oblique impact for the full scale honeycomb helmet and vinyl nitrile foam

Figure 6.15 shows that both liners with the pre-buckled honeycomb structure yield reductions in rotational when compared to the foam liners. The profile of each rotational acceleration, curve reports notably different behaviour. During loading, (refer to figure 6.18 for visualisation), values for rotational acceleration of the foam liners exceed that of the pre-buckled honeycomb liners. Peaks in rotational acceleration are observed at 5.9 ms and 4.4 ms for VN125 and VN183, respectively, where the values for PRA are 8.7 krad/s² and 11.2 krad/s². In comparison, the peaks in rotational acceleration for PTA_{opt} and HIC_{opt} are observed at 6.8 ms and 8.1 ms which are co-located with the peaks of translational acceleration,. At these points, the values for PRA are 7.1 krad/s² and 5.8 krad/s², representing a relative reduction of 18.4% and 33.3% percent when compared to the best performing foam (VN125). The impact duration recorded demonstrates a direct relationship to the RIC values calculated. For VN125 and VN183, the impact duration was 11.3 ms and 9.9 ms, whilst the RIC values were 25.2×10^6 and 30.2×10^6 . Similarly, for PTA_{opt} and HIC_{opt} the impact duration was 12.9 ms and 15 ms, whilst the RIC values were 15.5×10^6 and 11.1×10^6 . Comparatively, this represents a reduction of 38.3% and 56.0%.

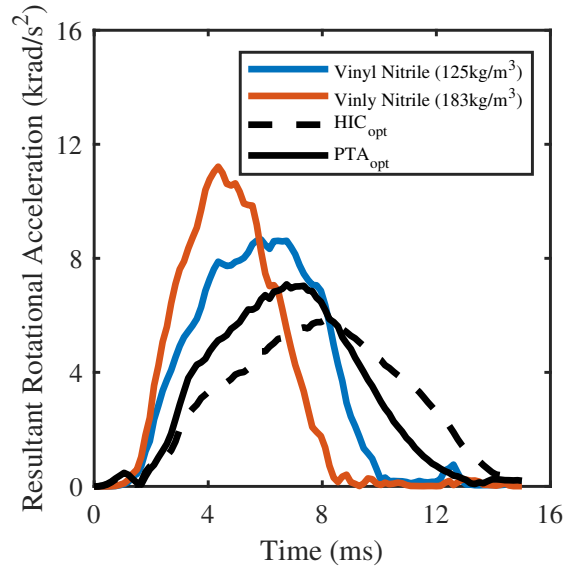


Figure 6.15: Comparison of rotational acceleration subject to the oblique impact for the full scale honeycomb helmet and vinyl nitrile foam

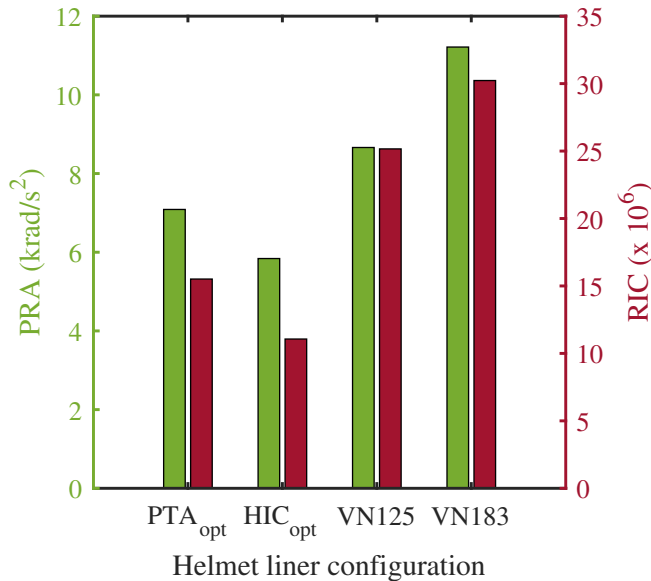


Figure 6.16: Comparison of translational severity metrics, PRA and RIC, subject to an oblique impact for the full scale honeycomb helmet and vinyl nitrile foam

Figure 6.17 reports the combined severity metric for the four different foam configurations. For the foam liner configurations VN125 and VN183, the reported GAMBIT values were 0.54 and 0.68 respectively. In comparison, for PTA_{opt} and HIC_{opt} the reported GAMBIT values were 0.45 and 0.38 respectively, representing a reduction of 16.7% and 29.6%. Similar results are observed for HIP, whereby

values reported by VN125 and VN183 were 41.06 kW and 48.53 kW respectively. In comparison, PTA_{opt} and HIC_{opt} were 29.17 kW and 24.32 kW respectively, representing a reduction of 29% and 40.8%.

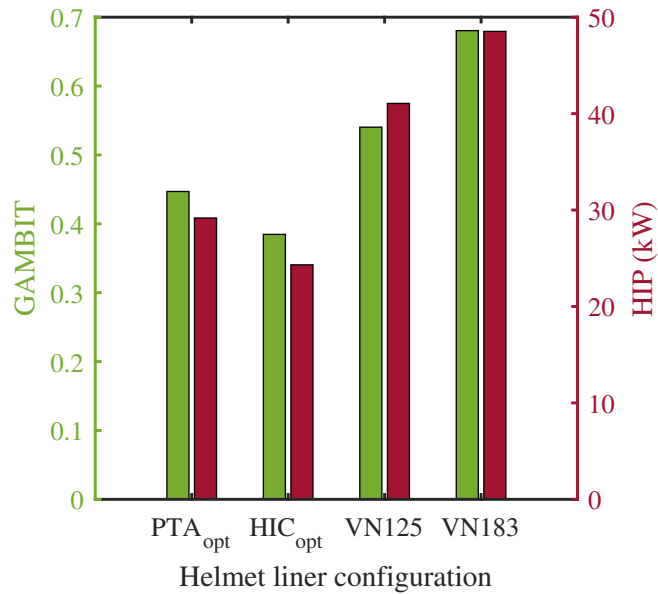


Figure 6.17: Comparison of combined, translational and rotational, severity metrics, GAMBIT and HIP, subject to an oblique impact for the full scale honeycomb helmet and vinyl nitrile foam

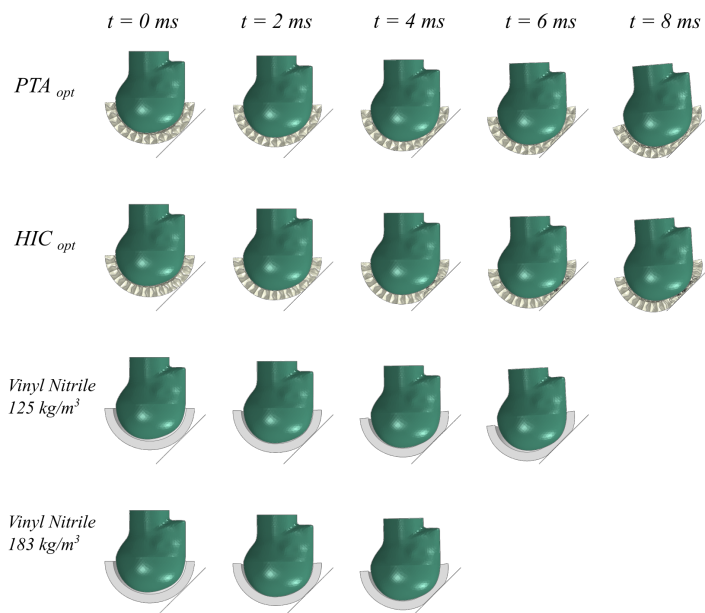


Figure 6.18: Snapshots of oblique impact finite element simulation for vinyl nitrile and honeycomb helmets up to the point of densification.

6.3.5 Traumatic Brain Injury Assessment

The kinematic-based severity metrics that have been used so far do not account for different tissues and details of the brain anatomy when considering traumatic brain injury. Therefore, a finite element model of the head was used to predict the Maximum Principal Strain (MPS) and volume fraction of elements, Cumulative Strain Damage Measure, (CSDM), with an MPS exceeding a predefined strain threshold of 0.25, as a result of the accelerations exposed to the head during each impact. For the computation of MPS the 95th percentile value was adopted to mitigate against spurious result that arise from single elements.

Figure 6.19 reports the MPS_{95} and $CSDM_{0.25}$ for the direct impact conditions reported in figure 6.10. The values of MPS_{95} reported for foam liner configurations exceed the values reported for the honeycomb liner configurations. For VN125 and VN183, the MPS_{95} was 0.116 and 0.155 respectively. In comparison, the MPS_{95} for PTA_{opt} and HIC_{opt} were 0.112 and 0.106 respectively, representing a reduction of 3.4% and 8.6%. Similarly, the values for $CSDM_{0.25}$ reported for foam liner configurations exceed the values reported for the honeycomb liner configurations. For VN125 and VN183, the $CSDM_{0.25}$ was 0.00097 and 0.0059 respectively. In comparison, the $CSDM_{0.25}$ for PTA_{opt} and HIC_{opt} were 0.00087 and 0.00074 respectively, representing a reduction of 10.3% and 23.7%.

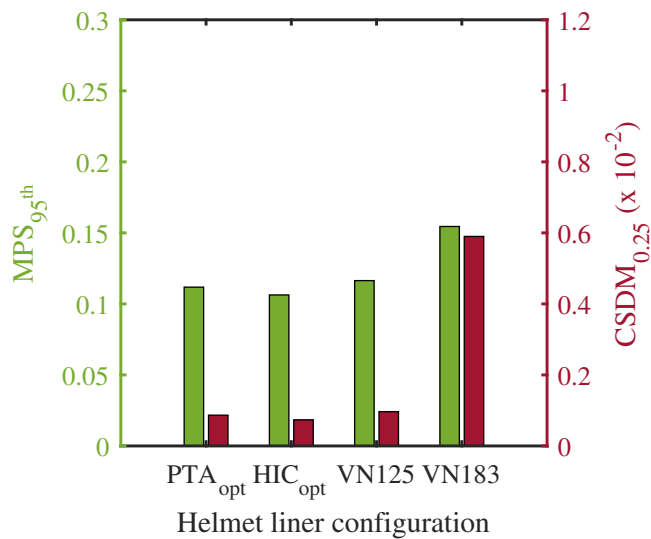


Figure 6.19: Comparison of TBI severity metrics, 95th percentile MPS and $CSDM_{0.25}$, subject to direct impact conditions for the full scale honeycomb helmet and vinyl nitrile foam

Figure 6.20 illustrates the distribution of MPS within the finite element head model. It is important to note that the visualised data includes 100th percentile values. The contours demonstrate that the MPS developed is 0.35 and 0.44 for VN125 and VN183 respectively. In comparison, the distribution and concentration of MPS is less notable for PTA_{opt} and HIC_{opt} where the maximum values recorded were 0.33 and 0.30.

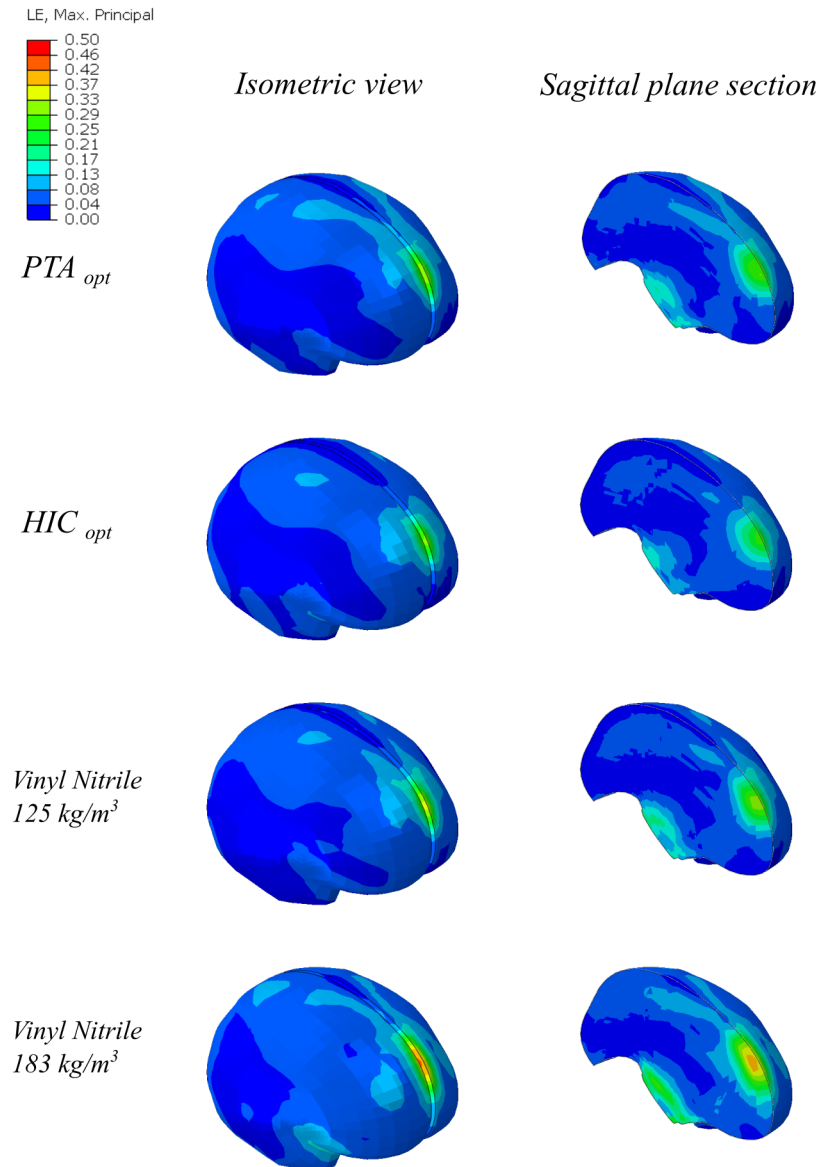


Figure 6.20: Comparison of the distribution of MPS within the finite element head model when subject to direct impact conditions for the full scale honeycomb helmet and vinyl nitrile foam

Figure 6.21 reports the MPS_{95} and $CSDM_{0.25}$ for the oblique impact conditions reported in figure 6.13 and 6.15. The values of MPS_{95} reported for foam liner configurations exceed the values reported for the honeycomb liner configurations. For VN125 and VN183, the MPS_{95} was 0.275 and 0.284 respectively. In comparison, the MPS_{95} for PTA_{opt} and HIC_{opt} were 0.252 and 0.234 respectively, representing a reduction of 8.4% and 14.9%. Similarly, the values for $CSDM_{0.25}$ reported for foam liner configurations exceed the values reported for the honeycomb liner configurations. For VN125 and VN183, the $CSDM_{0.25}$ was 0.105 and 0.102 respectively. In comparison, the $CSDM_{0.25}$ for PTA_{opt} and HIC_{opt} were 0.057 and 0.034 respectively, representing a reduction of 44.1% and 66.7%.

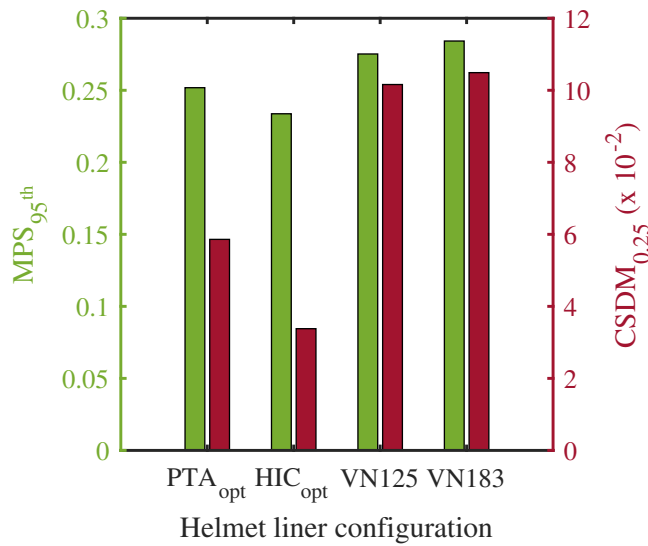


Figure 6.21: Comparison of TBI severity metrics, 95th percentile MPS and $CSDM_{0.25}$, subject to oblique impact conditions for the full scale honeycomb helmet and vinyl nitrile foam

Figure 6.22 illustrates the distribution of MPS within the finite element head model. The contours demonstrate that the MPS developed is 0.50 and 0.54 for VN125 and VN183 respectively. In comparison, the distribution and concentration of MPS is less notable for PTA_{opt} and HIC_{opt} where the maximum values recorded were 0.43 and 0.40.

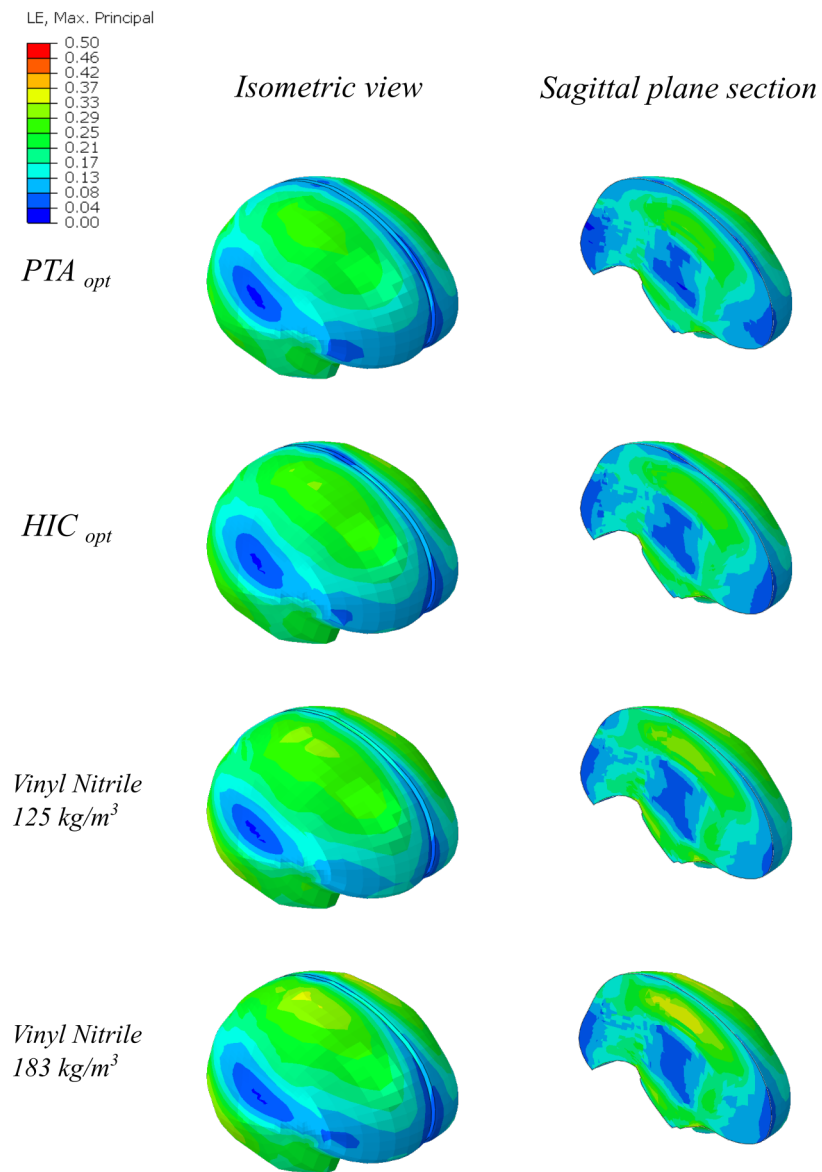


Figure 6.22: Comparison of the distribution of MPS within the finite element head model when subject to oblique impact conditions for the full scale honeycomb helmet and vinyl nitrile foam

6.4 Discussion

In this chapter, the proposed elastomeric pre-buckled honeycomb was optimised relative to the impact conditions of the EN 1078 design standard, informed by the anticipated contact area of the helmet design envelope. The aim of this chapter was to assess the predictive capacity of the periodic boundary condition model used within the optimisation by comparing it to a full scale helmet model, as well as identify the performance of the proposed structure relative to a commonly used impact mitigating material in terms of kinematic-based and tissue-based severity metrics when subject to direct and oblique conditions.

The improvements observed are due to adopting a structure with high stiffness and densification strain which can be optimised relative to specific boundary conditions (e.g., mass, velocity and contact area). Elastomeric foams, as well as other foams, do not possess the geometric freedom to facilitate this degree of optimisation, hence cellular structure such as the pre-buckled honeycomb holds an advantage for this application. Moreover, foam absorb the energy of the impact due to crushing, but they fail to distribute the load laterally due to their negligible Poisson's ratio. Since the foam deforms in a concentrated area, despite its large deformation and significant local energy absorption, it cannot distribute the energy of the impact. In contrast, honeycomb type structure, as well as other cellular structures, can better distribute the energy of the impact by engaging a larger portion of the liner in large deformation and energy absorption [176].

When subject to oblique conditions, the honeycomb structures yielded a reduction in both translational and rotational acceleration. The intrinsic geometric properties facilitate a helmet with a lower shear stiffness, whilst maintaining sufficient normal stiffness, such that the tangential force which gives rise to rotational acceleration is reduced. Furthermore, in-plane collapse of the honeycomb cells aids the mitigation of translational acceleration. This is attributed to the transversely isotropic properties of the prebuckled honeycomb structure. Foams possess notably greater isotropic behaviour, hence the rotational acceleration reported was larger [81].

The results demonstrated that the prebuckled honeycomb liners reduced the kinematic-based injury metrics when compared to the elastomeric foam liners.

Kinematic-based injury metrics, however, fail to account for different material and morphological details of the brain anatomy. Hence, established tissue-based metrics, 95th percentile maximum principal strain and cumulative strain damage measure were calculated using a finite element model of the head. Further analysis, demonstrated that both MPS_{95} and $CSDM_{0.25}$ were reduced for impacts including the prebuckled honeycomb liners. For direct impact conditions, marginal decreases in MPS_{95} and $MPS_{0.25}$ were observed. In contrast, for oblique conditions, notable reductions were observed. This is because the main mechanism of development of strain in the brain and ultimately brain injury, is rotational kinematics [10].

The mass of the helmet liner is an important design constraint in the development of helmet liners. Previous work has shown that a 20% increase in the mass of the head-helmet assembly can decrease the head acceleration by 10% [227]. Further analysis has identified that there is in fact an inverse relationship between peak head acceleration and the square root of mass [228]. Adopting designs with increased mass, however, is not an appropriate design strategy as this ultimately leads to user discomfort. The reported density for the PTA_{opt} and HIC_{opt} configurations were 277 kg/m^3 and 198 kg/m^3 , representing an increase in mass of 51.3% and 8.1%, respectively. Considering the inverse square law previously discussed, these increases in mass yield a reduction in peak accelerations of 7.2% and 2.8%. However, the reported reductions in translation and rotational acceleration were notably greater. Therefore, it can be concluded that the benefit was driven by the structure and not the addition of mass. Whilst the optimised configurations satisfied the design standard performance threshold, and exceeded the performance of materials currently used in helmets. It can be concluded that the material Luvosint is a limiting factor in the design. Adopting a stiffer base material is suggested, such as that available from EOS [166] (refer to figure 2.27) as this would maintain the recoverable nature of elastomeric materials but would allow use of thinner walls enabling weight reduction whilst retaining performance.

To approximate the helmet design envelope and better inform the periodic boundary condition (PBC) model used within the optimisation, the anticipated contact area between the headform and the liner was calculated using an established and previously used relationship [220]. The finite element based optimisation procedure identified optimal configurations that minimised peak translational acceler-

ation and head injury criterion. Comparison between the results for the periodic boundary condition model and the full-scale helmet model reported notable deviation in terms of PTA and HIC. Generally, the PBC model under-reports both the HIC ($r_d = 10.9 - 20.9\%$) and PTA values ($r_d = 12.7 - 35.2\%$). This is due to modelling discrepancies between the PBC model and full scale helmet model. Firstly, the kinematics of the PBC model do not match that of the helmet model. In the PBC model, motion is restrained to exclusively translate in the Z axis, whilst in the helmet model the headform is unrestrained and is therefore free to translate and rotate. As such, the PBC model better represents the guided fall loading conditions of the American standards (e.g. ASTM) which include a rigid neck that restrains motion rather than the free fall conditions of the British and European standards. Secondly, the PBC model fails to account for the curvature of the headform and shell, instead adopting for a flat-on-flat impact. Whilst this was adopted as a modelling simplification, in a typical helmet impact, the area of the liner engaged during the impact increases with increasing strain, reaching a maximum at the point of densification. Hence, mechanical behaviour which adopts a flat plateau may not be appropriate. As such, the optimal performance, based on the flat-on-flat performance, does not translate to the in-situ helmet loading conditions, this suggests that whilst foams are considered to have ideal energy absorption behaviour why they actually fail to show these characteristics for impact loading. Lastly, the PBC model doesn't account for the inclusion of the shell. The polymeric shell, serves to distribute the load under impact and behaves differently to the rigid plates used in the optimization. This modelling decision assumes an infinitely rigid shell, thus facilitating overly effective load distribution. In reality, the shell deforms away from the impact site and pushes the liner from the impact site. It is the culmination of these factors which realise the discrepancies between the PBC model and the full scale helmet model.

Commercially available helmet liners for cycling have been reported to achieve a peak translational acceleration of 100g [53] which is less than the values reported in this analysis. These helmets, however, are derived from rigid polymeric foam and therefore are only suitable for a single-hit. Given the high volumetric energy absorption of polymeric foams under impact, this is why lower peak translational accelerations are recorded. The proposed route for optimisation of cellular structures presented in this thesis has the potential to utilise low density,

rigid polymers such as Nylon [175], which could yield equivalent behaviour under impact. These materials were not investigated, however, as the focus of the thesis was on identifying a robust, multi-hit solution.

6.5 Conclusion

This chapter presents the numerical findings on the behaviour of the optimal configuration of the prebuckled honeycomb when subjected to the design envelope of a helmet. Anticipated contact area was identified to inform the numerical optimisation procedure presented in chapter 5. Comparison was then drawn to a contemporary impact mitigating material relative to kinematic-based and tissue-based severity metrics under direct and oblique conditions. Adopting this strategy when designing for new helmet liners has been reported to exceed the performance of an established material. A list of conclusions are presented below:

1. An established relationship for identifying contact area effectively informed the numerical optimisation such that it was suitable for the helmet design envelope.
2. Optimal configurations of the pre-buckled honeycomb structure, subject to objective functions PTA and HIC, were identified using a reduced number of iterations. Demonstrating that the optimisation time can be reduced to achieve expeditious optimisation.
3. The periodic boundary condition model acts as a suitable surrogate for identifying the potential structures for helmet liners.
4. For direct impact conditions, the pre-buckled honeycombs yielded a marginal increase in terms of PTA (3.8%) when compared to elastomeric foams. However, the calculated HIC values were notably reduced (34%).
5. For oblique impact conditions, the pre-buckled honeycombs decreased severity metrics PTA, HIC, PRA, RIC, GAMBIT and HIP by 28.8%, 49.9%, 33.3%, 56%, 29.6% and 40.8% respectively.

6. For the direct impacts, simulation of a finite element head model reported that the pre-buckled honeycomb reduced the MPS_{95} and $CSDM_{0.25}$ by 8.6% and 23.7% respectively.
7. For the oblique impacts, simulation of a finite element head model reported that the pre-buckled honeycomb reduced the MPS_{95} by 14.9% and 66.7% respectively.
8. For the direct impacts, PTA_{opt} yielded a reduction in PTA when compared to HIC_{opt} . This, however, was at the expense of an increase in HIC, MPS_{95} and $CSDM_{0.25}$.
9. For the oblique impacts, HIC_{opt} yielded a reduction in all severity metrics when compared to HIC_{opt} .

Chapter 7

Conclusion

7.1 Summary

This thesis aimed to improve head protection for helmets by exploiting the mechanical benefits of cellular structures and elastomeric materials by leveraging finite element analysis, numerical optimisation and additive manufacturing. To achieve this, the study had the following objectives:

1. Establish a pathway for the characterisation of additively manufactured elastomeric materials.
2. Calibrate and validate a material model for implementation within finite element analysis.
3. Identify relationships between structural parameters and performance parameters, to identify geometric bounds for the proposed honeycomb structure.
4. Validate a full scale and periodic boundary condition model for a honeycomb structure.
5. Establish a numerical pathway for finite element based optimisation of cellular structures subject to changing boundary conditions and objective function.
6. Validate the optimisation procedure through experimental impact testing.
7. Numerically test the candidate material versus contemporary liner materials, to quantify its ability to reduce kinematic based injury metrics.
8. Establish the traumatic brain injury mitigation effects of the proposed structure by use of an established finite element head model.

Characterisation of an additively manufactured elastomer revealed sensitivity to build orientation, strain state and strain rate. The culmination of this identified a pathway for efficiently characterizing materials used in transient, dynamic applications. Deriving model coefficients via uniaxial, planar and equibiaxial data, followed by validation in isolated and mixed deformation states, provides

an efficient pathway to perform accurate finite element simulations of elastomeric additively manufactured materials.

Various configurations of pre-buckled circular honeycombs were designed and fabricated using an elastomeric powder and the laser sintering method. The mechanical behaviour of the additively manufactured pre-buckled honeycombs was investigated under quasi-static and impact compression experiment to provide a basis for validation of finite element models. Further experimental testing identified rate dependant and multi-loading behaviour. Full scale and computationally efficient periodic boundary condition models were developed and used to run parameters sweeps to identify relationships between structural parameters and performance in terms of yield stress, energy absorption and efficiency. This culminated in a broad range of dynamic mechanical behaviour which provided a foundation for optimising this structure subject to loading regimes and acceptable performance thresholds.

An effective combined numerical framework was reported for optimisation of a parametrically defined honeycomb-type structure, subject to the boundary conditions of a common helmet design standard, was identified. Numerical optimisation was realised through use of an algorithm derived from a radial basis function based on finite element analysis, to form a surrogate model of the impact performance relative to the honeycomb's structural parameters. Numerical optimisation revealed the influence of objective function on the impact behaviour for this class of additively manufactured elastomeric honeycomb. For the limits prescribed in the analysis, optimising for peak translational acceleration resulted in a structure that mitigates the kinetic energy of the impact at a stress, which facilitates avoidance of the densification region. In contrast, optimising for head injury criterion results in a structure which yields at a relatively lower yield stress and resultant acceleration, however, densifies thus resulting in a higher peak translational acceleration but for a small duration.

Fabrication and experimental testing of the optimal configurations provided further insights regarding the impact performance. Samples were fabricated using laser sintering of a thermoplastic polyurethane powder, subjected to experimental impact conditions to validate the outcome of the numerical analysis, then to successive impacts to explore multi-impact behaviour and performance degrada-

tion. Both structures satisfied their respective objective function when subjected to experimental testing, therefore providing validity for the numerical procedure. Over repeat impacts, PTA optimised structures reported improved performance and stabilised after the third impact. performance was observed over multiple impacts, stabilizing after the third impact. In contrast, HIC optimised structures reported degrading performance over successive impacts.

Application of the proposed finite element based optimisation to the design envelope of a helmet liner was undertaken by identifying the anticipated contact area of the helmet liner interface. The results of the full scale honeycomb impact behaviour demonstrated that the optimisation procedure can identify a structure which satisfies the performance thresholds of the design standard. Comparison between the periodic boundary condition model used during optimisation and the behaviour of the full scale helmet model during a direct impact demonstrated the PBC model was a suitable surrogate model to enable efficient optimisation of the structure. Relative difference measures between the two models were less than 35% and 21% when comparing the PTA and HIC values.

Comparison was drawn between a common impact mitigating material, vinyl nitrile, and optimal configurations of the pre-buckled honeycomb for direct and oblique impact conditions to quantify its ability to reduce kinematic based injury metrics. For direct impacts, the recorded PTA was 3.4% greater than that of the foam liner. However, when comparing HIC values, a reduction of 34% was reported. For oblique conditions, favourable behaviour was observed, whereby reductions in metrics PTA, HIC, PRA, RIC and GAMBIT were reduced by 28.8%, 49.9%, 33.3%, 56% and 29.7%.

The traumatic brain injury mitigation effects of the pre-buckled honeycomb liner were identified through simulation of a finite element model subject to the translational and rotational acceleration behaviour recorded during simulation of the full scale model. 95th percentile MPS and the volume fraction of elements exceeding an MPS of 0.25 (CSDM_{0.25}) were calculated. Notably, for direct impact condition, MPS₉₅ and CSDM_{0.25} were reduced by 8.6% and 23.7%. Under oblique impact conditions, more notable reductions were observed, whereby MPS₉₅ and CSDM_{0.25} were reduced by 14.9% and 66.7%.

Comparison of the two configurations of pre-buckled honeycomb which were iden-

tified through optimisation of PTA and HIC respectively identified the following. For direct impacts, PTA_{opt} yielded the lowest PTA, however, this was at the expense of HIC, MPS_{95} and $CSDM_{0.25}$. For oblique conditions, HIC_{opt} yielded a lower value for all kinematic and tissue-based metrics when compared to the PTA_{opt} structure.

7.2 Further work

The work conducted in this thesis highlights a strategy to characterisation of a candidate additively manufactured material and finite element based optimisation of cellular structure for application to the design envelope of a helmet liner. Based on this work, five possible areas of additional study have been identified, which are related to the finite element material model, periodic boundary condition model, numerical optimisation, test conditions and severity metrics. These could further improve the fidelity and effectiveness of the proposed strategy.

The material model could be further investigated in a number of ways to improve its fidelity and accuracy. Firstly, in this thesis, the material model represented the non-linear elastic and rate-dependant behaviour. Elastomeric materials also demonstrate energy dissipation at the molecular level over cyclic testing as well as dependence on the maximum loading previously encountered, known as the Mullins effect. A number of constitutive models have been proposed to describe this effect (e.g., Ogden-Roxburgh) however, this was omitted as it would have yielded an inequitable behaviour when compared to the elastomeric foams used in this thesis which also demonstrate similar behaviour, although experimental data was unavailable for material model calibration. The optimisation pathway is focused on the structural aspect of the design so this omission was deemed acceptable, however, future study should include these phenomena as it effects the unloading portion of the impact behaviour. Secondly, data was collected to characterise the anisotropy as a result of build orientation for uniaxial tension, however, this degree of modelling was not included within the finite element simulations due to the complexity and associated computational cost required. Future work could include this and how it affects the behaviour when subjected to impacts aligned and misaligned with the build direction. Thirdly, new materials

could be identified and leveraged which demonstrate favourable properties. For example, rate-sensitive materials could facilitate improvements in impacts at velocities above and below that prescribed during optimisation. Highly dissipative materials also could reduce the period of unloading force exposed to the head. Lastly, global distribution of variable mechanical behaviour achieved through deliberate porosity via laser sintering could improve the transversely isotropic nature of the helmet liner to improve behaviour under oblique conditions.

The periodic boundary condition model used within the finite element based optimisation could be further improved to better represent the in-situ helmet loading conditions. Firstly, the presence of the head and its localised curvature could be included. By adopting varying curvatures, and associated contact areas, a localised optimisation could be achieved which provides protection on an impact orientation specific basis. Secondly, the PBC model leverages a 2×2 unit cell to emulate an equivalent 4×4 array, which achieved a computation reduction of 75%. However, future studies could investigate the use of a single unit or a periodic section of the single unit to improve computational efficiency, further enabling higher throughput of design iterations or a reduction in run-time. Moreover, the use of linear brick elements could be omitted for shell elements to further improve simulation time. Lastly, positioning of the symmetric boundary conditions could also be investigated such that it can simulate direct and oblique conditions. This would enable explicit optimisation of the oblique performance rather than implicit performance as a function of an optimisation guided by direct impact conditions.

The proposed optimisation strategy was initially informed by the performance thresholds of the design standards, however, results demonstrate that further improvements could be achieved by changing the objective function from peak translational acceleration to head injury criterion. Further improvements could be achieved by adopting an objective function which is better correlated with the development of strain within the brain. This could be achieved by using a different kinematic-based injury metric, or, by coupling the output of the periodic boundary condition model to the input of a finite element head model. By running a secondary simulation, structures which minimised strain or cumulative strain damage measure could be identified. Another consideration is the use of several boundary impact conditions either based on the location of the impact relative to the head surface (as previously discussed), or the different energy levels associated

with impact velocities or the inclusion of extra mass associated with the presence of the neck and body.

Although this work has shown the benefit of the pre-buckled honeycomb structure in outperforming vinyl nitrile foam, the level of energy absorption can still be further scrutinised. The optimal configurations were tested under in one orientation under direct and oblique conditions. It is well established that the location and direction of impact influences the resultant behaviour. Furthermore, helmets are likely to provide different levels of protection against impacts at different locations, whilst the brain is sensitive to the direction of loading. Hence, it is important to assess the performance of the newly proposed helmets under impacts with different directions and locations. Furthermore, design standards include secondary tests, based on application, such as impacts against kerbstones, as well as crush and penetration resistance. As such, further consideration should be given to these test conditions.

The likelihood of traumatic brain injury was assessed using the University College Dublin Brain Trauma Model. Analysis was restricted to the cerebrum due to the fact that is the only region that has been validated for the model. It is important to note that there are newer and more complex finite elements models than the UCDBTM that have been reported in the literature for head and brain injury research. These include improved morphological details as well as anisotropic material behaviour. Adopting models with greater fidelity, may provide further insights into the key regions of the brain, which are a common location of injury after severe TBI.

7.3 Academic contributions

The following academic contributions have been made to international journals, by the author, during the completion of this thesis:

- **R. Adams**, S. Townsend, S. Soe, P. Theobald. Mechanical behaviour of additively manufactured elastomeric pre-buckled honeycombs under quasi-static and impact loading (2022). *Materials & Design*.
- **R. Adams**, S. Townsend, S. Soe, P. Theobald. Finite element-based optimisation of an elastomeric honeycomb for impact mitigation in helmet liners (2022). *International Journal of Mechanical Sciences*.
- B. Hanna, **R. Adams**, S. Townsend, M. Robinson, S. Soe, M. Stewart, R. Burek, P. Theobald. Auxetic metamaterial optimisation for head impact mitigation in American football (2021). *International Journal of Impact Engineering*.
- S. Soe, **R. Adams**, M. Hossain, P. Theobald. Investigating the dynamic compression response of elastomeric, additively manufactured fluid-filled structures via experimental and finite element analysis. *Additive Manufacturing*.
- S. Townsend, **R. Adams**, M. Robinson, B. Hanna, P. Theobald. 3D printed origami honeycombs with tailored out-of-plane energy absorption behaviour (2020). *Materials & Design*.
- **R. Adams**, S. Soe, R. Celeghini, M. Robinson, B. Hanna, G. McShane, M. Alves, R. Burek, P. Theobald (2019). A novel pathway for efficient characterisation of additively manufactured thermoplastic elastomers (2019). *Materials & Design*.
- M. Robinson, S. Soe, R. Johnston, **R. Adams**, B. Hanna, R. Burek, G. McShane, R. Celeghini, M. Alves, P. Theobald (2019). Mechanical characterisation of additively manufactured elastomeric structures for variable strain rate applications. *Additive Manufacturing*.

Chapter 8

Appendix 1

8.1 Material Model Coefficients

Table 8.1: Hyperelastic material model, Ogden $N=5$, coefficients for implementation in Abaqus.

N	μ	α	D
1	903.01	3.72	0
2	-723.56	5.24	0
3	264.03	6.19	0
4	-669.43	2.26	0
5	236.66	1.42	0

Table 8.2: Linear viscoelastic material model, Prony series, coefficients for implementation in Abaqus.

N	G	K	τ
1	0.16	0	1.35E-03
2	0.13	0	7.13E-02
3	8.98E-02	0	0.92
4	7.29E-02	0	6.27
5	8.04E-02	0	49.41

Chapter 9

Reference List

- [1] Research Note, Heidi Coleman, and Krista Mizenko. *Traffic Safety Facts Pedestrian and Bicyclist Data Analysis*. 2018.
- [2] *Cycling Statistics - How popular is cycling in the UK? — 2020 - Finder UK*. URL: <https://www.finder.com/uk/cycling-statistics>.
- [3] A Murphy et al. “Reported Road Casualties Great Britain: 2019 Annual Report”. In: *The Department for Transport: London, UK* (2020).
- [4] Marko Tainio et al. “Can air pollution negate the health benefits of cycling and walking?” In: *Preventive Medicine* 87 (June 2016), pp. 233–236. ISSN: 0091-7435. DOI: 10.1016/J.YPMED.2016.02.002.
- [5] P. Oja et al. *Health benefits of cycling: A systematic review*. Aug. 2011. DOI: 10.1111/j.1600-0838.2011.01299.x.
- [6] Gerard Deenihan and Brian Caulfield. “Estimating the health economic benefits of cycling”. In: *Journal of Transport & Health* 1.2 (June 2014), pp. 141–149. ISSN: 22141405. DOI: 10.1016/j.jth.2014.02.001. URL: <https://linkinghub.elsevier.com/retrieve/pii/S221414051400022X>.
- [7] Thomas W Gaither et al. “Estimated total costs from non-fatal and fatal bicycle crashes in the USA: 1997–2013”. In: *Injury Prevention* 24.2 (Apr. 2018), pp. 135–141. ISSN: 1353-8047. DOI: 10.1136/injuryprev-2016-042281.

- [8] Philip Nilsson et al. “Modelling the effect on injuries and fatalities when changing mode of transport from car to bicycle”. In: *Accident Analysis & Prevention* 100 (Mar. 2017), pp. 30–36. ISSN: 0001-4575. DOI: 10.1016/J.AAP.2016.12.020.
- [9] *Casualty Summary Statistics*. URL: <https://app.powerbi.com/view?r=eyJrIjoieYlYmE1ZGQtNGIyZi00N2YyLWEyMTYtMjYzNzA5YTVkOWEzIiwidCI6IjFmYmQ2M>
- [10] A.H.S. Holbourn. “Mechanics of Head Injuries”. In: *The Lancet* 242.6267 (Oct. 1943), pp. 438–441. ISSN: 0140-6736. DOI: 10.1016/S0140-6736(00)87453-X.
- [11] Andrew S McIntosh, Adrian Lai, and Edgar Schilter. “Bicycle helmets: head impact dynamics in helmeted and unhelmeted oblique impact tests”. In: *Traffic injury prevention* 14.5 (2013), pp. 501–508. ISSN: 1538-9588.
- [12] Eric Bernes et al. *Helmets: A road safety manual for decision-makers and practitioners*. World Health Organization, 2006. ISBN: 9241562994.
- [13] Claire E. Baker et al. “The relationship between road traffic collision dynamics and traumatic brain injury pathology”. In: *Brain Communications* 4.2 (2022), fcac033. ISSN: 2632-1297. DOI: 10.1093/braincomms/fcac033.
- [14] Nick Dodds et al. “Evaluating the impact of cycle helmet use on severe traumatic brain injury and death in a national cohort of over 11000 pedal cyclists: A retrospective study from the NHS England Trauma Audit and Research Network dataset”. In: *BMJ Open* 9.9 (Sept. 2019), e027845. ISSN: 20446055. DOI: 10.1136/bmjopen-2018-027845.
- [15] Carl G. Mattacola et al. “Repeated impacts diminish the impact performance of equestrian helmets”. In: *Journal of Sport Rehabilitation* 28.4 (May 2019), pp. 368–372. ISSN: 15433072. DOI: 10.1123/jsr.2018-0355.
- [16] David E Tolhurst et al. “The surgical anatomy of the scalp”. In: *Plastic and reconstructive surgery* 87.4 (1991), pp. 603–612. ISSN: 0032-1052.
- [17] Richard W Young. “Age changes in the thickness of the scalp in white males”. In: *Human biology* 31.1 (1959), pp. 74–79. ISSN: 0018-7143.
- [18] Elisha S Gurdjian. “Recent advances in the study of the mechanism of impact injury of the head — a summary”. In: *Neurosurgery* 19.CN_suppl.1 (1972), pp. 1–42. ISSN: 0148-396X.

- [19] Antonia Trotta et al. “The Importance of the Scalp in Head Impact Kinematics”. In: *Annals of Biomedical Engineering* 46.6 (2018), pp. 831–840. ISSN: 15739686. DOI: 10.1007/s10439-018-2003-0.
- [20] info@blausen.com. *WikiJournal of Medicine/Medical gallery of Blausen Medical 2014 - Wikiversity*. 2014. URL: https://en.wikiversity.org/wiki/WikiJournal_of_Medicine/Medical_gallery_of_Blausen_Medical_2014.
- [21] T. J. Horgan and M. D. Gilchrist. “The creation of three-dimensional finite element models for simulating head impact biomechanics”. In: *International Journal of Crashworthiness* 8.4 (2003), pp. 353–366. ISSN: 17542111. DOI: 10.1533/ijcr.2003.0243.
- [22] Jesse Ruan and Priya Prasad. *The effects of skull thickness variations on human head dynamic impact responses*. Tech. rep. 2001.
- [23] A.I. King et al. “Recent Advances in Biomechanics of Brain Injury Research: A Review”. In: <https://home.liebertpub.com/neu> 12.4 (Jan. 2009), pp. 651–658. DOI: 10.1089/NEU.1995.12.651.
- [24] Queensland Brain Institute. *Lobes of the brain - Queensland Brain Institute - University of Queensland*. 2021. URL: <https://qbi.uq.edu.au/brain/brain-anatomy/lobes-brain>.
- [25] Yuan-cheng Fung. *Biomechanics: mechanical properties of living tissues*. Springer Science & Business Media, 2013. ISBN: 1475722575.
- [26] Bart Depreitere et al. “Bicycle-related head injury: A study of 86 cases”. In: *Accident Analysis and Prevention* 36.4 (July 2004), pp. 561–567. ISSN: 00014575. DOI: 10.1016/S0001-4575(03)00062-9.
- [27] Thomas A. Connor et al. “Do equestrian helmets prevent concussion? A retrospective analysis of head injuries and helmet damage from real-world equestrian accidents”. In: *Sports Medicine - Open* 5.1 (Dec. 2019), pp. 1–8. ISSN: 21989761. DOI: 10.1186/s40798-019-0193-0. URL: <https://sportsmedicine-open.springeropen.com/articles/10.1186/s40798-019-0193-0>.
- [28] Jack L Wood. “Dynamic response of human cranial bone”. In: *Journal of biomechanics* 4.1 (1971), pp. 1–12. ISSN: 0021-9290.

- [29] C Zee and J Go. “Imaging of Head Trauma—Neuroimaging Clinics of North America”. In: *American Journal of Neuroradiology* 24 (2003), pp. 1725–1726.
- [30] Thomas A Gennarelli and Lawrence E Thibault. “Biomechanics of acute subdural hematoma”. In: *The Journal of trauma* 22.8 (1982), pp. 680–686. ISSN: 0022-5282.
- [31] Thomas A Gennarelli, L E Thibault, and A K Ommaya. “Pathophysiologic responses to rotational and translational accelerations of the head”. In: *Proceedings: Stapp Car Crash Conference*. Vol. 16. Society of Automotive Engineers SAE, 1972. ISBN: 0585-086X.
- [32] Susan Sheps Margulies and Lawrence E Thibault. “A proposed tolerance criterion for diffuse axonal injury in man”. In: *Journal of biomechanics* 25.8 (1992), pp. 917–923. ISSN: 0021-9290.
- [33] Sabina J Strich. “Diffuse degeneration of the cerebral white matter in severe dementia following head injury”. In: *Journal of neurology, neurosurgery, and psychiatry* 19.3 (1956), p. 163.
- [34] Fidel Hernandez et al. “Six Degree-of-Freedom Measurements of Human Mild Traumatic Brain Injury”. In: *Annals of Biomedical Engineering* 43.8 (2015), pp. 1918–1934. ISSN: 15739686. DOI: 10.1007/s10439-014-1212-4.
- [35] H R Lissner, M Lebow, and F G Evans. “Experimental studies on the relation between acceleration and intracranial pressure changes in man”. In: *Surgery, gynecology & obstetrics* 111 (1960), pp. 329–338. ISSN: 0039-6087.
- [36] Elisha S Gurdjian, V L Roberts, and L Murray Thomas. “Tolerance curves of acceleration and intracranial pressure and protective index in experimental head injury”. In: *Journal of Trauma and Acute Care Surgery* 6.5 (1966), pp. 600–604. ISSN: 2163-0755.
- [37] Charles W Gadd. *Use of a weighted-impulse criterion for estimating injury hazard*. Tech. rep. 1966.
- [38] John Versace. “A review of the Severity Index”. In: *SAE Technical Papers*. SAE International, Feb. 1971. DOI: 10.4271/710881.

- [39] Thomas A Gennarelli. “Head injury in man and experimental animals: clinical aspects”. In: *Trauma and regeneration*. Springer, 1983, pp. 1–13.
- [40] Hideyuki Kimpara et al. “Head Injury Prediction Methods Based on 6 Degree of Freedom Head Acceleration Measurements during Impact”. In: *International Journal of Automotive Engineering* 2.2 (2011), pp. 13–19. ISSN: 2185-0984. DOI: 10.20485/jsaeijae.2.2{_}13.
- [41] James A Newman. “A generalised model for brain injury threshold (GAMBIT)”. In: *International IRCOBI Conference on the Biomechanics of Impact, International Research Council on the Biomechanics of Impact, Bron, France*. 1986, pp. 17–36.
- [42] Liying Zhang, King H Yang, and Albert I King. “Comparison of brain responses between frontal and lateral impacts by finite element modeling”. In: *Journal of neurotrauma* 18.1 (2001), pp. 21–30. ISSN: 0897-7151.
- [43] James A Newman and Nicholas Shewchenko. *A proposed new biomechanical head injury assessment function-the maximum power index*. Tech. rep. 2000.
- [44] Svein Kleiven. “Predictors for traumatic brain injuries evaluated through accident reconstructions”. In: *Stapp car crash J* 51.81 (2007), pp. 81–114.
- [45] Erik G Takhounts et al. *Development of brain injury criteria (BrIC)*. Tech. rep. 2013.
- [46] Madelen Fahlstedt et al. “Ranking and Rating Bicycle Helmet Safety Performance in Oblique Impacts Using Eight Different Brain Injury Models”. In: *Annals of Biomedical Engineering* 49.3 (2021), pp. 1097–1109. ISSN: 15739686. DOI: 10.1007/s10439-020-02703-w.
- [47] Haojie Mao et al. “Development of a finite element human head model partially validated with thirty five experimental cases”. In: *Journal of biomechanical engineering* 135.11 (2013), p. 111002. ISSN: 0148-0731.
- [48] Mazdak Ghajari, Peter J Hellyer, and David J Sharp. “Computational modelling of traumatic brain injury predicts the location of chronic traumatic encephalopathy pathology”. In: *Brain* 140.2 (2017), pp. 333–343. ISSN: 0006-8950.

- [49] Noritoshi Atsumi, Yuko Nakahira, and Masami Iwamoto. “Development and validation of a head/brain FE model and investigation of influential factor on the brain response during head impact”. In: *International journal of vehicle safety* 9.1 (2016), pp. 1–23. ISSN: 1479-3105.
- [50] Antonia Trotta et al. “Biofidelic finite element modelling of brain trauma: Importance of the scalp in simulating head impact”. In: *International Journal of Mechanical Sciences* 173 (2020), p. 105448. ISSN: 0020-7403.
- [51] Erik G Takhounts et al. “Development of Brain Injury Criteria (BrIC)”. In: 57.November (2013), pp. 243–266.
- [52] Andrew Post et al. “Analysis of the influence of independent variables used for reconstruction of a traumatic brain injury incident”. In: *Proceedings of the Institution of Mechanical Engineers, Part P: Journal of Sports Engineering and Technology* 226.3-4 (Sept. 2012), pp. 290–298. ISSN: 1754-3371. DOI: 10.1177/1754337112436629.
- [53] Fady Abayazid et al. “A New Assessment of Bicycle Helmets: The Brain Injury Mitigation Effects of New Technologies in Oblique Impacts”. In: *Annals of Biomedical Engineering* 49.10 (Oct. 2021), pp. 2716–2733. ISSN: 0090-6964. DOI: 10.1007/s10439-021-02785-0.
- [54] Remy Willinger and Daniel Baumgartner. “Human head tolerance limits to specific injury mechanisms”. In: *International journal of Crashworthiness* 8.6 (2003), pp. 605–617. ISSN: 1573-8965.
- [55] Andrew Post et al. “Examination of the relationship between peak linear and angular accelerations to brain deformation metrics in hockey helmet impacts”. In: *Computer Methods in Biomechanics and Biomedical Engineering* 16.5 (May 2013), pp. 511–519. ISSN: 1025-5842. DOI: 10.1080/10255842.2011.627559.
- [56] Hideyuki Kimpara and Masami Iwamoto. “Mild traumatic brain injury predictors based on angular accelerations during impacts”. In: *Annals of biomedical engineering* 40.1 (2012), pp. 114–126. ISSN: 0090-6964.
- [57] Faris A Bandak and Rolf H Eppinger. “A three-dimensional finite element analysis of the human brain under combined rotational and translational accelerations”. In: *SAE transactions* (1994), pp. 1708–1726. ISSN: 0096-736X.

- [58] Diane C Thompson, Fred Rivara, and Robert Thompson. “Helmets for preventing head and facial injuries in bicyclists”. In: *Cochrane database of systematic reviews* 4 (1999). ISSN: 1465-1858.
- [59] James A Newman. *Modern sports helmets: their history, science, and art*. Schiffer Pub., 2007. ISBN: 0764327186.
- [60] T. Whyte et al. “A Review of Impact Testing Methods for Headgear in Sports: Considerations for Improved Prevention of Head Injury Through Research and Standards”. In: *Journal of Biomechanical Engineering* 141.7 (July 2019), pp. 444–446. ISSN: 0148-0731. DOI: 10.1115/1.4043140.
- [61] Cornelis P. Bogerd et al. “A review on ergonomics of headgear: Thermal effects”. In: *International Journal of Industrial Ergonomics* 45 (Feb. 2015), pp. 1–12. ISSN: 01698141. DOI: 10.1016/j.ergon.2014.10.004.
- [62] Thomas A. Connor et al. “An Evidence Basis for Future Equestrian Helmet Lateral Crush Certification Tests”. In: *Applied Sciences* 10.7 (Apr. 2020), p. 2623. ISSN: 2076-3417. DOI: 10.3390/app10072623.
- [63] Nigel J Mills. *Polymer Foams Handbook: Engineering and Biomechanics Applications and Design Guide*. 2007, p. 531. ISBN: 0750680695.
- [64] Iman Ebrahimi, Farid Golnaraghi, and G. Gary Wang. “Factors Influencing the Oblique Impact Test of Motorcycle Helmets”. In: *Traffic Injury Prevention* 16.4 (2015), pp. 404–408. ISSN: 1538957X. DOI: 10.1080/15389588.2014.937804.
- [65] M. Rodríguez-Millán et al. “Development of numerical model for ballistic resistance evaluation of combat helmet and experimental validation”. In: *Materials and Design* 110 (2016), pp. 391–403. ISSN: 18734197. DOI: 10.1016/j.matdes.2016.08.015.
- [66] John D. Finan, Roger W. Nightingale, and Barry S. Myers. “The Influence of Reduced Friction on Head Injury Metrics in Helmeted Head Impacts”. In: *Traffic Injury Prevention* 9.5 (Oct. 2008), pp. 483–488. ISSN: 1538-9588. DOI: 10.1080/15389580802272427.
- [67] Gaetano Caserta. “The use of honeycomb in the design of innovative helmets”. PhD thesis. 2012, p. 1.

- [68] Praveen K. Pinnoji and Puneet Mahajan. “Analysis of impact-induced damage and delamination in the composite shell of a helmet”. In: *Materials and Design* 31.8 (2010), pp. 3716–3723. ISSN: 02641275. DOI: 10.1016/j.matdes.2010.03.011.
- [69] V. Kostopoulos et al. “Finite element analysis of impact damage response of composite motorcycle safety helmets”. In: *Composites Part B:Engineering* 33.2 (2002), pp. 99–107. ISSN: 13598368. DOI: 10.1016/S1359-8368(01)00066-X.
- [70] Shwe Soe et al. “Using FFF and Topology Optimisation to Increase Crushing Strength in Equestrian Helmets BT - Sustainable Design and Manufacturing 2020”. In: ed. by Steffen G Scholz, Robert J Howlett, and Rossi Setchi. Singapore: Springer Singapore, 2021, pp. 369–377. ISBN: 978-981-15-8131-1.
- [71] Somen K. Bhudolia et al. “Enhanced impact energy absorption and failure characteristics of novel fully thermoplastic and hybrid composite bicycle helmet shells”. In: *Materials and Design* 209 (2021), p. 110003. ISSN: 18734197. DOI: 10.1016/j.matdes.2021.110003.
- [72] Goram Gohel et al. “Development and impact characterization of acrylic thermoplastic composite bicycle helmet shell with improved safety and performance”. In: *Composites Part B: Engineering* 221.March (2021), p. 109008. ISSN: 13598368. DOI: 10.1016/j.compositesb.2021.109008.
- [73] N. Bourdet et al. “In-depth real-world bicycle accident reconstructions”. In: *International Journal of Crashworthiness* 19.3 (2014), pp. 222–232. ISSN: 17542111. DOI: 10.1080/13588265.2013.805293.
- [74] B. J. Ramirez and V. Gupta. “Evaluation of novel temperature-stable viscoelastic polyurea foams as helmet liner materials”. In: *Materials and Design* 137 (2018), pp. 298–304. ISSN: 18734197. DOI: 10.1016/j.matdes.2017.10.037.
- [75] Mazdak Ghajari et al. “Influence of the body on the response of the helmeted head during impact”. In: *International Journal of Crashworthiness* 16.3 (2011), pp. 285–295. ISSN: 13588265. DOI: 10.1080/13588265.2011.559798.

- [76] Lorna J. Gibson and Michael F. Ashby. *Cellular solids: Structure and properties, second edition*. Cambridge University Press, Jan. 2014, pp. 1–510. ISBN: 9781139878326. DOI: 10.1017/CB09781139878326. URL: <https://www.cambridge.org/core/books/cellular-solids/BC25789552BAA8E3CAD5E1D105612AB5>.
- [77] F.M. Shuaeib et al. “A new motorcycle helmet liner material: The finite element simulation and design of experiment optimization”. In: *Materials & Design* 28.1 (Jan. 2007), pp. 182–195. ISSN: 02613069. DOI: 10.1016/j.matdes.2005.04.015.
- [78] Yong Peng et al. “A study of pedestrian and bicyclist exposure to head injury in passenger car collisions based on accident data and simulations”. In: *Safety Science* 50.9 (2012), pp. 1749–1759. ISSN: 09257535. DOI: 10.1016/j.ssci.2012.03.005.
- [79] Chen Ling et al. “Deformation response of EPS foam under combined compression-shear loading. Part I: Experimental design and quasi-static tests”. In: *International Journal of Mechanical Sciences* 144 (Aug. 2018), pp. 480–489. ISSN: 00207403. DOI: 10.1016/j.ijmecsci.2018.06.014.
- [80] N. J. Mills and A. Gilchrist. “Oblique impact testing of bicycle helmets”. In: *International Journal of Impact Engineering* 35.9 (2008), pp. 1075–1086. ISSN: 0734743X. DOI: 10.1016/j.ijimpeng.2007.05.005.
- [81] Nicolas Bailly et al. “Strain Rate Dependent Behavior of Vinyl Nitrile Helmet Foam in Compression and Combined Compression and Shear”. In: *Applied Sciences* 2020, Vol. 10, Page 8286 10.22 (Nov. 2020), p. 8286. DOI: 10.3390/APP10228286.
- [82] Yasmine Mosleh et al. “Novel Composite Foam Concept for Head Protection in Oblique Impacts”. In: *Advanced Engineering Materials* 19.10 (2017). ISSN: 15272648. DOI: 10.1002/adem.201700059.
- [83] Helena Stigson et al. “Consumer testing of bicycle helmets”. In: *Proceedings of the IRCOBI Conference. Antwerp, Belgium*. 2017, pp. 173–181.
- [84] Megan L. Bland et al. “Development of the STAR Evaluation System for Assessing Bicycle Helmet Protective Performance”. In: *Annals of Biomedical Engineering* 48.1 (2020), pp. 47–57. ISSN: 15739686. DOI: 10.1007/s10439-019-02330-0.

- [85] Shiyang Meng et al. “The biomechanical differences of shock absorption test methods in the US and European helmet standards”. In: *International Journal of Crashworthiness* 24.4 (2019), pp. 399–412. ISSN: 17542111. DOI: 10.1080/13588265.2018.1464545.
- [86] Caroline Deck et al. “Protection performance of bicycle helmets”. In: *Journal of Safety Research* 71 (2019), pp. 67–77. ISSN: 00224375. DOI: 10.1016/j.jsr.2019.09.003.
- [87] R Willinger et al. “Towards advanced bicycle helmet test methods”. In: *International Cycling Safety Conference*. 2014, pp. 18–19.
- [88] Thomas A. Connor et al. “Influence of headform mass and inertia on the response to oblique impacts”. In: *International Journal of Crashworthiness* 24.6 (2019), pp. 677–698. ISSN: 17542111. DOI: 10.1080/13588265.2018.1525859.
- [89] M Ehmet K Urt et al. “Modeling and Optimization of Airbag Helmets for Preventing Head Injuries in Bicycling”. In: 45.4 (2017), pp. 1148–1160. DOI: 10.1007/s10439-016-1732-1.
- [90] Javid Abderezaei et al. “An Overview of the Effectiveness of Bicycle Helmet Designs in Impact Testing”. In: *Frontiers in Bioengineering and Biotechnology* 9.September (Sept. 2021), pp. 1–13. ISSN: 2296-4185. DOI: 10.3389/fbioe.2021.718407.
- [91] Peter Halldin et al. “Improved helmet design and test methods to reduce rotational induced brain injuries”. In: *RTO Specialist Meeting, the NATO’s Research and Technology Organization (RTO)*. 2003.
- [92] Michael Bottlang et al. “Impact Performance Comparison of Advanced Bicycle Helmets with Dedicated Rotation-Damping Systems”. In: *Annals of Biomedical Engineering* 48.1 (Jan. 2020), pp. 68–78. DOI: 10.1007/S10439-019-02328-8.
- [93] Emily Bliven et al. “Evaluation of a novel bicycle helmet concept in oblique impact testing”. In: *Accident Analysis and Prevention* 124 (Mar. 2019), pp. 58–65.
- [94] Megan L Bland et al. “Differences in the protective capabilities of bicycle helmets in real-world and standard-specified impact scenarios”. In: *Traffic injury prevention* 19.sup1 (2018), S158–S163. ISSN: 1538-9588.

- [95] Emily Bliven et al. “A Novel Strategy for Mitigation of Oblique Impacts in Bicycle Helmets Forensic Biomechanics”. In: *Article in Journal of Forensic Biomechanics* 10 (2019), p. 1. ISSN: 2090-2697. DOI: 10.4172/2090-2697.1000141. URL: <https://www.researchgate.net/publication/340634442>.
- [96] T N Bitzer. *Honeycomb technology: materials, design, manufacturing, applications and testing*. Springer Science & Business Media, 1997. ISBN: 0412540509.
- [97] Deqiang Sun et al. “In-plane crushing and energy absorption performance of multi-layer regularly arranged circular honeycombs”. In: *Composite Structures* 96 (2013), pp. 726–735. ISSN: 0263-8223.
- [98] Ying Liu and Xin-Chun Zhang. “The influence of cell micro-topology on the in-plane dynamic crushing of honeycombs”. In: *International Journal of Impact Engineering* 36.1 (2009), pp. 98–109. ISSN: 0734-743X.
- [99] Kumar P Dharmasena et al. “Mechanical response of metallic honeycomb sandwich panel structures to high-intensity dynamic loading”. In: *International journal of impact engineering* 35.9 (2008), pp. 1063–1074. ISSN: 0734-743X.
- [100] Yuanlong Wang et al. “On the out-of-plane ballistic performances of hexagonal, reentrant, square, triangular and circular honeycomb panels”. In: *International Journal of Mechanical Sciences* 173.November 2019 (2020), pp. 2–11. ISSN: 00207403. DOI: 10.1016/j.ijmecsci.2019.105402.
- [101] Mulalo Doyoyo and Dirk Mohr. “Microstructural response of aluminum honeycomb to combined out-of-plane loading”. In: *Mechanics of Materials* 35.9 (2003), pp. 865–876. ISSN: 0167-6636.
- [102] Tiju Thomas and Gaurav Tiwari. “Crushing behavior of honeycomb structure: a review”. In: *International Journal of Crashworthiness* (2019). ISSN: 1754-2111. DOI: 10.1080/13588265.2018.1480471.
- [103] A Hönig and W J Stronge. “In-plane dynamic crushing of honeycomb. Part II: application to impact”. In: *International journal of mechanical sciences* 44.8 (2002), pp. 1697–1714. ISSN: 0020-7403.

- [104] Alp Karakoç, Kari Santaoja, and Jouni Freund. “Simulation experiments on the effective in-plane compliance of the honeycomb materials”. In: *Composite Structures* 96 (2013), pp. 312–320. ISSN: 0263-8223.
- [105] Qing Zhou and Robert R Mayer. “Characterization of aluminum honeycomb material failure in large deformation compression, shear, and tearing”. In: *J. Eng. Mater. Technol.* 124.4 (2002), pp. 412–420. ISSN: 0094-4289.
- [106] J L Yu, J R Li, and S S Hu. “Strain-rate effect and micro-structural optimization of cellular metals”. In: *Mechanics of materials* 38.1-2 (2006), pp. 160–170. ISSN: 0167-6636.
- [107] Shunfeng Li et al. “Impact analysis of a honeycomb-filled motorcycle helmet based on coupled head-helmet modelling”. In: *International Journal of Mechanical Sciences* 199 (June 2021), p. 106406. ISSN: 00207403. DOI: 10.1016/j.ijmecsci.2021.106406.
- [108] Dirk Mohr and Mulalo Doyoyo. “Experimental investigation on the plasticity of hexagonal aluminum honeycomb under multiaxial loading”. In: *J. Appl. Mech.* 71.3 (2004), pp. 375–385. ISSN: 0021-8936.
- [109] Shanqing Xu et al. “Experimental study of the out-of-plane dynamic compression of hexagonal honeycombs”. In: *Composite Structures* 94.8 (2012), pp. 2326–2336. ISSN: 02638223. DOI: 10.1016/j.compstruct.2012.02.024.
- [110] Quoc Lam et al. “An examination of the low strain rate sensitivity of additively manufactured polymer, composite and metallic honeycomb structures”. In: *Materials* 12.20 (2019). ISSN: 19961944. DOI: 10.3390/ma12203455.
- [111] S. Xu et al. “Strength enhancement of aluminium honeycombs caused by entrapped air under dynamic out-of-plane compression”. In: *International Journal of Impact Engineering* 47 (2012), pp. 1–13. ISSN: 0734743X. DOI: 10.1016/j.ijimpeng.2012.02.008.
- [112] D. D. Radford et al. “Dynamic Compressive Response of Stainless-Steel Square Honeycombs”. In: *Journal of Applied Mechanics* 74.4 (July 2007), pp. 658–667. ISSN: 0021-8936. DOI: 10.1115/1.2424717.

- [113] Michael Robinson et al. “Mechanical characterisation of additively manufactured elastomeric structures for variable strain rate applications”. In: *Additive Manufacturing* 27 (May 2019), pp. 398–407. ISSN: 22148604. DOI: 10.1016/j.addma.2019.03.022.
- [114] ASM S.M. Ashab et al. “Quasi-static and dynamic experiments of aluminum honeycombs under combined compression-shear loading”. In: *Materials and Design* 97 (2016), pp. 183–194. ISSN: 18734197. DOI: 10.1016/j.matdes.2016.02.074.
- [115] Yu Duan et al. “Crushing behavior of honeycomb vs. foam under combined shear-compression loading”. In: *International Journal of Impact Engineering* 146.August (2020), p. 103696. ISSN: 0734743X. DOI: 10.1016/j.ijimpeng.2020.103696.
- [116] B. Hou et al. “Impact behavior of honeycombs under combined shear-compression. Part II: Analysis”. In: *International Journal of Solids and Structures* 48.5 (2011), pp. 687–697. ISSN: 00207683. DOI: 10.1016/j.ijsolstr.2010.11.005.
- [117] Dahai Zhang et al. “Quasi-static combined compression-shear crushing of honeycombs: An experimental study”. In: *Materials and Design* 167 (2019), p. 107632. ISSN: 18734197. DOI: 10.1016/j.matdes.2019.107632.
- [118] N. J. Mills and A. Gilchrist. “Shear and compressive impact of polypropylene bead foam”. In: *undefined* (1999).
- [119] Chen Ling et al. “Deformation response of EPS foam under combined compression-shear loading. Part II: High strain rate dynamic tests”. In: *International Journal of Mechanical Sciences* 145.February (2018), pp. 9–23. ISSN: 00207403. DOI: 10.1016/j.ijmecsci.2018.06.015.
- [120] Gaetano D. Caserta, Lorenzo Iannucci, and Ugo Galvanetto. “Shock absorption performance of a motorbike helmet with honeycomb reinforced liner”. In: *Composite Structures* 93.11 (2011), pp. 2748–2759. ISSN: 02638223. DOI: 10.1016/j.compstruct.2011.05.029.
- [121] Kirk Hansen et al. “Angular Impact Mitigation system for bicycle helmets to reduce head acceleration and risk of traumatic brain injury”. In: *Accident Analysis and Prevention* 59 (Oct. 2013), pp. 109–117. ISSN: 00014575. DOI: 10.1016/j.aap.2013.05.019.

- [122] Somen K Bhudolia, Goram Gohel, and Kah Fai Leong. “Enhanced energy absorption characteristics of novel integrated hybrid honeycomb/polystyrene foam”. In: *Journal of Cellular Plastics* (Oct. 2020). ISSN: 15307999. DOI: 10.1177/0021955X20965216. URL: https://journals.sagepub.com/doi/full/10.1177/0021955X20965216?casa_token=U-9XE84yzxcAAAA%3At0E5VyVAkw-CToTpYoXQYrQMuSr3iPA5AITB2rv73BbaDHOMdzVMQ2bPErzUffk4L09Szpb
- [123] Simon R.G. Bates, Ian R. Farrow, and Richard S. Trask. “3D printed polyurethane honeycombs for repeated tailored energy absorption”. In: *Materials & Design* 112 (Dec. 2016), pp. 172–183. ISSN: 18734197. DOI: 10.1016/j.matdes.2016.08.062.
- [124] Scott Townsend et al. “3D printed origami honeycombs with tailored out-of-plane energy absorption behavior”. In: *Materials & Design* 195 (2020), p. 108930. ISSN: 18734197. DOI: 10.1016/j.matdes.2020.108930.
- [125] Xinyu Fan, Ignaas Verpoest, and Dirk Vandepitte. “Finite element analysis of out-of-plane compressive properties of thermoplastic honeycomb”. In: *Journal of Sandwich Structures and Materials* 8.5 (2006), pp. 437–458. ISSN: 10996362. DOI: 10.1177/1099636206065862.
- [126] M. K. Khan, T. Baig, and S. Mirza. “Experimental investigation of in-plane and out-of-plane crushing of aluminum honeycomb”. In: *Materials Science and Engineering A* 539 (2012), pp. 135–142. ISSN: 09215093. DOI: 10.1016/j.msea.2012.01.070.
- [127] Luke Mizzi et al. “Implementation of periodic boundary conditions for loading of mechanical metamaterials and other complex geometric microstructures using finite element analysis”. In: *Engineering with Computers* 37.3 (2021), pp. 1765–1779. ISSN: 14355663. DOI: 10.1007/s00366-019-00910-1.
- [128] Michał Kucewicz et al. “Modelling, and characterization of 3D printed cellular structures”. In: *Materials and Design* 142 (2018), pp. 177–189. ISSN: 18734197. DOI: 10.1016/j.matdes.2018.01.028.
- [129] C A E User. “ABAQUS 6.14 Analysis User Guide”. In: *Dassault System* (2014).

- [130] Haydn N.G. Wadley. “Multifunctional periodic cellular metals”. In: *Philosophical Transactions of the Royal Society A: Mathematical, Physical and Engineering Sciences* 364.1838 (Jan. 2006), pp. 31–68. ISSN: 1364-503X. DOI: 10.1098/rsta.2005.1697.
- [131] *RHEON™ technology - The LABS*. URL: <https://rheonlabs.com/rheon-labs/>.
- [132] Callum J.C. Heath et al. “Morphing hybrid honeycomb (MOHYCOMB) with in situ Poisson’s ratio modulation”. In: *Smart Materials and Structures* 25.8 (2016). ISSN: 1361665X. DOI: 10.1088/0964-1726/25/8/085008.
- [133] *Koroyd Impact Protection - The Ultimate Damage Control System*. URL: <https://koroyd.com/>.
- [134] Jikai Liu et al. “Current and future trends in topology optimization for additive manufacturing”. In: *Structural and Multidisciplinary Optimization* 57.6 (2018), pp. 2457–2483. ISSN: 16151488. DOI: 10.1007/s00158-018-1994-3.
- [135] Yu-an Jin et al. “Additive manufacturing of custom orthoses and prostheses—a review”. In: *Procedia Cirp* 36 (2015), pp. 199–204. ISSN: 2212-8271.
- [136] Abid Haleem and Mohd Javaid. “Additive manufacturing applications in industry 4.0: a review”. In: *Journal of Industrial Integration and Management* 4.04 (2019), p. 1930001. ISSN: 2424-8622.
- [137] ISO/TC 261. *ISO/ASTM 52900:2015(en), Additive manufacturing — General principles — Terminology*. 2015. URL: <https://www.iso.org/obp/ui/#iso:std:iso-astm:52900:ed-1:v1:en>.
- [138] Tuan D. Ngo et al. “Additive manufacturing (3D printing): A review of materials, methods, applications and challenges”. In: *Composites Part B: Engineering* 143.December 2017 (2018), pp. 172–196. ISSN: 13598368. DOI: 10.1016/j.compositesb.2018.02.012.
- [139] R M German. *Sintering Theory And Practice*. New York: John Willy & Sons. 1996.
- [140] C Davidson. “Investigating the suitability of laser sintered elastomers for running footwear applications”. In: *Unpublished Doctoral Thesis Loughborough University* (2012).

- [141] T J Gornet et al. “Characterization of Selective Laser Sintering™ Materials to Determine Process Stability”. In: *2002 International Solid Freeform Fabrication Symposium*. 2002.
- [142] N. Raghunath and Pulak M. Pandey. “Improving accuracy through shrinkage modelling by using Taguchi method in selective laser sintering”. In: *International Journal of Machine Tools and Manufacture* 47.6 (May 2007), pp. 985–995. ISSN: 08906955. DOI: 10.1016/j.ijmachtools.2006.07.001.
- [143] R. D. Goodridge, C. J. Tuck, and R. J.M. Hague. “Laser sintering of polyamides and other polymers”. In: *Progress in Materials Science* 57.2 (Feb. 2012), pp. 229–267. ISSN: 00796425. DOI: 10.1016/j.pmatsci.2011.04.001.
- [144] Neil Hopkinson, Richard Hague, and Philip Dickens. *Rapid manufacturing: an industrial revolution for the digital age*. John Wiley & Sons, 2006. ISBN: 0470032863.
- [145] Dietmar Drummer, Dominik Rietzel, and Florian Kühnlein. “Development of a characterization approach for the sintering behavior of new thermoplastics for selective laser sintering”. In: *Physics Procedia* 5 (2010), pp. 533–542. ISSN: 1875-3892.
- [146] Hadi Zarringhalam et al. “Effects of processing on microstructure and properties of SLS Nylon 12”. In: *Materials Science and Engineering: A* 435 (2006), pp. 172–180. ISSN: 0921-5093.
- [147] Krassimir Dotchev and Wan Yusoff. “Recycling of polyamide 12 based powders in the laser sintering process”. In: *Rapid Prototyping Journal* (2009). ISSN: 1355-2546.
- [148] Wan Ahmad Yusoff. “The Application of Scanning Electron Microscope and Melt Flow Index for Orange Peel in Laser Sintering Process”. In: *Indonesian Journal of Electrical Engineering and Computer Science* 6.3 (2017), pp. 615–622.
- [149] Shwe P. Soe. “Quantitative analysis on SLS part curling using EOS P700 machine”. In: *Journal of Materials Processing Technology* 212.11 (Nov. 2012), pp. 2433–2442. ISSN: 09240136. DOI: 10.1016/j.jmatprotec.2012.06.012.

- [150] S. P. Soe, D. R. Eyers, and R. Setchi. “Assessment of non-uniform shrinkage in the laser sintering of polymer materials”. In: *The International Journal of Advanced Manufacturing Technology* 68.1-4 (Sept. 2013), pp. 111–125. ISSN: 0268-3768. DOI: 10.1007/s00170-012-4712-0.
- [151] Alva E Tontowi and T H C Childs. “Density prediction of crystalline polymer sintered parts at various powder bed temperatures”. In: *Rapid Prototyping Journal* (2001). ISSN: 1355-2546.
- [152] Jean-Pierre Kruth et al. “Consolidation of polymer powders by selective laser sintering”. In: *Proceedings of the 3rd international conference on polymers and moulds innovations*. 2008, pp. 15–30.
- [153] Brecht Van Hooreweder et al. “Microstructural characterization of SLS-PA12 specimens under dynamic tension/compression excitation”. In: *Polymer testing* 29.3 (2010), pp. 319–326. ISSN: 0142-9418.
- [154] H C H Ho, I Gibson, and W L Cheung. “Effects of energy density on morphology and properties of selective laser sintered polycarbonate”. In: *Journal of Materials Processing Technology* 89 (1999), pp. 204–210. ISSN: 0924-0136.
- [155] Siddharth Ram Athreya, Kyriaki Kalaitzidou, and Suman Das. “Processing and characterization of a carbon black-filled electrically conductive Nylon-12 nanocomposite produced by selective laser sintering”. In: *Materials Science and Engineering: A* 527.10-11 (2010), pp. 2637–2642. ISSN: 0921-5093.
- [156] David L Bourell et al. “Performance limitations in polymer laser sintering”. In: *Physics Procedia* 56 (2014), pp. 147–156. ISSN: 1875-3892.
- [157] Uzoma Ajoku et al. “Investigating mechanical anisotropy and end-of-vector effect in laser-sintered nylon parts”. In: *Proceedings of the Institution of Mechanical Engineers, Part B: Journal of Engineering Manufacture* 220.7 (2006), pp. 1077–1086. ISSN: 0954-4054.
- [158] Carsten Koch, Luke Van Hulle, and Natalie Rudolph. “Investigation of mechanical anisotropy of the fused filament fabrication process via customized tool path generation”. In: *Additive Manufacturing* 16 (2017), pp. 138–145. ISSN: 22148604. DOI: 10.1016/j.addma.2017.06.003.

- [159] Fady F. Abayazid and Mazdak Ghajari. “Material characterisation of additively manufactured elastomers at different strain rates and build orientations”. In: *Additive Manufacturing* 33 (May 2020), p. 101160. ISSN: 22148604. DOI: 10.1016/j.addma.2020.101160.
- [160] Ian Gibson and Dongping Shi. “Material properties and fabrication parameters in selective laser sintering process”. In: *Rapid prototyping journal* (1997). ISSN: 1355-2546.
- [161] J-P Kruth, Ming-Chuan Leu, and Terunaga Nakagawa. “Progress in additive manufacturing and rapid prototyping”. In: *Cirp Annals* 47.2 (1998), pp. 525–540. ISSN: 0007-8506.
- [162] J-P Kruth et al. “Consolidation phenomena in laser and powder-bed based layered manufacturing”. In: *CIRP annals* 56.2 (2007), pp. 730–759. ISSN: 0007-8506.
- [163] Samuel Clark Ligon et al. “Polymers for 3D Printing and Customized Additive Manufacturing”. In: *Chemical Reviews* 117.15 (Aug. 2017), pp. 10212–10290. ISSN: 0009-2665. DOI: 10.1021/acs.chemrev.7b00074.
- [164] Y Shi et al. “Effect of the properties of the polymer materials on the quality of selective laser sintering parts”. In: *Proceedings of the Institution of Mechanical Engineers, Part L: Journal of Materials: Design and Applications* 218.3 (2004), pp. 247–252. ISSN: 1464-4207.
- [165] *3D Printers, Software, Manufacturing & Digital Healthcare — 3D Systems*. URL: <https://www.3dsystems.com/>.
- [166] *Additive Manufacturing solutions & industrial 3D printer by EOS*. URL: <https://www.eos.info/en>.
- [167] Youquan Wen et al. “Enhancement of mechanical properties of metamaterial absorber based on selective laser sintering and infiltration techniques”. In: *Composites Communications* 21 (Oct. 2020), p. 100373. ISSN: 24522139. DOI: 10.1016/j.coco.2020.100373.
- [168] Leander Verbelen et al. “Analysis of the material properties involved in laser sintering of thermoplastic polyurethane”. In: *Additive Manufacturing* 15 (May 2017), pp. 12–19. ISSN: 22148604. DOI: 10.1016/j.addma.2017.03.001.

- [169] G.M. Vasquez et al. “A targeted material selection process for polymers in laser sintering”. In: *Additive Manufacturing* 1-4 (Oct. 2014), pp. 127–138. ISSN: 22148604. DOI: 10.1016/j.addma.2014.09.003. URL: <https://linkinghub.elsevier.com/retrieve/pii/S221486041400013X>.
- [170] Mike Vasquez et al. “Developing new laser sintering materials for snowboarding applications”. In: *Procedia Engineering* 34 (2012), pp. 325–330. ISSN: 18777058. DOI: 10.1016/j.proeng.2012.04.056.
- [171] *LUVOSINT® TPU – 3D-printing commercialized in the sports shoe industry*. URL: <https://www.luvocom.de/en/news-contact/news/details/article/luvosintr-tpu-3d-printing-commercialized-in-the-sports-shoe-industry/>.
- [172] Peter Frohn-Sörensen et al. “Additive Manufacturing of TPU Pneu-Nets as Soft Robotic Actuators”. In: (Nov. 2021), pp. 269–276. DOI: 10.1007/978-3-030-90700-6{_}30.
- [173] M Robinson et al. “Developing Elastomeric Cellular Structures for Multiple Head Impacts”. In: *IRCOBI conference 2017*. 2017.
- [174] S. P. Soe et al. “Feasibility of optimising bicycle helmet design safety through the use of additive manufactured TPE cellular structures”. In: *International Journal of Advanced Manufacturing Technology* 79.9-12 (Mar. 2015), pp. 1975–1982. ISSN: 14333015. DOI: 10.1007/s00170-015-6972-y.
- [175] S. Farajzadeh Khosroshahi, S. A. Tsampas, and U. Galvanetto. “Feasibility study on the use of a hierarchical lattice architecture for helmet liners”. In: *Materials Today Communications* 14 (Mar. 2018), pp. 312–323. ISSN: 2352-4928. DOI: 10.1016/J.MTCOMM.2018.02.002.
- [176] Siamak Farajzadeh Khosroshahi et al. “The effects of topology and relative density of lattice liners on traumatic brain injury mitigation”. In: *Journal of Biomechanics* 97 (Dec. 2019), p. 109376. ISSN: 0021-9290. DOI: 10.1016/J.JBIOMECH.2019.109376.
- [177] Eric C. Clough et al. “Elastomeric Microlattice Impact Attenuators”. In: *Matter* 1.6 (Dec. 2019), pp. 1519–1531. ISSN: 25902385. DOI: 10.1016/j.matt.2019.10.004.

- [178] Benjamin Hanna et al. “Auxetic Metamaterial Optimisation for Head Impact Mitigation in American Football”. In: *International Journal of Impact Engineering* (July 2021), p. 103991. ISSN: 0734-743X. DOI: 10.1016/J.IJIMPENG.2021.103991.
- [179] *HEXR - The world's first custom-fit cycling helmet*. URL: <https://hexr.com/>.
- [180] *KAV - Custom Bike and Hockey Helmets*. URL: <https://kavsports.com/>.
- [181] *Kupol — 3D gear*. URL: <https://www.kupol.ca/>.
- [182] Sun Deqiang, Zhang Weihong, and Wei Yanbin. “Mean out-of-plane dynamic plateau stresses of hexagonal honeycomb cores under impact loadings”. In: *Composite Structures* 92.11 (2010), pp. 2609–2621. ISSN: 0263-8223.
- [183] Simon R G Bates, Ian R Farrow, and Richard S Trask. “Compressive behaviour of 3D printed thermoplastic polyurethane honeycombs with graded densities”. In: *Materials & Design* 162 (2019), pp. 130–142. DOI: 10.1016/j.matdes.2018.11.019.
- [184] Jung Hyun Park and Jeong Ran Lee. “Developing fall-impact protection pad with 3D mesh curved surface structure using 3D printing technology”. In: *Polymers* 11.11 (Nov. 2019), p. 1800. ISSN: 20734360. DOI: 10.3390/polym11111800.
- [185] X. W. Zhang, Q. D. Tian, and T. X. Yu. “Axial crushing of circular tubes with buckling initiators”. In: *Thin-Walled Structures* 47.6-7 (2009), pp. 788–797. ISSN: 02638231. DOI: 10.1016/j.tws.2009.01.002.
- [186] V. Tinard, C. Deck, and R. Willinger. “New methodology for improvement of helmet performances during impacts with regards to biomechanical criteria”. In: *Materials & Design* 37 (May 2012), pp. 79–88. ISSN: 02613069. DOI: 10.1016/j.matdes.2011.12.005.
- [187] K. L. Johnson et al. “Constrained topological optimization of a football helmet facemask based on brain response”. In: *Materials and Design* 111 (2016), pp. 108–118. ISSN: 18734197. DOI: 10.1016/j.matdes.2016.08.064.

- [188] Vincent Caccese, James R. Ferguson, and Michael A. Edgecomb. “Optimal design of honeycomb material used to mitigate head impact”. In: *Composite Structures* 100 (June 2013), pp. 404–412. ISSN: 0263-8223. DOI: 10.1016/J.COMPSTRUCT.2012.12.034.
- [189] Rafael Santiago, Wesley Cantwell, and Marcílio Alves. “Impact on thermo-plastic fibre-metal laminates: Experimental observations”. In: *Composite Structures* 159 (Jan. 2017), pp. 800–817. ISSN: 0263-8223. DOI: 10.1016/J.COMPSTRUCT.2016.10.011.
- [190] Rafael C. Santiago et al. “The modelling of impact loading on thermo-plastic fibre-metal laminates”. In: *Composite Structures* 189 (Apr. 2018), pp. 228–238. ISSN: 0263-8223. DOI: 10.1016/J.COMPSTRUCT.2018.01.052.
- [191] Jörgen Bergström. *Mechanics of Solid Polymers: Theory and Computational Modeling*. 2015, pp. 1–509. ISBN: 9780323322966. DOI: 10.1016/C2013-0-15493-1.
- [192] Michael Robinson. “Developing novel materials to enhance motorcyclist safety”. PhD thesis. Dec. 2019.
- [193] Tod Dalrymple, Jaehwan Choi, and Kurt Miller. “Elastomer rate-dependance: A testing and material modelling methodology”. In.
- [194] Nikolaos Mavrodontis. *Modelling hyperelastic behavior using test data in Abaqus*. 2017. URL: <https://info.simuleon.com/blog/modelling-hyperelastic-behavior-using-test-data-in-abaqus>.
- [195] K. I. Romanov. “The drucker stability of a material”. In: *Journal of Applied Mathematics and Mechanics* 65.1 (Feb. 2001), pp. 155–162. ISSN: 0021-8928. DOI: 10.1016/S0021-8928(01)00017-X.
- [196] Shwe P. Soe et al. “Mechanical characterisation of Duraform® Flex for FEA hyperelastic material modelling”. In: *Polymer Testing* 34 (Apr. 2014), pp. 103–112. ISSN: 0142-9418. DOI: 10.1016/J.POLYMERTESTING.2014.01.004.
- [197] G. Berti et al. “Mechanical characterisation of PA-Al₂O₃ composites obtained by selective laser sintering”. In: *Rapid Prototyping Journal* 16.2 (Mar. 2010), pp. 124–129. DOI: 10.1108/13552541011025843.

- [198] *Calibrate a Material Model using DMA Data - PolymerFEM.com*. URL: <https://polymerfem.com/calibrate-a-material-model-using-dma-data/>.
- [199] G. Chagnon, G. Marckmann, and E. Verron. “A Comparison of the Hart-Smith Model with Arruda-Boyce and Gent Formulations for Rubber Elasticity”. In: *Rubber Chemistry and Technology* 77.4 (Sept. 2004), pp. 724–735. ISSN: 0035-9475. DOI: 10.5254/1.3547847.
- [200] Aidy Ali, M Hosseini, and B B Sahari. “A review of constitutive models for rubber-like materials”. In: *American Journal of Engineering and Applied Sciences* 3.1 (2010), pp. 232–239.
- [201] M. Forni, A. Martelli, and A. Dusi. “Implementation and Validation of Hyperelastic Finite Element Models of High Damping Rubber Bearings”. In: (Sept. 1999).
- [202] Mohammad Reza Khosravani and Tamara Reinicke. “On the Use of X-ray Computed Tomography in Assessment of 3D-Printed Components”. In: *Journal of Nondestructive Evaluation* 39.4 (2020), p. 75. ISSN: 15734862. DOI: 10.1007/s10921-020-00721-1.
- [203] Johannes Schneider and S. Kumar. “Multiscale characterization and constitutive parameters identification of polyamide (PA12) processed via selective laser sintering”. In: *Polymer Testing* 86.November 2019 (2020), p. 106357. ISSN: 01429418. DOI: 10.1016/j.polymeresting.2020.106357. URL: <https://doi.org/10.1016/j.polymeresting.2020.106357>.
- [204] K Manetsberger, J Shen, and J Muellers. “Compensation of non-linear shrinkage of polymer materials in selective laser sintering”. In: *2001 International Solid Freeform Fabrication Symposium*. 2001.
- [205] Fei Shen et al. “Energy absorption of thermoplastic polyurethane lattice structures via 3D printing: modeling and prediction”. In: *International Journal of Applied Mechanics* 8.07 (2016), p. 1640006. ISSN: 1758-8251.
- [206] K Dai and L Shaw. “Distortion minimization of laser-processed components through control of laser scanning patterns”. In: *Rapid Prototyping Journal* (2002). ISSN: 1355-2546.

- [207] Massimiliano Avalle, Giovanni Belingardi, and R Montanini. “Characterization of polymeric structural foams under compressive impact loading by means of energy-absorption diagram”. In: *International journal of impact engineering* 25.5 (2001), pp. 455–472. ISSN: 0734-743X.
- [208] Eric Qiuli Sun. “Shear locking and hourglassing in MSC Nastran, ABAQUS, and ANSYS”. In: *Msc software users meeting*. 2006, pp. 1–9.
- [209] *Friction and Friction Coefficients*. URL: https://www.engineeringtoolbox.com/friction-coefficients-d_778.html.
- [210] M. Launhardt et al. “Detecting surface roughness on SLS parts with various measuring techniques”. In: *Polymer Testing* 53 (2016), pp. 217–226. ISSN: 01429418. DOI: 10.1016/j.polymeresting.2016.05.022.
- [211] Genille Gimbel and Thomas Hoshizaki. “Compressive properties of helmet materials subjected to dynamic impact loading of various energies”. In: *European Journal of Sport Science* 8.6 (2008), pp. 341–349. ISSN: 17461391. DOI: 10.1080/17461390802438763.
- [212] *MathWorks - Makers of MATLAB and Simulink - MATLAB & Simulink*. URL: <https://uk.mathworks.com/>.
- [213] H.-M. Gutmann. “A Radial Basis Function Method for Global Optimization”. In: *Journal of Global Optimization* 2001 19:3 19.3 (Mar. 2001), pp. 201–227. ISSN: 1573-2916. DOI: 10.1023/A:1011255519438.
- [214] Erdem Acar. “Simultaneous optimization of shape parameters and weight factors in ensemble of radial basis functions”. In: *Structural and Multidisciplinary Optimization* 49.6 (Dec. 2014), pp. 969–978. ISSN: 16151488. DOI: 10.1007/s00158-013-1028-0.
- [215] *European Co-operation in the Field of Scientific and Technical Research COST 327 Motorcycle Safety Helmets Final Report of the Action European Commission Directorate General for Energy and Transport*. Tech. rep. 2001.
- [216] *Next-Generation Engineering Design Software — nTopology*. URL: <https://ntopology.com/>.
- [217] Linren Zhou et al. “Structural finite element model updating by using response surfaces and radial basis functions”. In: *Article Advances in Structural Engineering* 19.9 (2016), pp. 1446–1462. DOI: 10.1177/1369433216643876.

- [218] H Mustafa et al. “Impact attenuation of user-centred bicycle helmet design with different foam densities”. In: *Journal of Physics: Conference Series*. Vol. 1150. 1. 2019. DOI: 10.1088/1742-6596/1150/1/012043.
- [219] Yasmine Mosleh et al. “Designing safer composite helmets to reduce rotational accelerations during oblique impacts”. In: *Proceedings of the Institution of Mechanical Engineers, Part H: Journal of Engineering in Medicine* 232.5 (2018), pp. 479–491. ISSN: 20413033. DOI: 10.1177/0954411918762622.
- [220] F. M. Shuaeib et al. “Motorcycle helmet: Part II. Materials and design issues”. In: *Journal of Materials Processing Technology* 123.3 (May 2002), pp. 422–431. ISSN: 09240136. DOI: 10.1016/S0924-0136(02)00047-X.
- [221] B J Ramirez et al. “Tailoring the rate-sensitivity of low density polyurea foams through cell wall aperture size”. In: *Journal of Applied Physics* 121.22 (2017), p. 225107. ISSN: 0021-8979.
- [222] Michael Sandberg et al. “A computational study of the EN 1078 impact test for bicycle helmets using a realistic subject-specific finite element head model”. In: *Computer Methods in Biomechanics and Biomedical Engineering* 21.12 (2018), pp. 684–692. ISSN: 14768259. DOI: 10.1080/10255842.2018.1511775.
- [223] N J Mills and A Gilchrist. “Bicycle helmet design”. In: *Proceedings of the Institution of Mechanical Engineers, Part L: Journal of Materials: Design and Applications* 220.4 (2006), pp. 167–180. ISSN: 14644207. DOI: 10.1243/14644207JMDA100.
- [224] Alan M Nahum, Randall Smith, and Carley C Ward. *Intracranial pressure dynamics during head impact*. Tech. rep. 1977.
- [225] Warren N Hardy et al. “Investigation of head injury mechanisms using neutral density technology and high-speed biplanar X-ray.” In: *Stapp car crash journal* 45 (2001), pp. 337–368. ISSN: 1532-8546.
- [226] Xavier Trosseille et al. “Development of a FEM of the human head according to a specific test protocol”. In: *SAE transactions* 101.6 (1992), pp. 1801–1819. ISSN: 0096-736X.
- [227] Mazdak Ghajari et al. “Evaluation of the effective mass of the body for helmet impacts”. In: *International Journal of Crashworthiness* 16.6 (2011), pp. 621–631. ISSN: 13588265. DOI: 10.1080/13588265.2011.616078.

- [228] Petros Siegkas, David J. Sharp, and Mazdak Ghajari. “The traumatic brain injury mitigation effects of a new viscoelastic add-on liner”. In: *Scientific Reports* 9.1 (2019), pp. 1–10. ISSN: 20452322. DOI: 10.1038/s41598-019-39953-1.